

## INFORMATION TO USERS

This manuscript has been reproduced from the microfilm master. UMI films the text directly from the original or copy submitted. Thus, some thesis and dissertation copies are in typewriter face, while others may be from any type of computer printer.

**The quality of this reproduction is dependent upon the quality of the copy submitted.** Broken or indistinct print, colored or poor quality illustrations and photographs, print bleedthrough, substandard margins, and improper alignment can adversely affect reproduction.

In the unlikely event that the author did not send UMI a complete manuscript and there are missing pages, these will be noted. Also, if unauthorized copyright material had to be removed, a note will indicate the deletion.

Oversize materials (e.g., maps, drawings, charts) are reproduced by sectioning the original, beginning at the upper left-hand corner and continuing from left to right in equal sections with small overlaps. Each original is also photographed in one exposure and is included in reduced form at the back of the book.

Photographs included in the original manuscript have been reproduced xerographically in this copy. Higher quality 6" x 9" black and white photographic prints are available for any photographs or illustrations appearing in this copy for an additional charge. Contact UMI directly to order.

# UMI

A Bell & Howell Information Company  
300 North Zeeb Road, Ann Arbor MI 48106-1346 USA  
313/761-4700 800/521-0600



## **NOTE TO USERS**

**The original manuscript received by UMI contains pages with slanted print. Pages were microfilmed as received.**

**This reproduction is the best copy available**

**UMI**



**University of Alberta**

**Role of the Matrix in Bandbroadening on Polymeric HPLC Packings**

by

Barbara Ells



A thesis submitted to the Faculty of Graduate Studies and Research in partial  
fulfillment of the requirements for the degree of Doctor of Philosophy

Department of Chemistry

Edmonton, Alberta

Fall 1998



National Library  
of Canada

Acquisitions and  
Bibliographic Services

395 Wellington Street  
Ottawa ON K1A 0N4  
Canada

Bibliothèque nationale  
du Canada

Acquisitions et  
services bibliographiques

395, rue Wellington  
Ottawa ON K1A 0N4  
Canada

*Your file Votre référence*

*Our file Notre référence*

The author has granted a non-exclusive licence allowing the National Library of Canada to reproduce, loan, distribute or sell copies of this thesis in microform, paper or electronic formats.

The author retains ownership of the copyright in this thesis. Neither the thesis nor substantial extracts from it may be printed or otherwise reproduced without the author's permission.

L'auteur a accordé une licence non exclusive permettant à la Bibliothèque nationale du Canada de reproduire, prêter, distribuer ou vendre des copies de cette thèse sous la forme de microfiche/film, de reproduction sur papier ou sur format électronique.

L'auteur conserve la propriété du droit d'auteur qui protège cette thèse. Ni la thèse ni des extraits substantiels de celle-ci ne doivent être imprimés ou autrement reproduits sans son autorisation.


0-612-34759-1

**University of Alberta**  
**Library Release Form**

**Name of Author:** Barbara Ells  
**Title of Thesis:** Role of the Matrix in Bandbroadening on  
Polymeric HPLC Packings  
**Degree:** Doctor of Philosophy  
**Year this Degree Granted:** 1998

Permission is hereby granted to the University of Alberta Library to reproduce single copies of this thesis and to lend or sell such copies for private, scholarly, or scientific research purposes only.

The author reserves all other publication and other rights in association with the copyright in the thesis, and except as hereinbefore provided, neither the thesis nor any substantial portion thereof may be printed or otherwise reproduced in any material form whatever without the author's prior written permission.

  
\_\_\_\_\_

15 Main Street  
Middleton, Nova Scotia  
Canada  
B0S 1P0

Date: *Sept. 28, 1998*

**University of Alberta**

**Faculty of Graduate Studies and Research**

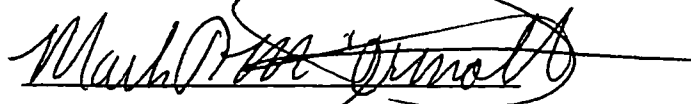
The undersigned certify that they have read, and recommended to the Faculty of Graduate Studies and Research for acceptance, a thesis entitled Role of the Matrix in Bandbroadening on Polymeric HPLC Packings submitted by Barbara Ells in partial fulfillment of the requirements for the degree of Doctor of Philosophy.



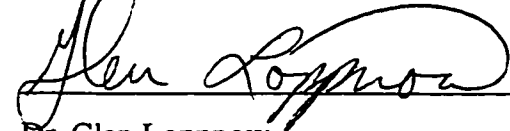
Dr. Frederick F. Cantwell




Dr. Norman Doyichi



Dr. Mark T. McDermott



Dr. Glen Loppnow



Dr. Janet Elliott



Dr. Charles H. Lochmüller

Date: *Sept. 28, 1998*

## Abstract

Due to slow diffusion within the polymer matrix, porous poly(styrene-divinylbenzene) (PS-DVB) HPLC packings give broad, tailed peaks for some compounds. Hamilton PRP- $\infty$  is a commercially available, nominally non-porous PS-DVB packing that can be used as a model for the matrix of these sorbents to study the offending processes.

Sorption isotherms and sorption rates are measured for naphthalene and octyl p-hydroxybenzoate, compounds having different solubility parameters. Sorption isotherms, measured by a column equilibration technique, show PRP- $\infty$  to have the same sorption capacity for both solutes, independent of solubility parameter. Sorption rate curves are measured by a shallow bed technique under conditions of "infinite solution volume". Fits of the curves with a monodisperse model show that diffusion of either solute through the sorbent is described by a single diffusion coefficient.

The literature shows that the addition of small amounts of THF to the mobile phase improves the efficiency of porous PS-DVB packings. The present work shows that the addition of 2% THF to an aqueous/methanol solvent decreases the sorption capacity of PRP- $\infty$  for naphthalene by 11%, while increasing the diffusion coefficient by 90%. Solvent swelling studies and sorption isotherms previously done in this laboratory show THF is sorbed by the polymer matrix from very low solution concentration, with no accompanying polymer swelling. This is interpreted as THF

sorption in permanent micropores, blocking sites within the polymer where diffusion is most hindered. This blockage reduces the sorption capacity of the polymer and increases the overall diffusion coefficient of the solute within the matrix.

Sorption isotherms of naphthalene on a commercial gigaporous PS-DVB packing, POROS 20 R2, indicate diffusion into the polymer matrix occurs. The addition of THF to the mobile phase decreases the sorption capacity for naphthalene, while improving the sorption kinetics, consistent with that seen on PRP- $\infty$ .

Elution peaks are predicted for columns of PRP- $\infty$  and POROS 20 R2 from the sorption rate data. The addition of small amounts of THF to the solvent is predicted to improve peak width and symmetry over that from a solvent containing no THF, consistent with the improvement in peak shape reported in the literature for porous PS-DVB packings.

*To my parents – for your love and support*

*... and your money!*

## **Acknowledgements**

I would like to thank Dr. Fred Cantwell for his guidance and patience over the course of this research. I am indebted to Clara Hernandez for many enlightening discussions. As well, I would like to thank Ying Wang for the providing the data for particle swelling and solvent sorption isotherms and Rakesh Bhatnager and George Braybrook for providing the electron micrographs. Financial support from the University of Alberta and NSERC is gratefully acknowledged.

## Table of Contents

	Page
<b>Chapter 1</b>	
<b>Introduction</b>	<b>1</b>
<b>Chapter 2</b>	
<b>Experimental Procedures</b>	
2.1	Sorbents 11
2.2	Reagents 11
2.3	Sample Solutions and Mobile Phases 13
2.4	Apparatus 14
2.5	Injection Loop Calibration 21
2.6	Hold-up Volume Measurements 22
2.7	Sorption Isotherm Measurements 23
2.8	Sorption Rate Measurements 27
2.9	Diffusion Coefficient Measurements 28
2.10	Electron Microscopy of PRP- $\infty$ 29
<b>Chapter 3</b>	
<b>Sorption Isotherms and Kinetics of Sorption of Naphthalene and Octyl p-Hydroxybenzoate on PRP-<math>\infty</math> from Methanol/Water Solutions</b>	
3.1	Introduction 32
3.2	Theory 33
3.2.1	Isotherms 33
3.2.2	Sorption Rate 38
3.2.2.1	Diffusion through a Monodisperse Sphere 41

3.2.2.2	Diffusion in Polymers	43
3.2.2.2.1	Diffusion through Pores	43
3.2.2.2.2	Diffusion through Polymers	48
3.2.3	Diffusion Coefficient Determination	50
3.2.4	Predicted Elution Profiles from Sorption Rate Curves	52
3.3	Results and Discussion	58
3.3.1	Sorption Isotherms	58
3.3.1.1	Naphthalene	59
3.3.1.2	Octyl p-hydroxybenzoate	61
3.3.2	Sorption Kinetics	63
3.3.2.1	Testing of Shallow Bed Conditions	65
3.3.2.2	Naphthalene Sorption Kinetics	67
3.3.2.3	Octyl p-hydroxybenzoate	71
3.3.2.3.1	Determination of Pre-Equilibration Time	71
3.3.2.3.2	Sorption Kinetics	72
3.3.3	Determination of Free-Solution Diffusion Coefficients	78
3.3.4	Predicted Elution Profiles	82
3.3.4.1	Predicted Profiles from Kinetic Studies	82
3.3.4.2	Effect of Flow Rate on Predicted Elution Profiles	89
3.3.5	Electron Microscopy Results	91
3.3.5.1	Transmission Electron Microscopy	91
3.3.5.2	Scanning Electron Microscopy	93

**Chapter 4      Effect of THF on Naphthalene Sorption Isotherms and Sorption Kinetics on PRP- $\infty$**

4.1	Introduction	97
4.2	Theory	98
4.3	Results and Discussion	99
4.3.1	Naphthalene Sorption Isotherms	100
4.3.2	Naphthalene Sorption Kinetics	107
4.3.3	Sorption of Methanol and THF by PRP- $\infty$ and the Resultant Swelling	113
4.3.4	Activity of Methanol and THF in Solution	122
4.3.5	Effect of THF on Naphthalene Sorption Isotherms	123
4.3.6	Effect of THF on Naphthalene Sorption Rate	126
4.3.7	Predicted Elution Profiles	130

**Chapter 5      Naphthalene Sorption Isotherms and Kinetics on POROS 20 R2**

5.1	Introduction	134
5.2	Theory	135
5.2.1	Perfusion Chromatographic Media	135
5.2.2	Diffusion in Bidisperse Media	142
5.3	Results and Discussion	144
5.3.1	Naphthalene Sorption Isotherms from Binary and Ternary Solutions	144
5.3.1.1	Naphthalene Sorption Isotherm from 70/30 Methanol/Water	145
5.3.1.2	Naphthalene Sorption Isotherm from 60/10/30 Methanol/THF/Water	150

5.3.2	Naphthalene Sorption Kinetics from Binary and Ternary Solutions	155
5.3.2.1	Testing of Shallow Bed Conditions	155
5.3.2.2	Naphthalene Sorption Kinetics from 70/30 Methanol/Water	155
5.3.2.3	Naphthalene Sorption Kinetics from Solutions of 68/2/30, 65/5/30, and 60/10/30 Methanol/THF/Water	161
5.3.3	Predicted Elution Profiles	170
<b>Chapter 6</b>	<b>Conclusions and Future Work</b>	
6.1	Conclusions	178
6.2	Future Work	181
	<b>Bibliography</b>	184
<b>Appendix 1</b>	<b>Experimental Data</b>	196
<b>Appendix 2</b>	<b>Matlab program used to predict elution profiles</b>	226

## List of Tables

Table	Page
2.1 Hold-up volumes for specific PRP- $\infty$ shallow beds	24
2.2 Hold-up volumes for specific POROS 20 R2 shallow beds	25
3.1 Fitting parameters from naphthalene sorption rate studies on PRP- $\infty$	69
3.2 Fitting parameters from octyl p-hydroxybenzoate sorption rate studies on PRP- $\infty$	75
3.3 Data for determination of free-solution diffusion coefficients	80
3.4 Verification of assumptions for determination of diffusion coefficients	81
3.5 Fitting parameters from bi-exponential fits to naphthalene and octyl p-hydroxybenzoate sorption kinetics on PRP- $\infty$	86
4.1 Values of $\kappa$ and $C_{s,max}$ for naphthalene sorption isotherms on PRP- $\infty$ from solvents of varying composition	107
4.2 Fitting parameters from naphthalene sorption rate studies on PRP- $\infty$ from binary and ternary solutions	111
4.3 Fitting parameters from bi-exponential fits to naphthalene sorption kinetics from ternary methanol/THF/water solutions	130
5.1 Fitting parameters from two-site Langmuir model fit to naphthalene isotherm on POROS 20 R2 from 70/30 methanol/water	148
5.2 Fitting parameters from two-site Langmuir fit to naphthalene sorption isotherm on POROS 20 R2 from 60/10/30 methanol/THF/water	153
5.3 Fitting parameters from fit of monodisperse model to naphthalene sorption kinetics on POROS 20 R2 from 70/30 methanol/water	158
5.4 Fitting parameters from fit of bidisperse model to naphthalene sorption kinetics on POROS 20 R2 from 70/30 methanol/water	158
5.5 Fitting parameters from fit of monodisperse model to naphthalene	165

sorption kinetics on POROS 20 R2 from ternary solutions of  
methanol/THF/water

5.6	Fitting parameters from bi-exponential fits to naphthalene sorption kinetics on POROS 20 R2	174
-----	--	-----

## List of Figures

Figure	Page
1.1 Schematic of structure of a non-porous PS-DVB particle	5
2.1 Solutes used in sorption isotherm and sorption kinetics studies	12
2.2 Apparatus for isotherm and kinetic measurements	16
2.3 Slider valve	17
2.4 Cross section of slider	19
2.5 Apparatus for diffusion coefficient measurements	30
3.1 Solute distribution isotherms with corresponding peak shapes	35
3.2 Spherical solute in a cylindrical pore	45
3.3 Naphthalene sorption isotherm on PRP- $\infty$ from 70/30 methanol/water	60
3.4 Octyl p-hydroxybenzoate sorption isotherm on PRP- $\infty$ from 70/30 methanol/water	62
3.5 Comparison of naphthalene and octyl p-hydroxybenzoate sorption isotherms on PRP- $\infty$ from 70/30 methanol/water	64
3.6 Testing of shallow bed conditions	66
3.7 Naphthalene sorption kinetics on PRP- $\infty$ from 70/30 methanol/water	68
3.8 Goodness of fit of monodisperse model to naphthalene sorption kinetics on PRP- $\infty$ from 70/30 methanol/water	70
3.9 Determination of pre-equilibration time	73
3.10 Octyl p-hydroxybenzoate kinetics on PRP- $\infty$ from 70/30 methanol/water	74
3.11 Goodness of fit of monodisperse model to octyl p-hydroxybenzoate sorption kinetics on PRP- $\infty$ from 70/30 methanol/water	76
3.12 Comparison of naphthalene and octyl p-hydroxybenzoate sorption kinetics on PRP- $\infty$ from 70/30 methanol/water	77
3.13 Bi-exponential fits to naphthalene sorption kinetics on PRP- $\infty$ from	83

70/30 methanol/water

3.14	Bi-exponential fits to octyl p-hydroxybenzoate sorption kinetics on PRP- $\infty$ from 70/30 methanol/water	84
3.15	Predicted naphthalene elution profiles from a PRP- $\infty$ column	87
3.16	Predicted octyl p-hydroxybenzoate elution profile from a PRP- $\infty$ column	88
3.17	Effect of flow rate on the predicted naphthalene elution profile from a PRP- $\infty$ column	90
3.18	Transmission electron micrograph of PRP- $\infty$ particles	92
3.19	Scanning electron micrograph of outer surface of a PRP- $\infty$ particle	95
3.20	Scanning electron micrograph of interior of a PRP- $\infty$ particle	96
4.1	Naphthalene sorption isotherm on PRP- $\infty$ from 68/2/30 methanol/THF/water	101
4.2	Naphthalene sorption isotherm on PRP- $\infty$ from 60/10/30 methanol/THF/water	103
4.3	Comparison of naphthalene sorption isotherms on PRP- $\infty$	104
4.4	Comparison of naphthalene sorption kinetics on PRP- $\infty$	109
4.5	Comparison of normalized naphthalene sorption kinetics on PRP- $\infty$	110
4.6	Goodness of fit of monodisperse model to naphthalene sorption kinetics on PRP- $\infty$ from ternary solutions	112
4.7	Solvent sorption isotherms on PRP- $\infty$	114
4.8	Swelling curves for PRP- $\infty$	116
4.9	Swelling-sorption curve for PRP- $\infty$ in methanol	118
4.10	Swelling-sorption curve for PRP- $\infty$ in THF	119
4.11	Bi-exponential fits to naphthalene sorption kinetics on PRP- $\infty$ from ternary solutions	132

4.12	Predicted naphthalene elution profiles from a column of PRP- $\infty$	133
5.1	Cross-section of a perfusive particle	137
5.2	van Deemter plots for macroporous and perfusive particles	139
5.3	The effect of electrochemical double-layer overlap on the electroosmotic flow profile	141
5.4	Naphthalene sorption isotherm on POROS 20 R2 from 70/30 methanol/water	146
5.5	Contributions of individual terms of two-site Langmuir fit to naphthalene sorption kinetics on POROS 20 R2 from 70/30 methanol/water	147
5.6	Naphthalene sorption isotherm on POROS 20 R2 from 60/10/30 methanol/THF/water	151
5.7	Contributions of individual terms of two-site Langmuir fit to naphthalene sorption kinetics on POROS 20 R2 from 60/10/30 methanol/THF/water	152
5.8	Comparison of naphthalene sorption isotherms on POROS 20 R2	154
5.9	Testing of shallow bed conditions	156
5.10	Naphthalene sorption kinetics on POROS 20 R2 from 70/30 methanol/water	157
5.11	Goodness of fit of monodisperse model to naphthalene sorption kinetics on POROS 20 R2 from 70/30 methanol/water	160
5.12	Comparison of naphthalene sorption isotherms from 70/30 methanol/water on PRP- $\infty$ and POROS 20 R2	162
5.13	Comparison of naphthalene sorption kinetics on POROS 20 R2 from binary and ternary solutions	163
5.14	Normalized naphthalene sorption kinetics on POROS 20 R2 from binary and ternary solutions	164
5.15	Goodness of fit of monodisperse model to naphthalene sorption kinetics on POROS 20 R2 from ternary solutions	166
5.16	Bi-exponential fits to naphthalene sorption kinetics from 70/30	171

methanol/water

5.17	Bi-exponential fits to naphthalene sorption kinetics on POROS 20 R2 from ternary solutions	172
5.18	Predicted elution profiles for naphthalene from a column of POROS 20 R2	176
5.19	Comparison of predicted elution profiles for naphthalene from columns of PRP- $\infty$ and POROS 20 R2	177
6.1	Predicted desorption rate curve for 5 $\mu\text{m}$ diameter silica particles	183

## List of Symbols

$a$	Tube radius (cm), eq. 3.25
$\bar{A}$	Term in van Deemter equation, eq. 3.6
$A_{\text{hold-up},T}$	Area of peak from unretained compound eluted from shallow bed, eq. 2.3
$A_{\text{inj}}$	Area of peak from unretained compound injected onto analytical column and eluted, eq. 2.3
$\bar{B}$	Term in van Deemter equation, eq. 3.6
$B$	Term in monodisperse model, eq. 3.9
$\bar{C}$	Term in van Deemter equation, eq. 3.6
$C_{\text{flask}}$	Concentration in flask used for injection loop calibration (M), eq. 2.1
$C_M$	Concentration in the mobile phase (M)
$C_S$	Concentration in the stationary phase (mol/g)
$C_{S,\text{max}}$	Maximum concentration of the solute in the stationary phase (mol/g)
$C_{\text{sat}}$	Concentration of a saturated solution (M), eq. 3.47
$C_0$	Concentration of external solution at pore entrance (M), eq. 3.16
$\langle C \rangle_0$	Concentration at pore entrance, averaged over pore cross-section (M), eq. 3.16
$C_L$	Concentration of external solution at pore exit (M), eq. 3.16
$\langle C \rangle_L$	Concentration at pore exit, averaged over pore cross-section (M), eq. 3.16
$D$	Intraparticle diffusion coefficient (cm <sup>2</sup> /s)
$D_i$	Intraparticle diffusion coefficient within the macropores (cm <sup>2</sup> /s), eq. 5.9

$D_i$	Intraparticle diffusion coefficient within the micropores ( $\text{cm}^2/\text{s}$ ), eq. 5.9
$D_M$	Diffusion coefficient in free solution ( $\text{cm}^2/\text{s}$ )
$D_p$	Diffusion coefficient in pure polymer ( $\text{cm}^2/\text{s}$ )
$D_{\text{pore}}$	Diffusion coefficient in pores corrected for solute sorption ( $\text{cm}^2/\text{s}$ ), eq. 5.8
$E$	Potential energy of a solute in a pore (J)
$F$	Fractional attainment of equilibrium in kinetic studies
$F$	Flow rate ( $\text{mL}/\text{min}$ ), eq. 3.30
$f$	Friction coefficient, eq. 3.18
$f(\lambda)$	Convection enhancement factor in van Deemter equation, eq. 5.1
$\bar{H}$	Plate height (mm)
$H_M$	Hindrance factor, eq. 3.21
$I_j$	Bessel function, eq. 3.41
$K$	Drag coefficient, eq. 3.15
$K_{\text{ads}}$	Thermodynamic equilibrium constant, eq. 3.3 and 5.10
$k_i$	Rate constant on site of type "i", eq. 3.33
$k_a$	Adsorption rate constant, eq. 3.36
$k_d$	Desorption rate constant, eq. 3.36
$k'$	Capacity factor
$L$	Length of tube or column (cm), eqs. 3.31 and 3.43
$n$	Integer, eq. 3.9
$n_{\text{elute}}$	Moles eluted from shallow bed (mol), eq. 2.5
$n_M$	Moles in mobile phase (mol), eq. 3.2
$n_s$	Moles sorbed by stationary phase (mol), eq. 2.5, 3.2

$n_i$	Moles sorbed at equilibrium on site of type "i" (mol), eq. 3.33
$n_0$	Total moles sorbed at equilibrium (mol), eq. 3.33
$p$	Equilibrium vapour pressure within a pore, eq. 4.6
$p_0$	Saturated vapour pressure of a liquid on a flat surface, eq. 4.6
$P'$	Polarity index, eq. 4.1
$P'_i(t_s)$	Probability associated with the fraction of molecules passing through the column without sorbing, eq. 3.40
$P_i(t_s)$	Probability associated with the fraction of molecules sorbing as they pass through the column, eq. 3.41
$Q_s$	Sorbed concentration of solute in macropores (mol/g), eq. 5.4
$Q_i$	Sorbed concentration of solute in micropores (mol/g), eq. 5.5
$Q_{av}$	Average concentration of solute through particle (mol/g), eq. 3.10
$Q_t$	Sorbed concentration of solute at time, $t$ (mol/g), eq. 3.9
$Q_0$	Sorbed concentration at time zero (mol/g), eq. 3.9
$Q_\infty$	Sorbed concentration at equilibrium (mol/g), eq. 3.9
$R$	Retardation factor, eq. 3.21
$R_g$	Gas constant, eq. 4.6
$r$	Particle radius (cm)
$r_p$	Pore radius (cm), Fig. 3.2, eq. 4.6
$r_s$	Solute radius (cm), Fig. 3.2
$r_x$	Radial distance from center of tube, eq. 3.25
$T$	Temperature, eq. 4.6
$t$	Time
$t_s$	Net retention time of solute
$t_M$	Retention time of unretained component, eq. 3.40

$U$	Flow velocity at radius, $r$ (cm/s), eq. 3.25
$U'$	Intraparticle velocity (cm/s), eq. 5.3
$\bar{U}$	Average linear velocity (cm/s), eq. 3.25
$\bar{U}_i$	Average linear velocity of sample (cm/s)
$\bar{U}_0$	Average linear velocity of mobile phase (cm/s)
$V$	Molar volume of a liquid, eq. 4.6
$V_{\text{hold-up}}$	Hold-up volume in shallow bed that is not part of the volume involved in the kinetic process (mL), eq. 2.4
$V_{\text{hold-up,T}}$	Total hold-up volume of the shallow bed (mL), eq. 2.3
$V_{\text{inj}}$	Injection volume (mL), eq. 2.2
$V_M$	Retention volume of an unretained component (mL), eq. 3.2
$V_{\text{pore}}$	Volume of pores in POROS 20 R2 involved in kinetic processes (mL)
$V_R$	Retention volume of peak at center of gravity (mL), eq. 3.44
$W_b$	Baseline width of eluted peak, eq. 3.27
$W_{\text{col}}$	Mass of sorbent in an analytical column (g), eq. 3.45
$W_s$	Mass of stationary phase (g), eq. 3.2
$W_{\text{SB}}$	Mass of shallow bed (g)
$\alpha$	Term in bidisperse model, eq. 5.6
$\beta$	Radial position of solute
$\chi_i$	Mole fraction of organic modifier or water, eqs. 4.6 and 4.7
$\delta$	Solubility parameter ( $\text{MPa}^{1/2}$ )
$\delta_N$	Thickness of Nernst diffusion film (cm), eqs. 3.4 and 3.5
$\delta(t_i)$	Dirac impulse function, eq. 3.40
$\epsilon$	Particle porosity, eq. 3.21

$\Phi$	Distribution coefficient of solute between bulk and pore solutions, eq. 3.15
$\phi$	Phase ratio of a real column, eq. 3.34
$\phi_{A/B/C}$	Volume-weighting term, eq. 4.2
$\gamma$	Surface tension of a liquid, eq. 4.6
$\gamma$	Term in bidisperse model, eq. 5.6
$\gamma_i$	Activity coefficient of organic modifier in solution, eqs. 4.7 and 4.8
$\eta$	Total sorption capacity of sorbent
$\eta_{gel}$	Sorption capacity of gel region, eqs. 3.23 and 3.24
$\eta_{\mu}$	Sorption capacity of micropores, eqs. 3.23 and 3.24
$\vartheta$	Free-volume of polymer
$\kappa$	Distribution coefficient ( mol/g/mol/L ), eq. 3.1
$\lambda$	Ratio of solute radius to pore radius, eq. 3.17
$\hat{\lambda}$	Ratio of hindrance parameter under the given conditions to the hindrance parameter in the pure polymer, eq. 3.22
$\hat{\lambda}_{gel}$	Ratio of hindrance parameter in the gel under the given conditions to the hindrance parameter in the gel in the pure polymer, eq. 3.22
$\hat{\lambda}_{\mu}$	Ratio of hindrance parameter in the micropores under the given conditions to the hindrance parameter in the micropores in the pure polymer, eq. 3.23
$\theta$	Contact angle, eq. 4.6
$\theta$	Tortuosity, eq. 3.21
$\hat{\theta}$	Ratio of tortuosity under the given conditions to tortuosity in the pure polymer, eq. 3.22
$\hat{\theta}_{gel}$	Ratio of tortuosity in the gel under the given conditions to tortuosity in the gel in the pure polymer, eq. 3.24

$\hat{\theta}_{\mu}$	Ratio of tortuosity in the micropores under the given conditions to tortuosity in the micropores in the pure polymer, eq. 3.24
$\rho$	Dry density of the particle (g/mL), eq. 3.21
$\sigma_t^2$	Variance of eluted peak, time units, eq. 3.27
$\sigma_{t,inj}^2$	Variance of injection plug, time units, eq. 3.32
$\tau$	Time required to inject sample plug, eq. 3.30

## Chapter 1

### Introduction

For Reversed-Phase High Performance Liquid Chromatography (RP-HPLC), silica-based packings have traditionally been the stationary phase of choice. In particular, totally porous microparticulate packings have gained widespread acceptance due to their high mechanical strength, efficiency, and the availability of a variety of particle diameters, pore diameters, surface modifications and surface areas (1, 2). The silica surface can be reacted with alkyl or alkyl-substituted chlorosilanes to give a bonded phase providing the functionality desired for a given separation, and endcapping can be used to eliminate some of the unreacted silanol groups on the silica surface. These packings are not ideal, however. After the processes of functionalization and endcapping, residual silanols still exist on the silica surface and act as strong adsorption sites. This can lead to an increase in retention, peak tailing, and column-to-column variability for basic compounds that undergo reaction with the acidic silanols (1-7). As well, xerogel type silicas should be used only within the pH range of 2 to 8. Under acidic conditions, the bonded silanes may be lost due to the acid hydrolysis of the Si-O-Si bond, while under basic conditions there is a dissolution of the silica support (1, 8). Recently, silicas formed by the aggregation of silica sols have been reported to be stable from a pH of 1 to a pH of 11 under appropriate operating conditions. This extension of the working pH range has been accomplished through the use of sterically protected functional groups, such as diisopropyl-substituted instead of dimethyl-substituted silanes, to protect the siloxane

bond, and by more highly endcapping the alkyl bonded silica to reduce the number of residual silanols (8-12).

An alternative to silicas for RP-HPLC are polymeric supports, such as those made from poly(styrene-divinylbenzene) (PS-DVB). These supports also offer high mechanical strength and narrow particle size distributions, as well as a variety of available pore sizes, functionalities, and surface areas. The advantages that these packings provide over silica include a homogeneous surface, little column-to-column variability, chemical stability over a pH range of 1 to 13, and the ability to derivatize the polymer to give stationary phases for RP-HPLC, normal phase HPLC, ion-exchange chromatography, and size exclusion chromatography (13-16).

The surface area of these polymers arises from an interconnecting series of pores whose classification is based on their diameter. Macropores are pores having a diameter  $\geq 50$  nm while mesopores have a diameter ranging between 2 and 50 nm (3, 17). The solid polymer matrix between the macro- and meso- pores is generally composed of highly cross-linked poly(styrene-divinylbenzene) (18, 19) in which there may be pores of diameter  $\leq 2$  nm called micropores.

These polymer stationary phases are synthesized by a suspension polymerization of styrene and a crosslinker, divinylbenzene, in a water-organic two-phase system. The styrene and divinylbenzene, along with an initiator for the polymerization, are stirred to form organic droplets in the water, the sizes of which determine the size of the resultant beads. If a macroporous polymer resin is desired, a porogen is present in the organic droplet. The porogen is a compound soluble in the

monomer but insoluble in the polymer. For a non-porous polymer, no porogen is present in the reaction mixture.

During the polymerization process, polymer chains grow and form highly crosslinked nuclei, as the result of the high concentration of crosslinking agent, divinylbenzene, initially present. These nuclei continue to grow outward, with the crosslinking density decreasing as the amount of available crosslinking agent is diminished, with the growing polymer chains precipitating as they reach a critical size. The beads produced then have highly crosslinked nuclei surrounded by regions with a gradation of crosslinking densities as the distance from a nucleus is increased. A non-porous particle bead consists of many of these highly crosslinked nuclei, closely spaced, connected by the less highly crosslinked regions, that have grown together and crosslinked to form a microsphere. For macroporous polymers, these microspheres grow together to form the particle bead with the porogen occupying a fraction of the particle volume between the microspheres. After polymerization, the porogen is removed leaving a rigid three-dimensional polymer having a network of pores, the size, distribution, volume and geometry of which are determined by the choice of porogen (15, 16, 20, 21).

Within the highly crosslinked nuclei are permanent micropores resulting from the spaces left between the polymer chains during synthesis, due to the rigidity imposed by the high crosslinking density. As the result of this rigidity, the permanent micropores are present whether the bead is dry or solvent-swollen. These permanent micropores are not easily swollen, even in good solvents. In the loosely crosslinked regions between the nuclei, which will be referred to as the gel region, the polymer

network completely collapses in the dry state, eliminating the spaces between the polymer chains. In the solvent-swollen state, the gel region is highly swellable and the spaces between the polymer chains become enlarged and accessible to solutes for diffusion. Between the highly crosslinked and gel regions, lies a continuum of crosslinking densities, which results in a continuum in the extent of collapse and swelling within the polymer network. In macroporous polymers, the pores resulting from the presence of the porogen during polymerization are not collapsed in the dry state (22-26). Figure 1.1 shows a representation of the structure of a non-porous particle bead.

The amount of crosslinker present during synthesis governs the microporosity and mechanical stability of the resultant polymer. A crosslinker percentage of less than 10% of the total monomer content produces polymers referred to as gels. In the presence of a good solvent, these gels can be swollen, pushing the polymer chains further apart, creating spaces. The lower the amount of crosslinker, the larger these spaces in the solvent-swollen gel, and the softer the polymer. Due to the lack of rigidity in these polymers, they are not suitable for the high pressures associated with HPLC but have been used in low and medium pressure chromatography (16, 20, 21, 27).

The commercially available microparticulate PS-DVB based packings for reversed-phase HPLC are highly crosslinked and most are of the macroporous type, although a non-porous material, PRP- $\infty$ , is available from Hamilton. Macroporous polymers available include PRP-1 and PRP-3 from Hamilton, PLRP-S (Polymer Laboratories),

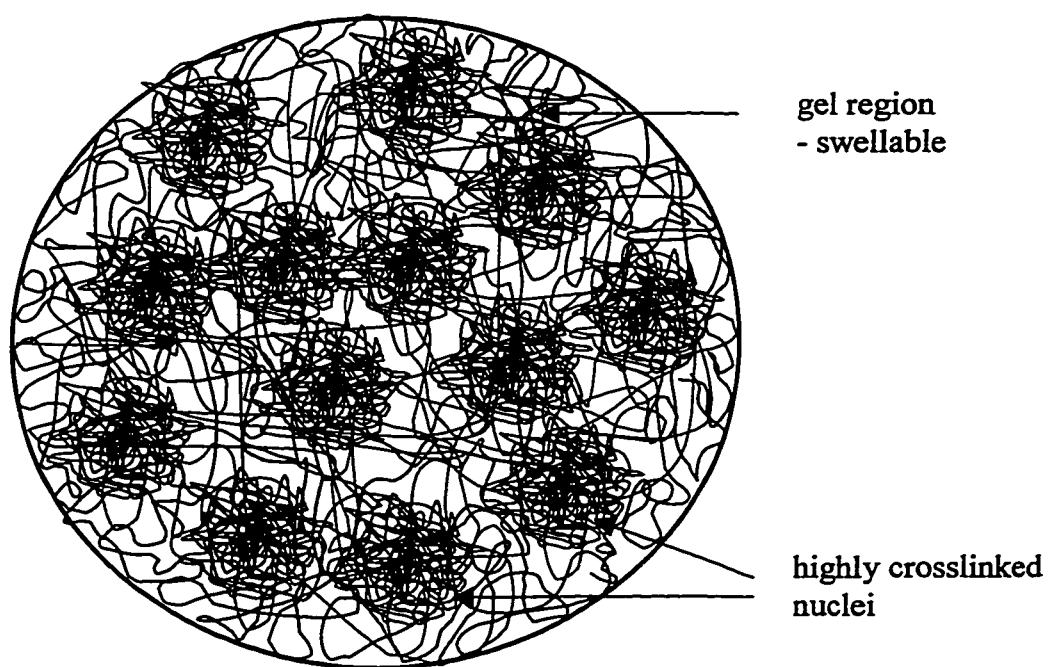


**Figure 1.1** Schematic of structure of a non-porous PS-DVB particle.

MCI Gel (Mitsubishi Kasei), Shodex RSpak (Showa Denko), Rogel (Bio-Rad), Polypore (Brownlee), Act-1 (Interaction), Finepak Gel (Jasco), and POROS (PerSeptive Biosystems).

Many of the applications of these polymers have focused on samples which exhibit poor efficiency with silica based packing materials due to their interaction with residual silanol groups on the surface of the silica. These types of compounds include relatively polar compounds such as amines, anilines, alkyl-substituted phenols, phenylalcohols, benzoic acids and carboxylic acids. Tailing, as seen with silica packings, was greatly reduced and linearity of calibration curves improved on PS-DVB (28, 29). As well, biologically active species such as proteins (14, 15, 30), peptides (31, 32), and pharmaceuticals (33-39) have been analyzed using PS-DVB packing materials. Non-porous PRP- $\infty$  and C<sub>18</sub> alkylated PRP- $\infty$  have been used in the separation of oligonucleosides, DNA fragments, and nucleic acids (32, 40, 41).

While most macroporous packings have pore diameters of under 500 Å, perfusion packings have recently been commercialized having pore diameters ranging between 4000 – 8000 Å. Two of these brands of packings materials are POROS (PerSeptive Biosystems) and PLRP-S 4000Å (Polymer Laboratories). The development of these packings was brought about as a way to reduce the resistance to mass transfer in the stagnant mobile phase (in the pores), which has been identified as being a major contributor to bandbroadening in liquid chromatography (2, 42, 43). The suspension polymerization of these packings results in microspheres approaching 1µm diameter being inter-adhered to give a particle with large throughpores, 4000-

8000 Å diameter. Convective, or "perfusive", flow through these gigapores can be obtained. The surface area from these large pores is small, so a second family of pores was introduced with diameters ranging from 800-1500 Å. These pores are diffusive in nature and have been kept shallow in order to ensure rapid transfer in the particle. The column efficiencies obtained with these columns only weakly depend on mobile phase velocity, and the reduced plate heights for 10 and 20 µm diameter particles have been found to be the same (44, 45). By taking advantage of the "perfusive" flow through these particles, separations can be achieved quickly and at high mobile phase velocities. These materials have been applied to the fast separations of proteins and peptides (15, 44-53).

Although PS-DVB polymer packings offer advantages over silica packings, they also have disadvantages. For non-polar aromatic and polyaromatic hydrocarbons they have been found to give asymmetric, tailing peaks (16, 54, 55) (56, 57). Several reasons, which are not totally independent of one another, have been suggested for this lack of efficiency, most of which relate back to the biporous nature of all macroporous PS-DVB polymers, arising from the presence of micropores (13, 55, 58, 59).

Steric selectivity has been suggested for the preferential retention of rigid, planar polyaromatic hydrocarbons over that of bulky aromatic compounds having rotational freedom of phenyl groups, which in turn are more highly retained than saturated hydrocarbons. This selectivity has been attributed, at least in part, to the structural matching between the rigid polymer matrix (micropores) and the solute (15, 55, 58, 60, 61).

Interaction between the  $\pi$  electrons of the underivatized PS-DVB matrix and the  $\pi$  electrons of solute molecules has also been said to contribute to peak tailing, bandbroadening, and strong retention. The retention of a solute is dependent on the electron withdrawing or donating nature of the compound. Since underivatized PS-DVB polymers are  $\pi$ -donors, electron-withdrawing substituents will promote stronger retention (16, 45, 54, 56, 62-64). The effects of the  $\pi$ - $\pi$  interactions have been seen to be decreased by reducing the electron density of the packing through modification of the surface (16, 65) to give lower retention times and more symmetrical peaks.

Slow diffusion of a solute molecule within the micropores or polymer matrix has also been thought to be a contributing factor to the poor efficiency seen with these packings (7, 15, 58, 66). The effects of microporosity have been studied using PS-DVB packings of different pore sizes with solutes of differing size (58). The column efficiencies for the different PS-DVB packings were found to be similar for a phthalate homologue, though the efficiency was expected to be better for the larger pore size packing since its mass transfer should have been faster. As a result, it was concluded that micropores were responsible for the column efficiencies found.

It has been suggested that the solubility parameters of the solvent and solute have an influence on the slow diffusion in the micropores. The solubility parameter,  $\delta$ , of a substance is defined as the square root of the cohesive energy density, which is a measure of the cohesive forces between molecules (67). If the solubility parameter of a solvent is not close to that of the polymer, such as is the case with methanol and PS-DVB, the solvent does not completely wet the polymer (68) and swelling in the

polymer is minimal. Efficiencies achieved on PS-DVB columns where methanol was the eluent have been found to be poor (54, 68). In good solvating systems where there is present an organic modifier with a solubility parameter close to that of the polymer matrix, such as THF, the polymer is swollen extensively. Swelling of the microporous structure increases the rate of diffusion in the polymer matrix (60). It has also been suggested that the solubility parameter plays a role in the ability of a solute to enter the polymer matrix (21, 66, 69). For a solute with a solubility parameter close to that of the matrix, the molecules sorb strongly to the polymer and are able to swell the polymer chains (56, 58), opening up micropores. The column efficiencies for some solutes that can enter the polymer matrix have been found to be temperature dependent (70) and have been interpreted as being due to a reduction in the restricted diffusion of the solute within the stationary phase.

The purpose of this study is to investigate the slow diffusion of solutes within the polymer matrix. Two solutes, naphthalene and octyl p-hydroxybenzoate, having different solubility parameters, are investigated under conditions where the solvent, methanol, poorly solvates the polymer matrix. Sorption isotherms, using a "column equilibration technique", and sorption rates, using a shallow bed technique under conditions of "infinite solution volume", are measured for both solutes from 70/30 methanol/water solutions and fit to theoretical equations. From the sorption rate curves, elution profiles for the solutes from a column of PRP- $\infty$  are predicted using a previously developed model.

Since the presence of a small amount of THF in the solvent has been shown in the literature to improve column efficiency, its effects on sorbent sorption capacity

and sorption rate for naphthalene are investigated. The sorption isotherms and sorption kinetics are measured from solutions of 68/2/30 methanol/THF/water and 60/10/30 methanol/THF/water and compared with those measured from 70/30 methanol/water solutions. Both the sorption isotherms and the sorption rate curves are fit with theoretical equations, and the elution profiles of naphthalene from a column of PRP- $\infty$  are predicted. An explanation of the role that THF plays within the polymer matrix is given.

A perfusion packing, POROS 20 R2, is also investigated to determine whether it is susceptible to the same losses in efficiency seen with the more traditional macroporous packings. It has been suggested that these types of packings may be applicable to capillary electrokinetic chromatography (71-73) since their wide pores would eliminate electrochemical double layer overlap within the pores (74) making electroosmotic flow through the particles possible. Naphthalene is used as the sample compound to investigate sorption capacity and sorption rate from a methanol/water solution and methanol/THF/water solutions. The sorption rate is described by the same model as that which describes diffusion into PRP- $\infty$  and changes occurring with the addition of THF to the mobile phase are compared to those seen on PRP- $\infty$ . Elution profiles for naphthalene from a column of POROS 20 R2 are predicted and compared with those predicted from a column of PRP- $\infty$ .

## Chapter 2

### Experimental Procedures

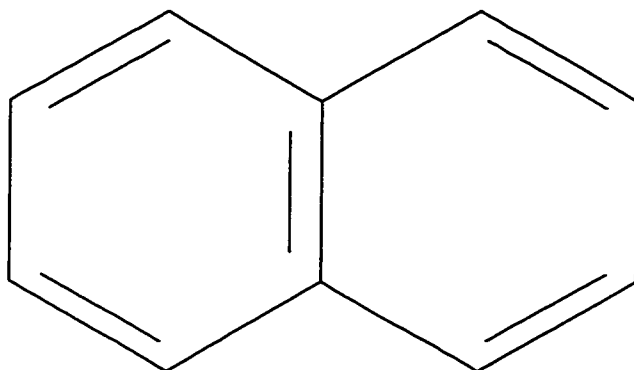
#### 2.1 Sorbents

Two poly(styrene-divinylbenzene) (PS-DVB) stationary phases were investigated in these experiments. PRP- $\infty$ , a 20  $\mu\text{m}$  diameter, spherical, nominally non-porous PS-DVB packing was donated by Hamilton Co. (Reno, NV). POROS 20 R2, a spherical, 20  $\mu\text{m}$  diameter, gigaporous packing was purchased from PerSeptive Biosystems (Framingham, MA).

#### 2.2 Reagents

Naphthalene (J. T. Baker Chemical Company, Phillipsburg, NJ) was recrystallized from methanol before use. Octyl p-hydroxybenzoate (Pfaltz & Bauer, Inc., Stamford, CN) was used as received. Phloroglucinol (Fisher Scientific Co., Fairlawn, NJ) was recrystallized from water. Anthraquinone (Aldrich) for injection loop calibration was used as received. Methanol (Fisher) was reagent grade and distilled and then filtered through a 0.45  $\mu\text{m}$  Nylon 66 membrane before use. Water was from a Barnstead NANOpure system, filtered through a 0.2  $\mu\text{m}$  filter. Reagent grade THF (Caledon) was distilled over sodium, passed through a column of alumina, and filtered through a 0.45  $\mu\text{m}$  Nylon 66 membrane before use.

a.



b.

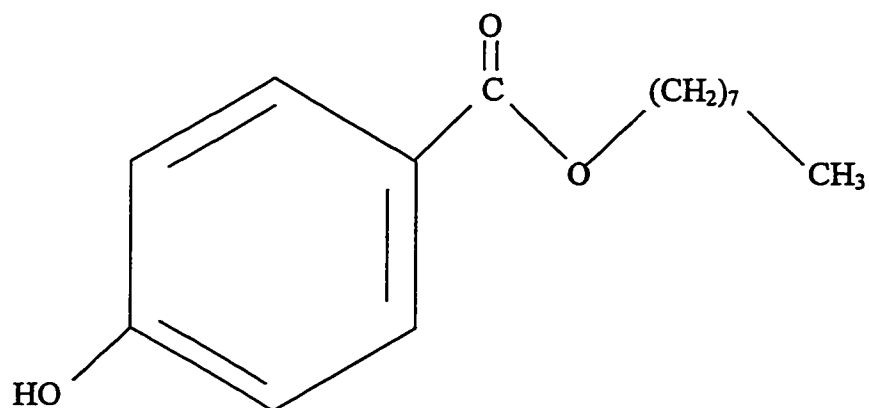


**Figure 2.1** Solutes used in sorption isotherm and sorption kinetics studies: a) naphthalene; b) octyl p-hydroxybenzoate

### 2.3 Sample Solutions and Mobile Phases

Both binary and ternary solutions were used in the measurement of sorption isotherms and sorption kinetics, with the solvent composition being determined by the combination of solvent volumes in the given proportions. The sorption kinetics and sorption isotherm of octyl p-hydroxybenzoate on PRP- $\infty$  were measured using a loading solution of 70/30 methanol/water. The eluent used was 100% methanol. Due to the high solubility of octyl p-hydroxybenzoate in 70/30 methanol/water, the solute was dissolved directly in the 70/30 methanol/water solution for each concentration studied.

For the naphthalene sorption kinetics and sorption isotherm on PRP- $\infty$ , a solution of 70/30 methanol/water was used for both loading and elution. At low concentrations, naphthalene was dissolved directly in the 70/30 methanol/water solution. For higher concentrations, where dissolution was slow, naphthalene was dissolved in the specified volume of organic solvent to which water, in the specified volume, was added after dissolution was complete. The saturation point for naphthalene in 70/30 methanol/water was determined by dissolving naphthalene, in the specified volume of organic solvent, in excess of its saturation concentration in the binary solution. After dissolution, the specified volume of water was added, and the solution was mixed well. The solution was then allowed to equilibrate for several hours in a 25°C water bath. The solution was then gravity filtered through Whatman #2 filter paper with the forerun being discarded. The concentration of the solution

was determined by diluting 50  $\mu$ L to 50 mL with a solvent of the appropriate composition and measuring its absorbance on a Hewlett-Packard UV-Vis diode-array spectrophotometer. The absorbance was converted to a concentration through the use of a calibration curve.

The sorption kinetics and sorption isotherms of naphthalene on PRP- $\infty$  were also measured at solution compositions of 68/2/30 and 60/10/30 methanol/THF/water, again where the solvent volumes were combined in the specified proportions. Naphthalene was dissolved in the solutions by the same method as detailed above.

Naphthalene sorption kinetics and sorption isotherm were measured from a 70/30 methanol/water solution on POROS 20 R2. The naphthalene sorption isotherm was also measured from a 60/10/30 methanol/THF/water solution, and the kinetics of sorption from solutions with solvent compositions 68/2/30, 65/5/30, and 60/10/30 methanol/THF/water. Again, naphthalene was put in solution by the method outlined above.

## 2.4 Apparatus

The apparatus used for the measurement of the sorption isotherms and sorption rates, not drawn to scale, is illustrated in Figure 2.2. Solutions were held in glass bottles within aluminum cylinders and delivered at constant pressure by use of  $N_2$  (75). The solutions passed through in-line 0.45  $\mu$ m pore diameter Durapore HV membrane filters (part HVLP04700, Millipore, Mississauga, ON) held in stainless

steel filter holders (part XX4404700, Millipore, Mississauga, ON), IF, and then to a 6-way rotary valve (ALTEX), V1. The solution being delivered to the shallow bed of sorbent was controlled by the position of the 6-way valve. The aluminum cylinders, in-line filters and connecting tubing were contained within a constant temperature water bath (not shown) kept at  $25 \pm 0.5^\circ\text{C}$  by a Haake D3 temperature controller (Fisher Scientific Co.).

The shallow bed of sorbent was contained within a slider valve mounted on an aluminum back plate. The valve and back plate were immersed in a plexiglass tank (not shown) on the front of the constant temperature bath and thermostated at  $25 \pm 0.5^\circ\text{C}$  by a circulating water bath (Colora Ultra-Thermostat, NB34784, Germany).

The heart of the apparatus was the slider valve and the shallow bed, which are illustrated in Figures 2.3 and 2.4, respectively, and are not drawn to scale. The slider valve has two 3 mm i.d. stainless steel tubes acting as inlets for solutions passing through the slider. The inlet on the left side of the slider valve allowed sample solutions to enter from the aluminum cylinders (via the 6-way valve), delivered under constant pressure by  $\text{N}_2$ , and flow through the shallow bed. The time of flow through the shallow bed was controlled by a 6-way valve (Cheminert, R 6031V6, LDC, Riviera Beach, FL), V2, placed after the slider valve and equipped with an infrared generator/detector position sensor (ECG 3101 P312, Dorval, QC) used for timing purposes. The time of loading was displayed to 0.1 ms on an electronic counter (5321B, Hewlett Packard). The inlet on the right side of the slider valve allowed the eluent, being pumped at

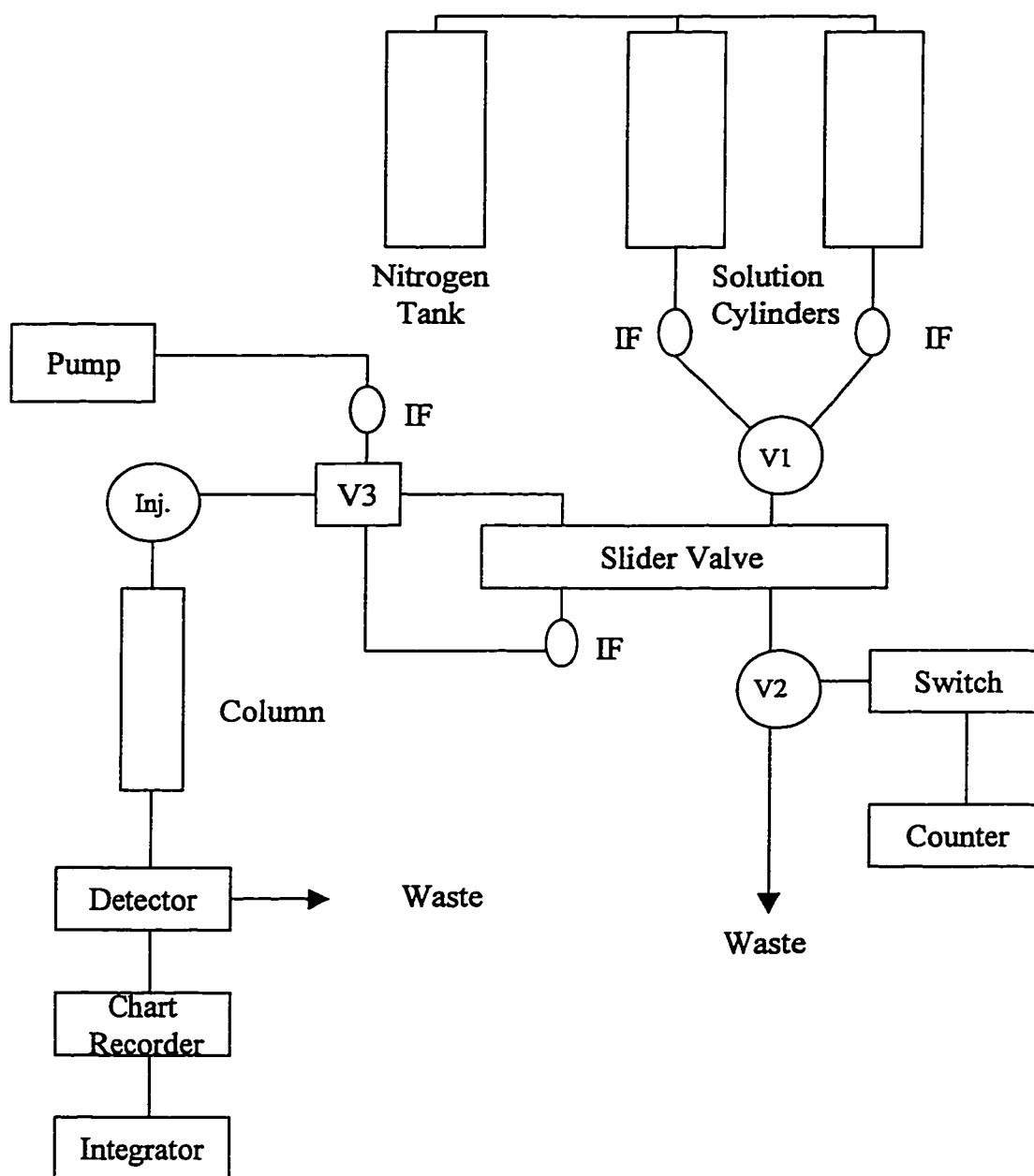


**Figure 2.2** Schematic of apparatus used for kinetic and isotherm measurements. V1, V2 and V3 are valves and IF is an inline filter.

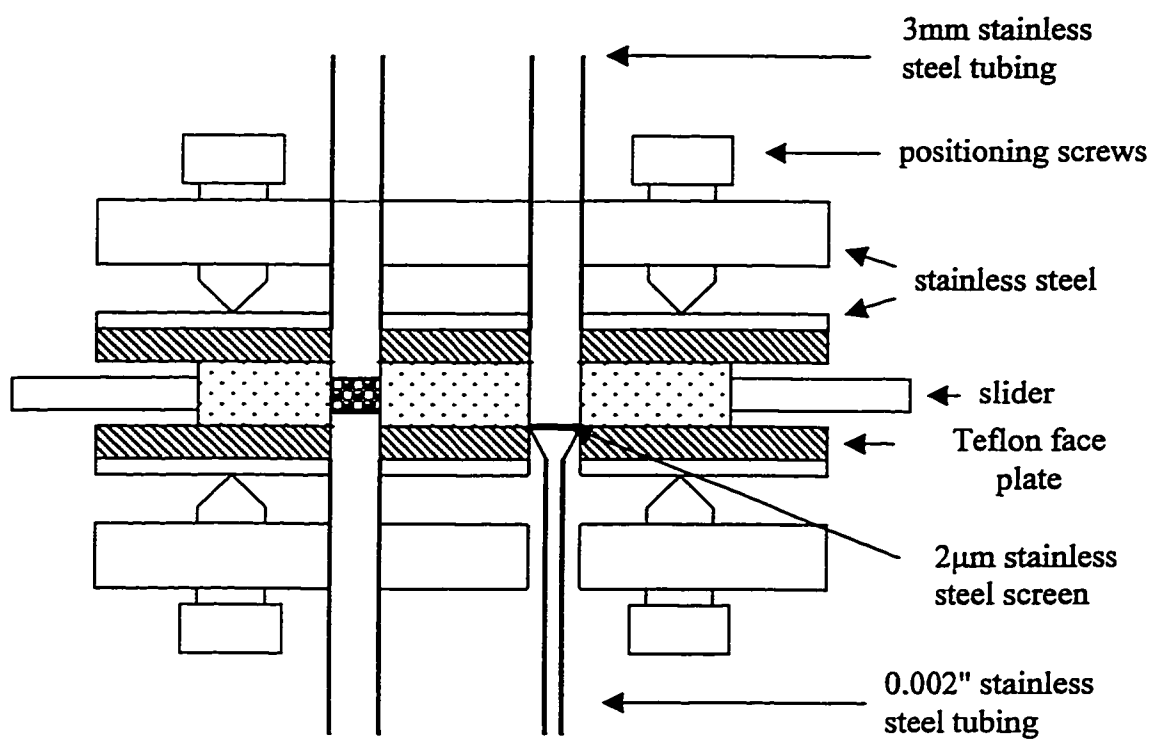


**Figure 2.3** Slider valve schematic.

constant flow (0.5 mL/min) by the HPLC pump (SP8000, Spectra-Physics, Santa Clara, CA), to flow through the shallow bed and elute the loaded sample. The flow path of the eluent solution being delivered by the HPLC pump was controlled with a four-way slider valve (Cheminert, CAV 4031, LDC, Riviera Beach, FL), V3. The flow from the HPLC pump was bypassing the slider valve except when the sample was being eluted from the shallow bed. This valve eliminated disturbances of the shallow bed due to solution flow during the moving of the slider between the loading and eluting positions.

The slider valve was made up of three parts: the stainless steel body, fabricated from ¼" stainless steel plates, the Teflon faceplates which provide the seal for the valve, and the slider. The stainless steel slider was 2 mm in height, 13 mm wide and 113 mm long and had an insert of Kel-F having dimensions of 2.2 mm x 9 mm x 73 mm. Two holes having diameters of 3 mm and spacing of 9.5 mm were made in the Kel-F to form a dummy hole and a hole for the shallow bed. The hole for the shallow bed had a stainless steel screen at the bottom with a diameter of 3 mm, a thickness of 0.076 mm, and a pore size of 2 µm, used to support the packing material. The packing material was kept in the top of the shallow bed by two 2.8 mm diameter Zitex membranes. One membrane was 0.2 mm thick with a pore size of 10-20 µm (H 662-123, Chemplast, Wayne, NJ). The other membrane was 0.64 mm thick with a pore size of 30-60 µm (K1064-122D, Chemplast, Wayne, NJ).

The slider was held in place in the valve body by two Teflon faceplates, having holes drilled in them to match up with the dummy and shallow bed holes. The

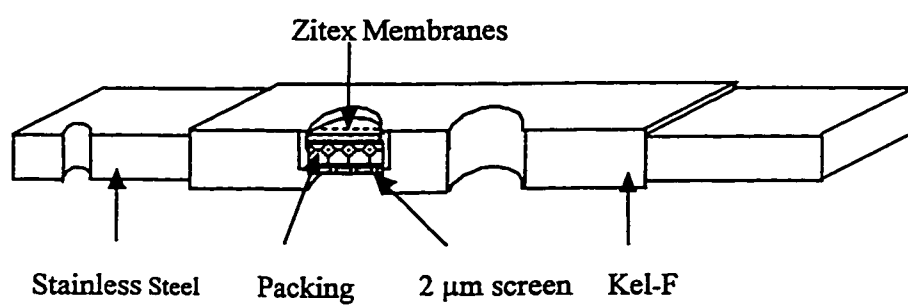


**Figure 2.4** Cross-section of the slider.

Teflon faceplates contacted only the Kel-F insert and provided the seal for the valve. The Teflon faceplates were attached to stainless steel plates by screws with Teflon tape placed between the Teflon faceplates and the stainless steel to ensure a good seal. The aforementioned inlets to the slider valve were silver-soldered to the stainless steel plates, which had holes drilled to match up with those in the Teflon faceplates and in the slider. Four positioning screws were used to provide the necessary pressure to the stainless steel plates to seal the valve. The slider is moved by means of two aluminum levers mounted on the back plate holding the slider valve. The slider is connected to the lever on the left side of the back plate by a cable, and to the lever on the right side by a stainless steel bar.

A 0.002" i.d. stainless steel tube acted as the outlet from the right side of the slider valve leading to an in-line filter (Model 7315, Rheodyne, Berkeley, CA), an injection valve (Model 7017, Rheodyne, Berkeley, CA), and to the analytical column. The analytical column was used to separate any impurities from the peak of interest, as well as to maintain backpressure. The analytical column used depended on the sample being studied. For octyl p-hydroxybenzoate, a 150 x 4.1 mm PRP-1 column (Hamilton Co., Reno, NV) was used. For naphthalene, a 150 x 3.9 mm  $\mu$ Bondapak phenyl column (Waters, Mississauga, ON) was chosen. The eluted sample passed through a UV detector (Lambda-Max Model 481 LC Spectrophotometer, Waters, Mississauga, ON) set at 256 nm for the determination of octyl p-hydroxybenzoate and at 276 nm for the determination of phloroglucinol and naphthalene. The resulting peaks were recorded on a chart recorder (Fisher) as well as on an integrator (Model 3390A, Hewlett Packard). For high concentrations in the isotherm studies, where the

maximum absorbances of the eluting sample exceeded a value of 2 absorbance units, the eluting samples were collected in volumetric flasks and the amount sorbed determined off-line using a diode-array UV-vis spectrophotometer (Model HP8452, Hewlett Packard).

## 2.5 Injection Loop Calibration

Calibration of the injection loop was necessary in order to make corrections for the hold-up volume in the shallow bed. To determine the volume of the injection loop,  $V_{inj}$ , the column and detector were disconnected from the injection valve. A  $1.633 \times 10^{-4}$  M anthraquinone solution in methanol,  $C_M$ , was injected and collected in a 10 mL volumetric flask, with five injections being collected per flask. A total of 25 injections, five flasks, were collected. Samples were diluted to volume with methanol and analyzed using a diode-array UV-vis detector (Model HP 8452 Hewlett Packard). Calculation of the concentration in a flask was through a calibration curve via the equation:

$$C_{flask} = \frac{\text{absorbance} - (y - \text{intercept})}{\text{slope}} \quad (2.1)$$

The injection volume could then be calculated using the equation:

$$V_{inj} = \frac{C_{flask} \cdot \frac{0.010L}{5_{inj}}}{C_M} \quad (2.2)$$

The volume of the injection loop,  $V_{inj}$ , was determined to be  $27.76 \pm 0.46 \mu\text{L}$  at the 95% confidence level.

## 2.6 Hold-up Volume Measurements

The hold-up volume of the shallow bed was determined using phloroglucinol as an unretained component. An  $8 \times 10^{-5}$  M solution of phloroglucinol was made up in the same solvent composition to be used in a particular sorption isotherm or sorption kinetics experiment. The solution was pumped through the shallow bed for 60 seconds, eluted through an analytical column, and the resulting peak integrated for area, to give  $A_{\text{hold-up,T}}$ . The detector was calibrated by injecting a volume of  $27.8 \pm 0.5 \mu\text{L}$  of the phloroglucinol solution onto the analytical column to give a peak with area,  $A_{inj}$ . The total hold-up volume,  $V_{\text{hold-up,T}}$ , of the column could then be calculated using the equation:

$$V_{\text{hold-up,T}} = V_{inj} \frac{A_{\text{hold-up,T}}}{A_{inj}} \quad (2.3)$$

For PRP- $\infty$ , a non-porous sorbent,  $V_{\text{hold-up,T}}$  was the total hold-up volume associated with the interparticle spaces in column as well as the spaces above and below the shallow bed in the slider. For POROS 20 R2 sorption rate studies,  $V_{\text{hold-up,T}}$

had to be corrected for the volume in the diffusive pores,  $V_{\text{pore}}$ , since diffusion of a sample in these pores is part of the kinetic process. The correction can be expressed by:

$$V_{\text{hold-up}} = V_{\text{hold-up,T}} - V_{\text{pore}} \quad (2.4)$$

The hold-up volume,  $V_{\text{hold-up}}$ , of POROS 20 R2 includes the volume of the perfusive pores since this volume is not involved in the kinetics process. The pore volume of the diffusive pores in the range of 20-1500 Å was estimated from mercury porosimetry measurements to be 0.71 mL/g (76). Multiplication of this value by the mass of packing in the shallow bed gave the volume of the diffusive pores. The hold-up volumes,  $V_{\text{hold-up,T}}$  or  $V_{\text{hold-up}}$ , for specific shallow beds can be found in Tables 2.1 and 2.2.

## 2.7 Sorption Isotherm Measurements

Prior to use in either a sorption isotherm or sorption kinetic study, the newly packed shallow bed had the eluent pumped through it for several hours to allow the unreacted monomer used in synthesis of the packing material to elute. The unreacted monomer was considered to be completely gone from the packing when the signal on the chart recorder returned to baseline.

**Table 2.1** Hold-up volumes for specific PRP- $\infty$  shallow beds.

Column number	Solute	Solvent (methanol/THF /water)	Study	Mass sorbent $W_{SB}$ (g)	$V_{hold-up,T}$ ( $\mu$ L)
1	Naphthalene	70/0/30	Isotherm	0.00268	9.0 $\pm$ 0.2
2			Kinetics	0.00283	9.0 $\pm$ 0.4
3				0.00284	10.0 $\pm$ 0.2
4				0.00275	9.4 $\pm$ 0.2
5	Octyl p-hydroxy-benzoate	68/2/30	Isotherm	0.00258	9.7 $\pm$ 0.3
6		68/2/30	Kinetics	0.00253	9.8 $\pm$ 0.2
7		60/10/30	Isotherm	0.00306	8.8 $\pm$ 0.2
8		60/10/30	Kinetics	0.00283	9.0 $\pm$ 0.2
9		70/0/30	Shallow Bed Conditions	0.00266	8.9 $\pm$ 0.2
10			Pre-equilibration time	0.00233	11.2 $\pm$ 0.3
11			Isotherm	0.00305	9.0 $\pm$ 0.4
12				0.00264	9.2 $\pm$ 0.5
13				0.00286	8.0 $\pm$ 0.2
14			Kinetics	0.00288	12.3 $\pm$ 0.4
15				0.00288	10.5 $\pm$ 0.4

**Table 2.2** Hold-up volumes for specific POROS 20 R2 shallow beds.

Column number	Solute	Solvent (methanol/THF/ water)	Study	Mass sorbent (g)	Hold-up Volume ( $\mu\text{L}$ )
1	Naphthalene	70/0/30	Isotherm	0.00076	$11.5 \pm 0.4^a$
2			Kinetics	0.00066	$10.7 \pm 0.3^b$
3		68/2/30	Kinetics	0.00068	$11.6 \pm 0.2^b$
4		65/5/30	Kinetics	0.00068	$10.4 \pm 0.2^b$
5		60/10/30	Kinetics	0.00068	$10.3 \pm 0.2^b$
6			Isotherm	0.00068	$10.8 \pm 0.2^a$

<sup>a</sup>  $V_{\text{hold-up},T}$  for POROS 20 R2 isotherm studies

<sup>b</sup>  $V_{\text{hold-up}}$  for POROS 20 R2 kinetic studies

The sorption isotherms of octyl p-hydroxybenzoate and naphthalene on PRP- $\infty$ , as well as the sorption isotherms of naphthalene on POROS 20 R2, were measured on the apparatus illustrated in Figure 2.2 using the "column equilibration technique" (77). The procedure used was as follows: With the eluent stream bypassing the shallow bed, the slider was pulled into the loading position. The selected sample solution was passed through the bed for the time found to be necessary for equilibrium to be reached. For octyl p-hydroxybenzoate on PRP- $\infty$ , this time was 60 minutes, while for naphthalene on the same sorbent from both binary and ternary solvents, the time was 90 minutes. For naphthalene on POROS 20 R2, the equilibrium time was 90 minutes from the binary solution and 45 minutes from the ternary solution. After loading for the desired amount of time, the flow of the loading solution was stopped and the slider pulled to the eluting position. The eluent stream was directed through the shallow bed, the sample was eluted, and the resulting peak integrated for area. The number of moles eluted,  $n_{\text{elute}}$ , was determined using a calibration curve which had been obtained by injecting appropriate standards through the analytical column to the detector. The number of moles eluted required correction due to the total hold-up volume of the shallow bed to determine the amount sorbed by the stationary phase,  $n_s$ .

$$n_s = n_{\text{elute}} - V_{\text{hold-up},T} \cdot C_M \quad (2.5)$$

Here,  $C_M$  is the concentration of the loading solution. The concentration sorbed by the stationary phase,  $C_s$ , was then obtained by dividing the amount sorbed by the mass of the packing in the shallow bed,  $W_{\text{SB}}$ .

$$C_S = \frac{n_S}{W_{SB}} \quad (2.6)$$

## 2.8 Sorption Rate Measurements

Sorption rate measurements were performed by a similar procedure to the sorption isotherm measurements. The apparatus used was again the one shown in Figure 2.2. The sample solution was allowed to flow through the shallow bed for some time ranging from 5 seconds to 90 minutes, depending on the sample being studied, while the eluent solution was bypassing the slider valve. The flow rate required to meet shallow bed conditions was exceeded during loading. After loading, the slider was moved to the elution position and the eluent stream switched to pass through the slider valve. The eluting sample peaks were integrated for area, and the amount of sample eluted calculated using a calibration curve. The correction for the hold-up volume in the kinetic studies on POROS 20 R2 used  $V_{\text{hold-up}}$  in place of the  $V_{\text{hold-up,T}}$  used in the sorption isotherm studies due to the amount of sample in the pores being involved in the kinetic processes. The concentration in the stationary phase was calculated using equations 2.5 and 2.6.

In the kinetic studies involving octyl p-hydroxybenzoate, the sample solution and eluent were of different composition. Therefore, between elution and loading, the shallow bed was pre-equilibrated for 30 minutes with a 70/30 methanol/water

solution, the same composition as the sample solution. This ensured that the packing was solvent-swollen to the same extent for each run within a kinetic study.

## 2.9 Diffusion Coefficient Measurements

Bulk diffusion coefficients were measured for octyl p-hydroxybenzoate in 70/30 methanol/water, for naphthalene in 70/30 methanol/water, and for naphthalene in 60/10/30 methanol/THF/water. The method used was based on the Taylor dispersion method (78-80) and was carried out on the apparatus illustrated in Figure 2.4.

To determine the diffusion coefficients, the solvent was degassed with helium and pumped at a constant pressure of 18 p.s.i. The solvent flowed through  $446 \pm 1$  cm of  $0.0279 \pm 0.0005$  cm i.d. stainless steel tubing, loosely coiled in a 9 cm diameter, kept in a constant temperature bath at  $25.0 \pm 0.2$  °C (Lauda K-2). Samples, with the same solvent composition as that being pumped, were injected via a six-port injection valve (Valco HP Series, Houston, TX) equipped with a 10  $\mu$ L injection loop. The resulting peak was detected using a Varian UV-50 flow cell detector set at 256 nm for octyl p-hydroxybenzoate and 276 nm for naphthalene, and recorded on a strip chart recorder.

The concentrations injected were  $8.628 \times 10^{-5}$  M octyl p-hydroxybenzoate in 70/30 methanol/water,  $9.685 \times 10^{-5}$  M naphthalene in 70/30 methanol/water, and  $1.026 \times 10^{-4}$  M naphthalene in 60/10/30 methanol/ THF/water.

## **2.10 Electron Microscopy of PRP- $\infty$**

Transmission and scanning electron microscopy were performed on the particles of PRP- $\infty$ . The sample preparation for the transmission electron microscopy involved wetting the particles with a 50% alcohol solution, and then immersing them for 2 hours in a 2% solution of OsO<sub>4</sub> in water. The particles were drained and embedded in an acrylic resin (LR white, Polysciences Inc., Warrington, PA) to ease the sectioning of the particles. The particles were sectioned to a thickness of 80 nm using an ultramicrotome. The sections were examined under the transmission electron microscope (Philips 201 Electron Microscope) at magnifications ranging from 3000 X to 100 000 X. Rakesh Bhatnager of the Department of Biological Sciences at the University of Alberta prepared the particles for sectioning and recorded the transmission electron micrographs.

The scanning electron microscopy was done on broken particles in order to examine the internal particle morphology. The particles were adhered to a stage and coated with a thin layer of chromium (10-15 Å) followed by a thin layer of gold (50 Å) to make them conductive. The scanning electron micrographs were obtained on a JEOL JSM 6301FXV microscope at magnifications ranging from 3500 X to 55 000

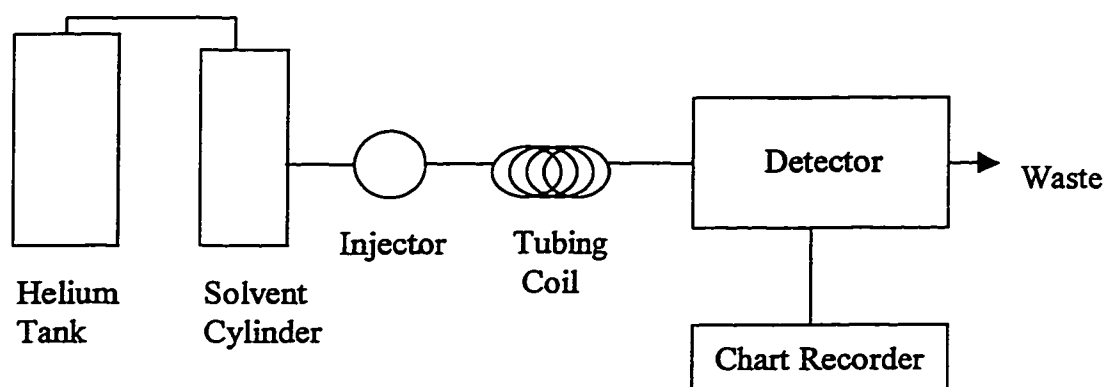


**Figure 2.5** Diffusion coefficient apparatus.

X. George Braybrook of the Department of Earth Sciences at the University of Alberta is responsible for the coating of the particles and the recording of the scanning electron micrographs.

## Chapter 3

### Sorption Isotherms and Kinetics of Sorption of Naphthalene and Octyl p-Hydroxybenzoate on PRP- $\infty$ from Methanol/Water Solutions

#### 3.1 Introduction

Poly(styrene-divinylbenzene), PS-DVB, stationary phases show poor efficiency for some compounds, most notably polyaromatic hydrocarbons, which have a solubility parameter close to that of the polymer matrix (21, 56, 66). Within the linear region of the isotherm, poor efficiency, i.e. bandbroadening and peak asymmetry, is the result of kinetic processes within the stationary phase. For naphthalene ( $\delta=20.2 \text{ (MPa)}^{1/2}$ ), a compound with a solubility parameter quite close to that of poly(styrene-divinylbenzene) ( $\delta=18.6\text{-}19.0 \text{ (MPa)}^{1/2}$ ), the slow kinetic processes in PRP- $\infty$  have previously been shown to be the result of hindered diffusion within the polymer matrix (81). In this study, the effect of solubility parameter is examined by comparing the sorption kinetics of naphthalene and octyl p-hydroxybenzoate ( $\delta=22.6 \text{ (MPa)}^{1/2}$ ), a compound whose solubility parameter is not quite as close to that of the polymer matrix.

The sorption isotherms for the solutes of interest, naphthalene and octyl p-hydroxybenzoate, on PRP- $\infty$  were obtained using the "column equilibration" method (77) in order to determine the linear regions of the isotherms and the sorbent capacity for the solute. From the linear regions of the isotherms, concentrations were chosen to perform the sorption kinetic studies. The kinetic studies for the two solutes were fit to a model for diffusion through a monodisperse sphere, as well as to a multi-

exponential equation that allowed for the prediction of an elution profile of the compounds from a chromatographic column.

## 3.2 Theory

### 3.2.1 Isotherms

As compounds move down a chromatographic column, they distribute themselves between the stationary and mobile phases. The ratio of the concentration of a compound in the stationary phase,  $C_S$ , to that in the mobile phase,  $C_M$  is the distribution coefficient,  $\kappa$ , for that compound:

$$\kappa = \frac{C_S}{C_M} \quad (3.1)$$

In the above equation, the units of concentration need not be the same in both phases. The capacity factor,  $k'$ , is the expression of the ratio of amounts in either phase, in the same units, thereby leading to a dimensionless term. This value can be related to the distribution coefficient through a phase ratio of the mass of stationary phase, expressed here as  $W_S$ , and the volume of the mobile phase,  $V_M$ .

$$k' = \frac{n_S}{n_M} = \kappa \frac{W_S}{V_M} \quad (3.2)$$

An isotherm is the description of the relationship between the concentration of a solute sorbed at equilibrium to the concentration of solute in solution, at a given

temperature. Three simple types of isotherms include linear, concave, and convex, while other more complex isotherms are also common (82, 83). In a linear isotherm, illustrated in Figure 3.1a, the distribution coefficient remains constant with a change in sample concentration. The distribution coefficient for a particular concentration in the mobile phase can be determined by taking the slope of the line that joins the origin to the point on the isotherm corresponding to the desired mobile phase concentration. Gaussian peak shapes result from linear isotherms as long as irreversible processes are rapid. A linear region can be found for most compounds at low concentration, even if the overall isotherm for the compound is non-linear.

Non-linearity in isotherms may be the result of a number of causes including non-homogeneity of the sorbent surface; interactions between sorbed sample molecules; surface saturation; and multilayer adsorption (82, 83). Concave isotherms, as illustrated in Figure 3.1b, often result when the solvent is strongly adsorbed, or when there is interaction between adsorbed solute molecules (83). This type of isotherm results in fronting chromatographic peaks. The fronting can be understood by considering the effect of concentration on  $k'$ , the fraction of the sample in the mobile phase, and the linear velocity of the sample,  $\bar{U}_i$ . The distribution coefficient,  $\kappa$ , and hence  $k'$ , is larger at higher concentrations for a concave isotherm. For a chromatographic band moving down a column, the center of the band is of higher concentration than the regions toward the front and back of the band, and as a result has a higher  $k'$ . A higher  $k'$  means the sample is spending less time in the mobile phase than those sample molecules in regions of lower concentration.

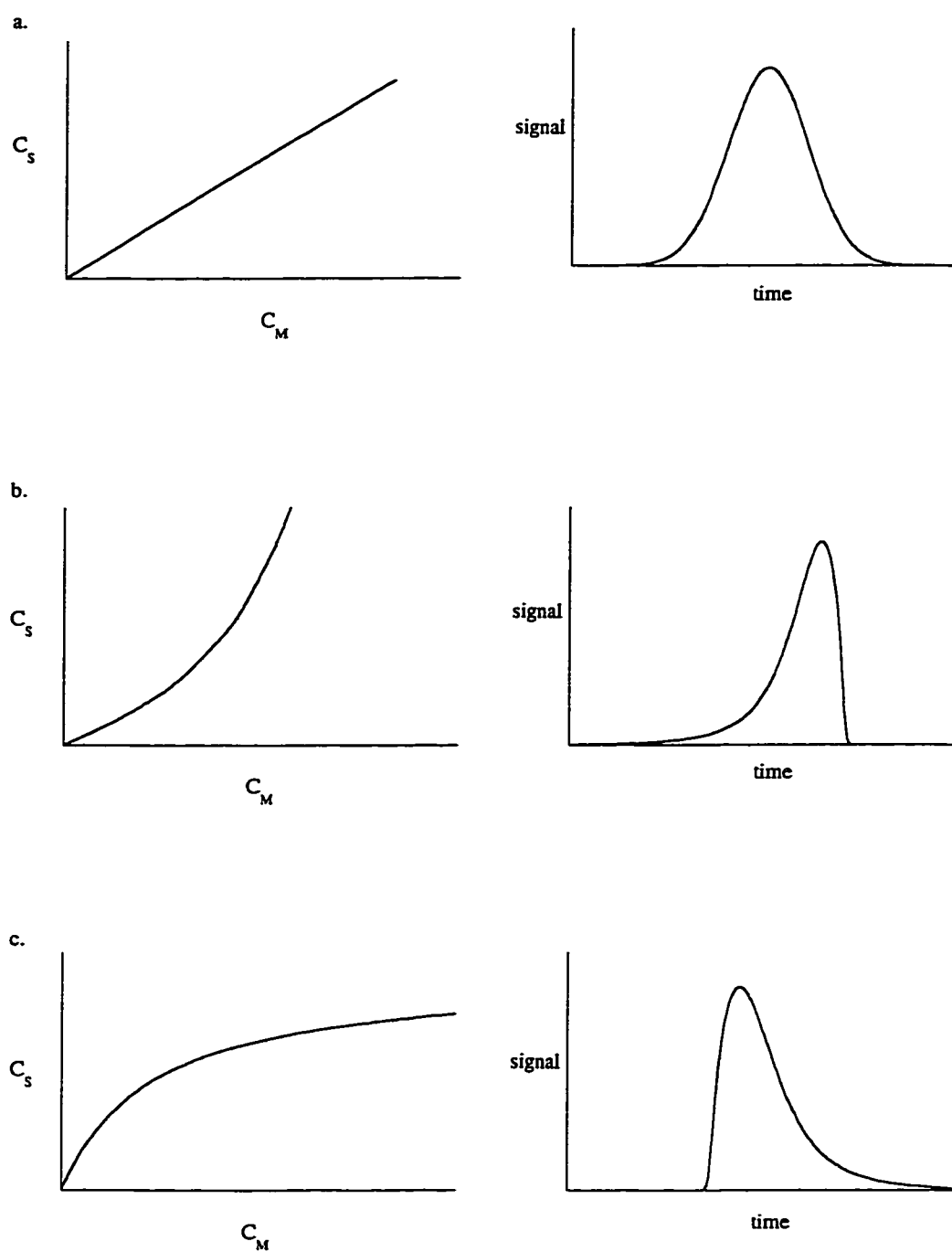


**Figure 3.1** Solute distribution isotherms shown with their corresponding chromatographic peak shapes. a) linear; b) concave; c) convex

For sample molecules in this high concentration region,  $\bar{U}_i$  is less than that for lower concentration regions. The lower concentration, more diffuse region of the band, travels through the column faster. The diffuse region in the back of the band catches up to the high concentration region, while the diffuse region on the leading edge of the band continues to move through the column faster and elutes first, producing a fronting peak.

Convex isotherms, illustrated in Figure 3.1c, are generally found for conditions of monolayer adsorption where there is little interaction between adsorbed sample molecules (82, 83). Convex isotherms produce tailing peaks, again as the result of concentration differences within the chromatographic band. At higher concentrations, the  $k'$  is lower, and the fraction of molecules in the mobile phase is higher than for the lower concentration regions. Therefore,  $\bar{U}_i$  in the more concentrated region is higher than in the lower concentration regions found toward the front and rear of the band. The higher concentration region overtakes the front part of the band in a "self-sharpening" fashion, while the diffuse back part of the band is more highly retained and elutes as a tail.

Convex isotherms are often fit by the Langmuir model given by the equation:

$$C_S = \frac{C_M \cdot K_{ads} \cdot C_{S,max}}{1 + C_M \cdot K_{ads}} \quad (3.3)$$

where  $C_{S,max}$  is the maximum concentration of the solute in the stationary phase, and  $K_{ads}$  is the thermodynamic equilibrium constant for adsorption. The model assumes that there is no lateral interaction between adsorbed sample molecules, all sites on the sorbent are equivalent, and a monolayer is the maximum amount of a sample that can be adsorbed (84). The Langmuir model has limiting forms at both low and high concentrations. At low concentration, the  $C_M \cdot K_{ads}$  term in the denominator of equation 3.3 becomes small with respect to 1, and the isotherm becomes linear. At high concentration, the  $C_M \cdot K_{ads}$  in the denominator becomes large with respect to one, and the amount sorbed in the stationary phase becomes a constant.

Isotherms can be measured using techniques that broadly fit into two categories: equilibrium and non-equilibrium methods. The non-equilibrium methods include using eluted peak maxima (85-89) and breakthrough profiles (85). Equilibrium methods include batch equilibrium (86-93), and column equilibration (85, 94-102). In this work, a column equilibration technique was used (77). The sample solution was passed through a shallow bed of packing until the stationary phase was in equilibrium with the loading solution, i.e., the influent and effluent were at the same concentration, and then eluted in order to quantitate the amount sorbed. Attainment of equilibrium was demonstrated by loading a sample for some time, followed by elution and quantitation of the sorbed solute. The same concentration sample was then loaded for a longer period of time, eluted and quantitated. When the amount sorbed no longer increased with loading time, equilibrium was assumed to be reached. Isotherm points were obtained over a wide range of concentrations in order

to determine the linear region of the isotherm as well as the capacity of the sorbent for the sample.

### 3.2.2 Sorption Rate

The transport of a solute from the bulk solution to the surface where it becomes sorbed can involve several processes. These process may include: film diffusion through the Nernst diffusion film surrounding the particle (103-105); intraparticle diffusion; and adsorption onto the pore wall surface (106, 107). Intraparticle diffusion may include the mass transfer processes of diffusion through the stagnant mobile phase in the macro- and meso- pores of the particle (104, 106-109), surface diffusion of the adsorbed solute along the walls lining the macro- and meso- pores (106, 109), and diffusion into the polymer matrix (105, 106).

Intraparticle diffusion and adsorption of a solute onto the surface of the particle are the processes controlling the intraparticle sorption rate. It has been suggested that a slow intraparticle sorption rate is responsible for poor efficiency of PS-DVB columns with some solutes. In most adsorbents, the adsorption step is considered to be very fast with respect to intraparticle diffusion and does not contribute to the observed sorption kinetics (107, 110). It is the intraparticle sorption rate that is of interest in this study. However, film diffusion, particle diffusion, or a combination of the two can control kinetics. Therefore, the contribution of film diffusion to the kinetics must be minimized.

The Nernst diffusion film is the quasi-stagnant mobile phase surrounding the sorbent particle. The thickness of this film,  $\delta_N$ , is dependent on the linear velocity of

the mobile phase,  $\bar{U}_0$ , and the radius of the particle,  $r$ , as expressed by the equations (103):

$$\delta_N \propto \frac{0.2r}{(1 + 70r\bar{U}_0)} \quad (3.4)$$

at a low linear velocity, and

$$\delta_N \propto \frac{0.0029}{\bar{U}_0} \quad (3.5)$$

at a high linear velocity. If the linear velocity through the column is sufficiently high, film thickness becomes negligible and diffusion through the layer becomes fast. At these high flow rates, the sorption rate is controlled entirely by intraparticle processes.

Intraparticle sorption rates have been studied using a variety of methods. Column chromatography has been used to obtain elution or frontal chromatograms for a solute on a particular packing. The plate heights,  $\bar{H}$ , can be calculated, plotted versus  $\bar{U}_0$ , and evaluated in terms of the vanDeemter equation (43, 58, 111, 112):

$$\bar{H} = \bar{A} + \frac{\bar{B}}{\bar{U}_0} + \bar{C}\bar{U}_0 \quad (3.6)$$

The intraparticle sorption rate, along with other bandbroadening processes, is found in the third term of this equation,  $\bar{C}\bar{U}_0$ , which is dependent upon the resistance to mass transfer in the stationary and stagnant mobile phases. In another method, moment analysis is performed on the chromatograms and evaluated in terms of theoretical equations to relate particle size and diffusion coefficients to the data (111,

113). With both of these methods, a correction for bandbroadening not related to intraparticle sorption rate must be made. These corrections include bandbroadening associated with eddy diffusion, resistance to mass transfer in the mobile phase, longitudinal diffusion, and extra-column sources, such as the detector, and may have to be estimated from theory.

As well, spectroscopic methods have been used to determine intraparticle sorption rates. Both pressure and temperature jump methods have been used to measure very fast adsorption-desorption rates as well as a slower relaxation which has been attributed to diffusion of molecules within the porous structure (114, 115). The interpretation of the relaxation data is ambiguous, and only measurements of intraparticle processes occurring within a short distance of the outer surface of the porous particle have been shown. Nuclear magnetic resonance (NMR) has also been used to measure diffusion rates in polymer systems (116, 117). Difficulties with this method have arisen due to the involvement of more than one diffusion coefficient whose magnitudes are often quite different, as well as the high magnetic field required to measure small diffusion coefficients.

Uptake measurements have also been used to determine intraparticle sorption rates. The uptake measurements can be performed using a batch mode, where a slurry of a known mass of packing is made in a solution of known concentration. The solution is stirred rapidly to eliminate Nernst diffusion films and the amount of uptake is measured as a function of time (103, 106, 109, 116, 118). This experiment can be performed under "infinite solution volume" conditions where the uptake is very small, such that the solute concentration is essentially constant throughout the

experiment, or "finite solution volume" where the uptake is significant. For "infinite solution volume" conditions, the uptake must be determined by removing some of the sorbent particles, eluting the solute, and quantitating the amount, while for "finite solution volume" either the sorbent or mobile phase can be monitored for differences.

A "shallow bed" column mode can be used for uptake rate measurements where sorbent particles are packed into a very short bed packed in a tube (21, 103, 119-121). A solution of known concentration is forced through the bed at a high linear velocity, such that the influent and effluent concentrations are nearly identical. This ensures that all particles in the bed are exposed to a solution of the same concentration, in essentially "infinite solution volume" conditions. The high linear velocity also ensures that Nernst diffusion films are minimized and intraparticle sorption is rate controlling. The exposure time of the sorbent to the solution is varied and the amount of uptake in that time determined through elution of the solute from the sorbent particles. The shallow bed method was used in these studies.

### **3.2.2.1 Diffusion through a Monodisperse Sphere**

Intraparticle diffusion through a monodisperse sphere where the external solution concentration is kept constant, i.e. infinite solution volume conditions, can be described using Fick's second law. For systems with spherical geometry and a single diffusion coefficient, the transport can be described by the equation (103, 109, 122):

$$\frac{\partial Q}{\partial t} = D \left( \frac{\partial^2 Q}{\partial r^2} + \frac{2}{r} \frac{\partial Q}{\partial r} \right) \quad (3.7)$$

where  $Q$  is the adsorbed concentration at time,  $t$ ;  $D$  is the diffusion coefficient within the particle; and  $r$  is the particle radius. The initial and boundary conditions for infinite solution volume conditions are given by:

$$Q(r,0) = Q_0 \quad Q(r \rightarrow \infty, t) = Q_\infty \quad \left( \frac{\partial Q}{\partial r} \right)_{r=0} = 0 \quad (3.8)$$

The uptake curve can then be described by the equation:

$$F = \frac{Q_{av} - Q_0}{Q_\infty - Q_0} = \frac{Q_t}{Q_\infty} = 1 - \frac{6}{\pi^2} \sum_{n=1}^{\infty} \frac{1}{n^2} \exp(-n^2 Bt) \quad (3.9)$$

where  $Q_{av}$  is the average concentration through the particle, as given by:

$$Q_{av} = \frac{3}{r^3} \int_0^r Q r^2 dr \quad (3.10)$$

and

$$B = \frac{\pi^2 D}{r^2} \quad (3.11)$$

Above,  $Q_0$  and  $Q_\infty$  represent the amounts sorbed at time zero and at equilibrium, respectively, and  $F$  is the fractional attainment of equilibrium.

To verify that the experimental data fit the above model, a plot of  $Bt$  versus  $t$  can be made. The data should fall on a straight line passing through the origin if the diffusion coefficient is not changing with the fractional attainment of equilibrium.

Equations for determining  $Bt$  have been previously derived (119). For values of  $F$  between 0 and 0.85:

$$Bt = 2\pi - \frac{\pi^2 F}{3} - 2\pi \left(1 - \frac{\pi F}{3}\right)^{1/2} \quad (3.12)$$

and for values of  $F$  between 0.85 and 1 the equation becomes:

$$Bt = -\ln \left( \frac{\pi^2}{6} (1 - F) \right) \quad (3.13)$$

This model has been applied to ion-exchangers (119, 120, 123), poly(styrene-divinylbenzene) adsorbents (121), and molecular sieves (124).

### 3.2.2.2 Diffusion in Polymers

The diffusion of a solute through  $PRP-\infty$  can be considered in terms of one of two models: diffusion through pores or diffusion through the polymer. If the polymer is considered to have pores that are filled with the bulk solvent in which the solute is dissolved, then the diffusion coefficient for the solute within the polymer pores can be referenced to that within free solution,  $D_M$ . If, however, the polymer is non-porous, or microporous, then diffusion is limited by the free volume within the matrix, and the reference for diffusion is that for diffusion within the pure polymer.

#### 3.2.2.2.1 Diffusion through Pores

The diffusion coefficient of a solute within a porous sorbent may be less than that in free solution due to the pores and the solute molecules being of comparable size. This is referred to as "hindered" or "restricted" diffusion. The decrease in the diffusion coefficient is the result of two effects: 1) increased hydrodynamic resistance, or frictional drag, on a solute molecule as the result of the close proximity of the pore walls and 2) steric exclusion of a solute from a fraction of the sorbent pore volume due to its large size with respect to the pore (125-127).

Models for hindered diffusion in porous media have generally been developed based on statistical and hydrodynamic considerations (126, 128-131). In the simplest case, a solute can be viewed as an uncharged hard sphere, having both Brownian and hydrodynamic characteristics, diffusing through an uncharged cylindrical pore. Assumptions for this theory include: the solute molecule is large with respect to solvent molecules; the pore wall is smooth on a particle scale; the length of the pore is much greater than its radius in order that mass transfer resistances at the entrance and exits may be ignored; and the bulk solution is sufficiently dilute that solute-solute interactions are negligible. Sorption and chemical interaction with the pore walls are not considered in the development of the model (125, 127, 131).

Consider a molecule of radius  $r_s$ , within a pore of radius  $r_p$ :

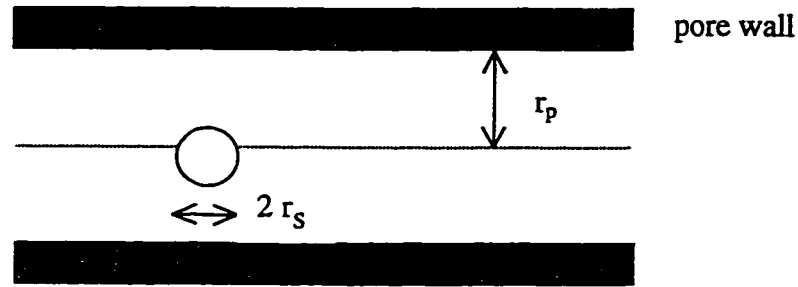


**Figure 3.2** Spherical solute in a cylindrical pore.

Let the ratio of the solute radius,  $r_s$ , to the pore radius,  $r_p$ , be represented by  $\lambda$ , and the radial position of the solute,  $r/r_p$ , be represented by  $\beta$ . The hinderance factor,  $D/D_M$ , can be expressed as (126):

$$\frac{D}{D_M} = K^{-1} \Phi \quad (3.15)$$

where  $K$  is the drag coefficient and  $\Phi$  is the distribution coefficient of a solute between the pore solution and bulk solutions. Brenner and Gaydos (131) give the relationship:

$$\Phi = \frac{\langle C \rangle_0}{C_0} = \frac{\langle C \rangle_L}{C_L} = 2 \int_0^{1-\lambda} e^{(-E/kT)} \beta d\beta \quad (3.16)$$

for the case where there is no interaction between the solute and the pore wall and the chances of finding a molecule at a given radial position follows the Boltzmann

distribution averaged over the pore cross-section.  $\langle C \rangle_0$  and  $\langle C \rangle_L$  are the molar concentrations of solute, averaged over the pore cross-section, just inside the pore entrance and exit, while  $C_0$  and  $C_L$  are the solute concentrations in the external solution at the pore entrance and exit. For the case of only steric interactions ( $E=0$ ), the above expression becomes (129, 132):

$$\Phi = (1 - \lambda)^2 \quad (3.17)$$

The center of a solute molecule cannot get closer to the pore wall than its radius,  $r_s$ , hence, only the fraction  $1 - \lambda$  of the pore cross-section is available to the solute.

The inverse of the drag coefficient,  $K^{-1}$ , the ratio of the drag on a solute molecule in the bulk solution to that within the pore, is given by the equation (126, 131):

$$K^{-1}(\lambda, \beta) = \frac{\int_0^{1-\lambda} \frac{f_\infty}{f(\lambda, \beta)} e^{(-E/kT)} \beta d\beta}{\int_0^{1-\lambda} e^{(-E/kT)} \beta d\beta} \quad (3.18)$$

The friction coefficients for the solute molecule outside and inside of the pore are given by  $f_\infty$  and  $f(\lambda, \beta)$ , respectively. A "centerline approximation",  $f(\lambda, 0)$ , is generally used for  $f(\lambda, \beta)$  since the values for a wide range of  $\lambda$  are known but only for  $\beta=0$ .

In order to determine the hindrance factor, the hydrodynamic function,  $K(\lambda, \beta)$ , is required. Again, only values of  $\lambda$  for the axisymmetric case ( $\beta=0$ , sphere

on the centerline) are available. There is evidence that this "centerline approximation" does give reasonably accurate estimates for the hindrance factor (127). For the case where  $E=0$ , the expression for  $K^{-1}$  becomes:

$$K^{-1}(\lambda, 0) = \frac{f_{\infty}}{f} \quad (3.19)$$

and the hindrance factor can be expressed as:

$$\frac{D}{D_M} = \frac{(1-\lambda)^2}{K} \quad (3.20)$$

Values for  $K$  have been tabulated for various values of  $\lambda$  (125, 133, 134).

For porous chromatographic sorbents, sorption on the pore walls, however, does occur. As well, pores in the sorbent particles are not cylindrical, but tortuous. Corrections to the above model for instantaneous adsorption onto the pore walls and tortuosity gives (108, 122):

$$D = \frac{D_M (1-\lambda)^2}{\theta \left( 1 + \frac{\kappa_i \rho}{\varepsilon} \right) K} = \frac{D_M H_M}{\theta (1+R)} \quad (3.21)$$

Here,  $H_M$  is the hindrance factor,  $\theta$  is the tortuosity factor,  $\kappa_i$  is the distribution coefficient for the solute on the sorbent,  $\rho$  is the density of the sorbent particle (dry g/swollen mL), and  $\varepsilon$  is the particle porosity. The term  $R$  is the retardation factor, comprised of the distribution coefficient and the particle density and porosity, thereby accounting for sorption on the pore walls.

PPR- $\infty$ , however, is a highly crosslinked, nominally non-porous polymer. The diffusion of a solute is through the polymer matrix itself and not through large pores. The matrix consists of a gel region that can be either solvent-swollen or collapsed, depending on solvent conditions, and permanent micropores within the highly crosslinked nuclei. Therefore the second model, diffusion through a polymer, may be the more appropriate model.

#### 3.2.2.2.2 Diffusion through Polymers

Due to the high crosslinking in PRP- $\infty$ , the diffusion of a small molecule may depend on the ease with which the polymer chains can move to accommodate the penetration of the molecule into the polymer matrix. If the solute molecule and the monomeric units of the polymer are of comparable size, then the co-operation of several polymer segments is needed to allow the penetration. The movement of several polymer segments to allow this penetration is easier as the free-volume of the solid is increased over that of the pure polymer (135). In a non-porous polymer where the polymer volume fraction ( $\vartheta$ ) is high, diffusion is free-volume ( $1-\vartheta$ ) limited (136-138). The measured diffusion coefficient of a solute within the matrix can no longer be related to that within the bulk solution, as only wetting solvents can enter the matrix and solvate the polymer chains. Organic solvents become enriched in the matrix and two distinct phases, bulk solution and matrix, do not exist. The diffusion coefficient can be related to the rate of diffusion of that solute within the pure polymer,  $D_p$  by the equation:

$$D = \frac{D_p \hat{\lambda}}{\hat{\theta}} \quad (3.22)$$

where  $\hat{\lambda}$  is the ratio of the hindrance parameter under the given conditions to the hindrance parameter within the pure polymer, and  $\hat{\theta}$  is the ratio of the tortuosity under the given conditions to the tortuosity in the pure polymer. The value of  $\hat{\lambda}$  is dependent on the ratio of solute to "pore" radius as described in section 3.2.2.2.1 and gets larger for less hindrance, while the value of  $\hat{\theta}$  gets smaller for less tortuosity. The "pores" in this case are the spaces between the polymer chains in either the gel or permanent micropore region. Equation 3.22 is similar to equation 3.21, with the exception that there is now no retardation term due to sorption of the solute. The distinction between sorption to the polymer chains and the molecule being present between two chains becomes blurred when diffusion is through a matrix of closely spaced polymer chains.

As described earlier, the polymer matrix is heterogeneous, with there being a continuum of crosslinking densities between the gel and permanent micropore regions. If for simplicity, this continuum is approximated by two regions, gel and permanent micropore ( $\mu$ ), then the relative contributions to the hindrance and tortuosity can be defined by:

$$\hat{\lambda}^{-1} = \frac{\eta_{gel} \hat{\lambda}_{gel}^{-1} + \eta_{\mu} \hat{\lambda}_{\mu}^{-1}}{\eta_{gel} + \eta_{\mu}} \quad (3.23)$$

and

$$\hat{\theta} = \frac{\eta_{gel}\hat{\theta}_{gel} + \eta_{\mu}\hat{\theta}_{\mu}}{\eta_{gel} + \eta_{\mu}} \quad (3.24)$$

where  $\eta$  is the sorption capacity of the sorbent and is equal to  $\eta_{gel} + \eta_{\mu}$ . For the reasons detailed above, it is this model that has been deemed more appropriate for the studies done here.

### 3.2.3 Diffusion Coefficient Determination

To determine the hindrance for a sample as it diffuses through the pores in a porous polymer, the diffusion coefficient in bulk solution,  $D_M$ , must be known. For diffusion through a non-porous polymer this value can be used only to show the differences in the magnitude of the diffusion coefficients within the polymer and that within bulk solution. The bulk solution diffusion coefficient can be measured using the Taylor dispersion method where an injected sample plug moves through a tube under laminar flow conditions. As the result of different flow velocities across the tube, a parabolic flow profile develops as described by the equation:

$$U = 2\bar{U}\left(1 - \left(\frac{r_x}{a}\right)^2\right) \quad (3.25)$$

where  $U$  is the flow velocity at radius  $r_x$ ,  $\bar{U}$  is the average linear velocity,  $r$  is the radial distance from the tube center, and  $a$  is the tube radius. The molecules in the

center of the tube ( $r_x = 0$ ) are moving the fastest, while molecules at the tube walls ( $r_x = a$ ) are not moving due to the drag exerted by the tube walls. The parabolic flow profile is partially relaxed by the lateral diffusion of sample molecules, giving a sample zone that is less dispersed than would be expected from laminar flow alone. The Taylor dispersion method relates the variance of the eluted peak,  $\sigma_t^2$ , to the diffusion coefficient,  $D_M$ , of the sample via the equation (139-143):

$$D_M = \frac{a^2 t}{24 \sigma_t^2} \quad (3.26)$$

where

$$\sigma_t^2 = \left( \frac{W_b}{4} \right)^2 \quad (3.27)$$

Here,  $t$  is the elution time of the peak and  $W_b$  is the baseline width of the eluted peak.

For equation 3.26 to be valid, three assumptions must hold (78, 79, 122, 144). First, the time necessary for lateral variations in concentration to become negligible is short with respect to the time required for changes to occur in concentration through longitudinal convection. This condition is met if:

$$\frac{a^2}{D_M t} \ll 1 \quad (3.28)$$

Secondly, longitudinal diffusion must be negligible with respect to the dispersion occurring as the result of the laminar flow and can be tested using the equation:

$$\frac{a^2 \bar{U}^2}{48 D_M^2} \gg 1 \quad (3.29)$$

Thirdly, the sample solutions used for the determination of the diffusion coefficient must be dilute.

It must also be determined that the contribution from the injector and detector cell to the overall peak variance is negligible. The time required to inject the plug of sample,  $\tau_{inj}$ , can be calculated using:

$$\tau_{inj} = \frac{V_{inj}}{F} \quad (3.30)$$

where  $V_{inj}$  is the injection volume in units of  $\text{cm}^3$ , and  $F$  is the flow rate in units of  $\text{cm}^3/\text{s}$ , which should be constant throughout the experiment.  $F$  can be calculated via:

$$F = \frac{\pi a^2 L}{t} \quad (3.31)$$

with  $L$  being the length of the tubing in units of  $\text{cm}$ . The injection plug variance,  $\sigma_{t,inj}^2$  can then be calculated (145) using the equation:

$$\sigma_{t,inj}^2 = \frac{\tau_{inj}^2}{12} \quad (3.32)$$

Similarly, assuming plug conditions, the contribution of the detector cell, with a volume  $V_{det}$  in units of  $\text{cm}^3$ , to the overall peak variance can be determined.

### 3.2.4 Predicted Elution Profiles from Sorption Rate Curves

A mathematical model has previously been developed and validated to predict the contribution of the intraparticle sorption rate to overall peak bandbroadening (146). Using this model, the elution profile of a compound from a specific HPLC column can be predicted. The model used was based on the fit of the kinetics of sorption to an empirical multi-exponential equation of the form:

$$F = 1 - \frac{n_1}{n_0} \cdot e^{-k_1 t} - \frac{n_2}{n_0} \cdot e^{-k_2 t} - \frac{n_3}{n_0} \cdot e^{-k_3 t} - \dots - \frac{n_i}{n_0} \cdot e^{-k_i t} \quad (3.33)$$

where  $F$  is the fraction of equilibrium moles sorbed at time,  $t$ ;  $n_1$  through  $n_i$  are the number of moles sorbed at equilibrium whose sorption rates can be described by the rate constants  $k_1$  through  $k_i$ , respectively; and  $n_0$  is the total number of moles sorbed, i.e.  $n_0 = n_1 + n_2 + n_3 + \dots + n_i$ . Within the linear region of the solute sorption isotherm, the values of  $n_1$  through  $n_i$  are proportional to the number of type 1 through type  $i$  "hypothetical sites" in the column, and  $n_0$  is proportional to the total number of hypothetical sites. It should be noted that the fit of the kinetics to this equation is not based on any theoretical model of particle or pore properties; it is purely empirical. There is no guarantee that a given set of experimental data will be fit by equation 3.33, but it has been the experience of this lab that data can usually be fit with a bi-exponential or tri-exponential equation.

This model for the prediction of elution peaks was developed based on the incorporation of the on-column rate expressions, from equation 3.33, into the mass balance equation for the column. For chromatography where slow kinetic processes are occurring, characterized by peak tailing, Giddings proposed a two-site model

based on statistical theory (147, 148). The first type of site exhibits rapid kinetics and produces the expected Gaussian profile, while the second type of site is responsible for the observed tailing due to its slow kinetic rate. The cause of the slow kinetics on the second type of site could be related to slow diffusion through the stagnant mobile phase occupying the pores of the sorbent, and/or slow adsorption-desorption onto the pore walls. Giddings showed how to solve the mass balance equations for kinetics following a bi-exponential sorption rate equation, by first solving two mass balance equations independently, each containing one of the exponential terms from the bi-exponential fit, to yield two elution profile equations. For molecules spending time on both the fast and slow sites, the profile of the peak is the convolution of these two equations, while for molecules only spending time on the faster sites the profile is only that from the faster sites. The overall predicted elution profile is the weighted sum of these two profiles.

The multi-exponential equation above is an extension of this model though no physical reality should be attached to the parameters in equation 3.33. In this model, a column is considered to have hypothetical types of sites,  $n_1$ ,  $n_2$ , through  $n_i$ , with the fractional amounts  $n_1/n_0$ ,  $n_2/n_0$ , through  $n_i/n_0$  which can be sorted based on type. Each type of site is then placed into its own hypothetical column, and the hypothetical columns are then considered to be placed in series. Each hypothetical column has the same length ( $L$ ), mobile phase linear velocity ( $\bar{U}_0$ ), retention time of an unretained component ( $t_M$ ), retention volume of an unretained component ( $V_M$ ), and weight of sorbent ( $W_{col}$ ), as the real chromatographic column.

For concentrations within the linear region of the isotherm, as is the case with the kinetic studies done here, the distribution coefficient,  $\kappa$ , of the solute on the real column is a constant. The capacity factor for a solute on the real column is then:

$$k' = \kappa \cdot \phi \quad (3.34)$$

where  $\phi$  is the phase ratio of the real column. For a solute on one of the hypothetical columns, the capacity factor becomes:

$$k'_i = \kappa \cdot \phi \cdot \frac{n_i}{n_0} \quad (3.35)$$

The rate constants obtained from fitting the multi-exponential equation to the sorption rate data are given by the  $k_i$  values. For reversible first-order sorption, the rate constant is related to the adsorption rate constant,  $k_{a,i}$ , and the desorption rate constant  $k_{d,i}$  by the equation:

$$k_i = k_{a,i} + k_{d,i} \quad (3.36)$$

The adsorption and desorption rate constants can be related to the capacity factor through the equation:

$$k'_i = \frac{k_{a,i}}{k_{d,i}} \quad (3.37)$$

By combining equations 3.34, 3.35, 3.36, and 3.37, the relation between the adsorption and desorption rate constants on a hypothetical column, to the rate

constant obtained from the multi-exponential fit and the capacity factor for that hypothetical column, are obtained:

$$k_{a,i} = k_i \cdot \frac{k_i'}{1+k_i'} \quad (3.38)$$

$$k_{d,i} = k_i \cdot \frac{1}{1+k_i'} \quad (3.39)$$

The peak resulting from injecting an impulse of solute onto any of the hypothetical columns can be predicted (107, 147, 148). For solute molecules which pass through the column without being sorbed,  $P'(t_s)$ , a spike at time  $t_M$  will result described by the equation:

$$P_i'(t_s) = \delta(t_s) \cdot e^{(-k_{a,i} \cdot t_M)} \quad (3.40)$$

Here,  $\delta(t_s)$  is the Dirac impulse function, an infinitely narrow pulse. The exponential term is the fraction of solute molecules that are not sorbed as they travel through the hypothetical column. With decreasing values for the adsorption rate constant, the number of molecules passing through the column without sorbing increases. As well, for increasing mobile phase velocity,  $t_M$  decreases and the number of molecules passing through the column without sorbing also increases. For fast sites, the value of the non-interacting fraction should be zero.

The elution profile for molecules that are sorbed as they travel through the column is given by:

$$P_i(t_s) = \left( \frac{k_{a,i} \cdot k_{d,i} \cdot t_M}{t_s} \right)^{1/2} \cdot I_j \left( \sqrt{4 \cdot k_{a,i} \cdot k_{d,i} \cdot t_M \cdot t_s} \right) \cdot e^{(-k_{a,i} \cdot t_M - k_{d,i} \cdot t_s)} \quad (3.41)$$

where

$$t_s = t - t_M \quad (3.42)$$

Above,  $I_j$ , is a Bessel function of imaginary argument for the parenthetic square root term. The elution profile predicted for each hypothetical column is the sum of  $P_i'(t_s)$  and  $P_i(t_s)$ . The overall predicted elution profile is the convolution of the elution profiles predicted from each exponential term, in series.

In order to predict the elution profiles, values for  $t_M$  and  $k'$  for a chromatographic column packed with the sorbent in question, are required. The value of  $t_M$ , in minutes, for a column of length,  $L$ , and linear velocity,  $\bar{U}_0$ , is:

$$t_M = \frac{L}{60 \cdot \bar{U}_0} \quad (3.43)$$

The value of  $k'$  can be determined from an experimental elution chromatogram, where:

$$k' = \frac{V_R - V_M}{V_M} = \frac{t_R - t_M}{t_M} \quad (3.44)$$

and the retention volume,  $V_R$ , or retention time,  $t_R$ , are measured at the peak's center of gravity (149, 150). As an alternative,  $k'$  can also be estimated using the equilibrium number of moles sorbed,  $n_0$ , found from the plateau in the sorption rate curve, as shown in equation 3.45:

$$k' = \frac{n_0 - C_M \cdot V_{\text{pore}}}{W_{\text{SB}} \cdot C_M} \cdot \frac{W_{\text{col}}}{V_M} \quad (3.45)$$

Here,  $C_M$  is the concentration of the solution used in the sorption rate study (mol/L);  $V_{\text{pore}}$  is the intraparticle pore volume in the shallow bed;  $W_{\text{SB}}$  is the mass of the shallow bed used in the experiment;  $W_{\text{col}}$  is the mass of the sorbent in the chromatographic column;  $V_M$  is the retention volume of an unretained compound on the chromatographic column; and  $\kappa$  is the slope of the isotherm in the linear region. In order to estimate  $k'$ , an accurate value of  $W_{\text{col}}$  is required. For a non-porous material,  $V_{\text{pore}}$  is equal to zero. For a sorption isotherm on a non-porous sorbent where mol/g sorbed have been plotted against the concentration in the mobile phase, equation 3.45 can be expressed using the distribution coefficient within the linear region of the isotherm:

$$k' = \kappa \frac{W_{\text{col}}}{V_M} \quad (3.46)$$

### 3.3 Results and Discussion

#### 3.3.1 Sorption Isotherms

### 3.3.1.1 Naphthalene

Before measuring sorption isotherm values for either naphthalene or octyl p-hydroxybenzoate, the hold-up volume of the shallow bed to be used was determined using the procedure described in section 2.6. The hold-up volumes for specific shallow beds can be found in Table 2.1. For PRP- $\infty$ , the hold-up volume included the spaces between the packing particles as well as the region above the shallow bed in the slider and that within and below the screen supporting the shallow bed.

The procedure used for obtaining the naphthalene sorption isotherm from 70/30 methanol/water was described in section 2.7, with the experiment being carried out on the apparatus illustrated in Figure 2.2. The isotherm was measured over a concentration range of  $1.07 \times 10^{-6}$  M to 0.04661 M, the latter being the saturation point for naphthalene in 70/30 methanol/water at 25°C.

The sorption isotherm for naphthalene on PRP- $\infty$  is shown in Figure 3.3. The solid line is the non-linear least squares fit of the solubility limited Langmuir equation (151):

$$C_S = \frac{C_{S,\max} \cdot K_{\text{ads}} \cdot \frac{C_M}{C_{\text{sat}}}}{1 + (K_{\text{ads}} - 1) \cdot \frac{C_M}{C_{\text{sat}}}} \quad (3.47)$$

where  $C_{\text{sat}}$  is the concentration of naphthalene in solution at saturation. The sorption capacity was measured at the saturation point to be  $(6.7 \pm 0.2) \times 10^{-4}$  mol/g and  $K_{\text{ads}}$  was found to be  $4.2 \pm 0.1$ . The linear region of the isotherm, up to  $2 \times 10^{-4}$  M, is

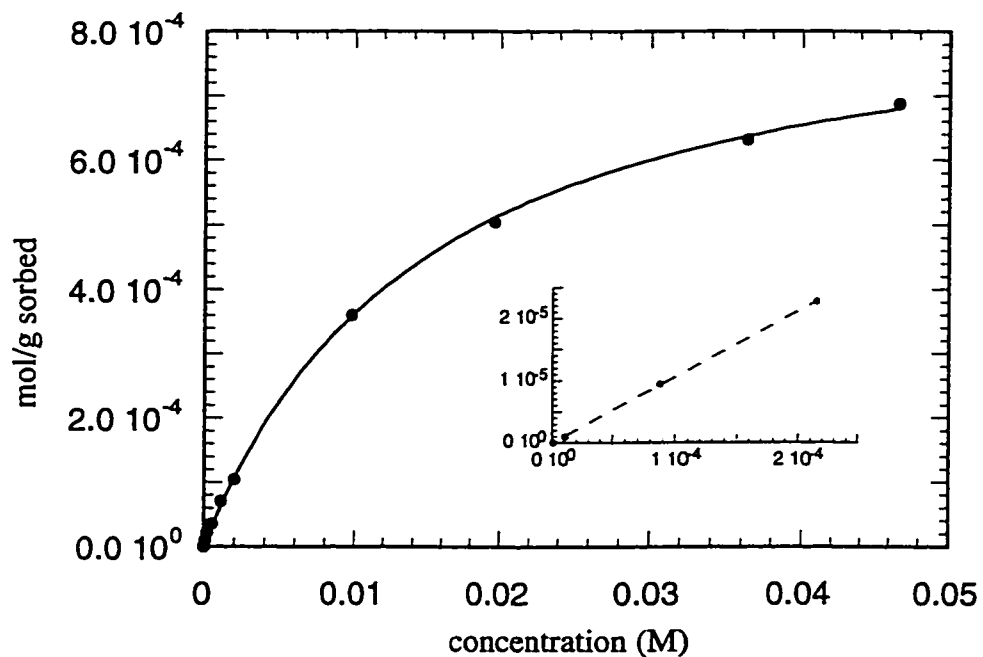


**Figure 3.3** Sorption isotherm of naphthalene on PRP- $\infty$  column 1 (Table 2.1) from 70/30 methanol/water. Solid line is the fit of the solubility limited Langmuir model, eq. 3.47. Linear region is inset with the dashed line being the linear least squares fit. Data can be found in Table A1.1.

shown inset Figure 3.3 where the dashed line is the linear least squares fit. The slope of the linear region of the isotherm gives the distribution coefficient,  $\kappa$ , for naphthalene between the bulk solution and the polymer and was found to be  $(0.106 \pm 0.001)$  L/g.

### 3.3.1.2 Octyl p-hydroxybenzoate

The procedure for the determination of the octyl p-hydroxybenzoate isotherm on PRP- $\infty$  from 70/30 methanol/water was similar to that for naphthalene, with the exception of the loading times for the two compounds being different, as described in section 2.7. The isotherm for octyl p-hydroxybenzoate was obtained over a concentration range of  $4.6 \times 10^{-7}$  M to 0.05165 M and is shown in Figure 3.4. The isotherm has been fit with the Langmuir equation, eq. 3.3, with  $C_{S,max}$  found to be  $(3.49 \pm 0.05) \times 10^{-4}$  mol/g and  $K_{ads}$  found to be  $275 \pm 13$  L/mol. The linear region of the isotherm, up to  $1 \times 10^{-4}$  M, is inset in Figure 3.4 with the line representing the linear least squares fit to the data. The distribution coefficient,  $\kappa$ , was found to be  $(0.132 \pm 0.001)$  L/g. The isotherm for octyl p-hydroxybenzoate was not taken to its saturation point due to its relatively high solubility in 70/30 methanol/water.

The comparison of the naphthalene and octyl p-hydroxybenzoate isotherms on a mol/g sorbed basis is misleading in that it appears that roughly twice as much naphthalene is sorbed by the polymer as octyl p-hydroxybenzoate. A more meaningful way to compare the two compounds is to convert the amount sorbed to volume sorbed using the molar volume that has been calculated from molecular

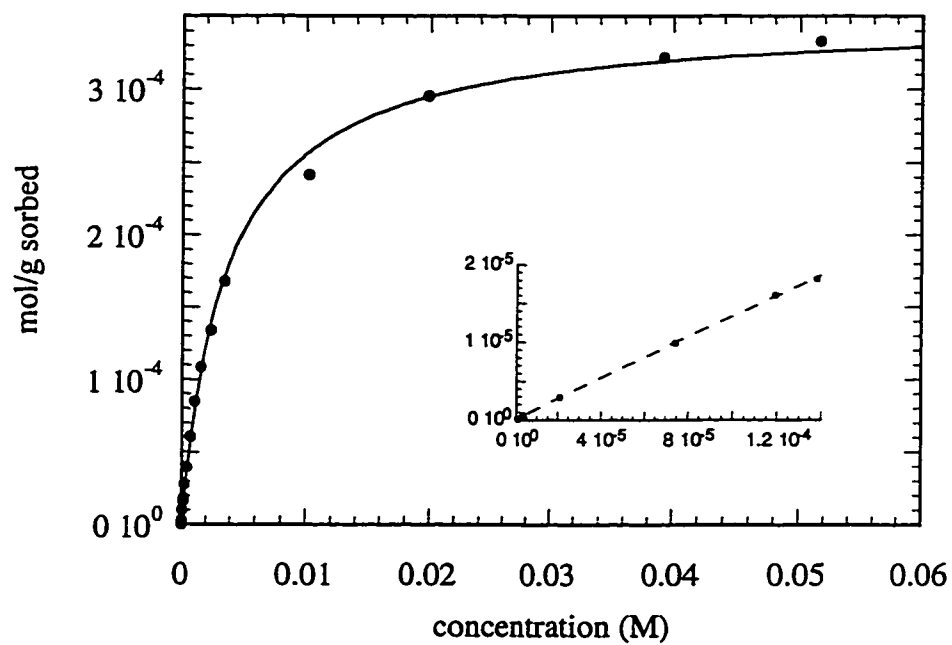


**Figure 3.4** Sorption isotherm of octyl p-hydroxybenzoate on PRP- $\infty$  columns 11-13 (Table 2.1) from 70/30 methanol/water. Solid line is the fit of the Langmuir model, eq. 3.3. Linear region is inset with the dashed line being the linear least squares fit. Data can be found in Table A1.2.

volume of the solute. The molar volumes for naphthalene and octyl p-hydroxybenzoate based on the volume of an isolated molecule are  $78.82 \text{ cm}^3/\text{mol}$  and  $150.61 \text{ cm}^3/\text{mol}$ , respectively, as calculated using the software, MMPro® (Windowchem Software Inc.). If the isotherms are plotted as volume sorbed ( $\text{mL/g}$ ) versus the concentration in solution ( $\text{mL}_i/\text{mL}_M$ ) as shown in Figure 3.5, it can be seen that the volumes sorbed for the two compounds do not differ appreciably. The volume sorbed for naphthalene at saturation was measured to be  $(0.053 \pm 0.002) \text{ mL/g}$  while the predicted maximum sorbed value for octyl p-hydroxybenzoate was found to be  $(0.0526 \pm 0.0007) \text{ mL/g}$ . It has been suggested that compounds with solubility parameters different from that of the polymer do not enter the polymer (21). However, the above results indicate that this is not the case. For octyl p-hydroxybenzoate, with an estimated surface area of  $110 \text{ \AA}^2$  (82) monolayer coverage on the outside of the spherical particle, with the molecules sorbing flat, would indicate that only  $4 \times 10^{-7} \text{ mol/g}$  should be sorbed at  $C_{S,\text{max}}$ , roughly 1000 times less than the value found experimentally. The data here suggests that octyl p-hydroxybenzoate is entering the polymer to the same extent as naphthalene, whose solubility parameter is close to that of the matrix.

### 3.3.2 Sorption Kinetics

The sorption rate curves have all been determined under conditions of equilibrium swelling in the polymer. That is, the polymer was equilibrated with

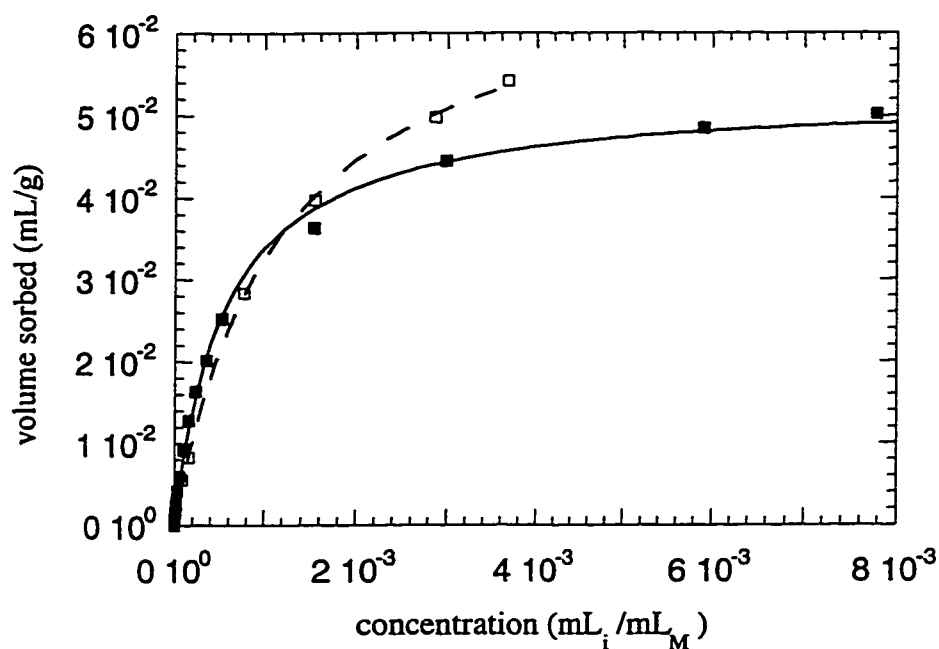


**Figure 3.5** Comparison of naphthalene (□) and octyl p-hydroxybenzoate (■) sorption isotherms on PRP-∞ from 70/30 methanol/water. Data is the same as that used in Figures 3.3 and 3.4 with the exception that the mobile phase concentration and amount sorbed are expressed in volume units. Data can be found in Tables A1.3 and A1.4.

solvent before the experiments, such that the free-volume of the polymer was not changing. As well, the solute was studied at trace levels so that its diffusion and sorption did not cause additional swelling in the polymer matrix.

### 3.3.2.1 Testing of Shallow Bed Conditions

For shallow bed conditions to be met, the linear velocity of the loading solution,  $\bar{U}_0$ , through the shallow bed must be high enough that the concentration of the solute in the mobile phase is essentially the same at the inlet as it is at the outlet of the shallow bed. The change in solution concentration as it moves through the shallow bed will be the greatest for short times where the rate of uptake is the highest. To test if shallow bed conditions were met, the effect of  $\bar{U}_0$  on the initial region of the sorption rate curve was examined. The amount of uptake in the initial region should increase with  $\bar{U}_0$  up to the point where  $\bar{U}_0$  is sufficiently high to maintain an essentially constant mobile phase concentration throughout the bed. Further increases in  $\bar{U}_0$  should show no change in the sorption rate curve. These shallow bed conditions also ensure that the Nernst diffusion films surrounding the sorbent particles are minimized and film diffusion is negligible.

Figure 3.6 shows the effect of  $\bar{U}_0$  on the sorption of octyl p-hydroxybenzoate by PRP- $\infty$ . Mobile phase linear velocities of 11.6, 14.0, 15.8, and 20.1 cm/s were examined. The initial rate, over the first 10 seconds of the plot, is the same for all four flow rates examined, with an initial rate of  $(4.67 \pm 0.07) \times 10^{-9}$  mol•s/gram. The

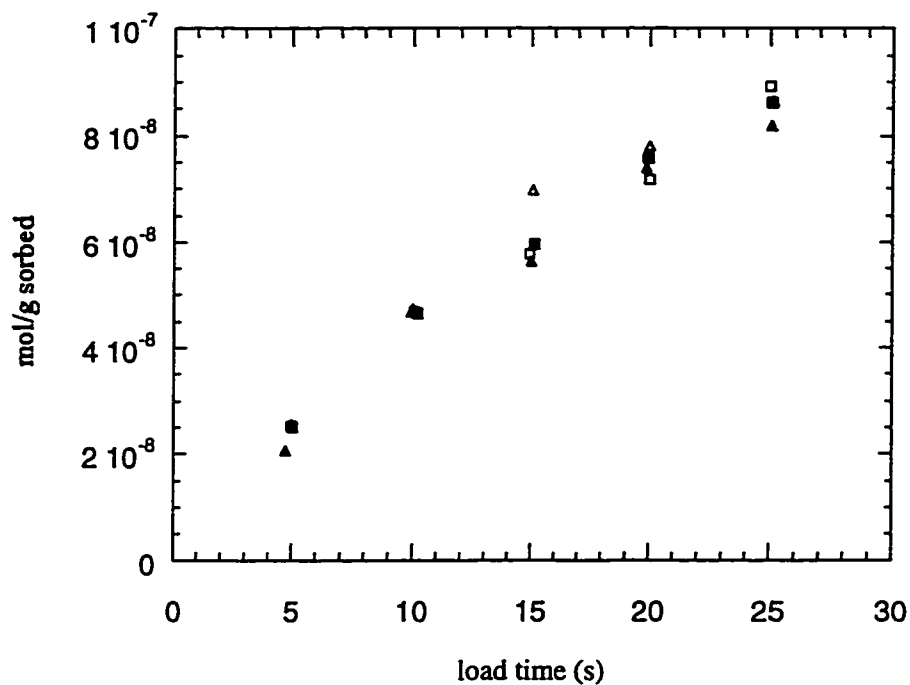


**Figure 3.6** Testing of shallow bed conditions at linear velocities,  $\bar{U}_0$ , of 11.6 cm/s ( $\Delta$ ), 14.0 cm/s ( $\square$ ), 15.8 cm/s ( $\blacktriangle$ ), and 20.1 cm/s ( $\blacksquare$ ) using a  $1.25 \times 10^{-6}$  M octyl p-hydroxybenzoate solution in 70/30 methanol/water on PRP- $\infty$  column 9 (Table 2.1). Data can be found in Table A1.5.

uptake over the entire region examined was the same for each  $\bar{U}_0$ . Therefore, at the lowest  $\bar{U}_0$ , 11.6 cm/s, shallow bed conditions have been met. All kinetic experiments in this study have been done at a linear velocity well above this value, ensuring shallow bed conditions exist.

### 3.3.2.2 Naphthalene Sorption Kinetics

Three separate trials for the sorption rate of naphthalene on PRP- $\infty$  from a  $9.685 \times 10^{-5}$  M solution made up in 70/30 methanol/water were performed and are shown in Figure 3.7. The  $\bar{U}_0$  for each trial was in excess of 19 cm/s, high enough to meet shallow bed conditions. The data have been normalized in each figure to the equilibrium amount sorbed as determined by the fit to the data. The points represent the experimental values, the lines represent the fit to the data. The data were fit with equation 3.9 which describes diffusion through a monodisperse sphere. The sorption rate is seen to be quite reproducible between trials, even with the use of different shallow beds.

Table 3.1 contains the fitting parameters from equation 3.9 which was used to fit the kinetic data, i.e. B which was defined in equation 3.11 and is a function of the diffusion coefficient within the polymer, and  $Q_\infty$ , the equilibrium number of moles sorbed per gram of sorbent. The diffusion coefficients, D, for the three runs are also shown and are seen to fall within approximately one standard deviation of one another.

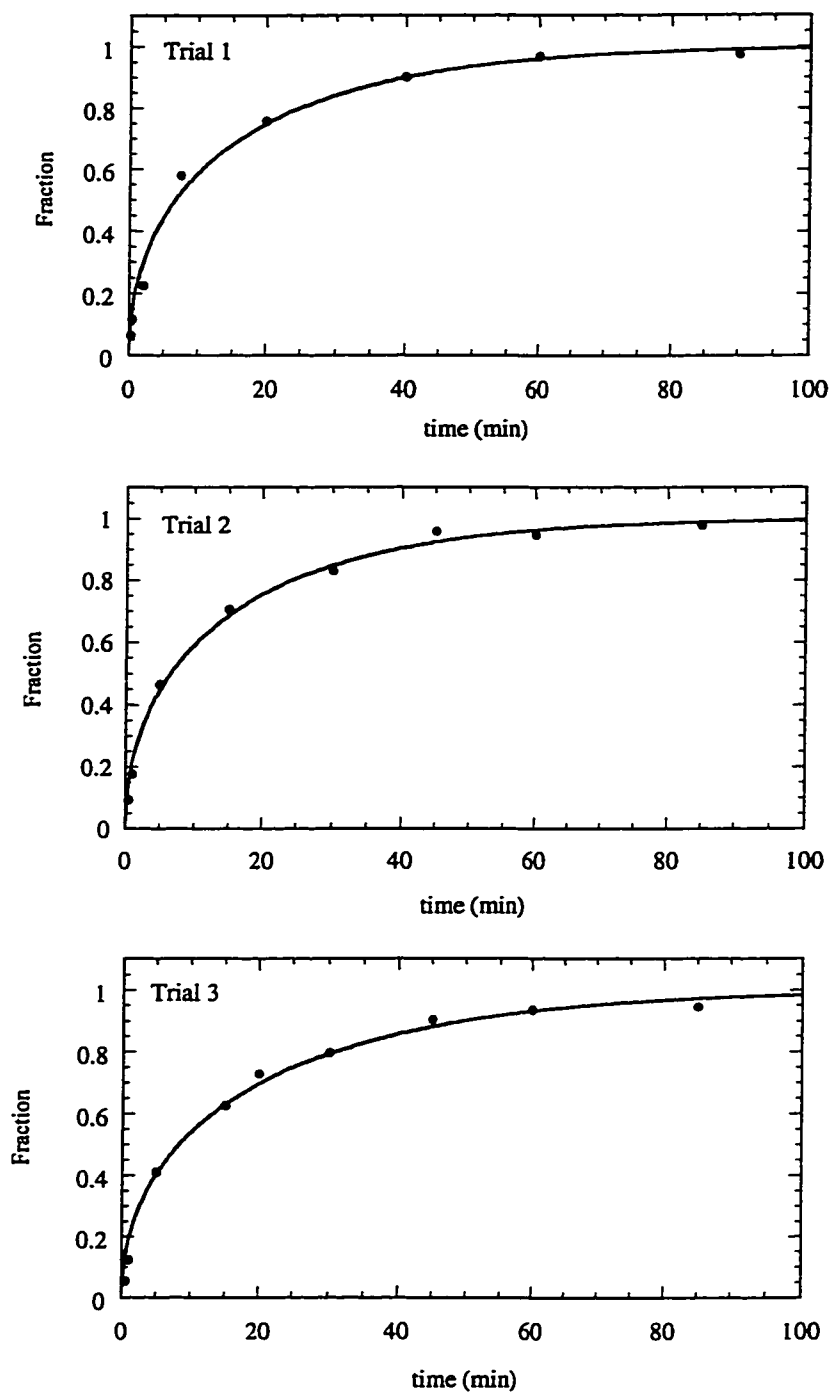


**Figure 3.7** Naphthalene sorption kinetics on PRP- $\infty$  columns 2-4, respectively (Table 2.1), from  $9.685 \times 10^{-5}$  M solution in 70/30 methanol/water.  $\bar{U}_0$  was greater than 19 cm/s for each trial. Solid line is fit of eq. 3.9, diffusion through a monodisperse sphere. Data can be found in Tables A1.6-A1.8.

**Table 3.1** Fitting parameters from eq. 3.9 used to fit naphthalene sorption kinetics on PRP- $\infty$ , and the calculated diffusion coefficient.

Trial	$B(s)^{-1} \times 10^4$	$Q_{\infty}(\text{mol/g}) \times 10^6$	$D (\text{cm}^2/\text{s}) \times 10^{11}$
1	$7.5 \pm 1.4$	$9.6 \pm 0.4$	$7.6 \pm 1.5$
2	$7.6 \pm 1.1$	$8.9 \pm 0.3$	$7.7 \pm 1.2$
3	$6.1 \pm 1.2$	$9.0 \pm 0.5$	$6.1 \pm 1.2$

Linearizing the data as described in equations 3.12 and 3.13 shows the appropriateness of the fit of the model for diffusion through a monodisperse sphere. In Figure 3.8 are shown the  $Bt$  versus  $t$  plots, indicative of the quality of fit of the model. As mentioned previously, if the model is appropriate, the data should fall on a straight line passing through the origin. The data in fact do lie on straight line passing through the origin up to a fraction sorbed of about 95%, and then are seen to curve off. The lines drawn in the figures are the linear least squares fits to the data points before the data begin to deviate from linearity. This deviation may be due to the errors associated with the assumptions made in the derivation of the equation for the calculation of  $Bt$ , or the experimental error in the determination of the fractional amount sorbed, where the calculation involves finding the difference between two similar, large numbers. Overall, the fit to the diffusion through a monodisperse sphere is found to be appropriate.

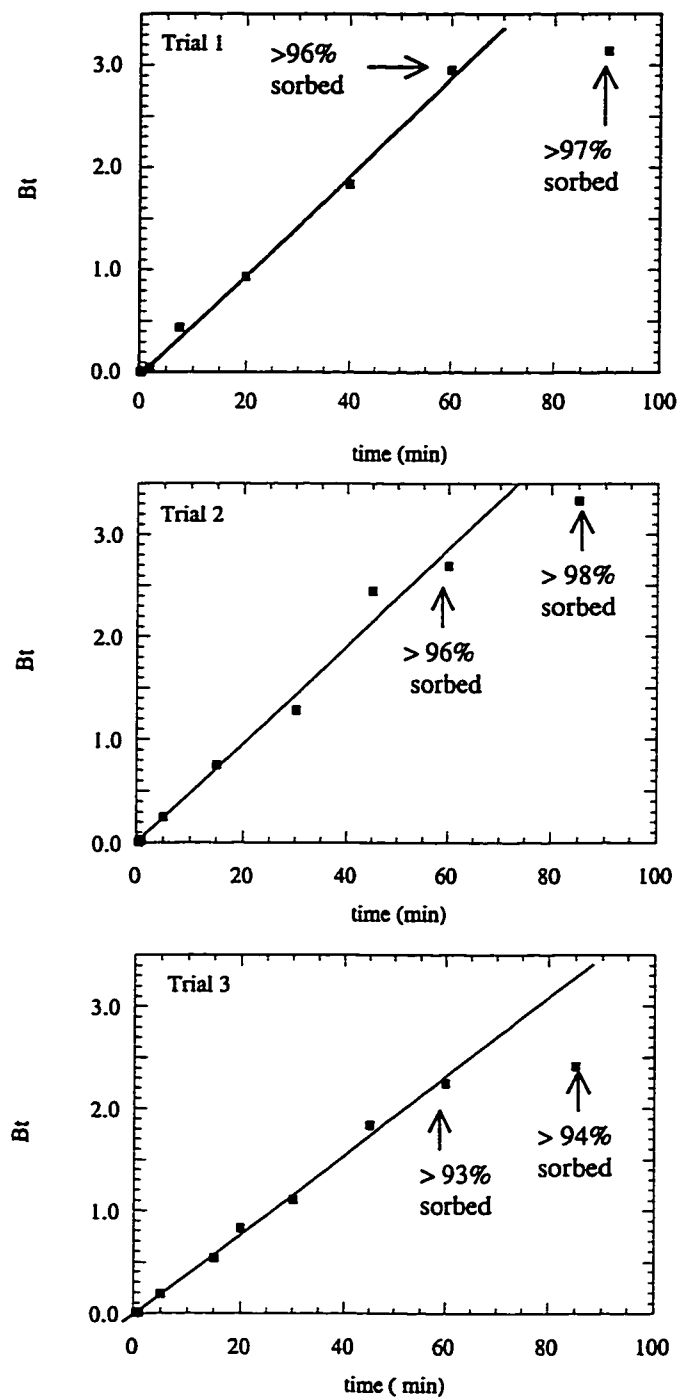


**Figure 3.8** Quality of fit of monodisperse model (eq. 3.9) to naphthalene sorption kinetics from  $9.685 \times 10^{-5}$  M solution in 70/30 methanol/water.  $Bt$  values have been calculated using equations 3.12 and 3.13. Lines are the linear least squares fit of the data within the linear region. Data can be found in Tables A1.6-A1.8.

The polymer has been described earlier as being heterogeneous in nature, having tightly crosslinked nuclei connected by looser crosslinked gel regions. However, the distance between these tightly crosslinked nuclei is very small, and a single diffusion coefficient is adequate to describe the diffusion through the polymer.

### **3.3.2.3 Octyl p-hydroxybenzoate**

#### **3.3.2.3.1 Determination of Pre-Equilibration Time**

The determination of the length of time required to equilibrate the shallow bed between changing solution compositions was necessary. This necessity was brought about by the shallow bed being loaded with a solution of octyl p-hydroxybenzoate in a 70/30 methanol/water solution in order that a detectable amount of the solute would be retained, but elution carried out using 100 % methanol in order to elute the solute in a reasonable amount of time. Therefore, between points on the kinetic curve, the column had to be pre-equilibrated with 70/30 methanol/water before loading the octyl p-hydroxybenzoate solution to ensure conditions of equilibrium swelling existed. To determine the length of pre-equilibration time necessary, the shallow bed had 70/30 methanol/water solution pumped through it for varying amounts of time. Then a solution of  $9.516 \times 10^{-5}$  M octyl p-hydroxybenzoate was loaded for 5 minutes and eluted. When the amount eluted became constant with increasing pre-equilibration time, the sorbent was in equilibrium with the 70/30 methanol/water solution. The results are shown in Figure 3.9.

For no pre-equilibration, the amount of octyl p-hydroxybenzoate sorbed is highest, and decreases as the pre-equilibration time is increased, eventually reaching a

plateau. With no pre-equilibration, the polymer is as swollen as it can be by methanol and the diffusion of octyl p-hydroxybenzoate within the polymer is the fastest. Under these conditions, the surface area available for the solute to sorb to the polymer is the highest, as it can diffuse the furthest into the packing in the loading time used. As the pre-equilibration time increases, the extent of the swelling of the polymer matrix decreases, and the diffusion rate of the solute through the polymer decreases. The solute cannot, therefore, reach the same amount of surface area as in the highly swollen polymer in the 5 minute loading time used, and the amount of solute sorbed decreases. The amount of solute sorbed becomes constant at 20 minute pre-equilibration time, a time sufficient to return the swelling of the polymer to that which exists at equilibrium in 70/30 methanol/water. A 30 minute pre-equilibration time was used in the octyl p-hydroxybenzoate kinetic studies to ensure equilibrium.

#### 3.3.2.3.2 Sorption Kinetics

Two kinetic trials were run for the sorption of octyl p-hydroxybenzoate on PRP- $\infty$  from a  $9.516 \times 10^{-5}$  M solution made up in 70/30 methanol/water. An approximate  $\bar{U}_0$  of 23 cm/s was used. The results can be seen in Figure 3.10 with the points being the experimental values and the lines being the fit to equation 3.9, for diffusion through a monodisperse sphere. Again, it is the normalized data that have been plotted, so that the fraction of equilibrium moles sorbed at any time can be seen. The reproducibility of the kinetics using different shallow beds is again seen to be quite good.

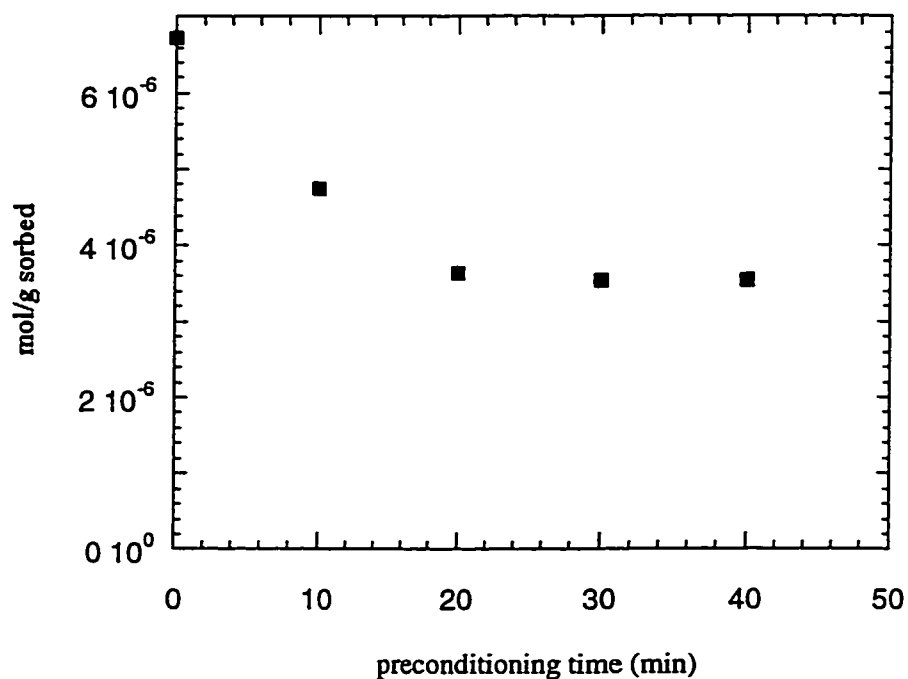


**Figure 3.9** Determination of pre-equilibration time necessary for the sorption kinetic studies of octyl *p*-hydroxybenzoate on PRP- $\infty$ . A  $9.516 \times 10^{-5}$  M solution made up in 70/30 methanol/water was used for loading, 100% methanol was used for elution of the sample, and 70/30 methanol/water was used for pre-equilibration. PRP- $\infty$  column 10 was used (Table 2.1).  $\bar{U}_0$  was greater than 19 cm/s. Data can be found in Table A1.9.

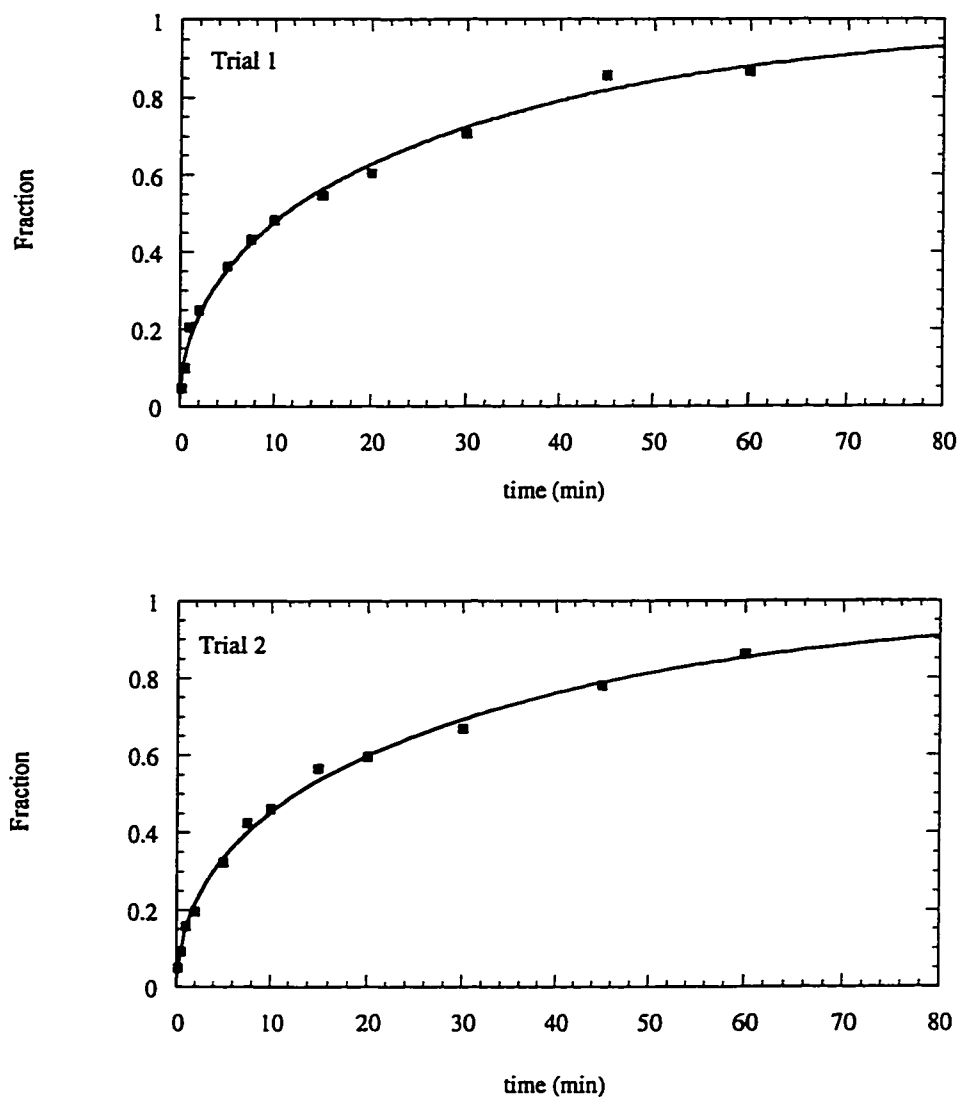


**Figure 3.10** Octyl p-hydroxybenzoate sorption rate on PRP- $\infty$  columns 14 and 15, respectively (Table 2.1), from  $9.516 \times 10^{-5}$  M solution made up in 70/30 methanol/water.  $\bar{U}_0$  was greater than 23 cm/s for each trial. Solid line is fit of eq. 3.9, diffusion through a monodisperse sphere. Data can be found in Tables A1.10-A1.11.

The fitting parameters from equation 3.9 and the calculated diffusion coefficients can be seen in Table 3.2. The plots of  $Bt$  versus  $t$ , which linearize the data and indicate goodness of fit to the model, can be seen in Figure 3.11. Values of  $Bt$  have been calculated using equation 3.12 and 3.13. The lines in Figure 3.11 are the linear least squares fit to the data. The fit to the monodisperse model was found to be appropriate.

**Table 3.2** Fitting parameters from equation 3.9 used to fit octyl p-hydroxybenzoate sorption kinetics on PRP- $\infty$ , and the calculated diffusion coefficients.

Trial	$B(s)^{-1} \times 10^4$	$Q_{\infty} (\text{mol/g}) \times 10^5$	$D(\text{cm}^2/\text{s}) \times 10^{11}$
1	$4.5 \pm 0.8$	$1.16 \pm 0.07$	$4.5 \pm 0.8$
2	$4.0 \pm 0.6$	$1.25 \pm 0.07$	$4.0 \pm 0.6$

The kinetics of sorption of naphthalene and octyl p-hydroxybenzoate on PRP- $\infty$  can be compared. Figure 3.12 is a plot with a representative run from each solute. The sorption rate of octyl p-hydroxybenzoate is seen to be slightly slower than that of naphthalene, as indicated by the lower fractions sorbed at any time and by the slower approach to equilibrium. These differences in the sorption rates are a

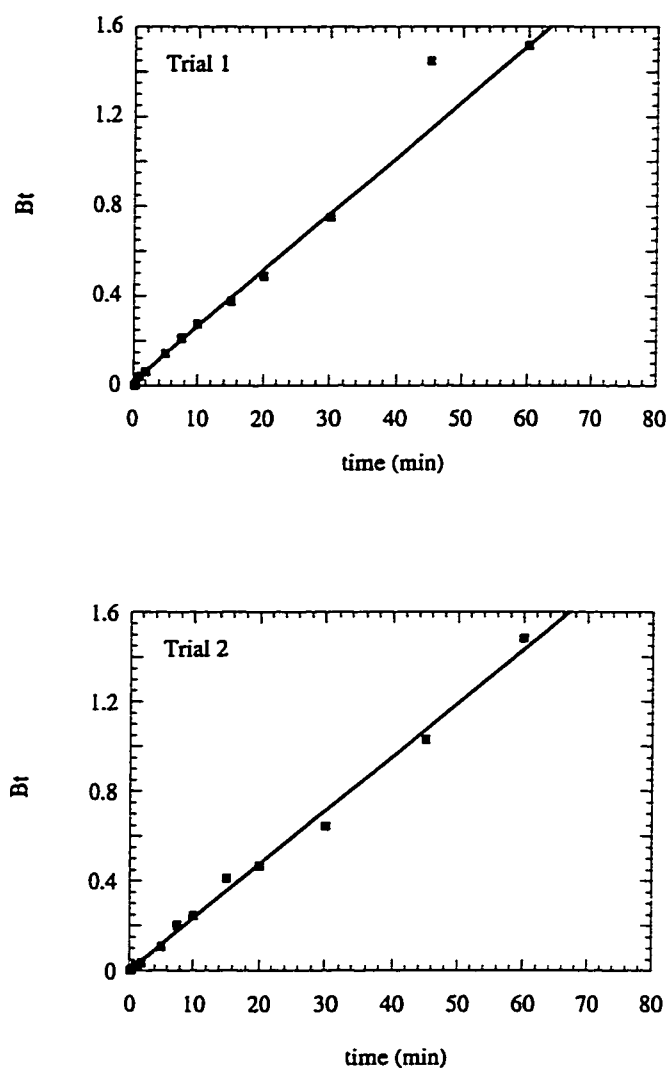


**Figure 3.11** Quality of fit of monodisperse model (eq. 3.9) to octyl p-hydroxybenzoate sorption kinetics from  $9.516 \times 10^{-5}$  M solution made up in 70/30 methanol/water.  $Bt$  values have been calculated using equations 3.12 and 3.13. Lines are the linear least squares fit to the data within the linear region. Data can be found in Tables A1.10-A1.11.

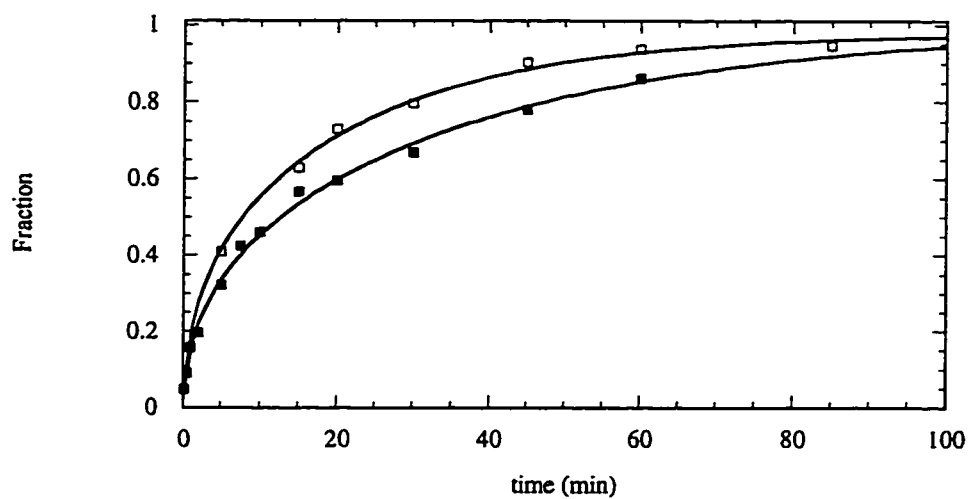


**Figure 3.12** Comparison of naphthalene (□) (Trial 3, Figure 3.7) and octyl p-hydroxybenzoate (■) (Trial 2, Figure 3.10) sorption kinetics on PRP- $\infty$  from 70/30 methanol/water.

consequence of the differences in the diffusion coefficients of the two solutes. From the fits of the data to equation 3.9, the model for diffusion through a monodisperse sphere, the diffusion coefficients were calculated to be  $7.1 \times 10^{-11}$  and  $4.3 \times 10^{-11}$  for naphthalene and octyl p-hydroxybenzoate, respectively, when the values from the respective trials were averaged. This 60% difference in the diffusion coefficients between the two solutes is also reflected in the measured free-solution diffusion coefficients, as will be shown in section 3.3.3. Therefore, the sorption rates for the two solutes are not found to be significantly different, and difference in the diffusion coefficients of the two solutes accounts for the differences seen.

It was initially thought that solutes having solubility parameters different from that of the polymer matrix, such as octyl p-hydroxybenzoate, would not enter the polymer matrix. Hence, it would have faster kinetics for sorption onto only the outside of the particle than would solutes having a solubility parameter similar to that of the polymer matrix, such as naphthalene. What is seen here, however, is that the differences in solubility parameter between the two solutes has not produced a difference in their kinetics of sorption. As well, it was shown above that the maximum solute volume sorbed at equilibrium, i.e. the capacity of the sorbent for the two solutes, was the same.

### **3.3.3 Determination of Free-Solution Diffusion Coefficients**

The free-solution diffusion coefficients were measured using the Taylor dispersion method. The eluted peaks were nearly symmetrical, with an asymmetry factor at 10% of peak height of about 1.1. Hence, the widths of the peaks were

measured using the "tangent" method (141) and the diffusion coefficients were calculated using equation 3.26. The diffusion coefficients were found to be  $(4.01 \pm 0.05) \times 10^{-6} \text{ cm}^2/\text{s}$  for octyl p-hydroxybenzoate in 70/30 methanol/water,  $(6.4 \pm 0.2) \times 10^{-6} \text{ cm}^2/\text{s}$  for naphthalene in 70/30 methanol/water, and  $(6.6 \pm 0.1) \times 10^{-6} \text{ cm}^2/\text{s}$  for naphthalene in 60/10/30 methanol/THF/water. The data used for calculating the diffusion coefficients can be found in Table 3.3.

The verification of the assumptions of the method given in equations 3.28 and 3.29 can be found in Table 3.4 with the conditions needing to be satisfied outlined in the footnote. The assumption given in equation 3.30, that the contributions from the injector and detector are negligible, can be checked using a value of  $V_{\text{inj}}$  of  $10^{-2} \text{ cm}^3$  and a value of  $V_{\text{det}}$  of  $8 \times 10^{-3} \text{ cm}^3$ . Values for the flow rate and the contribution to peak variance from the injector and detector are calculated using equations 3.31 and 3.32. Comparing the variance caused by the injector and detector to the overall peak variance, given by equation 3.27, shows their contributions to lie around 1%, i.e. negligible. Comparing the diffusion coefficient values of the solutes in the polymer, shown in Tables 3.1 and 3.2, and the diffusion coefficients in free solution, the diffusion coefficient is found to be five orders of magnitude larger in free solution than in the polymer matrix. Diffusion within the polymer matrix is highly hindered.

### **3.3.4 Predicted Elution Profiles**

#### **3.3.4.3 Predicted Profiles from Kinetic Studies**

**Table 3.3** Data for the determination of free-solution diffusion coefficients.

Solute	Trial #	t(s)	W <sub>k</sub> (s)	D <sub>M</sub> (cm <sup>2</sup> /s) x 10 <sup>6<sup>a</sup></sup>
Octyl p-hydroxybenzoate	1	7146	957	4.05
	2	7341	974	4.02
	3	7695	1004	3.96
	<b>Ave</b>			<b>4.01±0.05</b>
Naphthalene (70/30 methanol/water)	1	7051	768	6.21
	2	8528	827	6.47
	3	10323	898	6.65
	4	10760	933	6.41
	<b>Ave</b>			<b>6.4±0.2</b>
Naphthalene (60/10/30 MeOH/THF/water)	1	9720	886	6.43
	2	9886	886	6.54
	3	10441	910	6.55
	4	10630	910	6.67
	5	10902	921	6.67
	<b>Ave</b>			<b>6.6±0.1</b>

<sup>a</sup> from equation 3.26

**Table 3.4** Verification of assumptions for the determination of diffusion coefficients.

Solute	$\frac{a^2}{Dt}$ <sup>a,b</sup>	$\frac{a^2 \bar{U}^2}{48D^2}$ <sup>c,d</sup>	$\frac{\sigma_{t,inj}^2}{\sigma_t^2} \times 100\%$ <sup>a,e</sup>	$\frac{\sigma_{t,det}^2}{\sigma_t^2} \times 100\%$ <sup>a,e</sup>
Octyl p-hydroxybenzoate (70/30 methanol/water)	0.02	3000	0.6	0.4
Naphthalene (70/30 methanol/water)	0.01	800	1.3	0.8
Naphthalene (60/10/30 methanol/THF/water)	0.009	600	1.4	0.9

<sup>a</sup>  $t$  taken as the average of the trials for each solute

<sup>b</sup> for verification of equation 3.28, must be  $\ll 1$

<sup>c</sup>  $\bar{U} = L/t$

<sup>d</sup> for verification of equation 3.29, must be  $\gg 1$

<sup>e</sup>  $\sigma_t^2$  taken as the average of the trials for each solute

### 3.3.4 Predicted Elution Profiles

#### 3.3.4.3 Predicted Profiles from Kinetic Studies

The prediction of elution profiles, using a previously validated method that was discussed in section 3.2.4, was performed using a program written in Matlab, which can be found in Appendix 2. The program is based on only one type of site having a non-zero value for the fraction of molecules that pass through the column without being sorbed. If more than one type of site has a non-zero value for the fraction of molecules not sorbed, the program as written does not accurately predict the elution peak.

Naphthalene and octyl p-hydroxybenzoate kinetic studies have been fit with the bi-exponential form of equation 3.33, and can be seen in Figures 3.13 and 3.14. The parameters obtained from the fits can be found in Table 3.5. The bi-exponential and tri-exponential forms of equation 3.33 both fit the experimental data well. However, using the model to predict the elution profile where there are three types of sites gave a significant fraction of non-sorbed molecules on more than one type of site at flow rates above 0.008 mL/min (0.0049 cm/s). As a result, the peaks predicted using the three-site model were unrealistic as no consideration had been given to the non-interacting fraction on any site except the slowest. Use of the two-site model avoided this situation.

The overall elution profiles for naphthalene and octyl p-hydroxybenzoate from a 4.1 x 150 mm chromatographic column of PRP- $\infty$  have been predicted for a flow rate of 0.0637 mL/min (0.039 cm/s), where the fraction of molecules passing

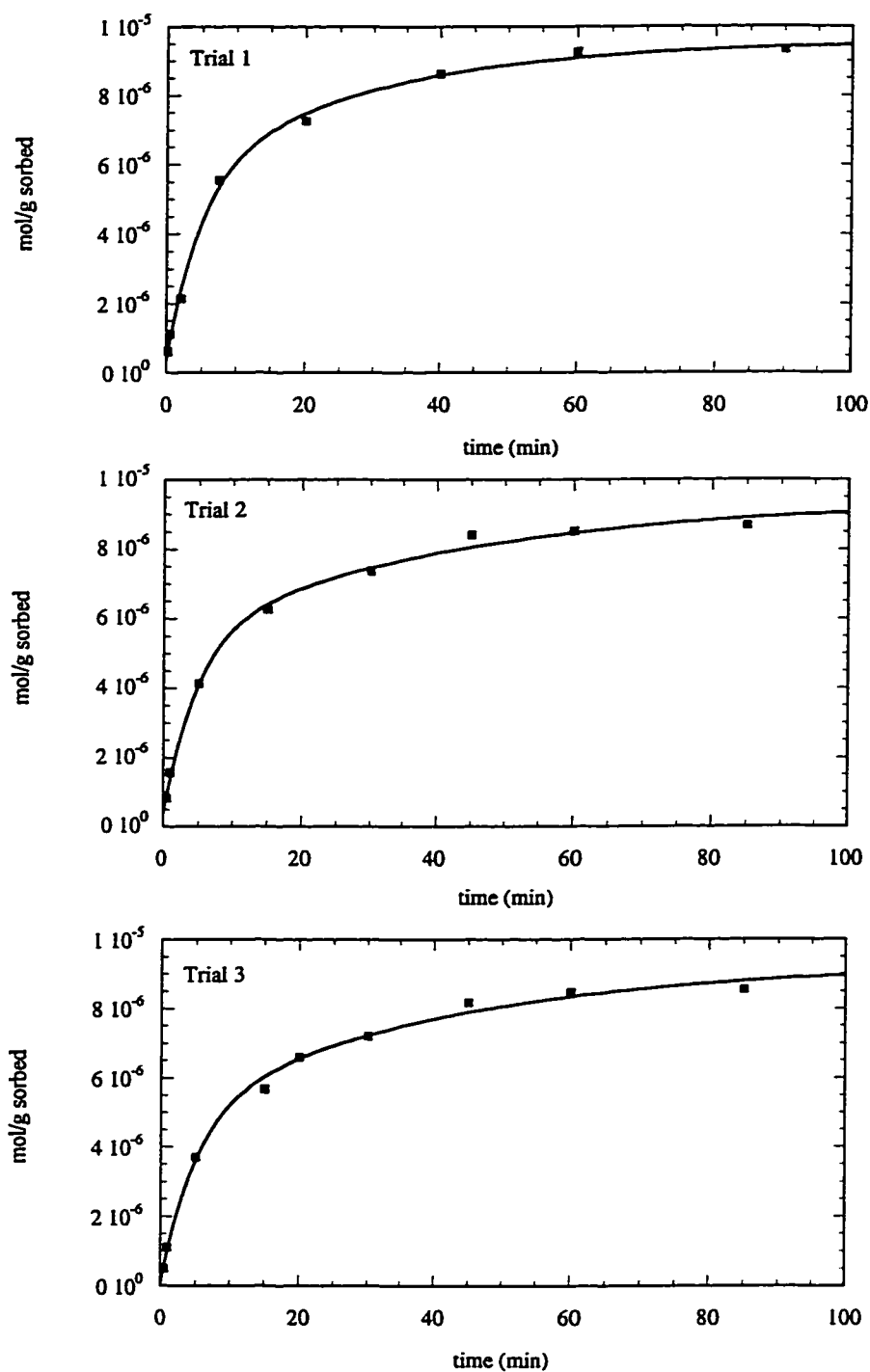


**Figure 3.13** Bi-exponential fits (solid lines) to naphthalene sorption kinetics on PRP- $\infty$  columns 2-4, respectively (Table 2.1), from  $9.685 \times 10^{-5}$  M solution in 70/30 methanol/water.  $\bar{U}_0$  was greater than 19 cm/s for each trial. Data can be found in Tables A1.6-A1.8.

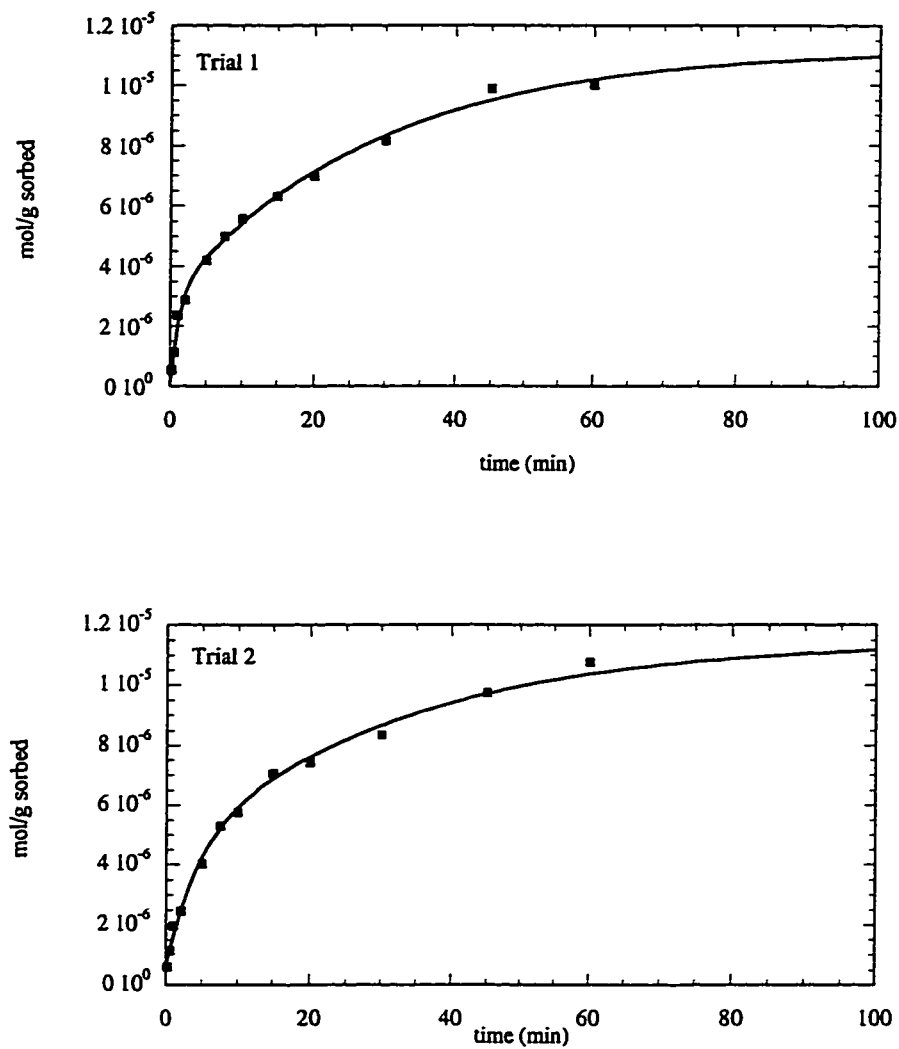


**Figure 3.14** Bi-exponential fits (solid lines) to octyl p-hydroxybenzoate sorption kinetics on PRP- $\infty$  columns 14 and 15, respectively (Table 2.1), from  $9.516 \times 10^{-5}$  M solution made up in 70/30 methanol/water.  $\bar{U}_0$  was greater than 23 cm/s for each trial. Data can be found in Tables A1.10-A1.11.

through the column without sorbing was significant only on the slow sites. The volume of the mobile phase,  $V_M$ , was given by the manufacturer to be 0.73 mL (152), giving a value for  $t_M$ , required for the prediction, of 11.46 minutes. The values for  $k'$  for the solutes from 70/30 methanol/water were calculated using the slopes of the linear regions of the isotherms, 105.8 mL/g and 132.1 mL/g for naphthalene and octyl p-hydroxybenzoate respectively, and a weight of the sorbent in a column of 1.36 g (152). Values of  $k'$  for naphthalene and octyl p-hydroxybenzoate were calculated using equation 3.46 and found to be 197.1 and 246.1, respectively. The predicted overall elution profiles can be found in Figures 3.15 and 3.16. The peaks have been normalized to have an area of one and are plotted as normalized signal versus elution volume. The predicted elution peaks for a particular solute are found to be quite similar. Trials 1, 2, and 3 for naphthalene had retention volumes,  $V_R$ , of 119 mL, 118 mL, and 107 mL, and trials 1 and 2 of benzoate had values of 151 mL and 159 mL, respectively. The retention volumes at the center of gravity ( $V_R$ ) are all significantly larger than the volumes at the peak maxima as the result of the severe peak tailing. The severe peak tailing is the result of slow kinetics on one type of site as described by Giddings (147).

**Table 3.5** Fitting parameters from bi-exponential fits to naphthalene and octyl p-hydroxybenzoate sorption kinetics on PRP- $\infty$ .

Solute	Trial	$n_0 \times 10^6$	$n_1 \times 10^6$	$k_1$	$n_2 \times 10^6$	$k_2$
Naphthalene	1	9.101	1.122	2.618	7.98	0.08721
	2	8.477	0.9086	5.545	7.568	0.08683
	3	8.528	0.7945	3.257	7.734	0.06777
Octyl	1	11.15	2.971	0.9375	8.181	0.0357
p-hydroxybenzoate	2	10.92	2.722	0.7822	8.195	0.04532

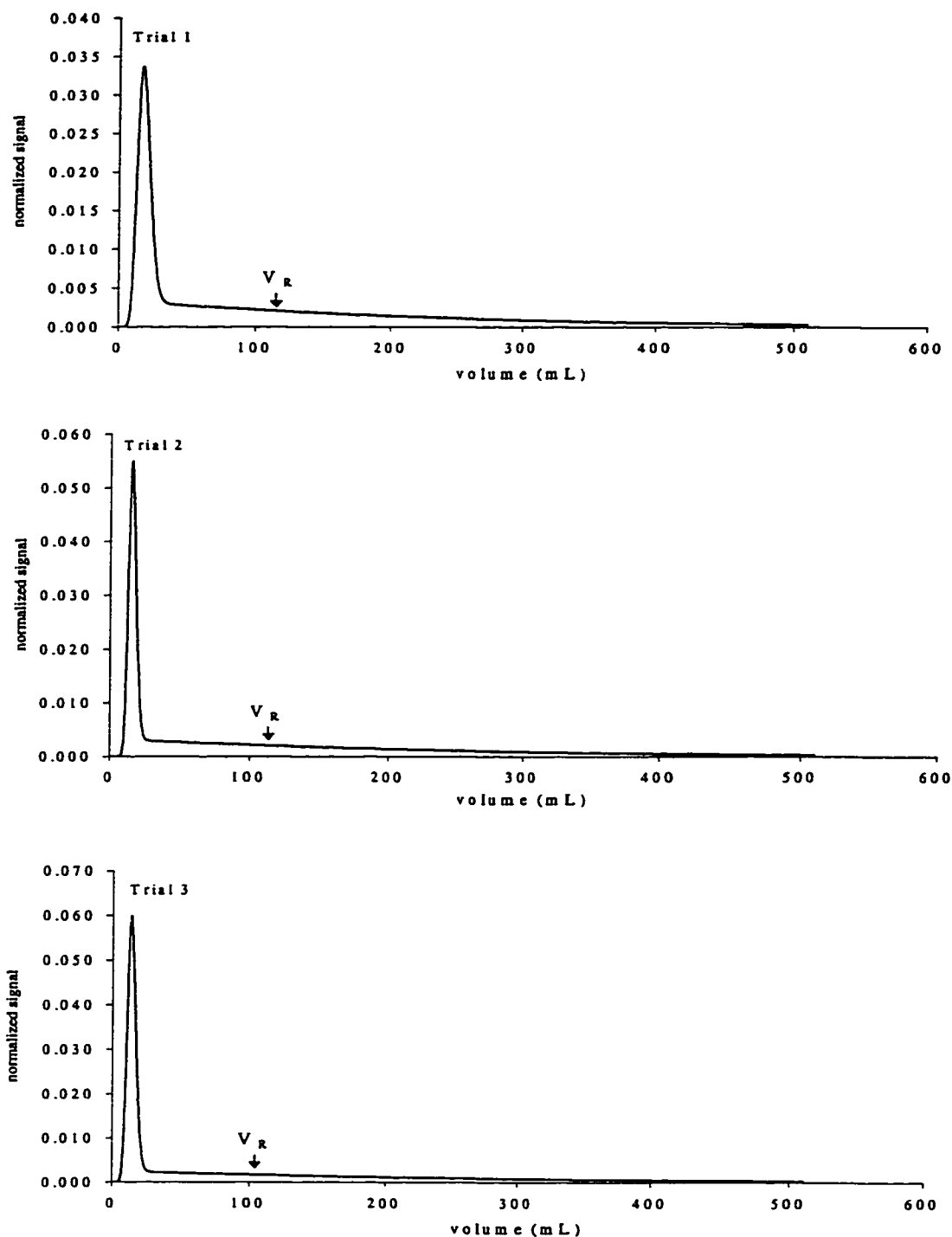


**Figure 3.15** Predicted naphthalene elution profiles at a flow rate of 0.0637 mL/min (0.039 cm/s) from a PRP- $\infty$  column using the parameters obtained from bi-exponential fits to sorption rate curves shown in Figure 3.13. Parameters from sorption rate curves are given in Table 3.5.  $V_R$  is the retention volume of the peak at its center of gravity.

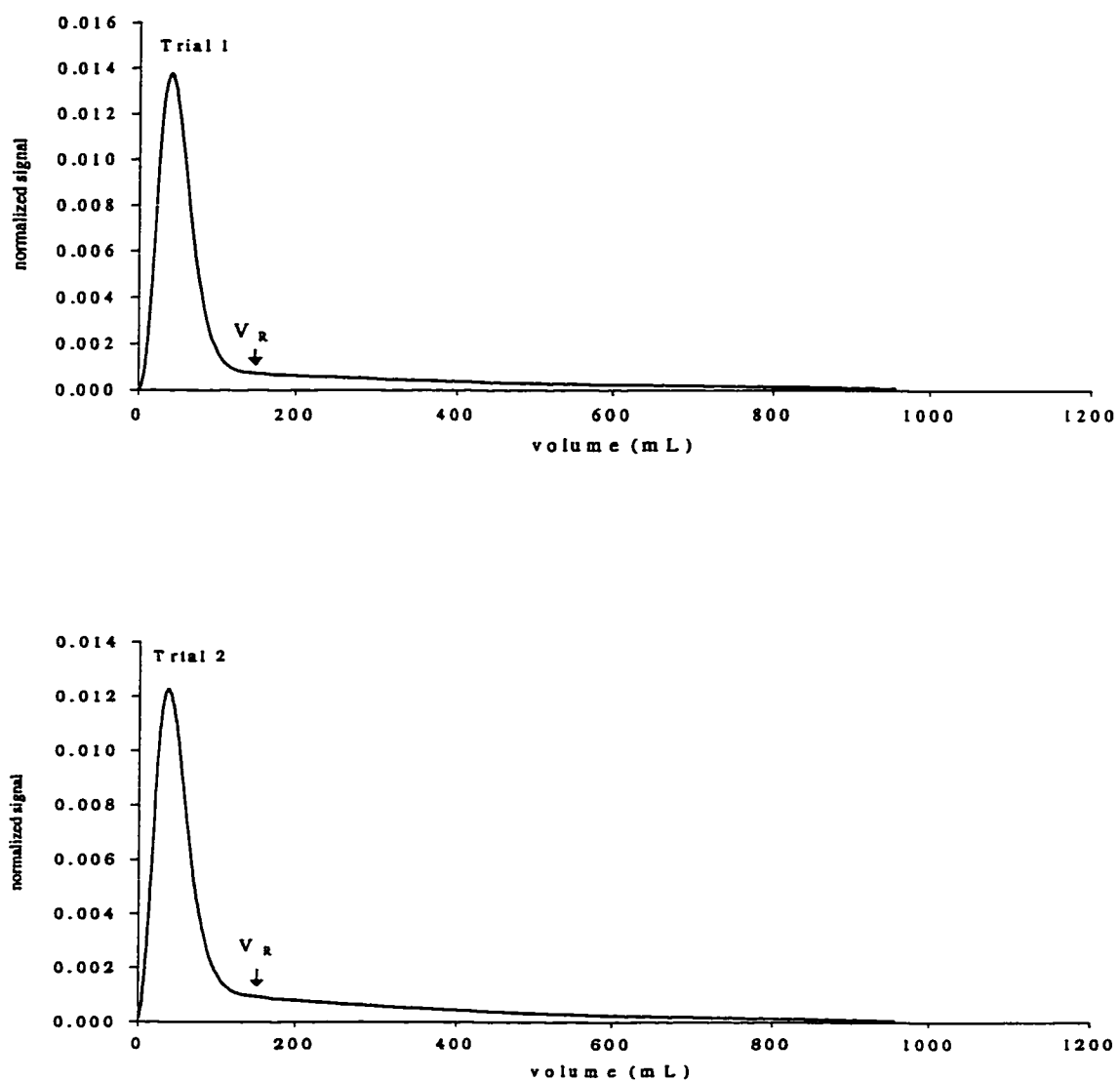


**Figure 3.16** Predicted octyl p-hydroxybenzoate elution profiles at a flow rate of 0.0637 mL/min (0.039 cm/s) from a PRP- $\infty$  column using the parameters obtained from bi-exponential fits to sorption rate curves shown in Figure 3.14. Parameters from sorption rate curves are given in Table 3.5.  $V_R$  is the retention volume of the peak at its center of gravity.

### 3.3.4.1 Effect of Flow Rate on Predicted Elution Profiles

The kinetic tailing on chromatographic peaks has been described by Giddings to be the result of the presence of both fast and slow sites (147). The resulting chromatographic peak shape from a column with more than one type of site will depend on the experimental flow rate used. At very high flow rates, the slow sites will not be accessed and the peak will elute with a Gaussian profile at a retention time determined by the interaction with the fast sites. At very slow flow rates, solutes will access both fast and slow sites. The elution profile will again be Gaussian, with the retention time being determined by the interaction of the solute with both types of sites. At intermediate flow rates, the elution profile may become tailed and may even be split into two peaks as the number of molecules interacting with the slow type of site changes (149, 150, 153-155). The effect of flow rate on peak shape can be predicted using the model outlined above. It should be noted that the retention time of a compound on a column, taken as the centre of gravity of the peak, is dependent only on equilibrium properties and not on mass-transfer processes. Hence, the  $k'$  value should remain constant for peak predictions at various flow rates even though the fraction of sites accessed by the solute may be changing (149, 150).

Using kinetic trial 2 for naphthalene, the effect of flow rate on elution peak shape has been predicted using the two-site model and is illustrated in Figure 3.17. At a relatively high flow, as shown in panels A and B, the fraction of molecules not sorbed by the slow sites as they moved through the column was quite large. The resulting peak was found to have an early Gaussian portion, arising from the elution from the fast sites,

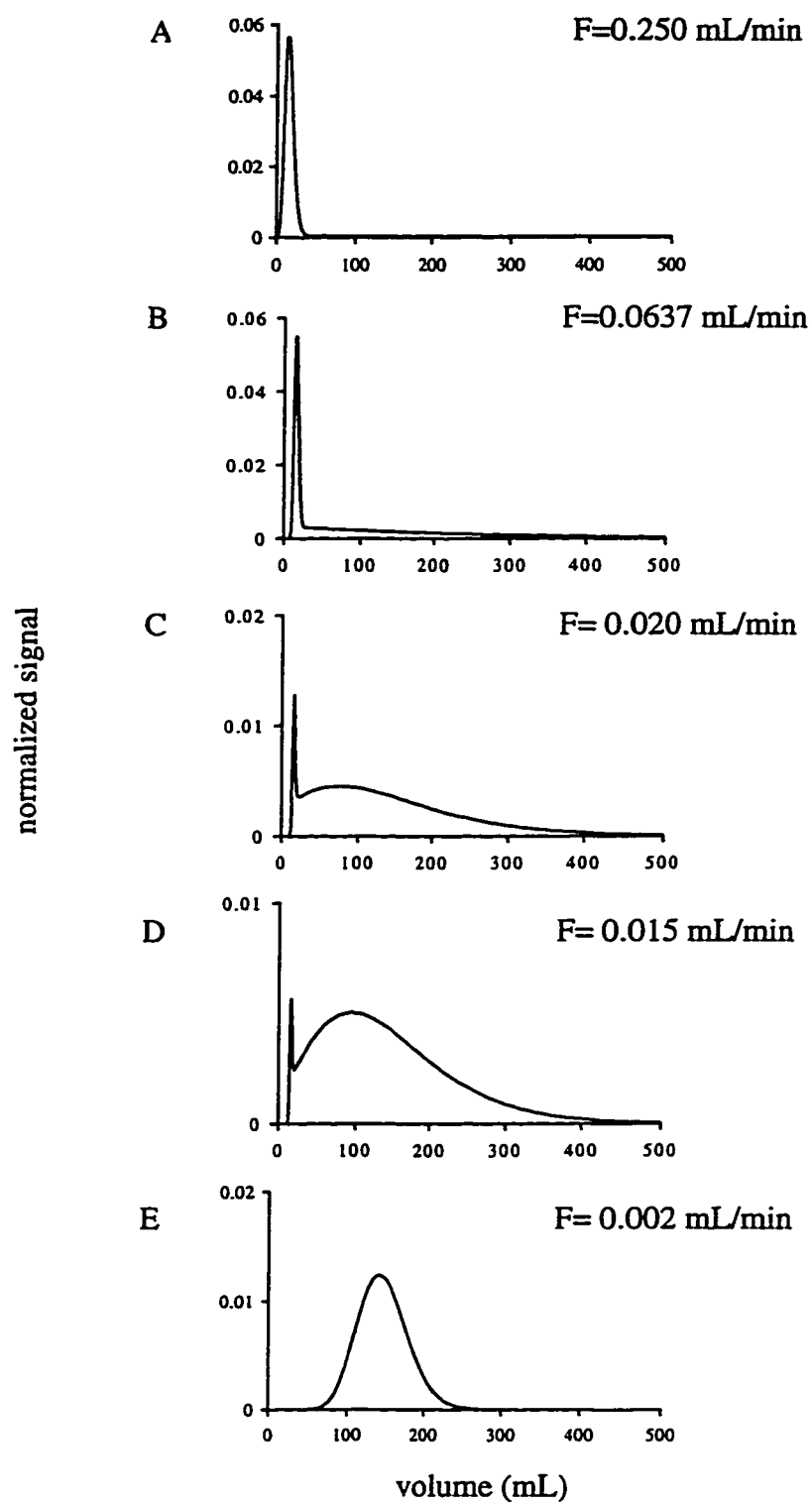


**Figure 3.17** Effect of flow rate on predicted elution profiles for naphthalene from a PRP- $\infty$  column from a 70/30 methanol/water solution. Parameters used for prediction are given in Table 3.5

followed by a long tail as solute eluted from the slow sites, which cannot be seen on panel A due to the vertical scale used. As the flow rate was decreased, the fraction sorbed by the slow sites increased. As a result, the initial peak decreased in signal intensity while the tail grew higher. For flow rates of 0.02 and 0.015 mL/min (0.012 and 0.0093 cm/s, respectively), as shown in panels C and D, two maxima are present - the first peak being the result of solute not sorbed by the slow sites and the second peak arising from solute molecules sorbed by both types of sites. As flow rate was decreased further, as shown in panel E, all of the molecules were sorbed on the slow sites and a single Gaussian peak was predicted. At low flow rates, the fraction of molecules not interacting with either site in the bi-exponential fit approaches zero. Under these conditions, the tri-exponential form of equation 3.33 can be used to predict elution profiles.

### **3.3.5 Electron Microscopy Results**

#### **3.3.5.1 Transmission Electron Microscopy**

Electron microscopy was performed to examine the internal particle morphology. A transmission electron micrograph is shown in Figure 3.18. Seen are slices of two particles with very different internal structure. The particle on the bottom is seen to have several large porous areas surrounded by particle matrix, while the particle on top is uniform in its appearance. This anomalous porosity in the bottom particle is likely due to the initiator used in synthesis, benzoyl peroxide, being cleaved to release carbon dioxide, which gets trapped in the particle. These

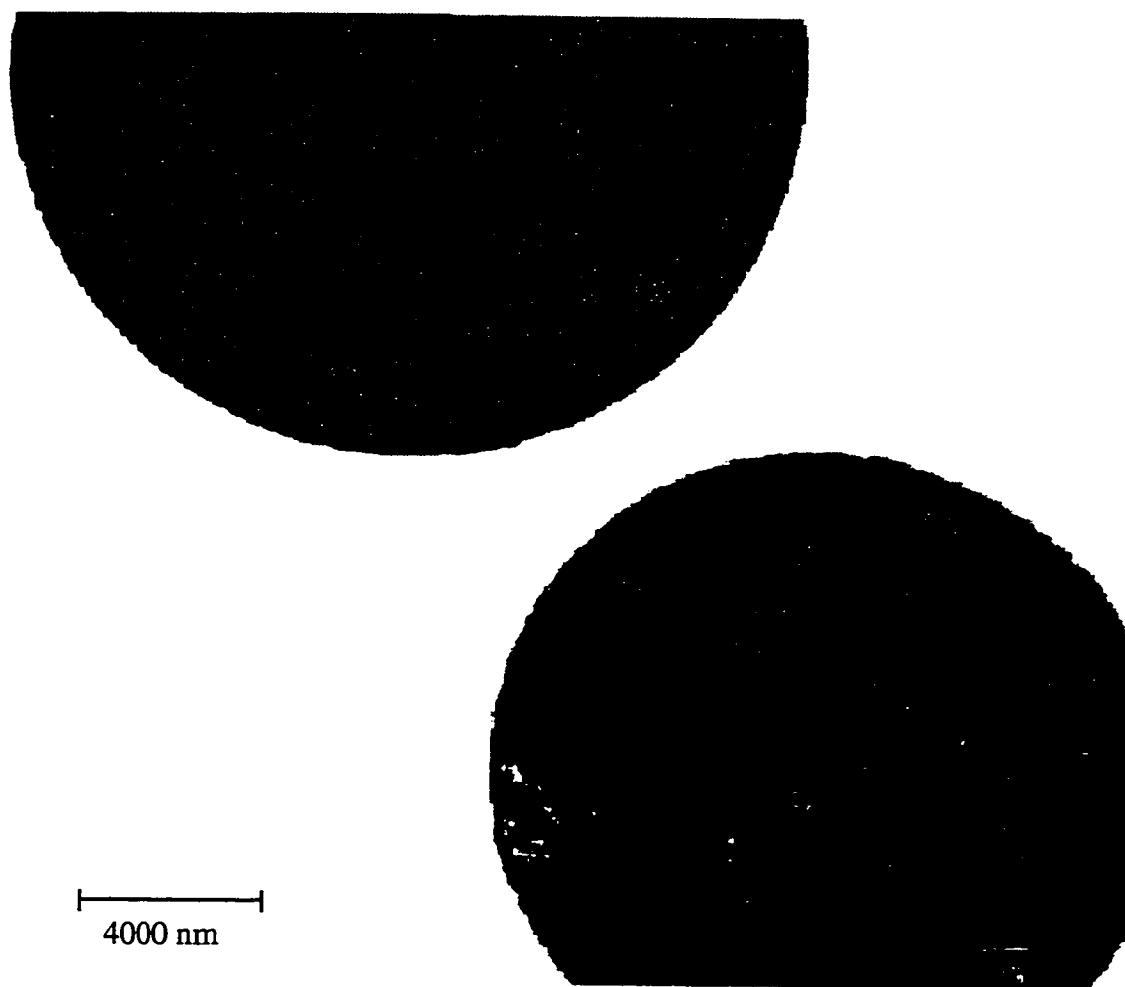


**Figure 3.18** Transmission electron micrograph of PRP- $\infty$  particles. Magnification 5655 X. Transmission electron microscopy was performed by Rakesh Bhatnager, Department of Biological Sciences, University of Alberta.

anomalous pores are not responsible for the increase in capacity over what was expected from monolayer coverage of the external surface of the particles as their surface area would not be 1000 times that of the external surface of the particle. Also, these pores are not affecting the sorption rate studies as diffusion through these pores would be similar to diffusion in free-solution.

The dark staining around the pores is from the  $\text{OsO}_4$  used in the staining process. The  $\text{OsO}_4$  is reduced in the reaction with unsaturated bonds, such as those present in the unreacted monomer, producing metallic osmium. The crosslinking, and hence the density, is the lowest in the darkly stained regions. It is assumed that this porosity is not common and that most particles have the internal morphology of the particle on the top. Also seen in the micrographs is a wave-like pattern. Since this wave-like pattern is seen to be perpendicular to knife scratches visible in the micrographs it is likely that it is "chatter". Chatter is a periodic variation in thickness of a section arising from the vibration in the knife or block or from improper knife speed or angle and is dependent on the hardness of the specimen being cut. The wave-like pattern may be indicative of the density of the particle – the less dense regions get pulled forward with cutting, while the more dense regions do not.

### **3.3.5.2 Scanning Electron Microscopy**

A scanning electron micrograph of the external surface of a PRP- $\infty$  bead is shown in Figure 3.19. It is seen to have a rough texture, resulting in an increase in its external surface area. However, this increase is not large enough to account for the high

uptake of solute as measured in the isotherm experiments. Evidence of the internal anomalous porosity seen in Figure 3.18 is also seen in the top middle of the micrograph as the crater-like feature. The holes in the surface of the bead acted as the outlet for the trapped gas. The occurrence of these pores in fractured polymer beads examined was rare.

The fractured surface of a polymer bead is shown in Figure 3.20. The surface, and hence the matrix of the particle, is seen to be quite uniform in appearance. Any micropores that may be present in the matrix, i.e. spaces between the polymer chains, are too small to be observed as features in the micrograph.



**Figure 3.19** Scanning electron micrograph of outer surface of a PRP- $\infty$  particle. Magnification 15 000 X. Scanning electron microscopy was performed by George Braybrook, Department of Earth Sciences, University of Alberta.

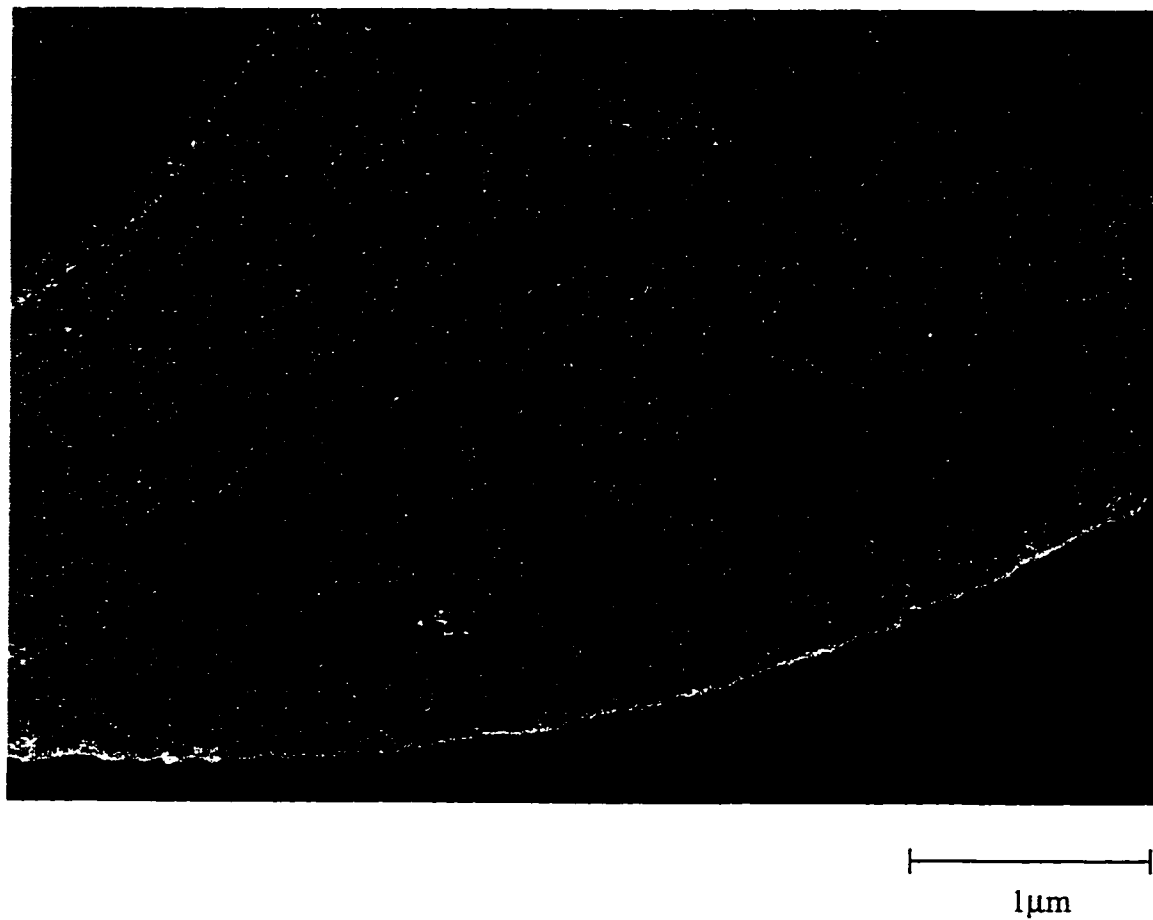


**Figure 3.20** Scanning electron micrograph of interior of a PRP- $\infty$  particle. Magnification 27 000 X. Scanning electron microscopy was performed by George Braybrook, Department of Earth Sciences, University of Alberta.

## Chapter 4

### Effect of THF on Naphthalene Sorption Isotherms and Sorption Kinetics on PRP- $\infty$

#### 4.1 Introduction

The excessive tailing and bandbroadening seen on PS-DVB stationary phases is significantly affected by the composition of the mobile phase. This effect is related to the similarity of the solubility parameters,  $\delta$ , of the organic component of the mobile phase (organic modifier) and the polymer, and not to changes in the solvent strength of the mobile phase (60, 68). For equieluotropic binary aqueous/organic mobile phases, narrower and more symmetric elution peaks have been obtained from mobile phases that contain an organic modifier with a  $\delta$  close to the polymer. Under these conditions, the column void volumes and permeabilities have also been found to be smaller. These effects have been attributed to an increase in swelling of the polymer. In ternary systems, the presence of small amounts of an organic modifier with a  $\delta$  close to PS-DVB, such as THF, has been found to significantly improve elution peak shape (54, 57, 60, 68, 156).

It has been shown previously for PS-DVB polymers, that the excessive tailing and bandbroadening of elution peaks arises from hindered diffusion within the polymer matrix (81). Therefore, any improvement in peak shape by the addition of an organic modifier, such as THF, to a macroporous sorbent is the result of the modifier being within the matrix and not from the modifier filling the sorbent

macropores or adsorbed to the macropore walls. The sorption of THF by PS-DVB is known to cause swelling within the matrix, and it has been generally thought that this increase in swelling results in less hindered diffusion within the polymer matrix, giving narrower, less tailed peaks (54, 57, 60, 68, 156). This, however, has not been verified experimentally and is the focus of this study.

The effect of THF on the sorption isotherm of naphthalene on PRP- $\infty$  has been investigated, as has its effect on the sorption kinetics, again using the column equilibration and shallow bed techniques. The changes in the sorption isotherm and sorption kinetics on the addition of THF to the mobile phase have been interpreted using solvent sorption isotherms and swelling measurements obtained by Ying Wang of this research group.

## 4.2 Theory

In order to get a complete picture of what is occurring within the polymer when a solute is sorbed, consideration must also be given to what occurs within the polymer when it is exposed only to the aqueous/organic mobile phase. When the crosslinked polymer is exposed to the mobile phase, it imbibes or "takes up" one or more of the mobile phase components and swells. The amount of swelling that occurs is dependent upon how good a solvent the imbibed mobile phase component is for the polymer. A good solvent generally has a molecular structure similar, chemically and physically, to the structural units of the polymer. In this case, the cohesive forces between the polymer molecules and between the solvent molecules are similar to the adhesive forces between the solvent and polymer. This similarity in

cohesive/adhesive forces is described by the solubility parameters of the solvent and polymer. The closer a solvent's solubility parameter to the polymer's, the better the ability of the solvent to wet, penetrate and swell the polymer (67, 157). Swelling equilibrium is reached when the free energy decrease due to the mixing of the solvent and the polymer is balanced by the free energy decrease due to the stretching of the polymer chains (157-159). It should be noted that not all solvent uptake causes swelling. In a macroporous resin, sorption in the permanent macropores, or simple filling of these macropores, does not cause swelling. Likewise, sorption in permanent micropores may occur without swelling.

Three commonly used organic modifiers in RP-HPLC include methanol ( $\delta = 29.7 \text{ (MPa)}^{1/2}$ ), acetonitrile ( $\delta = 24.7 \text{ (MPa)}^{1/2}$ ), and THF ( $\delta = 18.6 \text{ (MPa)}^{1/2}$ ). Their ability to swell PS-DVB ( $\delta \approx 18.6\text{-}19.0 \text{ (MPa)}^{1/2}$ ) is in the order THF>acetonitrile>methanol as expected based on  $\delta$  values, where methanol is considered to be a poor solvent. It has been found that even poor solvents are able to swell polymers. It has been suggested that this swelling is the result of strain within the dry polymer, arising from the inability of the polymer chains to rearrange because of the rigidity imposed by crosslinking. A weak interaction between the solvent and the polymer is sufficient to relieve part of this strain resulting in an expansion of the polymer network (26, 160). Water, with  $\delta = 47.9 \text{ (MPa)}^{1/2}$ , is not able to wet or swell PS-DVB (161, 162).

#### 4.3 Results and Discussion

### 4.3.1 Naphthalene Sorption Isotherms

In order to investigate the effect of THF on naphthalene sorption, isotherms were measured from a 68/2/30 methanol/THF/water solution and a 60/10/30 methanol/THF/water solution. The isotherms were measured up to their saturation points where the activity of naphthalene is defined as being equal to 1. Under this condition, pure naphthalene is in equilibrium with the sorbent, and any differences in the sorption at the saturation point are independent of the mobile phase composition. That is, any differences in the amount of naphthalene sorbed by PRP- $\infty$  at this point are the result of differences within the stationary phase.

The isotherms are plotted as moles sorbed per gram of PRP- $\infty$  versus concentration of naphthalene in solution, and can be seen in Figures 4.1 and 4.2. The 68/2/30 methanol/THF/water isotherm was measured over a concentration range of  $1.321 \times 10^{-6}$  M to 0.05570 M. The latter concentration is the saturation point for naphthalene in a solution of this composition at 25°C, as determined using the technique described in section 3.3.1.1. The sorption capacity of the sorbent for naphthalene was measured at the saturation point to be  $(6.14 \pm 0.08) \times 10^{-4}$  mol/g. The isotherm was found to be linear up to a concentration of  $1.2 \times 10^{-4}$  M and is seen in the inset of Figure 4.1. In the linear region, the distribution coefficient,  $\kappa$ , was found to be  $(0.0504 \pm 0.0009)$  L/g.

The 60/10/30 methanol/THF/water isotherm was measured over a concentration range of  $1.000 \times 10^{-5}$  M to 0.09941 M, the latter being the saturation

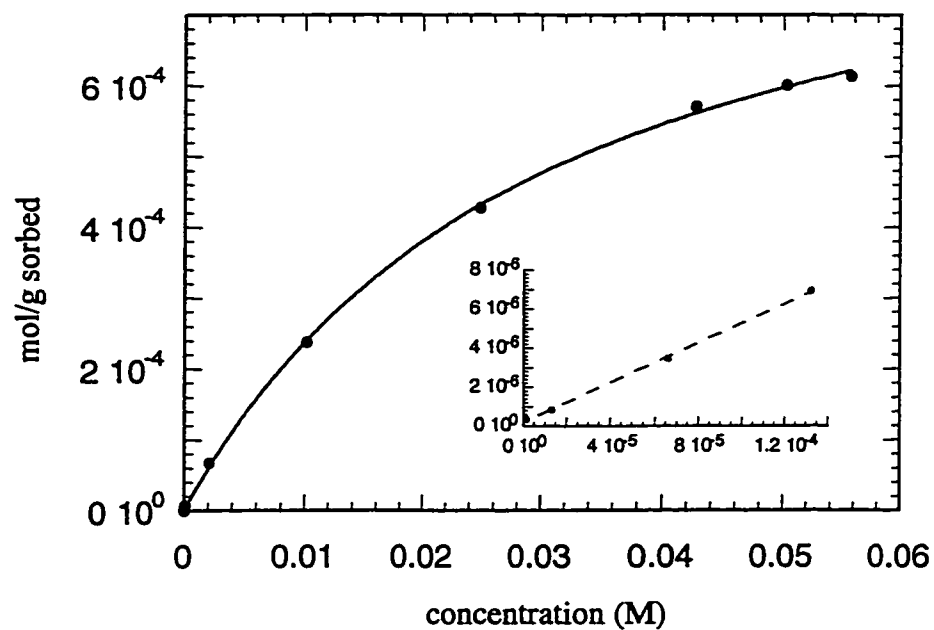


**Figure 4.1** Naphthalene sorption isotherm on PRP- $\infty$  column 5 (Table 2.1) from 68/2/30 methanol/THF/water. Solid line is the fit of the solubility limited Langmuir model, eq. 3.47. Linear region is inset with the dashed line being the linear least squares fit. Data can be found in Table A1.12.

point of naphthalene in solution at 25°C. The capacity of the sorbent at this solution composition was measured at the saturation point to be  $(5.7 \pm 0.1) \times 10^{-4}$  mol/g. The linear region of the isotherm has been inset in Figure 4.2, and ranges up to a concentration of 0.001 M. In the linear region, the distribution coefficient,  $\kappa$ , was measured to be  $(0.0248 \pm 0.0006)$  L/g .

To examine the effect of THF on solute sorption, the two isotherms described above, as well as the naphthalene sorption isotherm from the 70/30 methanol/water solution, have been plotted together in Figure 4.3. For later comparison with solvent uptake and sorbent swelling curves, the data are plotted as volume of naphthalene sorbed (mL /g) versus volume of naphthalene in solution ( $\text{mL}_i/\text{mL}_M$ ). The volume of naphthalene was calculated to be  $130.9 \text{ \AA}^3/\text{molecule}$  using the molecular modeling software, MMPro<sup>®</sup>, and is based on van der Waals radii. Shown in Table 4.1 are values of  $C_{s,\text{max}}$ ,  $\kappa$ , and  $\frac{K_{\text{ads}}}{C_{\text{sat}}}$  for the different solvent compositions. The sorption capacity of the sorbent for naphthalene,  $C_{s,\text{max}}$ , decreased as the amount of THF in solution was increased. The decrease in sorption capacity was 11% between the 70/30methanol/water and 68/2/30 methanol/THF/water solutions, and 17% between the 70/30 methanol/water and 60/10/30 methanol/THF/water solutions. Since the capacities were measured at a naphthalene activity of one, this decrease is due to some change in the polymer phase; specifically, the number of "sites" available to naphthalene for sorption decreased as the amount of THF in solution increased.

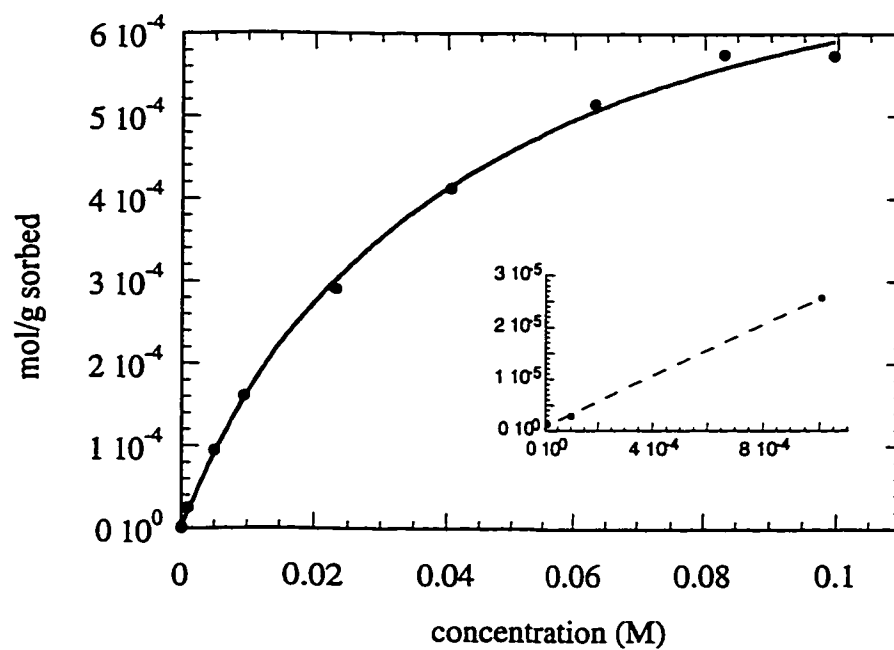


**Figure 4.2** Naphthalene sorption isotherm on PRP- $\infty$  column 7 (Table 2.1) from 60/10/30 methanol/THF/water. Solid line is fit of the solubility limited Langmuir model, eq. 3.47. Linear region is inset with dashed line being the linear least squares fit. Data can be found in Table A1.13.

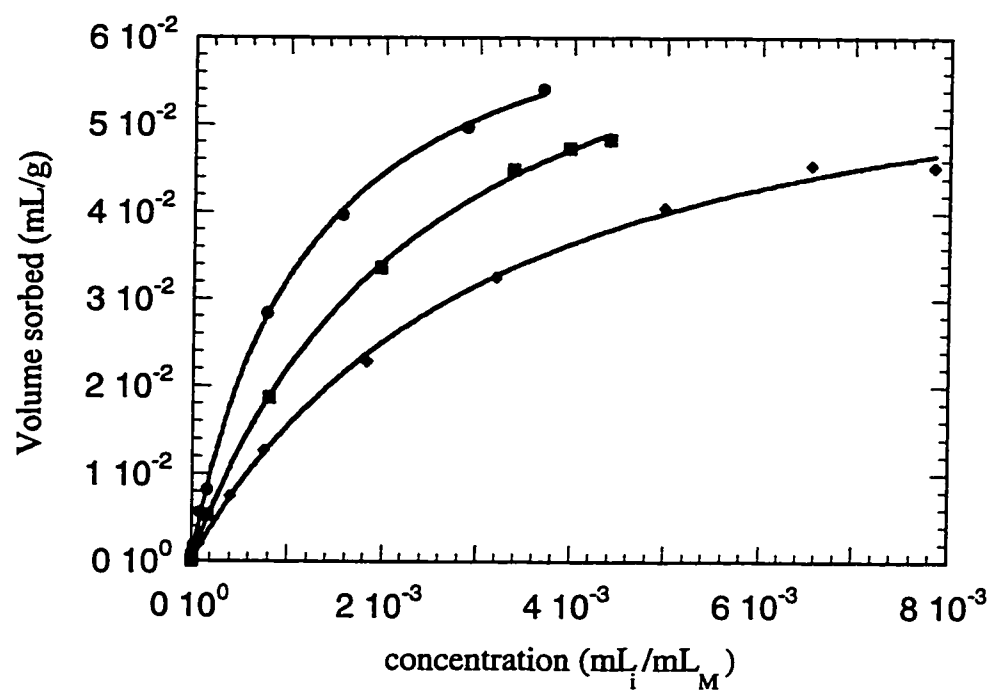


**Figure 4.3** Comparison of naphthalene sorption isotherms on PRP- $\infty$ , in volume units: ● - sorption from 70/30 methanol/water; ■ - sorption from 68/2/30 methanol/THF/water; ◆ - sorption from 60/10/30 methanol/THF/water. Data can be found in Tables A1.3, A1.14, and A1.15.

Differences in the overall free-energy of transfer from the solution phase to the polymer phase are found in the term,  $\frac{K_{ads}}{C_{sat}}$ . Differences in the parameter for naphthalene in different solvents may be the result of differences in solvent strength of the mobile phase and/or differences in the sorption energy per site in the polymer. Differences in solvent strength can be estimated using Snyder's semi-empirical Polarity Index (P') model based on the solubility data reported by Rohrschneider (2):

$$\frac{k'_2}{k'_1} = 10^{(P'_2 - P'_1)/2} \quad (4.1)$$

The polarity index, P', of binary and ternary solvent mixtures can be calculated using volume-weighting of individual solvent P' values via the equation (163, 164):

$$P' = \phi_A P'_A + \phi_B P'_B + \phi_C P'_C \quad (4.2)$$

where

$$\phi_A = \frac{v/v \ \%A}{100} \quad (4.3)$$

$$\phi_B = \frac{v/v \ \%B}{100} \quad (4.4)$$

and

$$\phi_C = \frac{v/v \ \%C}{100} \quad (4.5)$$

A, B, and C represent the different solvents in the mixture. Values for polarities of individual solvents,  $P'_i$ , have been tabulated (2), and are equal to 10.2, 5.1, and 4.0 for water, methanol, and THF, respectively. Therefore, for a 70/30 methanol/water mixture,  $P' = 6.63$ , for 68/2/30 methanol/THF/water,  $P' = 6.61$ , and for 60/10/30 methanol/THF/water,  $P' = 6.52$ . The changes in solvent strength can be calculated using equation 4.1 to give a ratio of  $\frac{k'_2}{k'_1}$ , the predicted ratio of  $k'$  in the stronger eluent to the  $k'$  in the weaker eluent, giving values of 0.98 for the ratio of 68/2/30 methanol/THF/water to 70/30 methanol/water, and 0.88 for the ratio of 60/10/30 methanol/THF/water to 70/30 methanol/water. Therefore, there is a predicted 2% increase in solvent strength for 68/2/30 methanol/THF/water over 70/30 methanol/water, and a predicted 12% increase for 60/10/30 methanol/THF/water over 70/30 methanol/water. The values of  $\frac{K_{ads}}{C_{sat}}$  in Table 4.1 are seen to decrease by more than 40% on going from 70/30 methanol/water to 68/2/30 methanol/THF/water, and by more than 60% on going from 70/30 methanol/THF/water. These values are larger than the 2% and 12% increases in solvent strength predicted from the Snyder model, suggesting that the presence of THF not only increases solvent strength but also decreases the sorption energy per site in the polymer.

The value of the distribution coefficient within the linear region of the isotherm,  $\kappa$ , reflects the changes in both the sorption capacity of the polymer and the overall free-energy of transfer. These effects combine to give the 52% decreases in  $\kappa$

between 70/30 methanol/water and 68/2/30 methanol/THF/water and the 76% between 70/30 methanol/water and 60/10/30 methanol/THF/water.

**Table 4.1** Values of  $C_{S,max}$ ,  $\frac{K_{ads}}{C_{sat}}$ , and  $\kappa$  for naphthalene sorption isotherms from solvents of varying composition.

Solvent Composition (methanol/THF/water)	$C_{sat}$ (mL <sub>i</sub> /mL <sub>M</sub> )	$C_{S,max}$ (mL/g)	$\frac{K_{ads}}{C_{sat}}$ (mL <sub>M</sub> /mL <sub>i</sub> )	$\kappa \left( \frac{mL/g}{mL/mL} \right)$
70/0/30	0.00367	0.0542±0.0003	1140	106±1
68/2/30	0.00439	0.0484±0.0006	643	50.4±0.9
60/10/30	0.00784	0.0452±0.0010	434	24.8±0.6

#### 4.3.2 Naphthalene Sorption Kinetics

To determine the effect of THF on sorption kinetics, sorption rate studies for naphthalene on PRP- $\infty$  were performed at solution compositions 68/2/30 and 60/10/30 methanol/THF/water as described in section 2.8. The rate studies are plotted in Figure 4.4 as moles sorbed per gram of PRP- $\infty$  versus time, and in Figure

4.5 as fraction of the equilibrium amount sorbed versus time, and have been fit with the model for diffusion through a monodisperse sphere (eq. 3.9). The fitting parameters,  $B$ ,  $Q_{\infty}$  and  $D$ , are given in Table 4.2, and will be discussed in section 4.3.5. Also plotted in Figures 4.4 and 4.5, is a representative kinetic study from 70/30 methanol/water solution, previously described in Chapter 3.

From Figure 4.4, it is seen that the amount sorbed at any time decreased as THF percentage increased. This decrease may in part be due to the change in  $k'$  as the solvent composition changed. By plotting the sorption rate as a function of fraction of the equilibrium amount sorbed, as in Figure 4.5, the  $k'$  effect is eliminated. The uptake rate was seen to improve as the fraction of THF was increased from 0% to 2% and then to 10%. That is, the initial rate of sorption became faster, as shown by the steeper initial slope, and the plateau, or equilibrium amount sorbed, was approached sooner. The change in the kinetics however, from 2% to 10% THF is not as dramatic as that seen on changing from 0% to 2% THF. For 2% and 10% THF, the initial rates of sorption are similar and the plateau value is approached around the same time. This suggests that the effect that THF has on improving elution peak shape occurs at a low percentage of THF in solution.

Plots of  $Bt$  versus  $t$ , indicating the quality of fit of the model, are shown in Figure 4.6. These  $Bt$  versus  $t$  plots are seen to be linear and have intercepts of approximately zero for fractions of coverage less than 95%, as expected if the model describes the data. Both the  $Bt$  versus  $t$  plots from 68/2/30 methanol/THF/water and 60/10/30 methanol/THF/water are seen to deviate from linearity at a high fraction sorbed (>95%), for reasons discussed in 3.3.2.2.

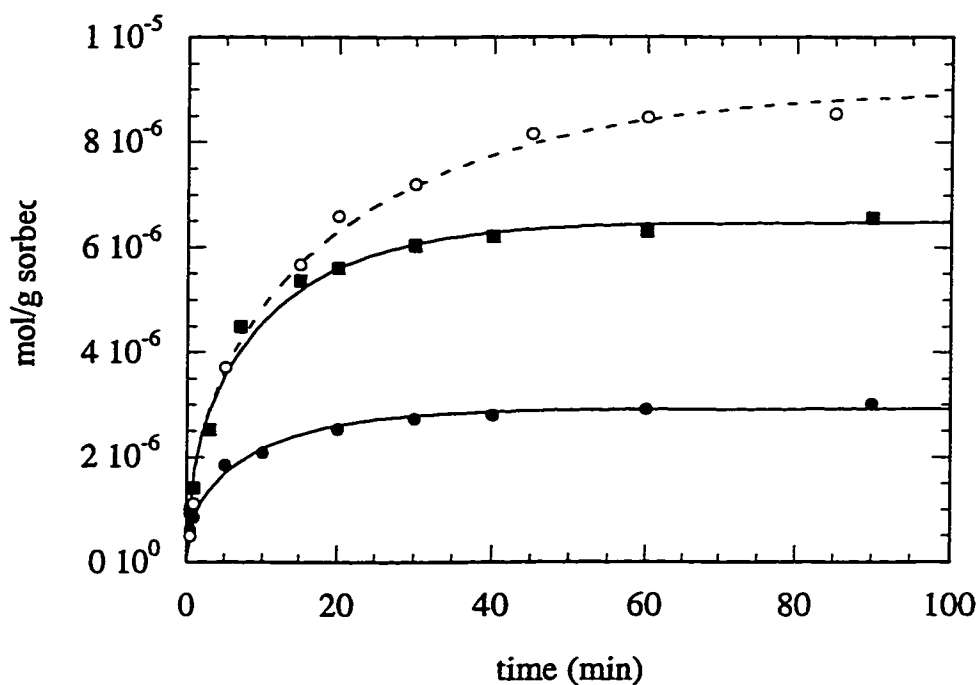


**Figure 4.4** Comparison of naphthalene sorption kinetics on PRP- $\infty$ : ○ - sorption from 70/30 methanol/water (Trial 3, Figure 3.7); ■ - sorption from  $9.747 \times 10^{-5}$  M naphthalene in 68/2/30/ methanol/THF/water on PRP- $\infty$  column 6 (Table 2.1) at  $\bar{U}_0 = 20.3$  cm/s; ● - sorption from  $9.747 \times 10^{-5}$  M naphthalene in 60/10/30 methanol/THF/water on PRP- $\infty$  8 (Table 2.1) at  $\bar{U}_0 = 15$  cm/s. Data for can be found in Tables A1.8, A1.16 and A1.17.

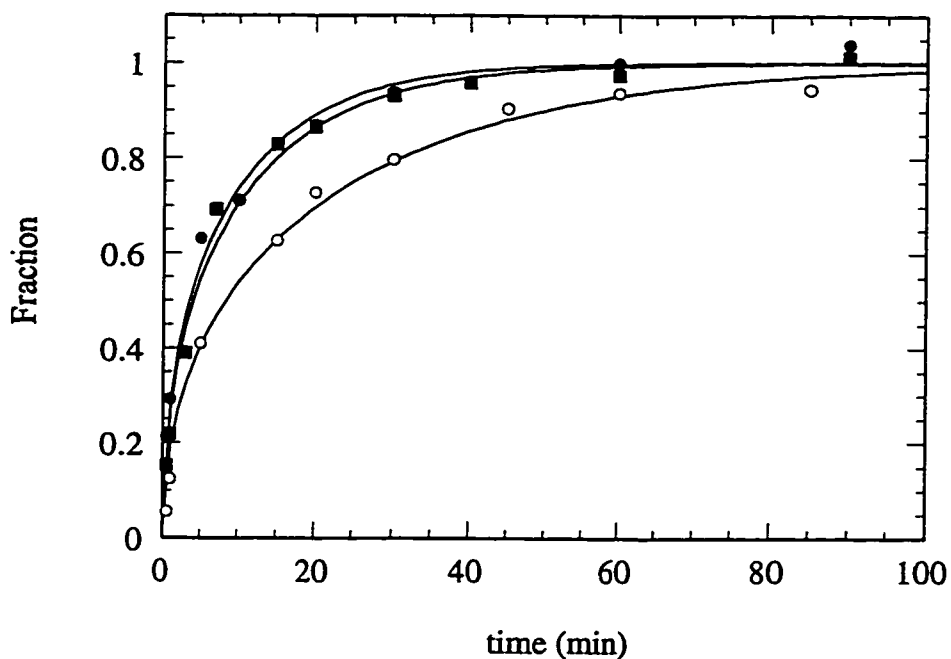


**Figure 4.5** Comparison of normalized naphthalene sorption kinetics on PRP- $\infty$ : ○ - sorption from 70/30 methanol/water (Trial 3); ■ - sorption from  $9.747 \times 10^{-5}$  M naphthalene in 68/2/30/ methanol/THF/water; ● - sorption from  $9.747 \times 10^{-5}$  M naphthalene in 60/10/30 methanol/THF/water. Data can be found in Tables A.8, A.16 and A.17.

**Table 4.2** Fitting parameters from naphthalene sorption rate studies on PRP- $\infty$  from binary and ternary solutions.

Solvent Composition methanol/THF/water	$B(s)^{-1} \times 10^3$	$Q_{\infty} (\text{mol/g}) \times 10^6$	$D(\text{cm}^2/\text{s}) \times 10^{10}$
70/0/30 <sup>a</sup>	0.70 $\pm$ 0.09	9.2 $\pm$ 0.4	0.7 $\pm$ 0.1
68/2/30	1.3 $\pm$ 0.2	6.5 $\pm$ 0.2	1.3 $\pm$ 0.2
60/10/30	1.4 $\pm$ 0.1	2.92 $\pm$ 0.05	1.5 $\pm$ 0.1

<sup>a</sup> average of three trials

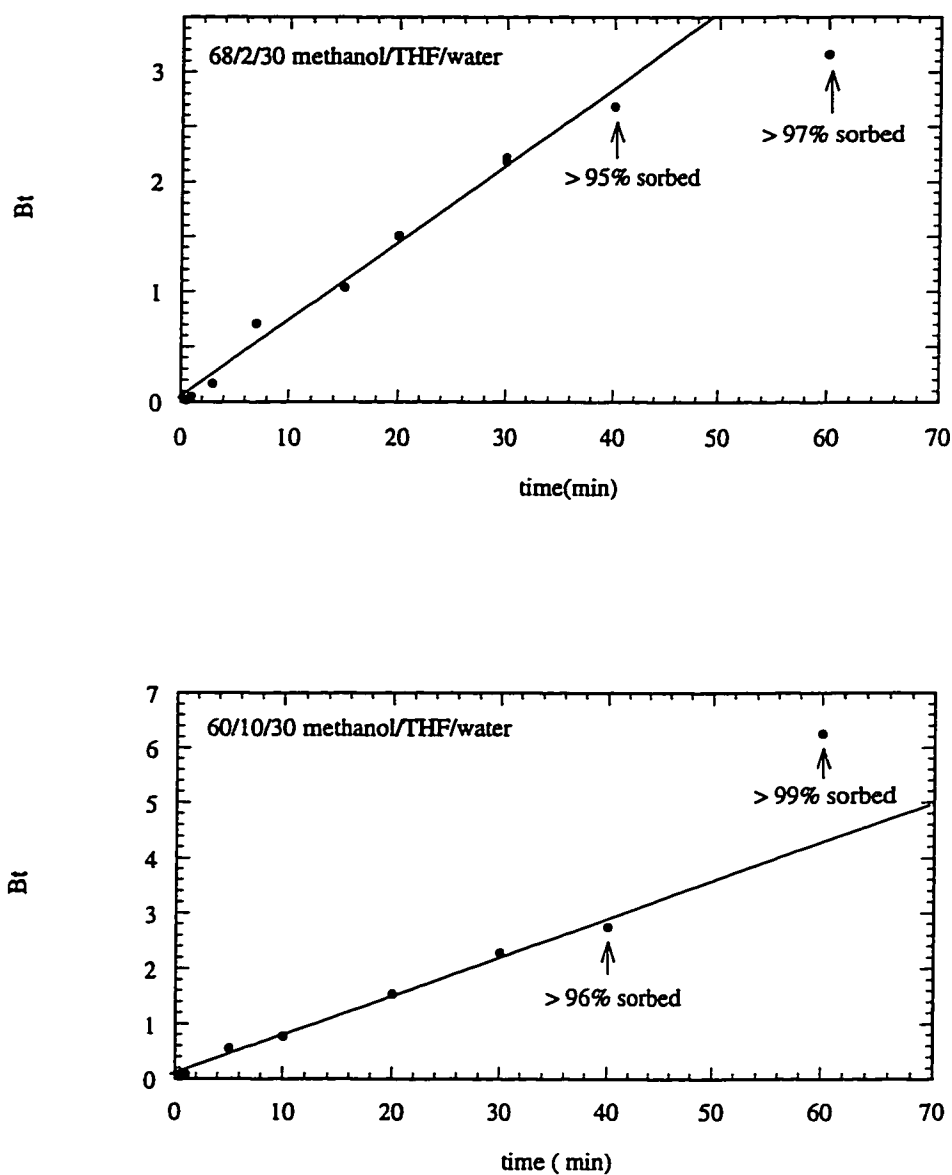


**Figure 4.6** Quality of fit of monodisperse model (eq. 3.9) to naphthalene sorption kinetics from  $9.747 \times 10^{-5}$  M naphthalene in ternary solutions.  $Bt$  values have been calculated using equations 3.12 and 3.13. Lines are the linear least squares fit to the data within the linear region. Data can be found in Tables A1.16-A1.17.

### 4.3.3 Sorption of Methanol and THF by PRP- $\infty$ and the Resultant Swelling

To understand the effect of THF on the sorption of a solute, it is necessary to consider the uptake by the polymer of methanol and THF, and the swelling that results from this uptake. This work was done by Ying Wang of this research group and is presented here for the purpose of explaining the experimental results described in the preceding sections of this chapter. Experimental details of the uptake and swelling experiments will be presented in Wang's thesis (165). Shown in Figure 4.7 are the solvent sorption isotherms for methanol and THF on PRP- $\infty$  from solutions of methanol/water or THF/water, plotted as molecular volume of solvent sorbed versus activity of the organic modifier in solution. The THF sorption isotherm is initially convex, while the methanol sorption isotherm is nearly linear. Methanol has a limiting value of 0.13 mL/g sorbed at a methanol activity of 1.00. The THF isotherm was found to increase sharply at an activity of about 0.8 as capillary condensation of THF within the micropores occurred and reached a limiting value of 0.23 g/mL at a THF activity of 1.00. It should be noted that the THF isotherm, before the onset of capillary condensation, appears to be heading to the same sorbed molecular volume as methanol. This indicates that methanol and THF both wet the polymer and, in pure organic modifier, they are occupying the same regions of the polymer.

In Figure 4.8 the swelling curves are shown for the sorbent particles in solutions of THF/water and methanol/water, plotted as the increase in volume per

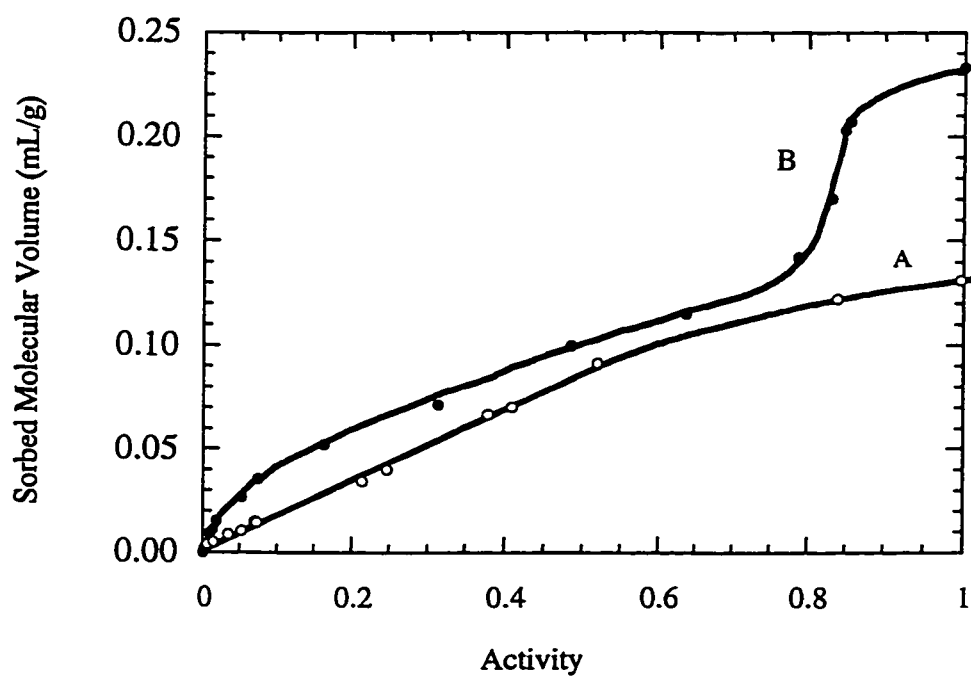


**Figure 4.7** Solvent sorption isotherms on PRP- $\infty$  for methanol (○) and THF (●). Data can be found in Tables A1.18 and A1.19. Adapted from Wang (165).

gram of PRP- $\infty$  versus the activity of the organic modifier in solution. Both swelling curves are convex, with THF swelling the polymer to roughly twice the extent that methanol does. The swelling of the particles in 70/30 methanol/water, 2/68/30 methanol/THF/water and 60/10/30 methanol/THF/water were also measured. The changes in volumes over that of a dry particle were found to be 0.0613 mL/g (i.e. 6.43 v/v %), 0.0645 mL/g (6.77 v/v%), and 0.1114 mL/g (11.7 v/v%), respectively. The presence of 2% THF caused a small change in swelling above that found in 70/30 methanol/water, while the presence of 10% THF caused a large increase in swelling over that in 70/30 methanol/water.

A clearer understanding of what is occurring within the polymer results from the comparison of the sorption and swelling curves. By plotting the vertical axes of Figures 4.7 and 4.8 against one another at equal solution activities for each organic modifier, i.e. volume change (mL/g) versus sorbed volume (mL/g), the volume of swelling produced by the volume sorbed can be seen. In regions of the polymer where the organic modifier is only causing "external" (21) or "isotropic" (166) swelling, the polymer network expands without the loss of any of the permanent porosity that was present in the dry state. In fact, this expansion opens pores in the previously collapsed regions of the gel where the crosslinking density is not high. Within this region, the change in volume of the polymer and the volume sorbed are expected to have a linear relationship. This swelling and increase in porosity is expected to lead to less hindered diffusion through the gel regions of the polymer matrix (81).

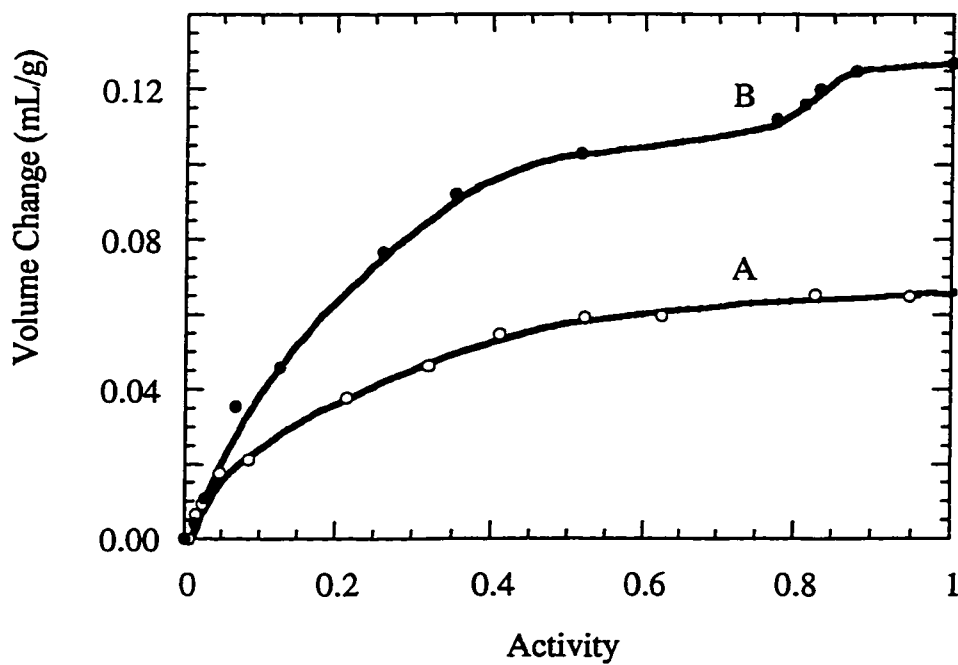


**Figure 4.8** Swelling curves for PRP- $\infty$  in methanol (○) and THF (●). Data can be found in Tables A1.20 and A1.21. Adapted from Wang (165).

For regions where the swelling of the polymer with sorbed volume deviates negatively from linearity, the organic modifier is occupying the permanent micropores. This occupancy of micropores can be by one of several processes: "internal" swelling where the polymer chains expand into the micropores as organic modifier is sorbed; adsorption of the organic modifier within the micropores (21); and under some circumstances, the condensation of the organic modifier within the micropores (167, 168).

The swelling vs. sorption curve for methanol is shown in Figure 4.9. It can be seen that methanol causes "external" swelling up to a molecular volume sorbed of about 0.025 mL/g, which has been fit by a straight line and is indicated as region SW in Figure 4.9. At higher sorbed volumes, above 0.025 mL/g, methanol causes less swelling, as the predominant process becomes sorption in the permanent micropores. This region is indicated by AD in Figure 4.9. Due to its weak solvent strength with respect to the polymer matrix, and the fact that the permanent micropores are in the more highly crosslinked regions of the polymer, it is likely that the methanol is adsorbing to the "walls" of the micropores rather than causing internal swelling. At equilibrium with pure methanol, the polymer is seen to sorb 0.13 mL/g and swell by 0.065 mL/g.

The swelling vs. sorption curve for THF on PRP- $\infty$  is shown in Figure 4.10. In the early part of this curve, for the first  $\approx 0.01$  mL/g sorbed THF as indicated by AD<sub>1</sub> in Figure 4.10, sorption occurs without swelling. In this region, THF is sorbing

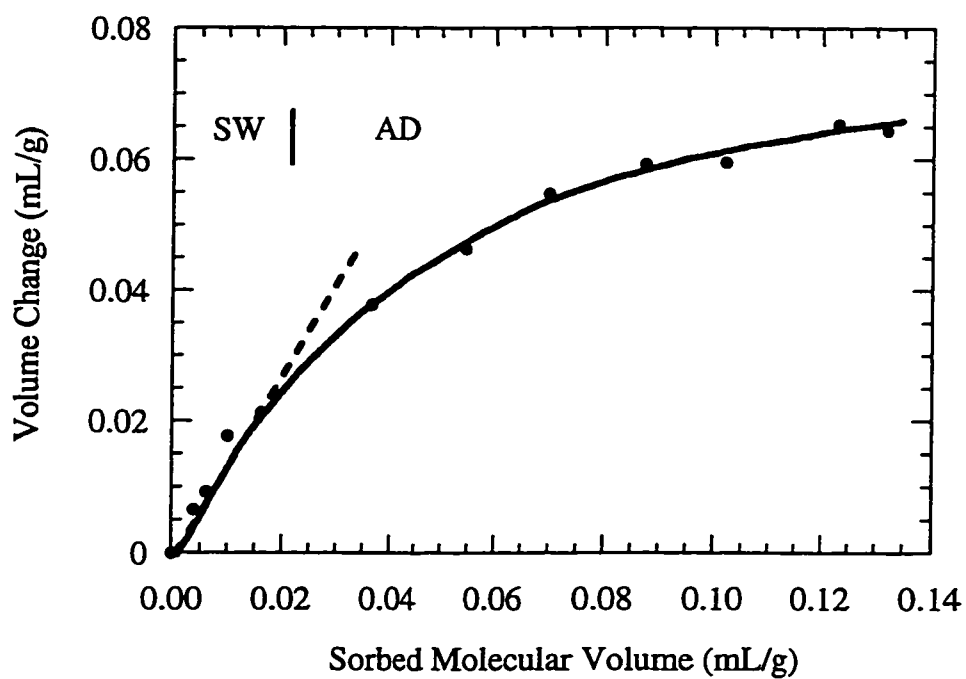


**Figure 4.9** Swelling-sorption curve for PRP- $\infty$  in methanol. Data can be found in Table A1.22. Adapted from Wang (165).

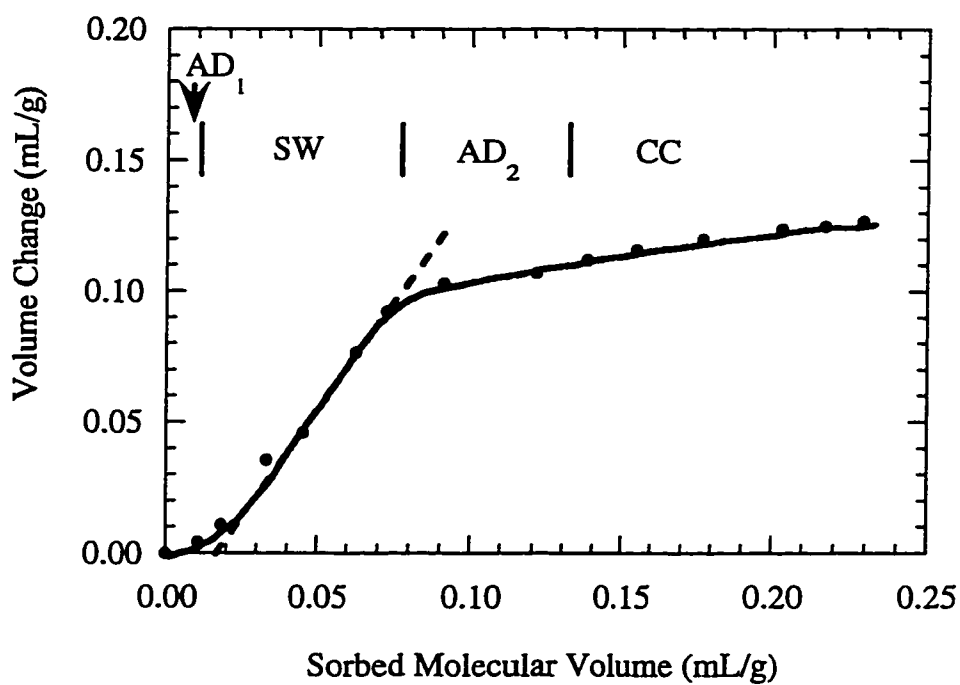


**Figure 4.10** Swelling-sorption curve for PRP- $\infty$  in THF. Data can be found in Table A1.23. Adapted from Wang (165).

within the smallest, most highly crosslinked, most hindered, rigid, of the permanent micropores. In region  $SW_1$  which has been fit to a straight line, THF causes "external" swelling of the polymer as it is sorbed in the gel region, reaching a sorbed molecular volume of 0.08 mL/g. THF, being a better solvent for PS-DVB than methanol, is able to swell the chains to a greater extent than was seen for methanol. This increase in swelling may be the result of the solvating of polymer chains between crosslinks in the gel region by THF, reducing their entanglement (169). Above a sorbed volume of 0.08 mL/g, region  $AD_2$  in Figure 4.10, the predominant process is again THF entering micropores where it is either adsorbed on the walls of the micropores, or causes internal swelling. From the THF isotherm in Figure 4.7, it is seen that the volume sorbed by  $PRP-\infty$  is 0.15 mL/g before capillary condensation within the micropores occurs, as indicated by the sudden upturn in the isotherm (Figure 4.7) at an activity of THF of approximately 0.8. CC indicates this capillary condensation region in Figure 4.10.

Adsorption in the smallest, most highly crosslinked, most highly hindered permanent micropores, such as seen for THF in region  $AD_1$ , is not seen for the sorption of methanol. The explanation for this effect lies in the difference in the surface tensions and molar volumes of the two organic components, and the conditions that must exist for capillary condensation to occur within the permanent micropores. The permanent micropores are in equilibrium with the gel, with the bulk solution, and with the headspace above the bulk solution. The vapour pressure of the solvent above the bulk solution is directly proportional to its activity in the bulk

solution. The activity that is required for the onset of capillary condensation is related to the Kelvin equation (109, 170, 171):

$$\ln(\text{activity}) \propto \ln \frac{p}{p_0} \approx -\frac{2\gamma V \cos \theta}{r_p R_g T} \quad (4.6)$$

where  $p$  is the equilibrium vapour pressure within the pore,  $p_0$  is the saturated vapour pressure of the solvent on a flat surface,  $\gamma$  is surface tension,  $V$  is the molar volume of the liquid,  $\theta$  is the contact angle,  $R_g$  is the gas constant, and  $T$  is temperature. THF has a molar volume of  $81.1 \text{ cm}^3/\text{mol}$  (MMPro<sup>®</sup>) and a surface tension of  $26.40 \text{ dynes/cm}$  (172) at  $25^\circ\text{C}$ , while methanol has a molar volume of  $40.7 \text{ cm}^3/\text{mol}$  (MMPro<sup>®</sup>) and a surface tension of  $21.85 \text{ dynes/cm}$  (172). The higher surface tension and larger molar volume of THF results in capillary condensation of THF in a pore at a bulk phase activity that is lower than for methanol. This condensation within the permanent micropores is consistent with the convex nature of the THF sorption isotherm at low THF activity, shown in Figure 4.7. A more linear region follows the initial convex region of the isotherm, as solvent is sorbed in the gel region of the polymer matrix. Capillary condensation is again seen at high activity, as THF condenses in larger micropores.

The near-linearity of the methanol sorption isotherm indicates that methanol does not experience capillary condensation from low concentration in solution. Linear sorption isotherms were also found for the solutes naphthalene and octyl *p*-hydroxybenzoate, as discussed in Chapter 3, indicating that they, too, do not undergo capillary condensation in the permanent micropores.

#### 4.3.4 Activity of Methanol and THF in Solution

In order to analyse the solute sorption data, it is necessary to know the amount of solvent sorbed by the polymer, and the resultant swelling. To determine where on the methanol sorption isotherm and sorption-swelling curve the 70/30 methanol/water solution lies, it was necessary to calculate the activity of methanol in a solution of this composition. The calculation of the methanol solution activity coefficient was via the equation (173, 174):

$$\ln \gamma_1 = (0.6304 - 0.4134\chi_1)\chi_2^2 \quad (4.7)$$

where  $\gamma_1$  is the activity coefficient of the methanol solution, and  $\chi_1$  and  $\chi_2$  are the mole fractions of methanol and water, respectively. Using the activity coefficient, the activity of methanol in a 70/30 methanol/water solution was calculated to be 0.610. From Figure 4.7, the sorbed molecular volume of methanol at this activity is found to be approximately 0.10 mL/g. Looking at Figure 4.9, it is seen that at this sorbed molecular volume, region SW is as swollen as it can be by methanol, and there is sorption in the micropore region, AD.

In the calculation of activities of THF containing solutions, the effect of methanol has been neglected, as sorption isotherms have not been measured under

conditions of mixed organic solvents. While this may introduce error in the determination of the overall activity of methanol and THF in the ternary solutions, it is assumed that the overall conclusions drawn from the data are not seriously affected by doing this. The activity of THF in a 2/98 THF/water solution and a 10/90 THF water solution were calculated via the equation (175, 176):

$$\ln \gamma_1 = \chi_2^2 \left( \frac{0.291}{(\chi_1 + 0.3624\chi_2)^2} + \frac{0.79129}{(\chi_2 + 0.4355\chi_1)^2} \right) \quad (4.8)$$

where  $\gamma_1$  is the activity coefficient of THF in solution, and  $\chi_1$  and  $\chi_2$  are the mole fractions of THF and water respectively. Using the values obtained for the activity coefficients, the activity of THF in a 2/98 THF/water solution and a 10/90 THF/water solution was calculated to be 0.0861 and 0.364 g/mL, respectively. For a 2/98 THF/water solution, the sorbed molecular volume of THF is about 0.035 mL/g, and at 10/90 THF/water is about 0.080 mL/g, as determined using Figure 4.7. These volumes sorbed are both greater than the volume sorbed within region AD<sub>1</sub> of Figure 4.9, where THF is sorbed within the permanent micropores.

#### 4.3.5 Effect of THF on Naphthalene Sorption Isotherms

The isotherms and kinetic studies on PRP- $\infty$  using varying amounts of THF revealed two important facts: 1) as the amount of THF was increased, the capacity of the sorbent for naphthalene was decreased; and 2) a small amount of added THF had

a dramatic effect on sorption kinetics. Literature on the role of THF in improving elution peak shape (54, 57, 60, 68, 156) implies that it does so exclusively because it swells the polymer thereby reducing the hindrance to diffusion within the polymer.

As mentioned earlier, and as shown in Figure 4.3, the sorption capacity for naphthalene on PRP- $\infty$ , as determined at the saturation point for naphthalene in the respective solutions, decreased as the amount of THF present in solution was increased. The activity of naphthalene in solution at the saturation point is equal to one, and any differences arising in the capacity reflect changes occurring within the stationary phase. The capacity for naphthalene when the solvent was 68/2/30 methanol/THF/water was found to decrease by 11% from that found when the solvent was 70/30 methanol/water. When the solvent was 60/10/30 methanol/THF/water, the decrease in capacity was 17% with respect to the 70/30 methanol/water solution, only 6% greater than that found at 68/2/30 methanol/THF/water. If swelling is the only effect of THF on the polymer, the same number of sites should be available within the polymer for sorption, irrespective of solution composition. Since the number of sites has decreased, it is suggested here that THF is having a "blocking" effect within the polymer that occurs at low concentrations of THF in the solvent. This blocking is being suggested to arise from the enrichment of THF in the permanent micropores and its subsequent condensation, as seen in region AD<sub>1</sub> in Figure 4.10. Because of the energy related with the association of the THF molecules within the permanent micropores, naphthalene cannot displace molecules of THF required for it to enter the permanent micropores. Hence, its local  $k'$  is essentially zero, i.e. these sites become "blocked" by THF. The volume associated with the total number of sorption sites in

the polymer has now been reduced by the volume associated with the sites within the permanent micropores to which THF has sorbed, i.e the volume of region  $AD_1$ , 0.01 mL/g.

In section 4.3.4, it was calculated that in 70/30 methanol/water solution, the sorbed volume of methanol is about 0.10 mL/g. The addition of THF to give a 68/2/30 methanol/THF/water solution caused little additional swelling ( $\sim 5\%$ ) in the polymer over that seen from 70/30 methanol/water. From Figure 4.7, and assuming that the volume of THF sorbed by the polymer is not affected by the presence of methanol, the sorbed volume of THF from a 2% THF solution is 0.03 mL/g, which is more than the 0.01 mL/g required to block sorption in the permanent micropores. This blockage of 0.01 mL/g of sites represents a 10% reduction in the capacity of the polymer. The 11% decrease in sorption capacity seen for naphthalene upon changing from 70/30 methanol/water to 68/2/30 methanol/THF/water is in good agreement with this value. The further reduction in capacity upon changing to a 10% THF solution arises from the blocking of additional sites by the increased amount of THF. This blocking of sites by THF is analogous to the blocking of active sites by water on polar adsorbents, which has been shown to result in the improvement in peak shapes (153). This blocking effect in the permanent micropores is not seen with methanol, i.e. there is not a region on the swelling-sorption curve in Figure 4.9 where sorption occurs without swelling, as methanol does not condense in this region. Hence, naphthalene can diffuse into the permanent micropores and compete with methanol for sorption. The same holds true for the sorption of octyl p-hydroxybenzoate, which was shown in Chapter 3 to have the same volume sorbed as naphthalene, by PRP- $\infty$ .

It is expected that the addition of THF to octyl p-hydroxybenzoate solutions would result in the same decreases in sorption capacities as seen for naphthalene.

#### 4.3.5 Effect of THF on Naphthalene Sorption Rate

The kinetic studies, plotted in Figure 4.5, show that the improvement in the sorption kinetics of naphthalene on PRP- $\infty$  with the addition of 2% THF to give a 68/2/30 methanol/THF/water is significant with respect to the kinetics from the 70/30 methanol/water solution, though the increase in particle swelling is minimal. However, the improvement in the kinetics on going to 60/10/30 methanol/THF/water from 68/2/30 methanol/THF/water is not very significant, though the increase in swelling is 70% over that in 68/2/30 methanol/THF/water. This also suggests that the blocking effect THF has within the polymer matrix occurs at low THF concentration, and the improvement in the sorption kinetics is not solely dependent on swelling in the polymer matrix.

When the polymer sorbs a solvent, the effects are different within different regions of the matrix. As described earlier, the polymer matrix is heterogeneous, with there being a continuum of crosslinking densities between the gel and permanent micropore regions. If, for simplicity, this continuum is approximated by two regions, gel and permanent micropore, then the relative effect of solvent sorption within the polymer can be determined (eqs 3.23-3.24). Within the gel region as the solvent is sorbed, the capacity of the region should remain unchanged, as the swelling that occurs does not block sorption sites. The free-volume of the region increases as the amount of solvent present increases. As well,  $\hat{\theta}$  may decrease slightly (136) because

the swelling decreases the tortuosity in the gel and increases the free volume. Also,  $\hat{\lambda}$  should become significantly larger because a small change in pore diameter with swelling has a large effect on hindrance (125). In the permanent micropore region, essentially no swelling occurs and the capacity decreases as sites become blocked by condensed solvents. The free-volume of the matrix, as well as  $\hat{\theta}$  and  $\hat{\lambda}$  therefore, do not change.

The values for the diffusion coefficients for naphthalene under conditions of varying percentages of THF are given in Table 4.2. It is seen that the diffusion coefficient increased by approximately 100% on going from 70/30 methanol/water to 68/2/30 methanol/THF/water, but did not experience a further significant increase when the percentage of THF was raised to 10% (i.e. 60/10/30 methanol/THF/water). From equation 3.22, it is seen that this increase must be due to either an increase in  $\hat{\lambda}$  (less hindrance) or a decrease in  $\hat{\theta}$  (less tortuosity), since  $D_p$  is based on diffusion within the pure polymer and must remain unchanged. As described in Chapter 3, under the two-region approximation, gel and permanent micropore ( $\mu$ ), the hindrance and tortuosity terms can be expressed as:

$$\hat{\lambda}^{-1} = \frac{\eta_{\text{gel}}\hat{\lambda}_{\text{gel}}^{-1} + \eta_{\mu}\hat{\lambda}_{\mu}^{-1}}{\eta_{\text{gel}} + \eta_{\mu}} \quad (3.23)$$

and

$$\hat{\theta} = \frac{\eta_{\text{gel}}\hat{\theta}_{\text{gel}} + \eta_{\mu}\hat{\theta}_{\mu}}{\eta_{\text{gel}} + \eta_{\mu}} \quad (3.24)$$

where  $\eta$  is the sorption capacity and is equal to  $\eta_{\text{gel}} + \eta_{\mu}$ . Since there was little change in swelling between 70/30 methanol/water and 68/2/30 methanol/THF water,  $\hat{\theta}_{\text{gel}}$  and

$\hat{\theta}_\mu$  remain essentially unchanged. As well, the values of  $\hat{\theta}_{gel}$  and  $\hat{\theta}_\mu$  must be approximately equal because tortuosity does not typically have a wide range of values (between 1 and 5) and the change in tortuosity in going from the gel region to the permanent micropore region is, in all likelihood, small. From the naphthalene sorption isotherms, it was seen that THF blocked roughly 10% of the polymer sites that have been attributed earlier to sites within permanent micropores. Therefore,  $\eta_\mu$  has changed and become approximately zero, while  $\eta_{gel}$  has remained unchanged. Taking these facts into consideration and looking back at equation 3.24, it is seen that the changes that occur in the variables are insufficient to account for the changes seen in the diffusion coefficient. That is,  $\hat{\theta}$  in equation 3.22 is being controlled by the gel region which has approximately the same tortuosity as the permanent micropore region but accounts for 90% of the sites. Blockage of the permanent micropore sites will not appreciably change the value of  $\hat{\theta}$ . The increase in the diffusion coefficient must therefore be related to the hindrance term,  $\hat{\lambda}$ , in equation 3.23. If the blockage of the permanent micropores, which account for 10% of the sites, doubles the diffusion coefficient, it must be that  $\hat{\lambda}_{gel} \gg \hat{\lambda}_\mu$  (i.e. diffusion within the permanent micropores is highly hindered) because the blockage of these sites doubles the value of  $\hat{\lambda}$  in equation 3.23. The further addition of THF to give 60/10/30 methanol/THF/water was seen to increase swelling by 70% over that seen in 68/2/30 methanol/THF/water, but did not have a big effect on the diffusion coefficient. The most highly hindered sites, which have a large effect on the overall value of  $\hat{\lambda}$ , have already been blocked at low THF concentration. While the diffusion coefficient in

the polymer in 68/2/30 methanol/THF/water has doubled over that seen in 70/30 methanol/water, it's value is still four orders of magnitude smaller than that in free solution as measured in section 3.3.3.

In Chapter 3, the kinetics of sorption for naphthalene and octyl p-hydroxybenzoate from 70/30 methanol/water solutions were found to be quite similar. Under the above interpretation, this would be the expected result. In both cases, the solvent was 70/30 methanol/water, with the sorbent being pre-equilibrated with the solvent, so the polymer was solvent-swollen to the same extent for both solutes, and for each trial of a kinetic study. As well, loading was done under conditions of trace loading of the solute such that the solute sorption and diffusion caused no additional swelling of the polymer. Since both naphthalene and octyl p-hydroxybenzoate have a solubility parameter closer to the matrix than methanol, they can compete with methanol for sorption in the matrix. Both solutes access all regions of the polymer that the solvent reaches, and can sorb on all sites, including the highly hindered sites within the permanent micropores. As THF was added to the naphthalene containing solutions, these hindered sites were blocked and an improvement in naphthalene kinetics was observed. This is also the effect that would be expected as THF is added to octyl p-hydroxybenzoate solutions, though this experiment has not been performed.

It should be noted that if the kinetic studies were run in a pure THF mobile phase with a solute that has a significant  $k'$  from this solution, it is likely that the sorption kinetics would still be slow. If a solute can sorb to the polymer from pure THF, then it can do so in any region of the polymer, including the highly hindered

sites within the permanent micropores that are blocked by THF when it is present at low concentration in solution.

#### 4.3.6 Predicted Elution Profiles

Elution profiles for naphthalene on PRP- $\infty$  from solutions of 68/2/30 and 60/10/30 methanol/THF/water have been predicted using a previously validated method, as described in section 3.3.4, again using the bi-exponential form of equation 3.33. The bi-exponential fits to the data can be found in Figure 4.11 and the fitting parameters are shown in Table 4.3. The flow rate used for prediction was 0.004 mL/min (0.0024 cm/s), which allowed for the fraction of sites not sorbed as the molecule passes through the column to be significant only on the slow sites. The  $k'$  values for the 68/2/30 methanol/THF/water solution and the 60/10/30 methanol/THF/water solution were calculated as in section 3.3.4, and found to be 93.9 and 46.3, respectively.

**Table 4.3** Fitting parameters from bi-exponential fits to naphthalene sorption kinetics from ternary methanol/THF/water solutions.

Trial	$n_0 \times 10^6$	$n_1 \times 10^6$	$k_1$	$n_2 \times 10^6$	$k_2$
68/2/30	6.542	4.013	0.3207	2.53	0.05471
60/10/30	3.007	1.46	0.8523	1.547	0.05672

The overall predicted elution profiles are shown in Figure 4.12 along with a predicted elution profile for naphthalene from a 70/30 methanol/water solution, all at the same flow rate, 0.004 mL/min (0.0013 cm/s). The figure is plotted as the normalized signal versus  $t/t_r$ , where  $t_r$  is the center of gravity of the peak. Normalizing the x-axis in this manner eliminates the effect of the changing  $k'$  on the peak position and shape, so that any improvement in peak shape arises due to an increase in the diffusion coefficient,  $D$ , as hindrance is decreased. As the amount of THF is increased, the peak is seen to become narrower with its maximum signal approaching its center of gravity. However, even in a 60/10/30 methanol/THF/water solution (i.e. 10% THF), the peak is still seen to be asymmetric. The results are consistent with improvements in peak symmetry on a macroporous 5  $\mu\text{m}$  particle size PS-DVB column that have been seen experimentally upon the addition of THF to the mobile phase (54), though the improvement in symmetry predicted is not as great as that seen experimentally. A narrow, symmetric peak, however, may be an unrealistic expectation when dealing with non-porous particles of this size (20  $\mu\text{m}$ ).

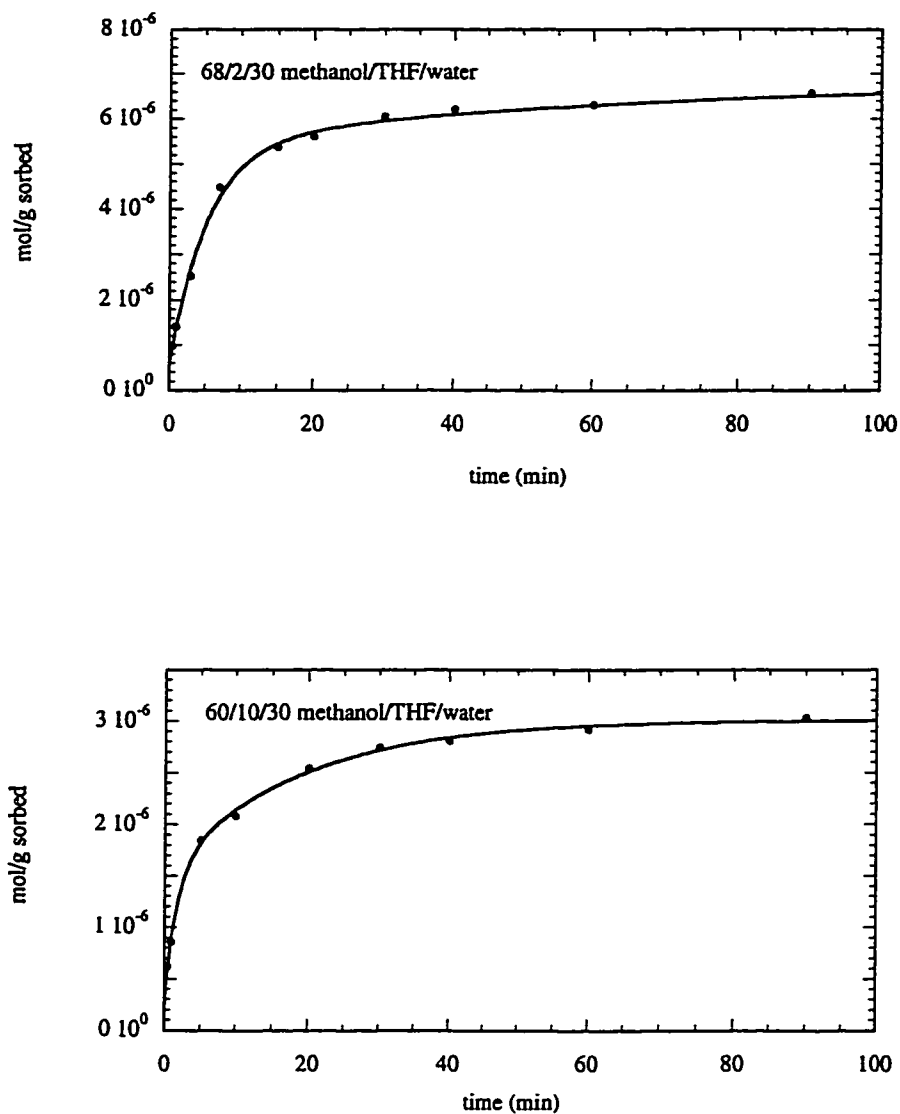


**Figure 4.11** Bi-exponential fits (solid lines) to naphthalene sorption kinetics on PRP- $\infty$  columns 6 and 8 (Table 2.1), respectively, from ternary solutions with a concentration of naphthalene of  $9.747 \times 10^{-5}$  M. Data can be found in Tables A1.10-A1.11.

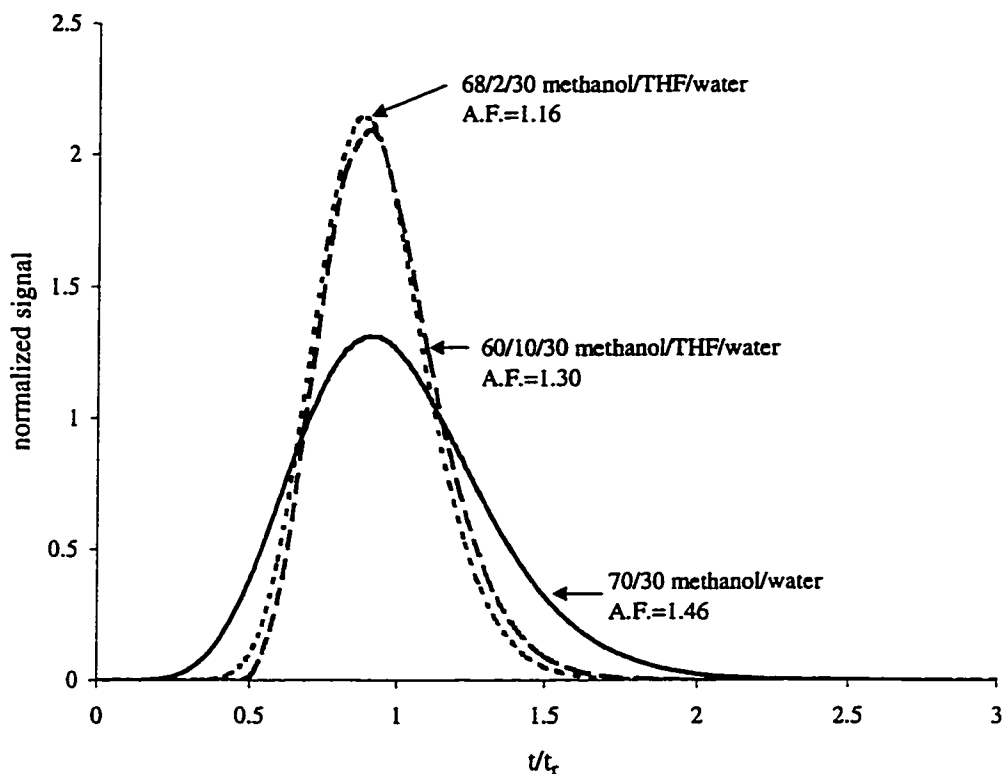


**Figure 4.12** Predicted naphthalene elution profiles at a flow rate of 0.004 mL/min from a PRP- $\infty$  column using the parameters obtained from bi-exponential fits to sorption rate curves from ternary solutions shown in Figure 4.11 and in Figure 3.13 for the binary solution. Parameters from sorption rate curves from ternary solutions are given in Table 4.3 and for the binary solution in Table 3.5. The corresponding asymmetry factors (A.F.) were measured at 10% of peak height.

## Chapter 5

### Naphthalene Sorption Isotherms and Sorption Kinetics on POROS 20 R2

#### 5.1 Introduction

POROS 20 R2 is a 20  $\mu\text{m}$ , gigaporous, reversed phase, PS-DVB sorbent. Gigaporous particles are those having a ratio of the pore diameter to the particle diameter greater than 0.01 (108). These types of packings were developed in order to reduce efficiency losses seen with macroporous packings that result from diffusion in the stagnant mobile phase. With the large pore sizes in gigaporous materials, convective flow through the particles can be achieved. This flow through the particles has been referred to as "perfusive" flow, and the chromatography done with these types of materials as "perfusion" chromatography (44, 45).

To date, these packings have been applied mainly to protein and peptide analysis (15, 44-53). However, it has been suggested that these "perfusive" packings may find an application in capillary electrokinetic chromatography (CEC). With the wide channels within the particles, the electrochemical double layer overlap within the pores would be eliminated and electroosmotic flow through the particles would be possible.

In this study, the focus was to determine if these packings, too, are subject to slow diffusion within the polymer matrix when the solute is a small, neutral molecule. In the case that slow diffusion is still a factor, the applications of these polymers to CEC when the sample contains small, neutral solutes may be limited. To study the

diffusion within the matrix, the naphthalene sorption isotherms and sorption kinetics from binary methanol/water and ternary methanol/THF/water solutions on POROS 20 R2 were measured and fit to theoretical equations. Elution profiles were then predicted for naphthalene from a POROS 20 R2 column as done in the previous chapters for a column of PRP- $\infty$ .

## 5.2 Theory

### 5.2.1 Perfusion Chromatographic Media

As mentioned earlier, perfusion packings were developed to reduce efficiency losses due to diffusion within the stagnant mobile phase. As well, they are an alternative to non-porous packings which eliminate stagnant mobile phase but have the disadvantages of low loading capacities, difficulty in packing well due to their small size (1-3  $\mu\text{m}$ ), and high column back-pressures (45). The packings are synthesized in a multi-step co-polymerization of styrene and divinylbenzene (177). The resulting particles consist of fused microspheres of highly crosslinked PS-DVB having diameters of approximately 1  $\mu\text{m}$  (178), giving an interconnected bimodal pore network of "throughpores" ( $d = 6000\text{-}8000\text{\AA}$ ), and diffusive macropores ( $d = 800\text{-}1500\text{\AA}$ ). The throughpores have a very low surface area and contribute little to the overall sorption capacity. The presence of the diffusive macropores increases the surface area and capacity of the packing. These diffusive pores are kept shallow (depth is less than 1  $\mu\text{m}$ ) in order to minimize their contribution to resistance to mass transfer. The microspheres, being made up of highly crosslinked PS-DVB, likely have a structure similar to that described earlier for PRP- $\infty$ , consisting of highly

crosslinked nuclei surrounded by a region with a continuum of crosslinking densities. A sketch of the cross-section of a perfusive particle is shown in Figure 5.1. The native PS-DVB polymer behaves as a reversed phase sorbent. These packings, however, can be functionalized to provide stationary phases for ion exchange, hydrophobic and hydrophilic interaction, affinity, and metal chelate chromatographies.

Convective flow can be achieved through the perfusive particles and is dependent upon the pressure drop across the column and therefore across a particle. The linear velocity of flow in a throughpore has been estimated to be roughly 5% of the linear velocity through the column. It has been approximated that 2% of the flow is through, rather than around, the particles. The pressure drop across a column is therefore essentially unaffected by flow through the particle (44, 178). The flow through the particle effectively divides the particles into aggregates of smaller particles. The microspheres that make up the larger particles begin to control the "effective" diameter of the packing material and therefore the efficiency, but the large pressure drop seen with small particles is avoided due to the large "true" particle diameter.

The optimal efficiency with perfusive particles occurs at high flow rates. At low flow rates, their performance is similar to macroporous HPLC packings, where the plate height is controlled by pore diffusion, while at high flow rates, intraparticle convective transport exceeds diffusive transport (177, 179-181). The van Deemter equation (eq 3.6) has been extended to account for enhancement due to intraparticle

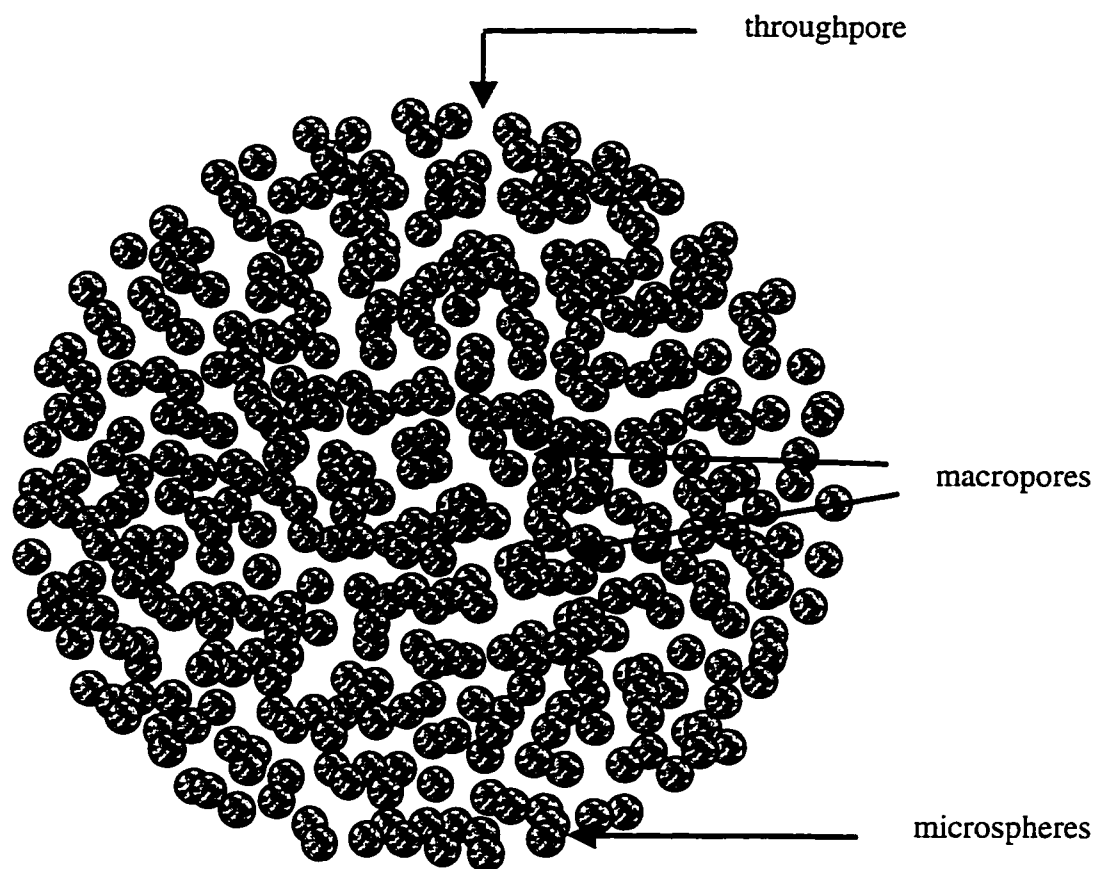


**Figure 5.1** Cross-section of a perfusive particle.

convection (182, 183):

$$\bar{H} = \bar{A} + \frac{\bar{B}}{\bar{U}_0} + \bar{C}\bar{U}_0 f(\lambda) \quad (5.1)$$

where

$$f(\lambda) = \frac{3}{\lambda} \left( \frac{1}{\tanh \lambda} - \frac{1}{\lambda} \right) \quad (5.2)$$

and

$$\lambda = \frac{U'r}{2D_a} \quad (5.3)$$

Here,  $U'$  is the intraparticle velocity,  $r$  is the particle radius, and  $D_a$  is the effective diffusion coefficient in the throughpores. In general, van Deemter plots ( $\bar{H}$  vs  $\bar{U}_0$ ) for perfusive packings have a much shallower slope than macroporous particles at high flow rates and a plateau is reached as intraparticle convection controls mass transport (44, 47, 108, 181, 182, 184) as illustrated in Figure 5.2.

The ability to achieve flow through these types of packing materials has brought about an interest in their applicability to CEC. CEC uses the separation mechanisms of both HPLC and CZE (capillary zone electrophoresis). The separation of neutral species can be achieved by their partitioning in the stationary phase, as occurs in HPLC separations, while charged species can be separated by both partitioning and electrophoretic mobility. This technique provides the high efficiency

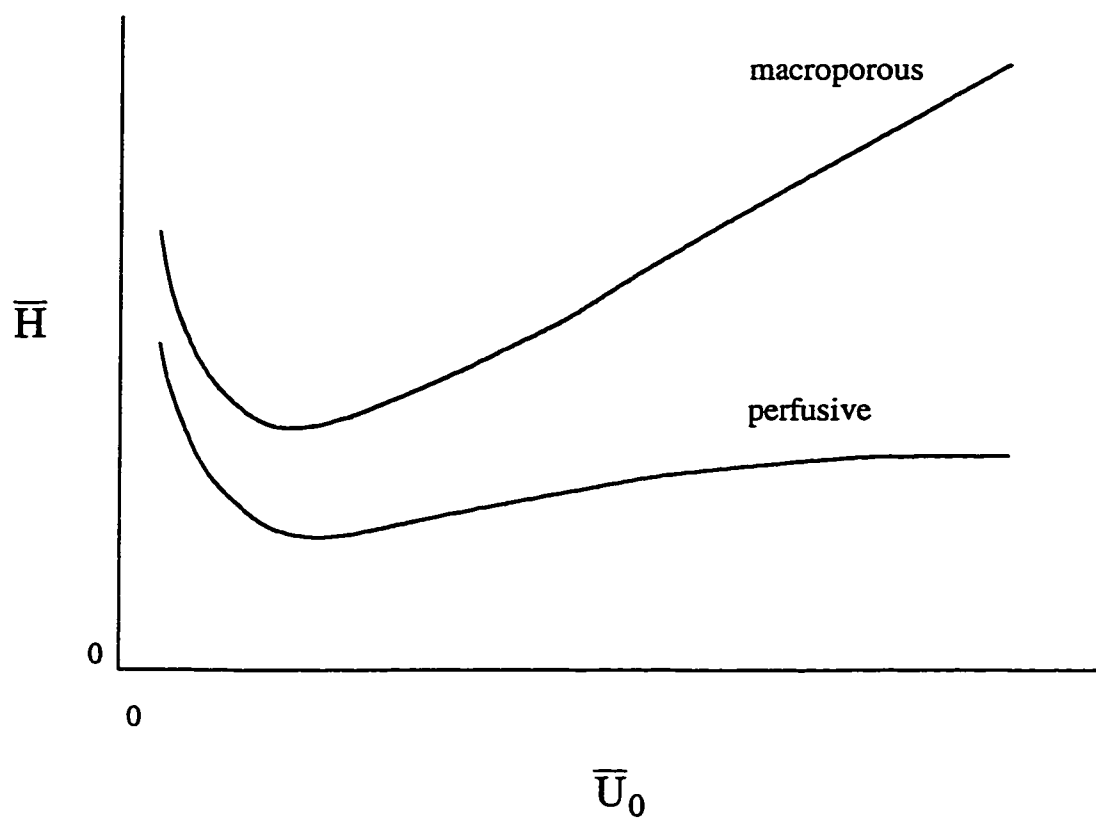


**Figure 5.2** vanDeemter plots for macroporous and perfusive particles.

and resolution seen with CZE with the selectivity and versatility of HPLC (185-187).

As with most surfaces in contact with a liquid, an electrochemical double-layer can form within the pores of the packing (187, 188). The double-layer results from the development of a charge on the surface of the pores as the result of ionization, ion adsorption, or ion dissolution as the surface is brought into contact with a polar medium. The solution then has an excess of oppositely charged ions to balance the charge on the surface. The area of excess charge in solution is quite thin and is generally considered to consist of two regions: the Stern plane consisting of ions attached to the surface by either electrostatic or van der Waals interactions, and the diffuse region (Guoy-Chapman layer), where the ions carrying the remainder of the excess charge are distributed following the Boltzmann distribution and can exchange with ions in the bulk solution (187, 188). Electrochemical double-layer overlap within the pores of the packing can cause distortion of the flow profile through the pores to a Poiseuille-like distribution (parabolic), and in extreme cases, may eliminate electroosmotic flow altogether. With wide pores, the double-layer overlap can be minimized, or eliminated, to give electroosmotic flow through the pores having the flat profile traditional with CZE. Illustration of the effect of overlap on the electroosmotic flow profile is shown in Figure 5.3 (74, 185). Electroosmosis has been seen in wide-channel silica (7  $\mu\text{m}$  particle diameter, 4000 Å pores) with investigations on the effect of pore size on the van Deemter plots showing that perfusive electroosmotic transport occurs (185).

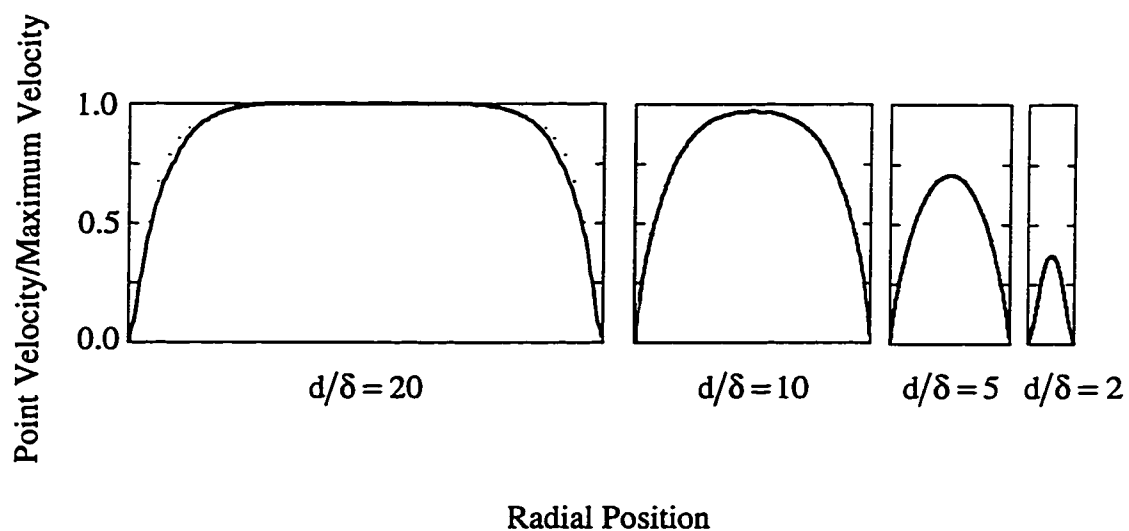


**Figure 5.3** The effect of electrochemical double-layer overlap on the electroosmotic flow profile.  $d$  = pore diameter,  $\delta$  = electrochemical double-layer thickness. Adapted from Li and Remcho (185) after Rice and Whitehead (74).

### 5.2.2 Diffusion in Bidisperse Media

A bidisperse pore model describes diffusion within most porous media (180) where diffusion occurs in both the macropores and micropores. Bidisperse models have been developed to describe diffusion and to calculate effectiveness factors in porous catalysts (189-191), diffusion in zeolites (192), adsorption of an organic compound on activated carbon and synthetic adsorbents (193), and for irreversible sorption in a bidisperse pore system based on the Turner model (194).

Recently, a bidisperse model has been developed to describe the case where convection is also occurring within the particles (180, 183). With knowledge of the diffusional time constants of a solute within the microparticles and throughpores, the model may be used to evaluate the effect of intraparticle convection on plate height and the relative importance of the resistances to mass transfer in the microspheres and throughpores. Since the diffusional time constants are not known, this model cannot be used in this work.

Ruckenstein (195) has developed a model for the sorption in porous solids having a bidisperse structure. The solid is envisaged as being a macrosphere made up of microspheres, where the macropores are present between the microspheres and the micropores are present within the microspheres themselves, as is the case with POROS. Unlike the model for diffusion in pores of uniform size, as given in equation 3.9, this model considers the competing effects of simultaneous diffusion and sorption in the macro- and micro- pores. The model assumes that the sorption is

occurring under infinite bath conditions, the sorption process is isothermal, and the concentration of solute lies within the linear region of its isotherm.

For conditions where the diffusion and sorption within the macropores is much faster than in the micropores, a two-stage sorption process can be considered to be occurring. In the first stage, only macropore sorption occurs, and in the second stage, macropore sorption is at equilibrium and the slower micropore sorption is occurring. The uptake in the macropores can be described by the equation:

$$\frac{Q_a}{Q_{a,\infty}} = 1 - \frac{6}{\pi^2} \sum_{n=1}^{\infty} \frac{1}{n^2} \exp\left(-n^2 \pi^2 \frac{D_a \cdot t}{r_a^2}\right) \quad (5.4)$$

while the uptake in the micropores is given by:

$$\frac{Q_i}{Q_{i,\infty}} = 1 - \frac{6}{\pi^2} \sum_{n=1}^{\infty} \frac{1}{n^2} \exp\left(-n^2 \pi^2 \frac{D_i \cdot t}{r_i^2}\right) \quad (5.5)$$

where the subscript "a" refers to the whole particle and the macropores, and "i" refers to the microspheres and the matrix within the particle. All parameters are as earlier defined.

The total uptake at any time is the sum of the above two equations. For conditions of quasi-saturation in the macropores and constant surface concentration at the micropore surface, and ignoring any interaction of the two sorption steps, the total uptake can be expressed by:

$$\frac{Q_t}{Q_\infty} = \frac{\left[ 1 - \frac{6}{\pi^2} \sum_{n=1}^{\infty} \frac{1}{n^2} \exp(-n^2 \pi^2 \gamma t) \right] + \frac{\beta}{3\alpha} \left[ 1 - \frac{6}{\pi^2} \sum_{n=1}^{\infty} \frac{1}{n^2} \exp(-n^2 \pi^2 \gamma \alpha t) \right]}{1 + \frac{\beta}{3\alpha}} \quad (5.6)$$

where

$$\gamma = \frac{D_a}{r_a^2}, \quad (5.7)$$

$$\beta = \frac{3(1-\epsilon_a)\epsilon_i}{\epsilon_a} \cdot \frac{r_a^2 D_{i,pore}}{r_i^2 D_{a,pore}}, \quad (5.8)$$

and

$$\alpha = \frac{D_i r_a^2}{D_a r_i^2} \quad (5.9)$$

Above,  $\epsilon$  is the porosity, and  $D_{pore}$  is the diffusion coefficient within the pores. This model has been used to describe the diffusion of naphthalene in the macroporous packing PRP-1 over short exposure times (81). The applicability of this model to describe diffusion of naphthalene in POROS 20 R2 will be examined.

### 5.3 Results and Discussion

#### 5.3.1 Naphthalene Sorption Isotherms from Binary and Ternary Solutions

### 5.3.1.1 Naphthalene Sorption Isotherm from 70/30 Methanol/Water

The naphthalene sorption isotherm from 70/30 methanol/water was obtained using the procedure described in section 2.7 using a loading time of 90 minutes, which allowed equilibrium to be achieved. The isotherm was measured over the concentration range of  $1.09 \times 10^{-6}$  M to 0.04689 M, the latter concentration being the saturated solution of naphthalene in 70/30 methanol/water at 25°C. The isotherm was linear up to a concentration of  $1 \times 10^{-4}$  M, with  $\kappa = 0.139 \pm 0.003$  L/g. The capacity of the sorbent was measured to be  $(7.8 \pm 0.2) \times 10^{-4}$  mol/g at the saturation point, where the activity of naphthalene in solution is equal to 1. The isotherm is plotted in Figure 5.4, as moles sorbed per gram of POROS 20 R2 vs. concentration of naphthalene in solution, with the linear region inset.

The isotherm has been fit with a two-site Langmuir model according to the equation:

$$C_S = \frac{C_{1,S,\max} K_{1,\text{ads}} C_M}{1 + K_{1,\text{ads}} C_M} + \frac{C_{2,S,\max} K_{2,\text{ads}} C_M}{1 + K_{2,\text{ads}} C_M} \quad 5.10$$

where the subscripts "1" and "2" refer to the two types of sites. The parameters are as defined in Chapter 3 and their values can be found in Table 5.1. The overall isotherm is the summation of the Langmuir isotherms on two individual types of sites as shown in Figure 5.5 for the naphthalene isotherm on POROS 20 R2. The assumptions for Langmuir adsorption on an adsorbent with more than one type of site include no

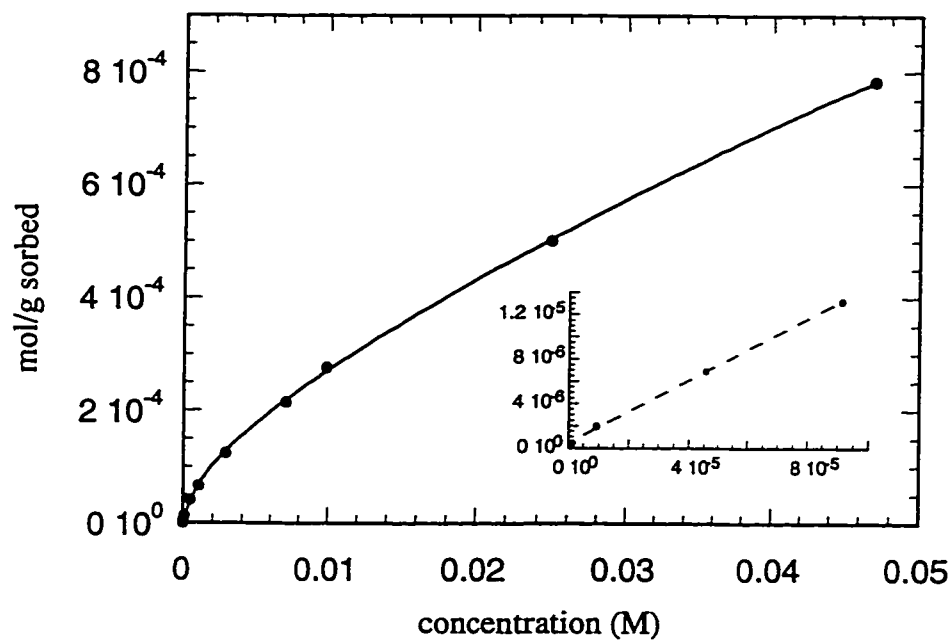


**Figure 5.4** Naphthalene sorption isotherm on POROS 20 R2 column 1 (Table 2.2) from 70/30 methanol/water. Solid line is the fit of the two-site Langmuir model, eq. 5.10. Linear region is inset with the dashed line being the linear least squares fit. Data can be found in Table A1.24.

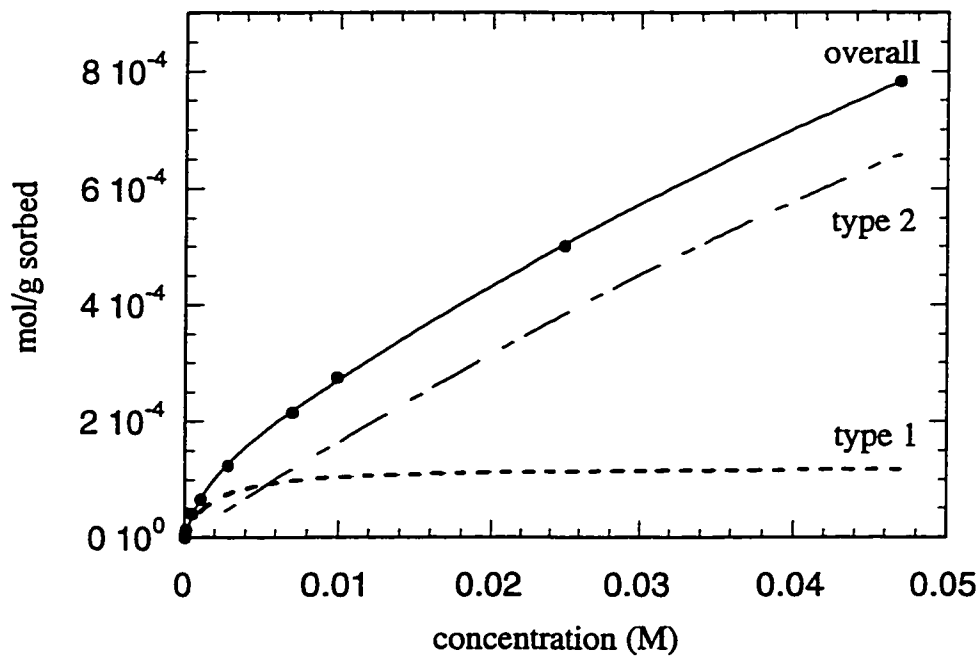


**Figure 5.5** Contributions of individual terms of two-site Langmuir to overall fit of the model to the naphthalene sorption isotherm on POROS 20 R2 from 70/30 methanol/water, shown in Figure 5.4.

lateral interactions between adsorbed solute molecules and the maximum coverage on any one type of site is a monolayer.

**Table 5.1** Parameters from two-site Langmuir model fit to naphthalene isotherm on POROS 20 R2 from 70/30 methanol/water.

Parameter	Value
$C_{1,S,max}$	$(1.22 \pm 0.24) \times 10^{-4} \text{ mol/g}$
$K_{1,ads}$	$575 \pm 195 \text{ L mol}^{-1}$
$C_{2,S,max}$	$(3.9 \pm 1.4) \times 10^{-3} \text{ mol/g}$
$K_{2,ads}$	$4.3 \pm 2.0 \text{ L mol}^{-1}$

Consideration of the morphology of the particle bead leads to one possible explanation of why the data fit the two-site Langmuir model. POROS 20 R2 has large throughpores and macropores. The sorption of naphthalene from bulk solution to the walls of these large pores has a distribution coefficient that is different than the distribution coefficient for naphthalene between the polymer matrix and the bulk solution, thereby giving two types of "sites". The fit of the two-site Langmuir isotherm gave the value of  $C_{1,S,max}$ , the monolayer coverage on the first type of site, to

be  $(1.2 \pm 0.2) \times 10^{-4}$  mol/g, 15% of the total sorption capacity measured at the saturation concentration for naphthalene in solution. Using the surface area of naphthalene,  $141 \text{ \AA}^2/\text{molecule}$  (MMPro®), along with  $C_{1,S,\text{max}}$ , a surface area of  $103 \pm 20 \text{ m}^2/\text{g}$  for the first type of site is obtained. The literature value for the surface area of POROS 20, which only includes the surface area of the through- and macropores, is  $100 \text{ m}^2/\text{g}$  (196), in good agreement with the monolayer coverage seen here. The second type of site, which is within the polymer matrix, sorbs  $(6.6 \pm 0.3) \times 10^{-4}$  mol/g, accounting for 85% of the total sorption capacity measured for a saturated naphthalene solution. Since the sorption isotherm is solubility limited, but the two-site Langmuir equation used to fit the data is not,  $C_{2,S,\text{max}}$  is not representative of the amount sorbed by the second type of site. Instead, the amount sorbed by the polymer matrix was calculated by subtracting the amount sorbed on the first type of site from the experimentally measured amount sorbed at saturation,  $(7.8 \pm 0.2) \times 10^{-4}$  mol/g.

The sorption capacity of the matrix of POROS 20 R2 for naphthalene from a saturated solution in 70/30 methanol/water at  $25^\circ\text{C}$ ,  $(6.6 \pm 0.3) \times 10^{-4}$  mol/g, is the same as the sorption capacity of PRP- $\infty$  for naphthalene under the same conditions,  $(6.7 \pm 0.2) \times 10^{-4}$  mol/g. The similarity in capacity supports the fit of the naphthalene sorption isotherm by the two-site Langmuir: the surface area for the first type of site agrees with the literature value for the surface area of the through- and macro-pores, and the sorption capacity of the matrix is the same as found for PRP- $\infty$ , a non-porous packing used as the model for the matrix of porous PS-DVB packing materials.

### 5.3.1.2 Naphthalene Sorption Isotherm from 60/10/30 Methanol/THF/Water

In Chapter 4, it was seen that the presence of THF in the mobile phase reduced the sorption capacity for naphthalene on PRP- $\infty$ . To determine if this effect is also present with the gigaporous POROS 20 R2 packing, the naphthalene sorption isotherm from 60/10/30 methanol/THF/water solution was measured using a loading time of 45 minutes, sufficient to ensure equilibrium had been reached. The concentration range examined was from  $9.8 \times 10^{-6}$  M to 0.0932 M. The latter concentration is approximately 5% below the saturation concentration of 0.09941 M for naphthalene in this composition solution at 25°C, as determined in section 4.3.1. The isotherm is plotted as moles per gram sorbed vs. concentration in Figure 5.6, with the linear region of the isotherm, ranging up to 0.001 M, inset. The distribution coefficient was found to be  $0.030 \pm 0.001$  L/g. The amount sorbed at saturation was found from the two-site Langmuir fit to be  $6.41 \times 10^{-4}$  mol/g. The parameters from the fit are shown in Table 5.2. The contributions to the overall isotherm from the individual terms in the two-site Langmuir model are shown in Figure 5.7.

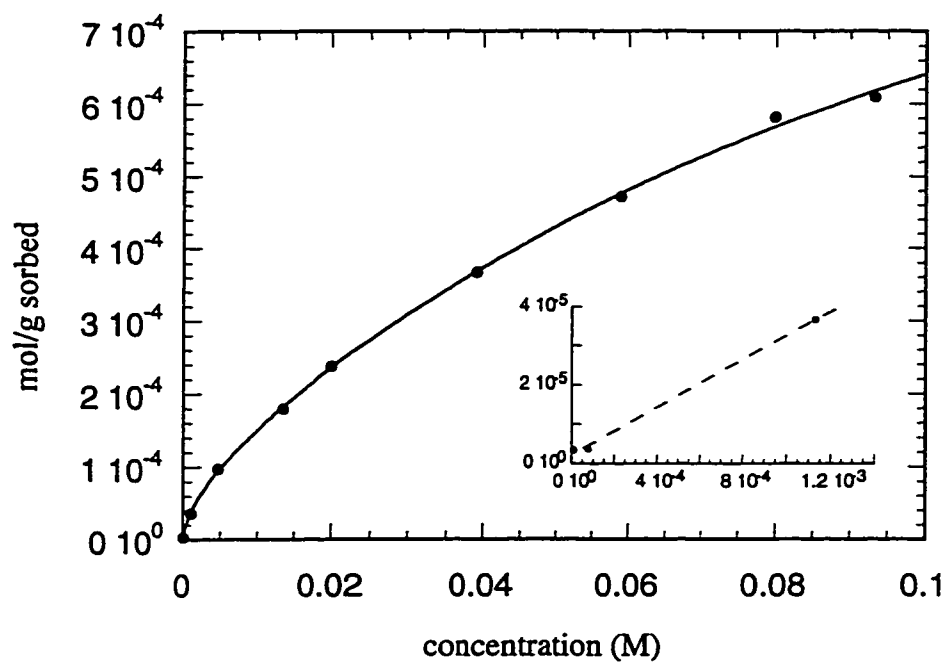


**Figure 5.6** Naphthalene sorption isotherm on POROS 20 R2 column 6 (Table 2.2) from 60/10/30 methanol/THF/water. Solid line is the fit of the two-site Langmuir model, eq. 5.10. Linear region is inset with the dashed line being the linear least squares fit. Data can be found in Table A1.25.

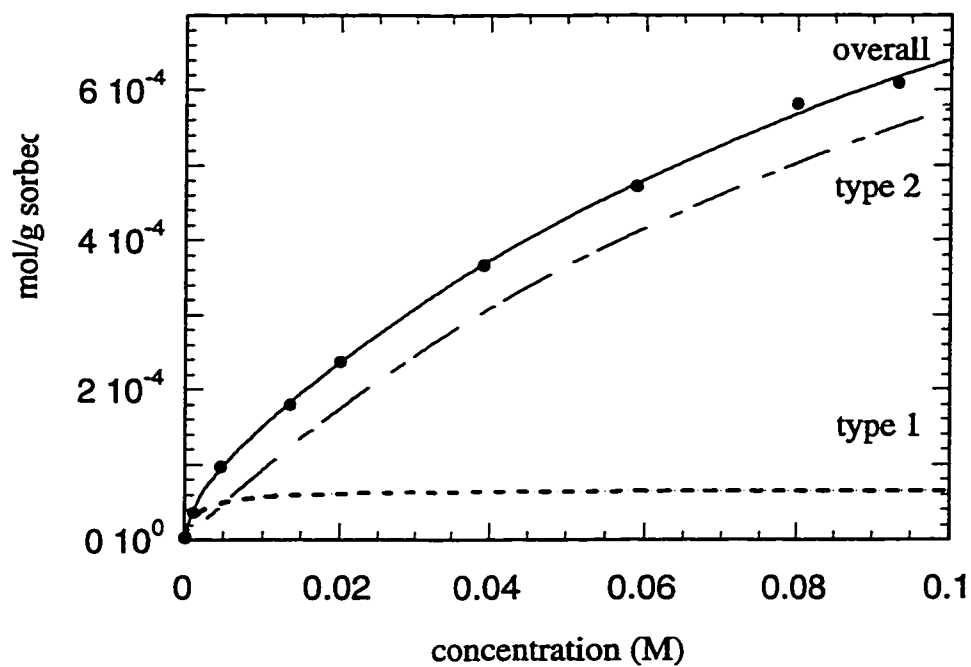


**Figure 5.7** Contributions of individual terms of two-site Langmuir to overall fit of the model to the naphthalene sorption isotherm on POROS 20 R2 from 60/10/30 methanol/THF/water, shown in Figure 5.6.

**Table 5.2** Fitting parameters from two-site Langmuir fit to naphthalene sorption isotherm on POROS 20 R2 from 60/10/30 methanol/THF/water.

Parameter	Value
$C_{1,S,max}$	$(6.7 \pm 2.3) \times 10^{-5} \text{ mol/g}$
$K_{1,ads}$	$609 \pm 474 \text{ L/mol}$
$C_{2,S,max}$	$(1.35 \pm 0.15) \times 10^{-3} \text{ mol/g}$
$K_{2,ads}$	$7.4 \pm 1.7 \text{ L/mol}$

The change in the sorption capacity of the sorbent with changing mobile phase composition at the saturation concentration for naphthalene in solution, where naphthalene's activity is defined as being equal to 1, reflect changes occurring within the sorbent as the mobile phase composition is changed. The capacity of the sorbent in the presence of THF decreased by 18% from that seen with the binary solution as shown in Figure 5.8. This decrease is comparable to the drop in capacity seen for PRP- $\infty$  (17%) under the same conditions. The decrease in capacity can be attributed to the sorption of THF within the permanent micropores ( $\eta_\mu$ ), resulting in their blockage, similar to what was seen in PRP- $\infty$ .

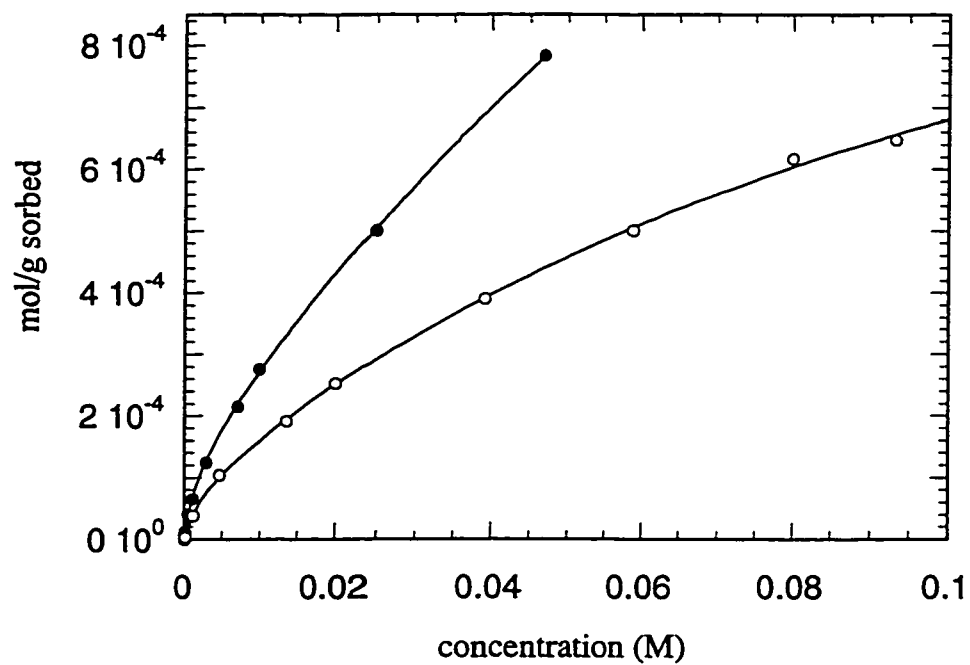


**Figure 5.8** Comparison of naphthalene sorption isotherms on POROS 20 R2 from 70/30 methanol/water (●) and 60/10/30 methanol/THF/water (○).

### 5.3.2 Naphthalene Sorption Kinetics from Binary and Ternary Solutions

#### 5.3.2.1 Testing of Shallow Bed Conditions

In order to ensure that shallow bed conditions were achieved, the effect of  $\bar{U}_0$  on the sorption kinetics was studied, as described in section 3.3.2.1. Linear velocities of 4.0, 7.0, and 8.9 cm/s were examined at short loading times (up to 30 s), where the rate of uptake is highest. The results are shown in Figure 5.9. It is seen that the rate of uptake was unchanged for the  $\bar{U}_0$  examined. Therefore, shallow bed conditions exist at a linear velocity of 4.0 cm/s corresponding to a flow rate of 13 mL/min. The kinetic studies were performed at a  $\bar{U}_0$  above this value to ensure shallow bed conditions were met.

#### 5.3.2.2 Naphthalene Sorption Kinetics from 70/30 Methanol/Water

Naphthalene sorption kinetics from a  $7.844 \times 10^{-5}$  M solution in 70/30 methanol/water were measured and are shown in Figure 5.10. The results are plotted as the amount sorbed vs. time, with the points being the experimental data which have been fit to both equation 3.9, diffusion through a monodisperse sphere, and equation 5.6, diffusion in bidisperse media. The fitting parameters are found in Tables 5.3 and 5.4.

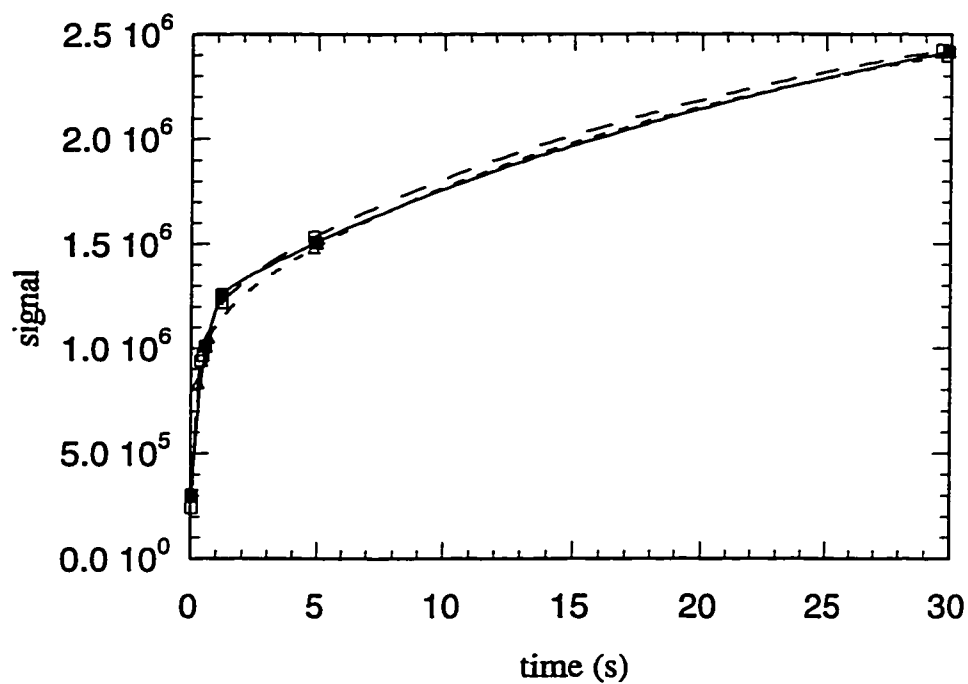


**Figure 5.9** Testing of shallow bed conditions at linear velocities of 4.0 cm/s (○), 7.0 cm/s (■), and 8.9 mL/min (△) using a  $2.052 \times 10^{-4}$  M solution of naphthalene in 70/30 methanol/water on POROS 20 R2 column 1 (Table 2.2). Data can be found in Table A1.26.

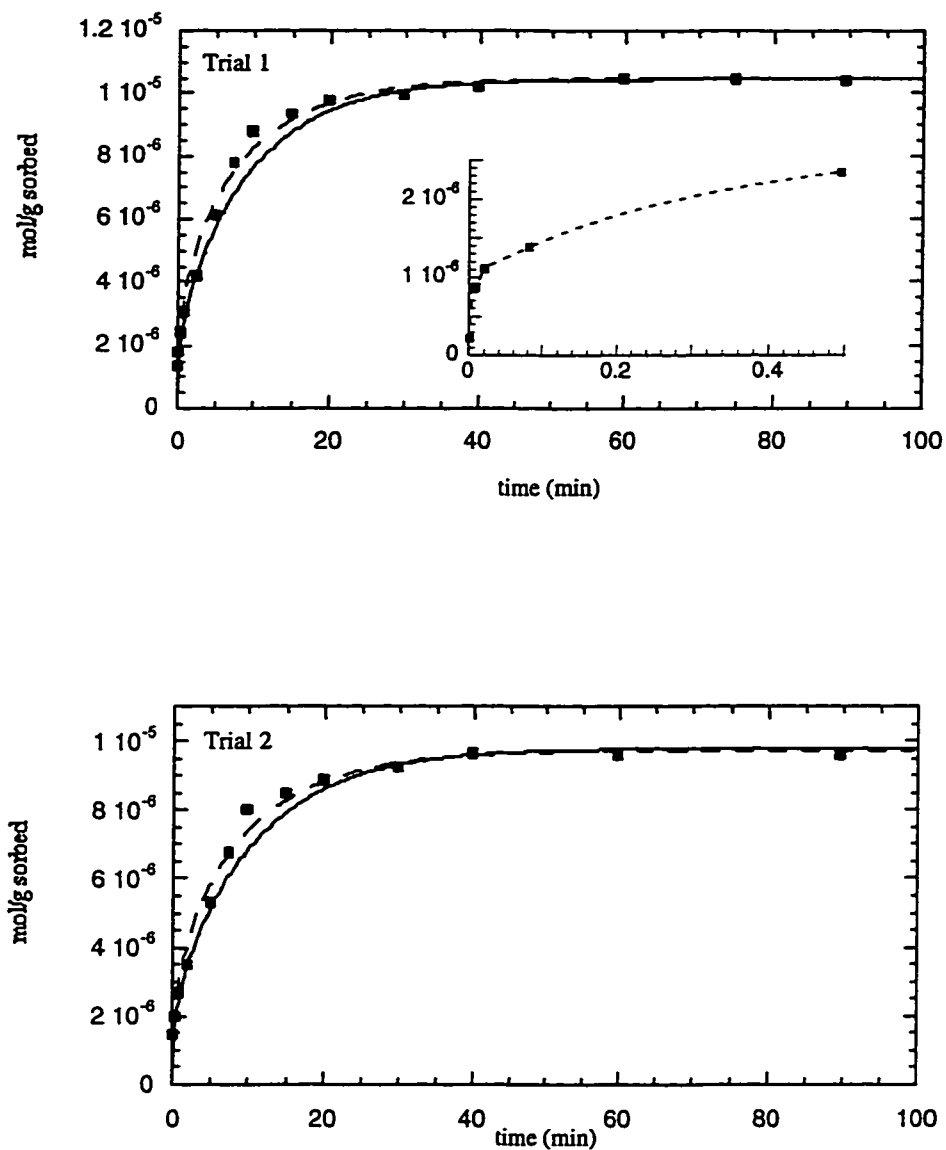


**Figure 5.10** Naphthalene sorption kinetics on POROS 20 R2 column 2 (Table 2.2) from  $7.844 \times 10^{-5}$  M naphthalene in 70/30 methanol/water.  $\bar{U}_0$  was greater than 4.6 cm/s for each trial. Dashed line is fit of monodisperse model (eq. 3.9); solid line is fit of bidisperse model (eq. 5.6). In Trial 1, the inset is the sorption at very short times as adapted from the examination of shallow bed conditions. Data can be found in Tables A1.27 and A1.28.

**Table 5.3** Fitting parameters from fit of monodisperse model, eq. 3.9, to naphthalene sorption kinetics on POROS 20 R2 from 70/30 methanol/water.

<i>Trial</i>	$B(s^{-1}) \times 10^3$	$Q_{\infty} (\text{mol/g}) \times 10^5$	$D(\text{cm}^2/\text{s}) \times 10^{10}$
1	$1.7 \pm 0.1$	$1.04 \pm 0.02$	$1.7 \pm 0.1$
2	$1.5 \pm 0.1$	$0.97 \pm 0.02$	$1.6 \pm 0.1$

**Table 5.4** Fitting parameters from fit of bidisperse model, eq. 5.6, to naphthalene sorption kinetics on POROS 20 R2 from 70/30 methanol/water.

<i>Trial</i>	$Q_{\infty}$ (mol/g) $\times 10^5$	$\gamma(s^{-1})$ $\times 10^4$	$\alpha\gamma(s^{-1})$ $\times 10^4$	$\beta/\alpha$	$D_{e,eff}$ ( $\text{cm}^2/\text{s}$ ) $\times 10^{10}$	$D_{i,eff}$ ( $\text{cm}^2/\text{s}$ ) $\times 10^{13}$	$\beta/3\alpha$
1	1.045	1.76	1.50	0.1914	1.76	3.76	0.0638
2	0.978	1.56	1.65	0.2006	1.56	4.12	0.0667

The fit to the monodisperse model, eq. 3.9, is seen in Figure 5.10 to be much better than the fit to the bidisperse model, eq. 5.6, even though the particles have a bidisperse pore structure. The reason for this apparent discrepancy lies in the time scale over which the kinetic study was performed. The inset in Trial 1 of Figure 5.10 is the amount sorbed at very short time, up to 30 seconds, as adapted from the examination of shallow bed conditions. This inset plot shows that the initial sorption is very fast and then becomes slower after about 1 second, indicated by the change in slope of the line in this region. This change in sorption rate between being very fast and then somewhat slower may be indicative of the bidisperse nature of the packing. The fast, initial sorption rate is due to sorption on the walls of the giga- and macropores which is almost instantaneous as the result of the convective flow within the particles and no hindrance to diffusion. The amount sorbed on the pore walls is low with respect to the overall amount sorbed. The slower kinetics occur as the solute begins to diffuse within the polymer matrix. It is this slower diffusion within the polymer matrix that is seen in the plots of Trial 1 and Trial 2 in Figure 5.10, and is this hindered diffusion within the polymer matrix that is fit by model for diffusion into a monodisperse sphere. The diffusion within the polymer at very short times may not be fit well by this model, but the slow sorption process into the polymer matrix outweighs the contribution of this region to the overall kinetics. The quality of fit to the monodisperse model can be seen in the  $Bt$  vs.  $t$  plots in Figure 5.11. The plot has a zero intercept and is linear up to a coverage of about 95%. Above 95%, the values of  $Bt$  begin deviating from linearity for reasons discussed in section 3.3.2.2.

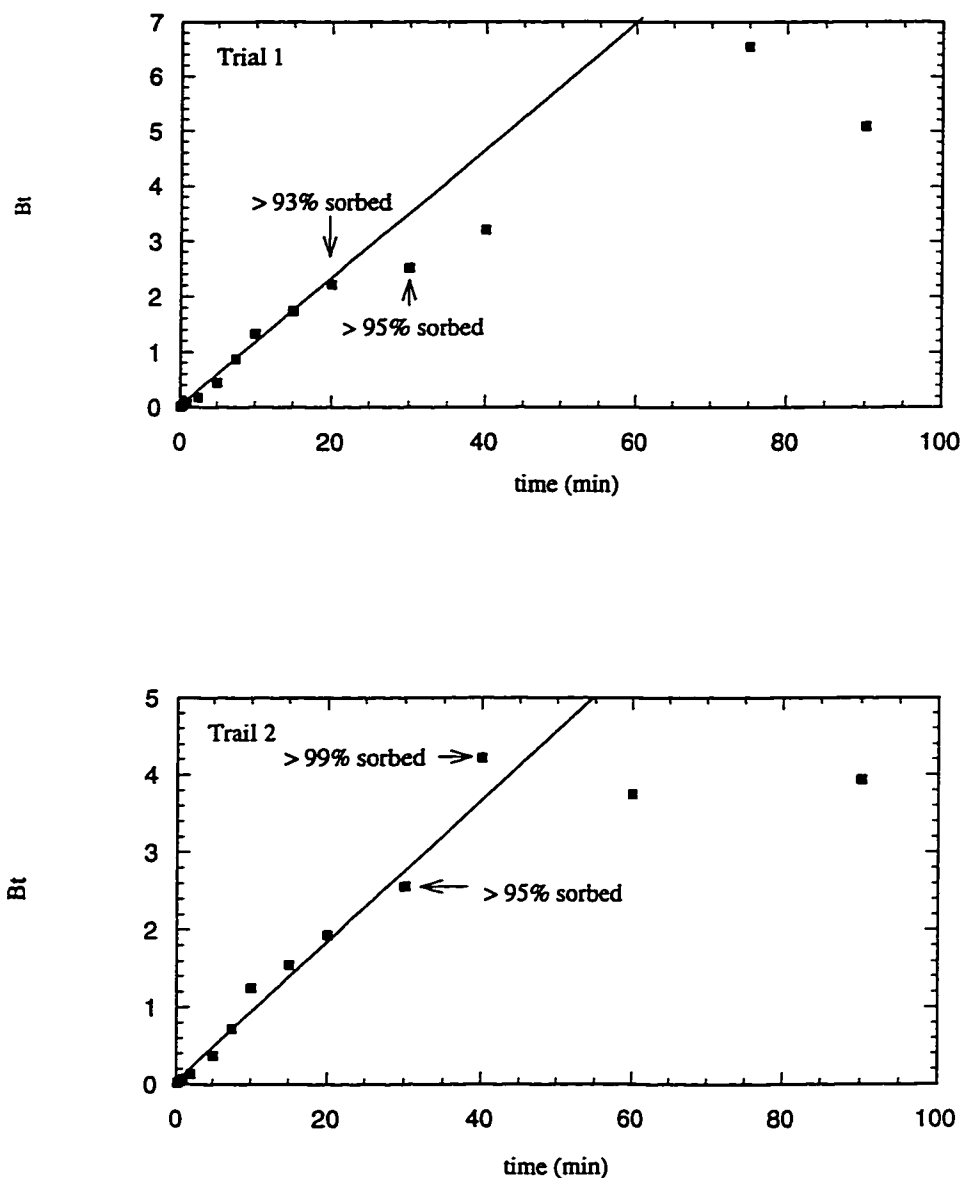


**Figure 5.11** Quality of fit of monodisperse model (eq. 3.9) to naphthalene sorption kinetics on POROS 20 R2 from  $7.844 \times 10^{-5}$  M naphthalene in 70/30 methanol/water. Bt values have been calculated using equations 3.12 and 3.13. Lines are the linear least squares fit of the data within the linear region. Data can be found in Tables A1.27 and A1.28.

The rate of naphthalene sorption on POROS 20 R2 differs significantly from that on PRP- $\infty$ , as shown in Figure 5.12, even though both kinetic studies are looking essentially at diffusion within the polymer matrix. On POROS 20 R2, the initial rate is faster than that on PRP- $\infty$ , as indicated by its steeper initial slope, and equilibrium is approached sooner. The faster kinetics on POROS 20 R2 are the result of the microbead structure of the particle. The time for diffusion within the polymer bead is dependent on the square of the particle diameter, and since the microbead diameter is 1  $\mu\text{m}$  while that of PRP- $\infty$  is 20  $\mu\text{m}$ , the observed sorption kinetics for POROS 20 R2 are faster.

### **5.3.2.3 Naphthalene Sorption Kinetics from Solutions of 68/2/30, 65/5/30, and 60/10/30 Methanol/THF/Water**

The effect of THF on naphthalene sorption kinetics was examined using three different composition mobile phases: 68/2/30, 65/5/30, and 60/10/30 methanol/THF/water. The concentration of naphthalene used in each kinetic trial was the same as that used for the binary solution kinetic studies,  $7.8 \times 10^{-5}$  M. The results from the kinetic studies are plotted in Figure 5.13 as moles/g sorbed vs. time, and in Figure 5.14 as fraction of the equilibrium amount sorbed vs. time, where the points are the experimental data, and the lines are the fit of equation 3.9 to the data. As for the sorption kinetics from the binary solution, the contribution of the giga- and macro-

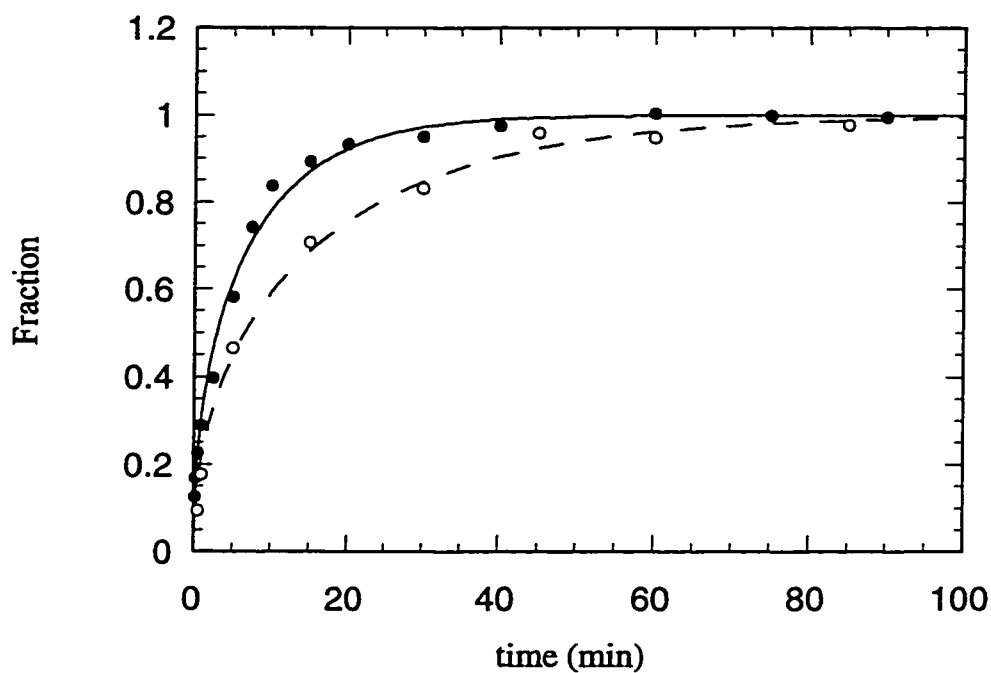


**Figure 5.12** Comparison of naphthalene sorption kinetics from 70/30 methanol/water on PRP- $\infty$  (Trial 2, Figure 3.7) (○) and POROS 20 R2 (Trial 1, Figure 5.10)(●).

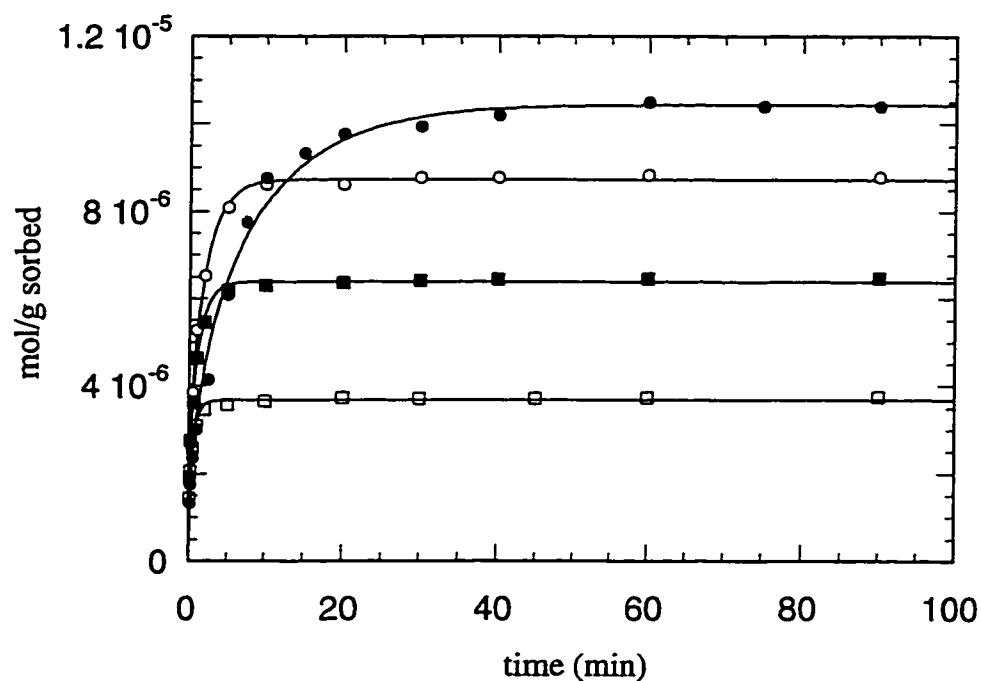


**Figure 5.13** Naphthalene sorption kinetics on POROS 20 R2 columns 2-5, respectively (Table 2.2), from  $7.844 \times 10^{-5}$  M naphthalene in: 70/30 methanol/water (●); 68/2/30 methanol/THF/water (○), 65/5/30 methanol/THF/water (■), and 60/10/30 methanol/THF/water (□). Lines are fits to diffusion through a monodisperse sphere model (eq. 3.9). Data can be found in Tables A1.29 – A1.31.

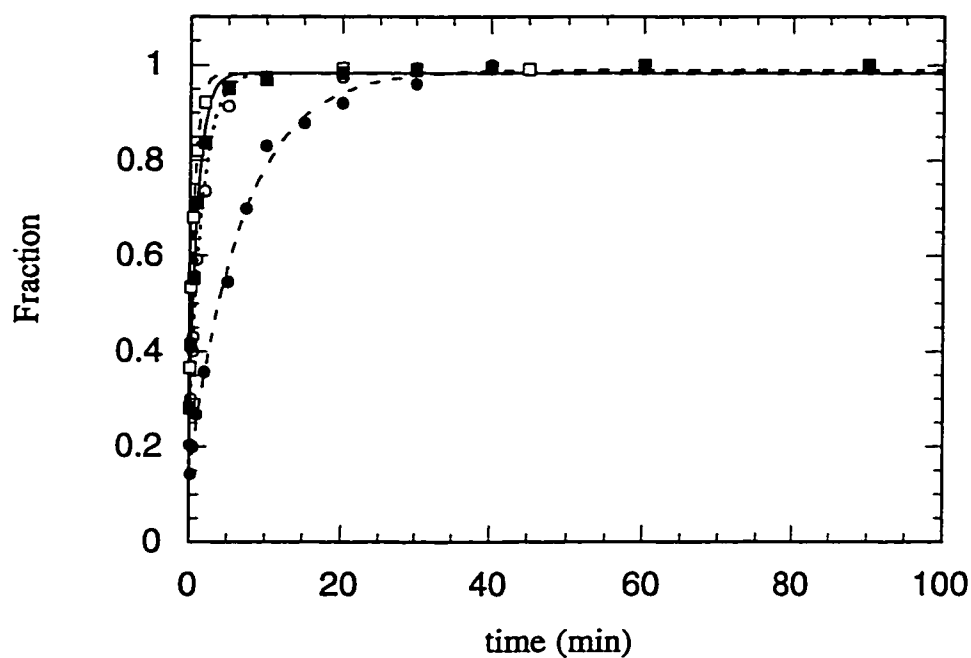


**Figure 5.14** Normalized naphthalene sorption kinetics on POROS 20 R2 from  $7.844 \times 10^{-5}$  M naphthalene in: 70/30 methanol/water (●), 68/2/30 methanol/THF/water (○), 65/5/30 methanol/THF/water (■), and 60/10/30 methanol/THF/water (□).

pores to the overall sorption rate are small and are outweighed by the effect of diffusion within the polymer matrix. Therefore, the monodisperse model fits the data. The fitting parameters can be found in Table 5.5. The  $Bt$  vs.  $t$  plots, indicating the goodness of fit of the model can be seen in Figure 5.15. Again, the plots are linear up to a fractional coverage of about 95%. Measured values, that have been defined by the fit of equation 3.9 to be at equilibrium, have been omitted, as the value of  $Bt$  at these points is defined as being infinite.

**Table 5.5** Fitting parameters from fit of monodisperse model, eq. 3.9, to naphthalene sorption kinetics on POROS 20 R2 from ternary solutions of methanol/THF/water. Also given are diffusion coefficients for naphthalene within the matrix, calculated for two different particle radii, as will be discussed in the text.

Solution Composition	$B \text{ (s}^{-1}\text{)}^b$ $\times 10^3$	$Q_\infty \text{ (mol/g)}$ $\times 10^6$	$D \text{ (cm}^2\text{/s)} \times 10^{10}$ ( $r = 10 \times 10^{-4} \text{ cm}$ )	$D \text{ (cm}^2\text{/s)} \times 10^{10}$ ( $r = 0.5 \times 10^{-4} \text{ cm}$ )
70/0/30 <sup>a</sup>	$1.6 \pm 0.1$	$10.1 \pm 0.03$	$1.6 \pm 0.1$	$0.0039 \pm 0.0002$
68/2/30	$7.6 \pm 0.2$	$8.74 \pm 0.04$	$7.7 \pm 0.2$	$0.019 \pm 0.001$
65/5/30	$13.4 \pm 0.7$	$6.39 \pm 0.04$	$13.5 \pm 0.7$	$0.034 \pm 0.002$
60/10/30	$24.8 \pm 1.4$	$3.68 \pm 0.03$	$25.1 \pm 1.4$	$0.063 \pm 0.004$

<sup>a</sup> Average of two trials

<sup>b</sup> 
$$B = \frac{\pi^2 D}{r^2}$$

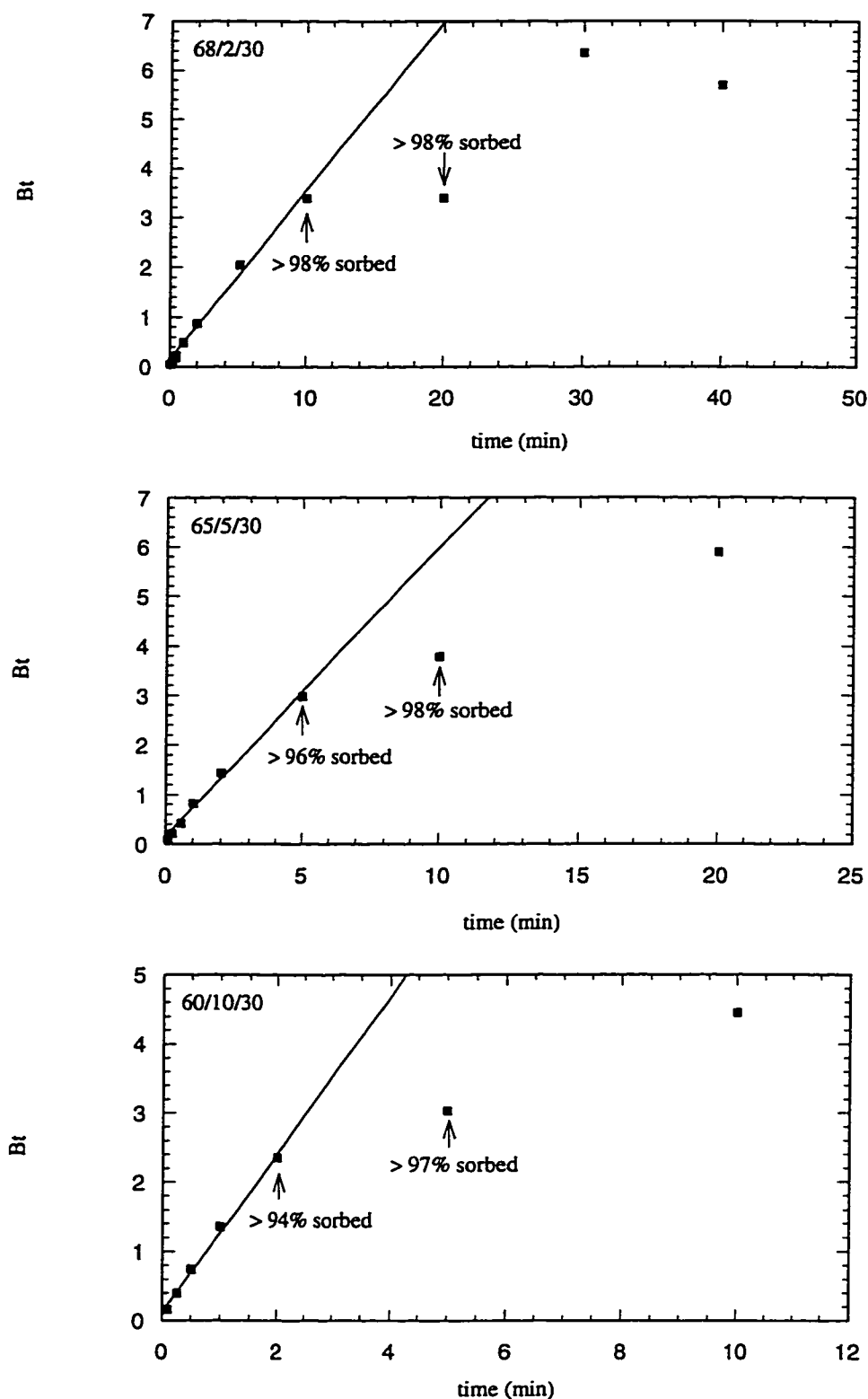


**Figure 5.15** Quality of fit of monodisperse model (eq. 3.9) to naphthalene sorption kinetics on POROS 20 R2 from  $7.844 \times 10^{-5}$  M naphthalene in ternary solutions.  $Bt$  values have been calculated using equations. 3.12 and 3.13. Lines are the linear least squares fit to the data within the linear region. Data can be found in Tables A1.29 – A1.31.

From Figure 5.13, it is seen that the amount sorbed at any time decreased as the percentage of THF in solution increased. The decrease in the amount sorbed is in part due to the change in solvent strength as the amount of THF increased. From Figure 5.14 and Table 5.5, it is seen that the most significant increase in the sorption rate occurred with the addition of 2% THF, as was seen in the studies on PRP- $\infty$ . The diffusion coefficient, on the addition of 2% THF, increased by more than 450% while swelling is assumed to have remained essentially unchanged based on the swelling measurements of PRP- $\infty$ . In terms of equations 3.22-3.24,  $\eta_{\mu}$ , the sorption capacity within the micropores has become approximately zero, and the overall hindrance within the matrix has been greatly reduced as  $\hat{\lambda}_{gel}$  must be  $\gg \hat{\lambda}_{\mu}$ . On the addition of 5% and 10% THF, the diffusion coefficients continued to become larger as the result of further blockage of slow sites and an increase in the swelling of the polymer, but still remain 3 orders of magnitude smaller than those in free solution. Again, the results are consistent with those seen for PRP- $\infty$ , where a small amount of THF caused a large change in the kinetics. Under the previous interpretation presented in section 4.3.6, THF is blocking the sites within the permanent micropores. This blocking occurs as THF condenses in the permanent micropores, which occurs at low THF concentration, as shown by the work done by Wang (165), see section 4.3.3, above. The further increase in the kinetic rates, and the calculated diffusion coefficients with increasing concentration of THF was not seen for PRP- $\infty$ , and will be discussed below.

In Table 5.5 are shown the fitting parameters from the fit of eq. 3.9 to the sorption rate data, and the calculated diffusion coefficients for naphthalene within the polymer matrix, for various solution compositions. The parameter,  $B$ , is equal to  $\frac{\pi^2 D}{r^2}$ , and is therefore used to calculate the diffusion coefficient of a solute within the polymer matrix. However, due to the structure of POROS 20 R2, i.e. the particle being made up of inter-adhered microspheres, there is uncertainty in the value of the radius that should be used in the calculation of the diffusion coefficient. The fourth column of Table 5.5 contains the diffusion coefficients calculated assuming that  $r$  is equal to the particle radius of 10  $\mu\text{m}$ . The diffusion coefficient of naphthalene in POROS 20 R2 from 70/30 methanol/water is seen to be double that what was found for the diffusion of naphthalene in the matrix of PRP- $\infty$ ,  $(7 \pm 1) \times 10^{-11} \text{ cm}^2/\text{s}$ . The change in the diffusion coefficient on the addition of 2% THF to the solution is larger for POROS 20 R2 (450% increase) than for PRP- $\infty$  (100% increase), and the addition of larger amounts of THF (5% and 10%) to the solutions when POROS 20 R2 is the sorbent, continued to increase the diffusion coefficient.

In the last column of Table 5.5, are the diffusion coefficients calculated assuming that  $r$  is equal to the literature value for the radii of the microspheres (44) that are inter-adhered to produced the gigaporous particle, 0.5  $\mu\text{m}$ . These diffusion coefficients are found to be 2 orders of magnitude smaller than the diffusion coefficients calculated in the PRP- $\infty$  matrix. In reality, the effective radius of a particle is not known because the microspheres that make up the particle beads are not isolated, but are fused together to some extent. This fusing of the microspheres

increases their effective diameter, which must lie between the radius of a microsphere and the radius of a particle. Therefore, the diffusion coefficient in the matrix of POROS 20 R2 lies between the values given in the 4<sup>th</sup> and 5<sup>th</sup> columns of Table 5.5. The effective diameter of the particle is not likely to be 20  $\mu\text{m}$  because of the presence of the large throughpores and macropores through which diffusion is fast. A value between 1  $\mu\text{m}$  and several  $\mu\text{m}$  is a more realistic estimation for the effective particle diameter. For the diffusion coefficient of naphthalene in POROS 20 R2 to have the same value as that found for PRP- $\infty$  from 70/30 methanol/water, the effective radius of a particle bead is 6.5  $\mu\text{m}$ .

Sorption isotherms on both PRP- $\infty$  and POROS 20 R2 show a similar decrease in the sorption capacity for naphthalene on changing from 70/30 methanol/water to 60/10/30 methanol/THF/water, 17% for PRP- $\infty$  and 18% for POROS 20 R2. This suggests that THF is having a blocking effect in both sorbents. In the case of POROS 20 R2, this blocking effect cannot be compared to the swelling-sorption curves, because solvent sorption isotherms and swelling studies have not been performed on the particles.

The similarities between PRP- $\infty$  and POROS 20 R2, i.e. the similar sorption capacity for naphthalene within the polymer matrix, the similar reduction in sorption capacity for naphthalene on the addition of 10% THF in the sorption isotherms studies, and the improvement in the sorption rate on the addition of small amounts of THF to the solvent, indicate that the two polymer sorbents have the same basic micropore – gel structure. The differences outlined above between POROS 20 R2

and PRP- $\infty$  may be indicating some differences in the "details" of the structure of the polymer matrix of the two sorbents. It may be that POROS 20 R2 has a bigger range of permanent micropore sizes that can become blocked by the addition of THF. In this circumstance, more THF would be required for POROS 20 R2 than was needed to block the permanent micropores in PRP- $\infty$ , which would explain the continued increase in the diffusion coefficient on the addition of larger amounts of THF. PRP- $\infty$  may not be an exact model for the matrix of POROS 20 R2, but may be an approximate representation of the matrix.

### 5.3.3 Predicted Elution Profiles

Elution profiles for naphthalene from a chromatographic column of POROS 20 R2 have been predicted as described in section 3.3.4 when the solution composition is 70/30 methanol/water, 68/2/30 methanol/THF/water, 65/5/30 methanol/THF/water, or 60/10/30 methanol/THF/water. To obtain the values of  $n_i$  and  $k_i$  required to predict the peaks, the kinetic data have been fit by the bi-exponential form of equation 3.33 and can be seen in Figures 5.16 and 5.17. The fitting parameters are shown in Table 5.6.

To allow for the prediction of peaks from a column of POROS 20 R2, a value for the  $k'$  for naphthalene on a chromatographic column of POROS 20 R2 had to be estimated. To do this, equation 3.45 was used which requires values for  $V_{\text{pore}}$ ,  $W_{\text{col}}$ ,

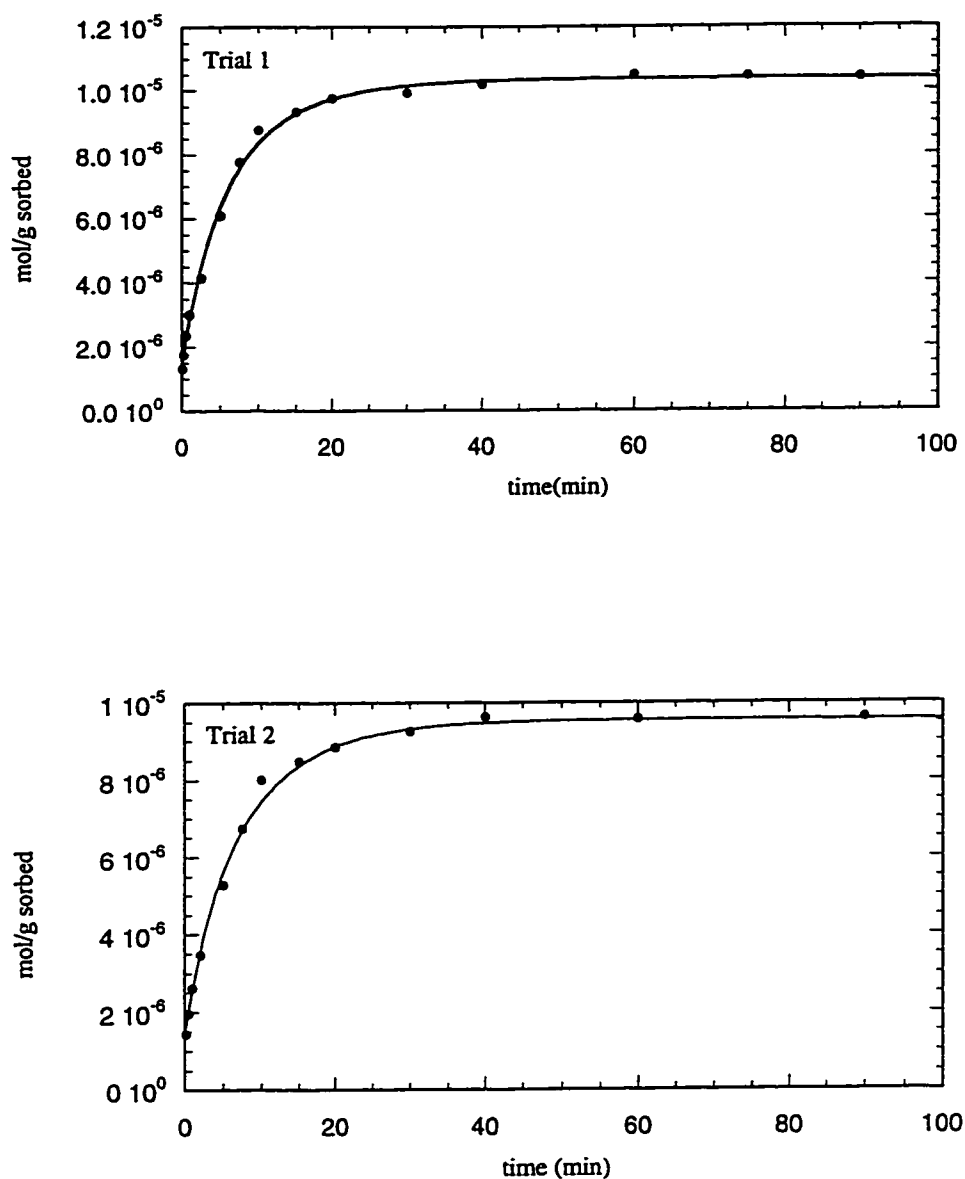


**Figure 5.16** Bi-exponential fits (solid lines) to naphthalene sorption kinetics on POROS 20 R2 column 2 (Table 2.2) from  $7.844 \times 10^{-5}$  M naphthalene in 70/30 methanol/water.  $\bar{U}_0$  was greater than 4.6 cm/s for each trial. Data can be found in Tables A1.27 and A1.28.

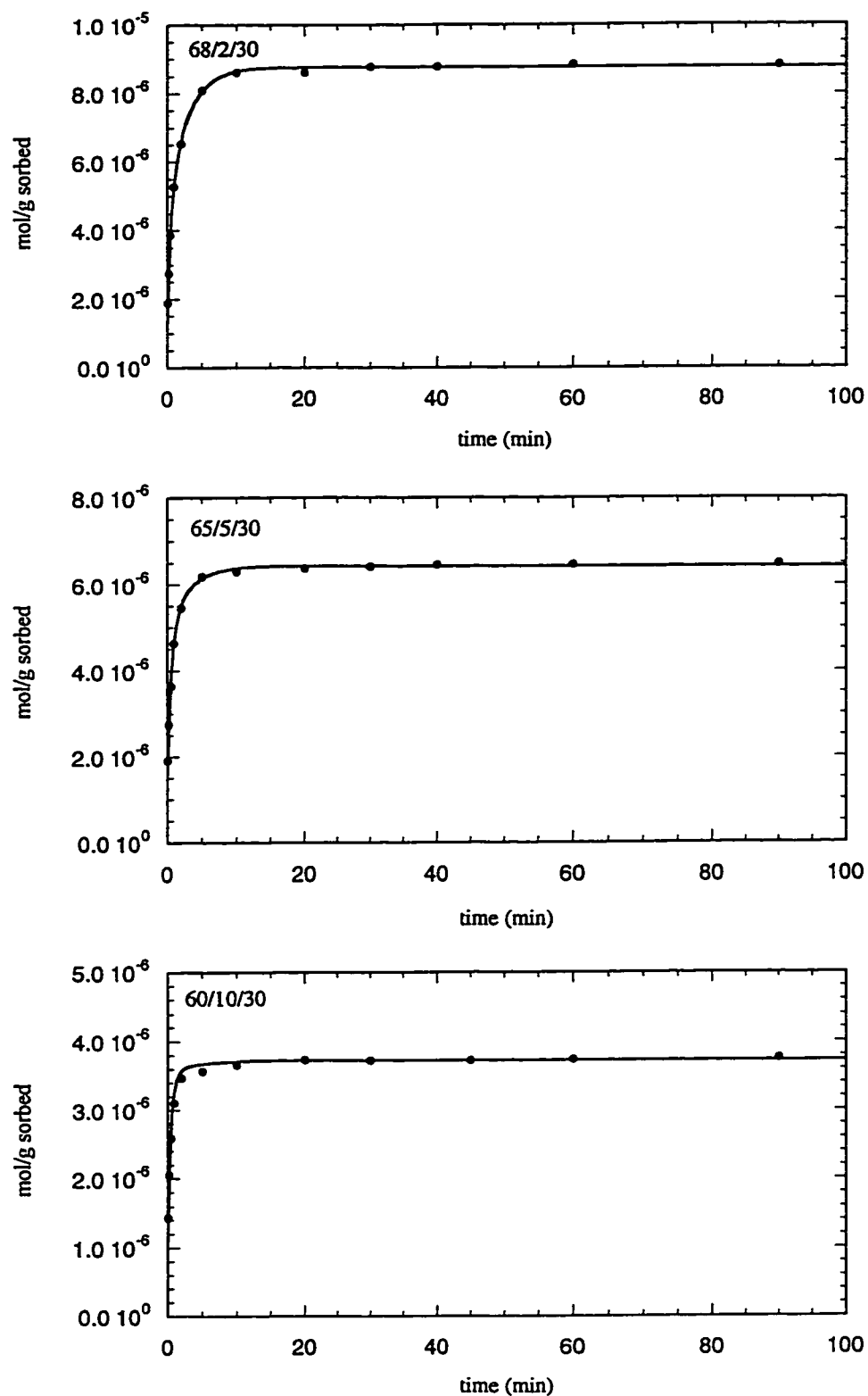


**Figure 5.17** Bi-exponential fits (solid lines) to naphthalene sorption kinetics on POROS 20 R2 from  $7.844 \times 10^{-5}$  M naphthalene in ternary solutions.  $\bar{U}_0$  was greater than 4.6 cm/s for each trial. Data can be found in Tables A1.29 - A1.31.

and  $V_M$  be known. As mentioned in section 2.6,  $V_{\text{pore}}$  is equal to 0.71 mL/g (76), but  $W_{\text{col}}$  and  $V_M$  are not known and must be estimated from what is known about the packing material. For a 4.1 x 150 mm column which has a volume of 2 mL,  $W_{\text{col}}$  was estimated to be 0.56g using the bulk density of the packing, 0.28 g/mL.  $V_M$  was estimated using the column void fraction, 0.35 (44), and the porosity of the particles. For a column with a volume of 2 mL, such as the one assumed here, the column void volume, i.e. the volume between the particles, is 0.7 mL. The particles therefore have a volume of 1.3 mL. Using the porosity of the particles, 0.65 (197), gives an intraparticle pore volume of 0.845 mL, and a retention volume of an unretained compound of 1.545 mL. Using a mass of the shallow bed of 0.68 mg (Trials 3-6, Table 2.2), and a concentration of  $7.844 \times 10^{-5}$  M, typical values of  $\frac{n_0 - C_M \cdot V_{\text{pore}}}{W_{\text{SB}} \cdot C_M}$  are 127.2, 110.4, 80.8, and 46.1 for solutions with compositions 70/30 methanol/water, 68/2/30, 65/5/30, and 60/10/30 methanol/THF/water, respectively. When these values are taken together with  $V_m$  and  $W_{\text{col}}$ , values for  $k'$  of naphthalene from a column of POROS 20 R2 of 46.1, 40.0, 29.3, and 16.7 from solutions with compositions 70/30 methanol/water, 68/2/30, 65/5/30, and 60/10/30 methanol/THF/water, respectively, are obtained.

**Table 5.6** Fitting parameters from bi-exponential fits to naphthalene sorption kinetics on POROS 20 R2.

Composition (methanol/THF/water)		$n_0 \times 10^6$	$n_1 \times 10^6$	$k_1$	$n_2 \times 10^6$	$k_2$
70/0/30	Trial 1	10.21	1.594	16.62	8.716	0.1549
70/0/30	Trial 2	9.579	1.432	54.29	8.147	0.144
68/2/30		8.71	2.055	16.76	6.655	0.5821
65/5/30		6.391	1.997	19.78	4.394	0.8431
60/10/30		3.696	1.50	19.99	2.195	1.29

The peaks were predicted at a flow rate of 0.03 mL/min and are shown in Figure 5.18. The peaks have been plotted as the normalized signal vs.  $t/t_r$ , where  $t_r$  is the center of gravity of the peak. The peaks have been normalized such that the area under any peak is equal to 1, and the effect of the changing  $k'$  on peak position and shape has been removed. The peak predictions from a 70/30 methanol/water solution are found to be quite broad and slightly tailed (A.F. = 1.85). As the amount of THF is increased, the peaks become narrower and more symmetric as indicated by the asymmetry factors shown on the plot.

Shown in Figure 5.19 is a comparison of the predicted elution profiles of naphthalene from columns of PRP- $\infty$  and POROS 20 R2, at a flow rate of 0.004 mL/min. The overall efficiency of POROS 20 R2, as indicated by the tailing and bandbroadening, is seen to be better than that of PRP- $\infty$  as expected due to the porosity of the material. Both peaks predicted from 70/30 methanol/water are found to be quite broad, and the asymmetry factor is higher on POROS 20 R2 than on PRP- $\infty$ . The addition of THF to the mobile phase has a larger effect on peak shape with POROS 20 R2, which can be attributed in part to the shorter diffusional distances within the gigaporous particles.

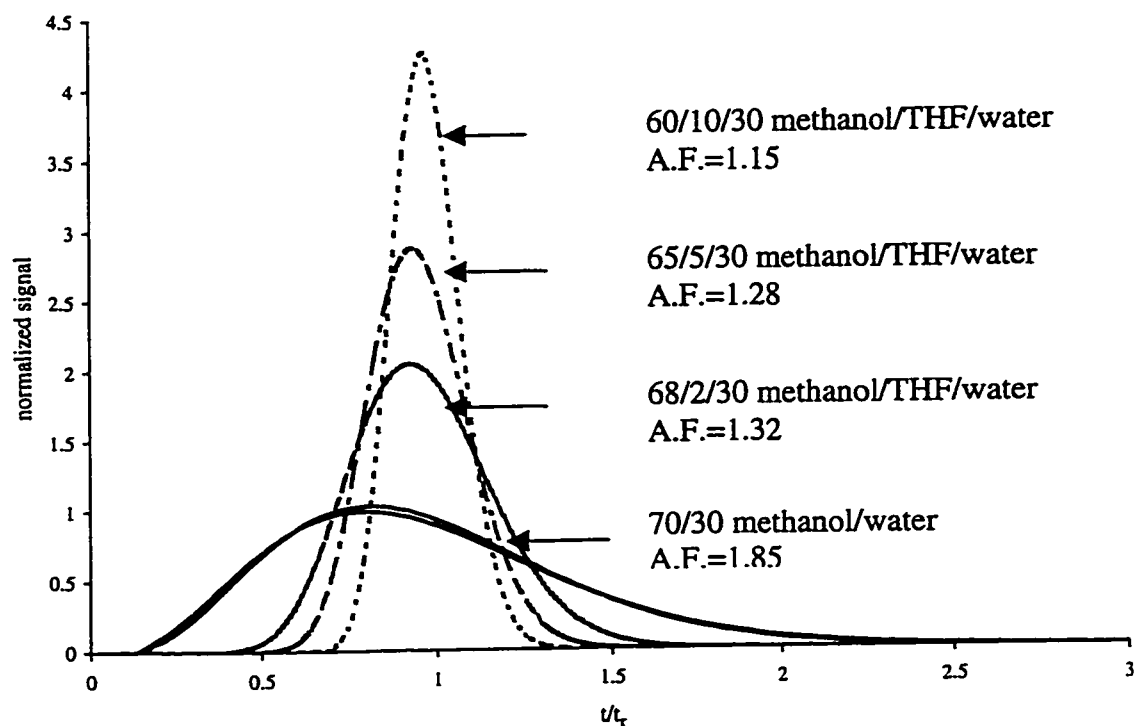


**Figure 5.18** Elution profiles for naphthalene from a column of POROS 20 R2 predicted at a flow rate of 0.03 mL/min from bi-exponential fits to sorption rate curves. Parameters from bi-exponential fits are in Table 5. 6. Asymmetry factors (A.F.) were measured at 10% of peak height.

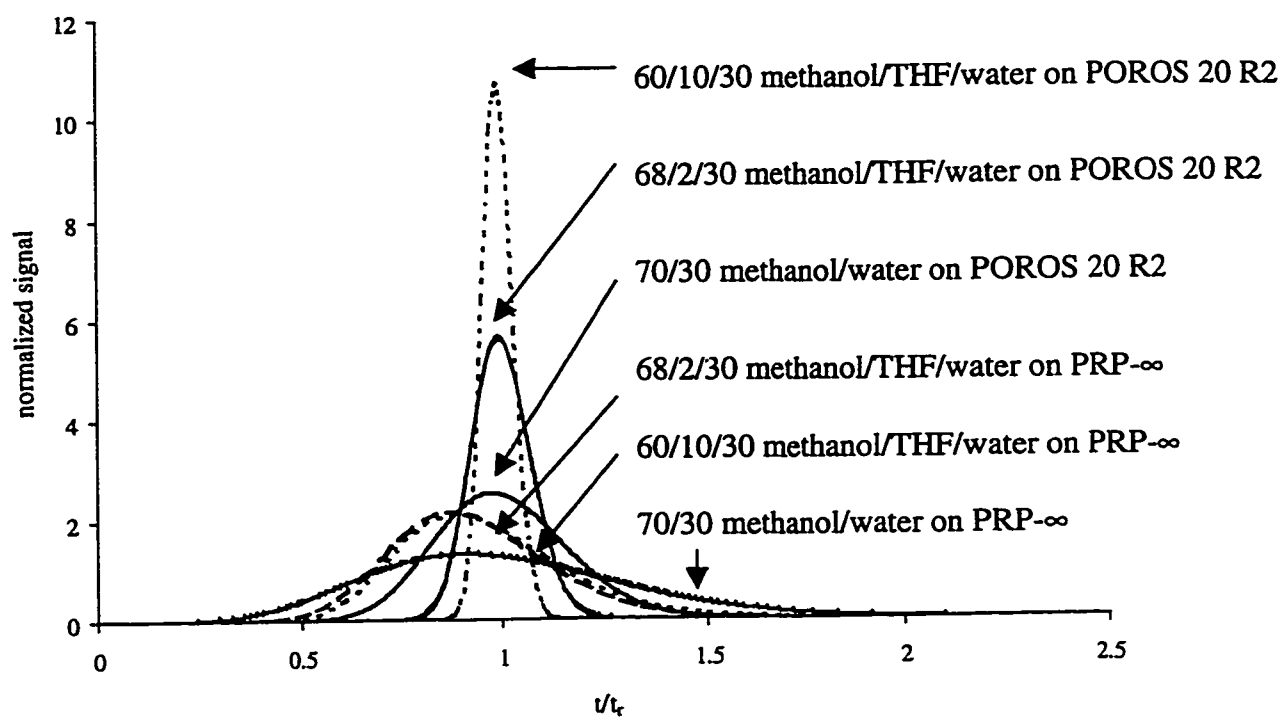


**Figure 5.19** Comparison of predicted naphthalene elution profiles at a flow rate of 0.004 mL/min from columns of PRP- $\infty$  and POROS 20 R2 using parameters from bi-exponential fits to sorption kinetics given in Tables 3.5, 4.3 and 5.6.

## Chapter 6

### Conclusions and Future Work

#### 6.1 Conclusions

Nominally non-porous PRP- $\infty$  was used in this work as a model for the matrix of porous PS-DVB packing materials for HPLC. Investigations into the cause for the poor performance often associated with these materials involved using solutes with varying solubility parameters and solvents of differing compositions of the organic modifiers, methanol and THF. It had been previously suggested that solutes with a solubility parameter similar to that of the matrix could dissolve in the matrix resulting in broad, tailed peaks, while solutes with solubility parameters dissimilar to that of the matrix would not enter the matrix. Naphthalene, with a solubility parameter quite close to that of the matrix ( $\Delta\delta \approx 1.2 \text{ (MPa)}^{1/2}$ ) in this study was found to enter the matrix, as expected, from a methanol/water solution. Octyl p-hydroxybenzoate, with a solubility parameter not quite as close to that of the matrix ( $\Delta\delta \approx 3.6 \text{ (MPa)}^{1/2}$ ), was also found to enter the polymer matrix from methanol/water solution, resulting in the same sorption capacity of the packing for the benzoate as for naphthalene. Evidently, a difference of 3.6 in the solubility parameter between the polymer and solute is not large enough to affect solute sorption.

It is known that the addition of a small amount of THF greatly improves peak shape. This improvement was previously thought only to be the result of a decrease in the hindrance to diffusion of the solute through the polymer matrix due to an increase in swelling of the PS-DVB polymer by the good solvent. In this study, it

was found that the addition of 2% THF to give a 68/2/30 methanol/THF/water solution decreased the capacity of the sorbent from that measured at a solution composition of 70/30 methanol/water, by 10% at an activity of naphthalene equal to 1. On the addition of THF in the sorption rate studies, to give a 68/2/30 methanol/THF/water solution, the diffusion coefficient of naphthalene within the polymer was found to have increased by 100% over that found from a solution of 70/30 methanol/water, though swelling had changed little. The addition of THF to give a solution of composition 60/10/30 methanol/THF/water did not increase the diffusion coefficient significantly above that found in 68/2/30 methanol/THF/water, though the swelling of the polymer was 70% greater in 60/10/30 methanol/THF/water than in 68/2/30 methanol/THF/water. Using a proposed structure for the polymer matrix of highly crosslinked nuclei surrounded by a gel region having a continuum of crosslinking densities, it is suggested here that the THF enters the smallest, most highly crosslinked, most highly hindered, of the permanent micropores and condenses, effectively blocking the most hindered sites within these permanent micropores. The presence of a small amount of THF in the methanol/water solvent when performing chromatographic separations on PS-DVB columns means the highly hindered sites in the matrix will be blocked and diffusion of the solute will be faster, resulting in narrower, less tailed elution profiles. The loss in capacity due to the addition of THF can be compensated for by reducing the amount of methanol in the solvent (i.e. decreasing the solvent strength). Thus, column efficiency, peak resolution and overall chromatographic performance are improved by the presence of THF.

Investigations of a perfusive PS-DVB packing, POROS 20 R2, showed that small, neutral solute molecules are susceptible to the same slow processes as they are on non-porous, PRP- $\infty$ . The isotherm studies showed that the sorption capacity for naphthalene within the matrix of POROS 20 R2 was the same as that found on PRP- $\infty$ . The reduction in capacity at the saturation point for naphthalene, was similar to that seen for PRP- $\infty$ , as a result of changing the solution composition from 70/30 methanol/water to 60/10/30 methanol/THF/water. Also, as with PRP- $\infty$ , the kinetics of sorption were greatly improved by the addition of a small amount of THF to the solvent. The addition of 2% THF to give a 68/2/30 methanol/THF/water solution increased the diffusion coefficient of naphthalene in POROS 20 R2 by 450%, while addition of further amounts (5% and 10% THF) increased the diffusion coefficient further, likely due to the combination of increased swelling of the polymer and further blockage of slower sites. As with PRP- $\infty$ , the diffusion kinetics were fit with a monodisperse model. The bidisperse nature of POROS 20 R2 was not apparent in the sorption kinetics, because the surface area contribution of the giga- and macro-pores was significantly less than that provided by the polymer matrix. The rates of sorption, as related to B in Tables 4.2 and 5.5, were faster on the 20  $\mu\text{m}$  diameter perfusive packing than on the 20  $\mu\text{m}$  diameter non-porous packing, as the result of the smaller effective diameter of the matrix.

The application of these perfusive packings to CEC where samples contain small, neutral molecules will be limited due to nature of the polymer matrix. While these packings can be made to experience intraparticle electroosmotic flow, small neutral molecules will still be able to enter the polymer matrix where diffusion

becomes hindered, resulting in broad, tailed peaks, similar to those seen with macroporous PS-DVB polymers.

## 6.2 Future Work

Due to the high mechanical strength and chemical stability of PS-DVB polymers, they are attractive alternatives to silica based packings for HPLC. The drawback of hindered diffusion, which produces broad, tailed peaks due to slow diffusion within the permanent micropores, must be addressed if these packings are to find widespread use in HPLC. Investigations into permanently blocking micropores in the rigid regions of the sorbent through polymerization to provide an interpenetrating network may prove beneficial. This may be accomplished using a molecule such as vinyltoluene. A small amount of vinyltoluene could be sorbed into the permanent micropores of the matrix and polymerization initiated by heat, light, radical initiation, etc.

Further work into the effect of the solubility parameter of a solute on the efficiency of PS-DVB packings could be undertaken. The solute, however, should have a solubility parameter that is further away from that of the matrix than the organic component of the mobile phase, methanol. In this circumstance it may be found that the solute cannot compete with methanol for sorption resulting in an improvement in its kinetics and a decrease in the amount which sorbs in the packing at equilibrium from a saturated solution.

The kinetic studies as performed using the shallow bed apparatus, where a solute is loaded for some time, eluted, and then loaded again for some other time and

eluted are very time consuming. One kinetic study requires loading and eluting the shallow bed 8 –10 times, and takes on the order of 24 hours. In order to shorten this time, a solute could be loaded to equilibrium and then desorbed, giving the entire desorption rate curve, i.e the decay of signal with time, in one run (Figure 6.1). The area under the desorption curve between zero and various times could provide the same information as the adsorption rate curve, but significantly reduce the time required to obtain the data. Also, using the apparatus in the adsorption mode, as was done in this thesis, the shortest adsorption time possible was limited by the operator, i.e. how fast the switch that allowed loading solution flow could be switched from off to on and then back to off, approximately 0.04 s. In the desorption mode, with computer collection of data, the shortest desorption time measurable will be limited by the detector response and the sampling interval. Using the shallow bed technique in the desorption mode, small diameter packing materials, e.g. 5  $\mu\text{m}$ , such as silica or zirconia, where the diffusion is less hindered could be studied. As shown in Figure 6.1, the sampling interval needed would be on the order of milliseconds in order to record the high initial rate of desorption.

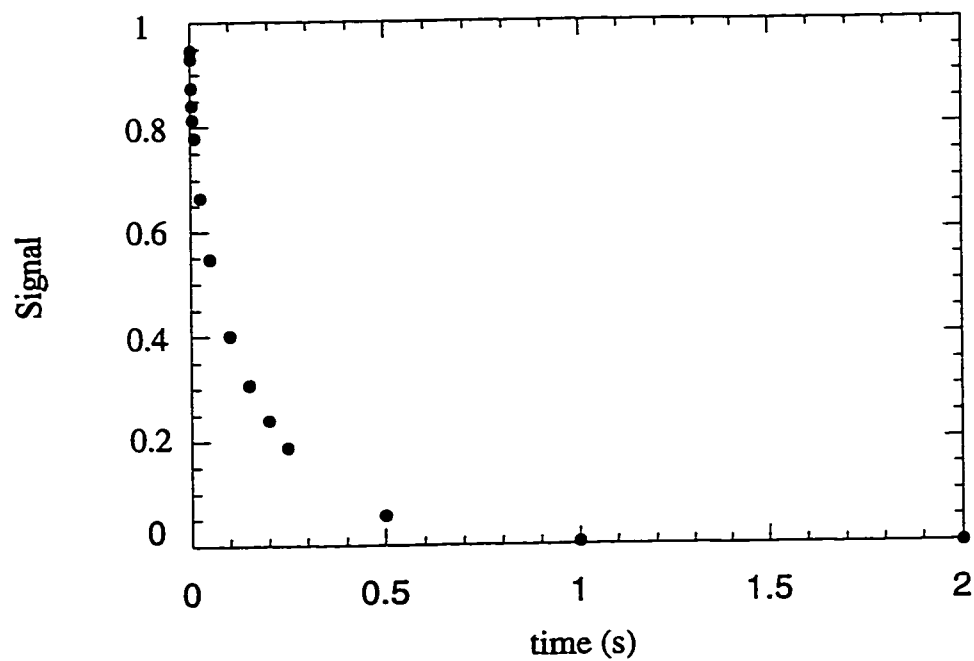


**Figure 6.1** Predicted desorption rate curve from a 5  $\mu\text{m}$  diameter particle, assuming a diffusion coefficient typical for silica,  $3 \times 10^{-8} \text{ cm}^2/\text{s}$ .

### Bibliography

- (1) Snyder, L. R.; Kirkland, J. J.; Glatch, J. L., *Practical HPLC Method Development*, 2nd ed.; John Wiley & Sons, Inc.: Toronto, 1997, Ch. 5.
- (2) Snyder, L. R.; Kirkland, J. J., *Introduction to Modern Liquid Chromatography*, 2nd ed.; John Wiley & Sons, Inc.: Toronto, 1979, Ch. 6.
- (3) Unger, K. K., *Porous Silica*; Elsevier: Amsterdam, 1979.
- (4) Sokolowski, A.; Wahlund, K. G., *J. Chromatogr.* **1980**, *189*, 299.
- (5) Kohler, J.; Chase, D. B.; Farlee, R. D.; Vega, A. J.; Kirkland, J. J., *J. Chromatogr.* **1986**, *352*, 275.
- (6) Majors, R. E., *LC/GC* **1986**, *4*, 872-876.
- (7) Stuurman, H. W.; Pettersson, C.; Heldin, E., *Chromatographia* **1988**, *25*, 685.
- (8) Kirkland, J. J.; vanStraten, M. A.; Claessens, H. A., *J. Chromatogr.* **1995**, *691*, 3.
- (9) Kirkland, J. J.; Henderson, J. W., *J. Chromatogr. Sci.* **1994**, *32*, 473.
- (10) Kirkland, J. J.; Henderson, J. W.; DeStefano, J. J.; vanStraten, M. A.; Claessens, H. A., *J. Chromatogr.* **1997**, *762*, 97.
- (11) Kirkland, J. J., *J. Chromatogr. Sci.* **1996**, *34*, 309.
- (12) Claessens, H. A.; vanStraten, M. A.; Kirkland, J. J., *J. Chromatogr.* **1996**, *728*, 259.
- (13) Tanaka, N.; Araki, M. In *Advances in Chromatography Selectivity and Retention in Chromatography*; Giddings, J. C., Grushka, E., Brown, P. R., Eds.; Marcel Dekker: New York, 1989; Vol. 30, pp 81-122.
- (14) Tweeten, K. A.; Tweeten, T. N., *J. Chromatogr.* **1986**, *359*, 111.

- (15) Lloyd, L. L., *J. Chromatogr.* **1991**, *544*, 201.
- (16) Benson, J. R.; Woo, D. J., *J. Chromatogr. Sci.* **1984**, *22*, 386.
- (17) *Pure Appl. Chem.* **1972**, *31*, 578.
- (18) Seidl, J.; Malinsky, J.; Dusek, K.; Heitz, W., *Adv. Polymer Sci.* **1967**, *5*, 113.
- (19) Kun, K. A.; Kunin, R. , *J. Polym. Sci. Part A-1* **1968**, *6*, 2689.
- (20) Hearn, J.; Smelt, P. L.; Wilkinson, M., C., *J. Colloid Interface Sci.* **1989**, *133*, 284.
- (21) Cornel, P.; Sontheimer, H., *Chem. Eng. Sci.* **1986**, *41*, 1791.
- (22) Heitz, W.; Kern, W., *Angew. Makromol. Chemie* **1967**, *1*.
- (23) Millar, J. R.; Smith, D. G.; Marr, W. E.; Kressman, T. R. E., *J. Amer. Chem. Soc.* **1963**, 218.
- (24) Galina, H.; Kolarz, B. N. *J. Appl. Polym. Sci.* **1979**, *24*, 891.
- (25) Poinescu, I. C.; Beldie, C.; Vlad, C., *J. Appl. Polym. Sci.* **1984**, *29*, 23.
- (26) Jun, Y.; Rongnan, X.; Juntan, Y., *J. Appl. Polym. Sci.* **1989**, *38*, 45.
- (27) Lloyd, L. L.; Kennedy, J. F. In *Process scale liquid chromatography*; Subramanian, G., Ed.; VCH Publishers: New York, 1995, pp 99-130.
- (28) Smith, R. M. J., *Chromatogr.* **1984**, *291*, 372.
- (29) Reeuwijk, H. J. E. M.; Tjaden, U. R., *J. Chromatogr.* **1986**, *353*, 339.
- (30) Lee, D. P., *J. Chromatogr.* **1988**, *443*, 143.
- (31) Lee, D. P.; Kindsvater, J. H., *Anal. Chem.* **1980**, *52*, 2425.
- (32) Reh, E.; Kapfer, U., *Chromatographia* **1990**, *30*, 666.
- (33) Lee, D. P., *J. Chromatogr. Sci.* **1982**, *20*, 203.
- (34) Paesen, J.; Roets, E.; Hoogmartens, J., *Chromatographia* **1991**, *32*, 162.

- (35) Gawdzik, B., *J. Chromatogr.* **1992**, *1992*, 115.
- (36) Roets, E.; Hoogmartens, J., *J. Chromatogr.* **1993**, *628*, 49.
- (37) Hoogmartens, J., *J. Pharm. Biomed. Anal.* **1992**, *10*, 845.
- (38) Katoh, S.; Terashima, M.; Sada, E.; Utsumi, H.; Kamiya, Y.; Yamada, K.; Majima, T. *J. Ferment.and Bioeng.* **1994**, *78*, 246.
- (39) Aramaki, K.; Hanai, T.; Walton, H. F., *Anal. Chem.* **1980**, *52*, 1963.
- (40) Huber, C. G.; Oefner, P. J.; Bonn, G. K., *Chromatographia* **1993**, *37*, 653.
- (41) Huber, C.; Oefner, P. J.; Bonn, G. K., *Anal. Biochem.* **1993**, *212*, 351.
- (42) Giddings, J. C. *Dynamics of Chromatography, Part I, Principles and Theory*; Marcel Dekker: New York, 1965.
- (43) Horvath, C.; Lin, H.-J., *J. Chromatogr.* **1978**, *149*, 43.
- (44) Afeyan, N. B.; Gordon, N. F.; Mazsaroff, I.; Varady, L.; Fulton, S. P.; Yang, Y. B.; Regnier, F. E., *J. Chromatogr.* **1990**, *519*, 1.
- (45) Afeyan, N. B.; Fulton, S. P.; Regnier, F. E., *J. Chromatogr.* **1991**, *544*, 267.
- (46) Fulton, S. P.; Afeyan, N. B.; Gordon, N. F.; Regnier, F. E., *J. Chromatogr.* **1991**, *547*, 452.
- (47) Lloyd, L. L.; Warner, F. P., *J. Chromatogr.* **1990**, *512*, 365.
- (48) Hofstetter, H.; Hofstetter, O.; Schurig, V., *J. Chromatogr.* **1997**, *764*, 35.
- (49) Schmidbauer, S.; Strobel, O., *Biochemica* **1997**, *1*, 28.
- (50) Schmidbauer, S.; Strobel, O., *Biochemica* **1997**, *2*, 24.
- (51) Matsumoto, H.; Kahn, E.; Komori, N., *Anal. Biochem.* **1997**, *251*, 116.
- (52) Rodrigues, A. E.; Chenou, C.; delaVega, M. R., *Chem. Eng. J.* **1996**, *61*, 191.
- (53) Ellerberger, T.; Doublié, S., *Biochemica* **1996**, *1*, 12.

- (54) Bowers, L. D.; Pedigo, S., *J. Chromatogr.* **1986**, *371*, 243.
- (55) Tanaka, N.; Kimata, K.; Hosoya, K.; Miyanishi, H.; Araki, T., *J. Chromatogr.* **1993**, *656*, 265.
- (56) Mori, S., *Anal. Chem.* **1978**, *50*, 745.
- (57) Stuurman, H. W.; Kohler, J.; Jansson, S. O.; Litzen, A., *Chromatographia* **1987**, *23*, 341.
- (58) Nevejans, F.; Verzele, M., *J. Chromatogr.* **1987**, *406*, 325.
- (59) Jerabek, K., *Anal. Chem.* **1985**, *57*, 1598.
- (60) Tanaka, N.; Ebata, T.; Hashizume, K.; Hosoya, K.; Araki, M., *J. Chromatogr.* **1989**, *475*, 195.
- (61) Tanaka, N.; Kimata, K.; Araki, T., *J. Chromatogr.* **1991**, *544*, 319.
- (62) Hennion, M.-C.; Coquart, V.; Guenu, S.; Sella, C., *J. Chromatogr.* **1995**, *712*, 287.
- (63) Lundgren, J. L.; Schilt, A. A., *Anal. Chem.* **1977**, *49*, 974.
- (64) Ordemann, D. M.; Walton, H. F., *Anal. Chem.* **1976**, *48*, 1728.
- (65) Grobe-Rhode, C.; Kicinski, H. G.; Kettrup, A., *Chromatographia* **1988**, *26*, 209.
- (66) Liru, D.; Xizhang, H.; Qihui, W.; Qingcheng, M.; Yuliang, L.; Youliang, Z., *Scientia Sinica (Series B)* **1982**, *25*, 905.
- (67) Allcock, H. R.; Lampe, F. W., *Contemporary Polymer Chemistry*; Prentice-Hall Inc: Toronto, 1981, Ch. 14.
- (68) Smith, R. M.; Garside, D. R., *J. Chromatogr.* **1987**, *407*, 19.

- (69) Cornel, P.; Sontheimer, H.; Summers, R. S.; Roberts, P. V., *Chem. Eng. Sci.* **1986**, *41*, 1801.
- (70) Dawkins, J. V.; Lloyd, L. L.; Warner, F. P., *J. Chromatogr.* **1986**, *352*, 157.
- (71) Li, D.; Remcho, V. T., *J. Micro. Sep.* **1997**, *9*, 389.
- (72) Choudhary, G.; Horvath, C., *J. Chromatogr.* **1997**, *781*, 161.
- (73) Nilsson, S.; Schweitz, L.; Petersson, M., *Electrophoresis* **1997**, *18*, 884.
- (74) Rice, C.; Whitehead, R., *J. Phys. Chem.* **1965**, *69*, 4017.
- (75) Fossey, L.; Cantwell, F. F., *Anal. Chem.* **1982**, *54*, 1693.
- (76) Loh, K.-C.; Wang, D. I. C., *J. Chromatogr.* **1995**, *718*, 239.
- (77) May, S.; Hux, R. A.; Cantwell, F. F., *Anal. Chem.* **1982**, *54*, 1279.
- (78) Taylor, G., *Proc. R. Soc. A* **1953**, *219*, 186.
- (79) Taylor, G., *Proc. R. Soc. A* **1954**, *225*, 473.
- (80) Aris, R., *Proc. R. Soc. A* **1956**, *235*, 67.
- (81) Li, J.; Cantwell, F. F., *J. Chromatogr.* **1996**, *726*, 37.
- (82) Snyder, L. R., *Principles of Adsorption Chromatography*; Marcel Dekker: New York, 1968, Ch. 3 and 4.
- (83) Kipling, J. J., *Adsorption from Solutions of Non-Electrolytes*; Academic Press: New York, 1965.
- (84) Ponec, V.; Knor, Z.; Cerny, S., *Adsorption on Solids*; Butterworths: London, 1974, Ch. 10.
- (85) Dondi, F.; Betti, A.; Blo, G.; Bigli, C.; Versino, B., *J. Chromatogr.* **1979**, *68*, 293.

- (86) deJong, A. W. J.; Kraak, J. C.; Poppe, H.; Nooitegedacht, F., *J. Chromatogr.* **1980**, *193*, 181.
- (87) Scott, R. P. W.; Kucera, P., *J. Chromatogr.* **1979**, *175*, 51.
- (88) Slaats, E. H.; Makarovski, W.; Fekete, J.; Poppe, H., *J. Chromatogr.* **1981**, *207*, 299.
- (89) Huber, J. F. K.; Alderlieste, E. T.; Harren, H.; Poppe, H. *Anal. Chem.* **1973**, *45*, 1337.
- (90) Scott, R. P. W.; Kucera, P., *J. Chromatogr.* **1977**, *142*, 213.
- (91) Scott, R. P. W.; Kucera, P., *J. Chromatogr.* **1978**, *149*, 93.
- (92) Scott, R. P. W.; Kucera, P., *J. Chromatogr.* **1979**, *171*, 37.
- (93) Cantwell, F. F.; Puon, S., *Anal. Chem.* **1979**, *51*, 623.
- (94) Terweij-Groen, C. P.; Heemstra, S.; Kraak, J. C., *J. Chromatogr.* **1978**, *161*, 69.
- (95) Knox, J. H.; Laird, G. R., *J. Chromatogr.* **1976**, *122*, 17.
- (96) Tomlinson, E.; Riley, C. M.; Jefferies, T. M., *J. Chromatogr.* **1979**, *173*, 89.
- (97) Hansen, S. H.; Helboe, P.; Thomsen, M.; Lund, U., *J. Chromatogr.* **1981**, *210*, 453.
- (98) Eksborg, S., *J. Chromatogr.* **1981**, *208*, 78.
- (99) Deelder, R. S.; Linssen, H. A. J.; Konignendijk, A. P.; Venne, J. L. M. v. d., *J. Chromatogr.* **1979**, *185*, 241.
- (100) Hung, C. T.; Taylor, R. B., *J. Chromatogr.* **1980**, *202*, 333.
- (101) Hung, C. T.; Taylor, R. B., *J. Chromatogr.* **1981**, *209*, 175.
- (102) Li, J.; Litwinson, L. M.; Cantwell, F. F., *J. Chromatogr.* **1996**, *726*, 25.

- (103) Helfferich, F., *Ion Exchange*; McGraw-Hill: New York, 1962, Ch. 6 and 9.
- (104) Horvath, C.; Lin, H. J., *J. Chromatogr.* **1976**, *126*, 401.
- (105) Weber, W. I. , Schloss Elmau, Bavaria, Germany 1983; Engineering Foundation; 679-692.
- (106) Suzuki, M., *Adsorption Engineering*; Elsevier: New York, 1990, 4-7.
- (107) Giddings, J. C., *Dynamics of Chromatography*; Dekker: New York, 1965, Ch. 2 and 6.
- (108) Frey, D. D.; Schweinheim, E.; Horvath, C., *Biotechnol. Prog.* **1993**, *9*, 273.
- (109) Ruthven, D. M., *Principles of Adsorption and Adsorption Processes*; Wiley: New York, 1984, Ch. 5 and 6.
- (110) Smith, J. M., In *Adsorption from Aqueous Solution: ACS Symposium Series*; W. J. Weber, J., Matijevic, E., Eds.; Amer. Chem. Soc., 1968; Vol. 79, pp 8-22.
- (111) Lenhoff, A. M., *J. Chromatogr.* **1987**, *384*, 285.
- (112) Groh, R.; Halasz, I., *Anal. Chem.* **1981**, *53*, 1325.
- (113) Condor, J. R.; Young, C. L., *Physicochemical Measurement by Gas Chromatography*; Wiley: New York, 1979, Ch. 12.
- (114) Marshall, D. B.; Burns, J. W.; Connolly, D. E., *J. Chromatogr.* **1986**, *360*, 13.
- (115) Waite, S. W.; Marshall, D. B.; Harris, J. M., *Anal. Chem.* **1994**, *66*, 2052.
- (116) Ruthven, D. M., In *Adsorption Sci. Technol.: NATO Adv. Study Inst. on Adsorption: Sci. Technol. Proceedings*; Rodrigues, A. E., LeVan, M. D., Tondeur, D., Eds.; Kluwer Academic Publishing: Boston, 1988; Vol. 158, pp 87-114.

- (117) vonMeerwall, E. D., *J. Non-Cryst. Solids* **1991**, 131-132 (Part2), 735.
- (118) Sarzanini, C.; Porta, V.; Mentasti, E., *New Journal of Chemistry* **1989**, 13, 463.
- (119) Reichenberg, D. *J. Amer. Chem. Soc.* **1953**, 75, 589.
- (120) Boyd, G. E.; Adamson, A. W.; L.S. Myers, J., *J. Amer. Chem. Soc.* **1947**, 69, 2836.
- (121) Aguwa, A. A.; Patterson, J. W.; Haas, C. N.; Noll, K. E., *J. Water Pollut. Control Fed.* **1984**, 56, 442.
- (122) Crank, J., *The Mathematics of Diffusion*, 2nd ed.; Oxford University Press: London, 1975, Ch. 6.
- (123) Anderson, D. J.; Walters, R. P., *J. Chromatogr. Sci.* **1984**, 22, 353.
- (124) Ruthven, D. M.; Garg, D. R., *Chem. Eng. Sci.* **1972**, 27, 417.
- (125) Paine, P. L.; Scherr, P., *Biophysical Journal* **1975**, 15, 1087.
- (126) Malone, D. M.; Anderson, J. L., *Chem. Eng. Sci.* **1978**, 33, 1429.
- (127) Deen, W. M., *AIChE J* **1987**, 33, 1409.
- (128) Bean, C. P., In *Membranes*; Eisenman, G., Ed.; Marcel Dekker Inc.: New York, 1972; Vol. 1.
- (129) Giddings, J. C.; Kucera, E.; Russell, C. P.; Myers, M. N., *J. Phys. Chem.* **1968**, 72, 4397.
- (130) Mavrovouniotis, G. M.; Brenner, H., *J. Coll. Int.erface Sci.* **1988**, 124, 269.
- (131) Brenner, H.; Gaydos, L. J., *J. Colloid Interface Sci.* **1977**, 58, 312.
- (132) Renkin, E. M., *J. Gen. Physiol.* **1954**, 38, 225.

- (133) Haberman, N. L.; Sayre, R. M. ; David W. Taylor Model Basin: Washington, D.C., 1958.
- (134) Wang, H.; Shalak, R., *J. Fluid Mech.* **1969**, *38*, 75.
- (135) Fujita, H.; Kishimoto, A.; Matsumoto, K., *Trans. Faraday Soc.* **1960**, *56*, 424.
- (136) Muhr, A. H.; Blanshard, J. M. V., *Polymer* **1982**, *23*, 1012.
- (137) Vrentas, J. S.; Duda, J. L., *J. Polym. Sci., A2* **1977**, *15*, 403-416.
- (138) Fujita, H., In *Diffusion in Polymers*; Crank, J., Park, G. S., Eds.; Academic Press: New York, 1968, pp 98-100.
- (139) Grushka, E.; E. J. Kikta, J., *J. Phys. Chem.* **1974**, *78*, 2297.
- (140) Grushka, E.; Maynard, V. R., *J. Phys. Chem.* **1973**, *77*.
- (141) Ouano, A. C., *Ind. Eng. Chem. Fundam.* **1972**, *11*, 268.
- (142) Pratt, K. C.; Slater, D. H.; Wakeham, W. A. ,*Chem. Eng. Sci.* **1973**, *28*, 1901.
- (143) Levenspiel, O.; Smith, W. K., *Chem. Eng. Sci.* **1957**, *6*, 227.
- (144) Cussler, E. L., *Diffusion: Mass Transfer in Fluid Systems*; Cambridge University Press: Cambridge, 1984, Ch. 4 and 5.
- (145) Sternberg, J. C., In *Advances in Chromatography*; Giddings, J. C., Keller, R. A., Eds.; McGraw-Hill: New York, 1966; Vol. 2.
- (146) Gowanlock, D.; Bailey, R.; Cantwell, F. F., *J. Chromatogr.* **1996**, *726*, 1.
- (147) Giddings, C., *Anal. Chem.* **1963**, *35*, 1999.
- (148) Giddings, J. C.; Eyring, H., *J. Phys. Chem* **1955**, *59*, 416.
- (149) Villermaux, J., *J. Chromatogr. Sci.* **1974**, *12*, 822.
- (150) Villermaux, J., *J. Chromatogr.* **1987**, *406*, 11.
- (151) Jandera, P.; Guiochon, G., *J. Chromatogr.* **1992**, *605*, 1.

- (152) Personal communication with Dan Lee; Hamilton Co., September 1996.
- (153) Ohkuma, T.; Hara, S., *J. Chromatogr.* **1987**, *400*.
- (154) Ohkuma, T.; Dobashi, A.; Hara, S., *J. Chromatogr.* **1996**, *728*, 97.
- (155) Fornstedt, T.; Zhong, G.; Guiochon, G., *J. Chromatogr.* **1996**, *741*, 1.
- (156) Coppi, S.; Betti, A.; Bighi, C.; Cartoni, G. P.; Coccioli, F., *J. Chromatogr.* **1988**, *442*, 97.
- (157) Treloar, L. R. G., *The Physics of Rubber Elasticity*; Clarendon Press: Oxford, 1975, Ch. 7.
- (158) Wilks, A. D.; Pietrzyk, D. J., *Anal. Chem.* **1972**, *44*, 676.
- (159) Mark, J. E.; Eisenberg, A.; Graessley, W. W.; Mandelkern, L.; Samulski, E. T.; Koenig, J. L.; Wignall, G. D., *Physical Properties of Polymers*, 2nd ed.; ACS: Washington, D.C, 1993, Ch. 1.
- (160) Davankov, V. A.; Rogozhin, S. V.; Tsyurupa, M. P., In *Ion Exchange and Solvent Extraction*; Marinsky, J. A., Marcus, Y., Eds.; Marcel Dekker, Inc: New York, 1977; Vol. 7.
- (161) Barton, A. F. M., *Handbook of Solubility Parameters and Other Cohesion Parameters*, 2nd ed.; CRC Press, 1991.
- (162) Errede, L. A.; Stoesz, J. D.; Sirvio, L. M., *J. Appl. Poly. Sci.* **1986**, *31*, 2721.
- (163) Snyder, L. R., *J. Chromatogr.* **1974**, *92*, 223.
- (164) Glajch, J. C.; Kirkland, J. J.; Squire, K. M.; Minor, J. M., *J. Chromatogr.* **1980**, *199*, 57.
- (165) Wang, Y. Ph.D. thesis, University of Alberta, Edmonton, 1998.
- (166) Errede, L. A., *Polymer Preprints, Japan* **1985**, *26*, 77.

- (167) Bolton, B. A.; Kint, S.; Bailey, G. F.; Scherer, J. R., *J. Phys. Chem.* **1986**, *90*, 1207.
- (168) Stamatialis, D. F.; Wessling, M.; Sanopoulou, M.; Strathmann, H.; Petropoulos, J. H., *J. Membrane Sci* **1997**, *130*, 75.
- (169) Hermans, P. H., *Physics and Chemistry of Cellulose Fibres*; Elsevier: New York, 1949, Ch. 2.
- (170) Hiemenz, P. C., *Principles of Colloid and Surface Chemistry*; Marcel Dekker: New York, 1986, Ch. 9.
- (171) Gregg, S. J.; Sing, K. S. W., *Adsorption, Surface Area and Porosity*; Academic Press: New York, 1967, Ch. 3.
- (172) Riddick, J. A.; Bunger, W. B., *Organic Solvents - Physical Properties and Methods of Purification*, 2 ed.; Wiley-Interscience: Toronto, 1970.
- (173) Margules, M. S. B., *Akad. Wiss. Wien, Math. - Naturwiss. KI. II* **1895**, *104*, 1234.
- (174) Signer, R.; Arm, H.; Daeniker, H., *Helv. Chim. Acta* **1969**, *52*, 2347.
- (175) Renon, H.; Prausnitz, J. M., *AIChE J* **1968**, *14*, 135.
- (176) Hall, D. J.; Mash, C. J.; Pemberton, R. C. ; NPL Report Chem 95, 1979.
- (177) Regnier, F. E., *Nature* **1991**, *350*, 634.
- (178) McCoy, M.; Kalghatgi, K.; Regnier, F. E.; Afeyan, N. J., *Chromatogr.* **1996**, *743*, 221.
- (179) McCoy, M. A.; Liapis, A. I.; Unger, K. K., *J. Chromatogr.* **1993**, *644*, 1.
- (180) Rodrigues, A. E.; Lu, Z. P.; Loureiro, J. M.; Carta, G., *J. Chromatogr.* **1993**, *653*, 189.

- (181) Rodrigues, A. E.; Loureiro, J. M.; Chenou, C.; delaVega, M. R., *J. Chromatogr. B* **1995**, *664*, 233.
- (182) Rodrigues, A. E.; Ramos, A. M. D.; Loureiro, J. M.; Diaz, M.; Lu, Z. P., *Chem. Eng. Sci.* **1992**, *47*, 4405.
- (183) Carta, G.; Rodrigues, A., *Chem. Eng. Sci.* **1993**, *48*, 3927.
- (184) Gustavsson, P.-E.; Larsson, P.-O., *J. Chromatogr.* **1996**, *734*, 231.
- (185) Li, D.; Remcho, V. T., *J. Micro Sep* **1997**, *9*, 389.
- (186) Rathore, A. S.; Horvath, C., *J. Chromatogr.* **1997**, *781*, 185.
- (187) Crego, A. L.; Gonzalez, A.; Marina, M. L., *Critical Reviews in Analytical Chemistry* **1996**, *26*, 261.
- (188) Shaw, D. J., *Introduction to Colloid and Surface Chemistry*, 4th ed.; Butterworth-Heinemann: Toronto, 1992, Ch. 7.
- (189) Wakao, N.; Smith, J. M., *Chem. Eng. Sci.* **1962**, *17*, 825.
- (190) Carberry, J. J., *AIChE. J.* **1962**, *8*, 557.
- (191) Mingle, J. O.; Smith, J. M., *AIChE. J.* **1961**, *7*, 243.
- (192) Doong, S. J.; Yang, R. T., *AIChE. J.* **1987**, *33*, 1045.
- (193) vanVliet, B. M., *Water Research* **1980**, *14*, 1719.
- (194) Petersen, E. E., *AIChE. J.* **1991**, *37*, 671.
- (195) Ruckenstein, E.; Vaidyanathan, A. S.; Youngquist, G. R., *Chem. Eng. Sci.* **1971**, *26*, 1305.
- (196) Nash, D. C.; Chase, H. A., *J. Chromatogr.* **1997**, *776*, 65.
- (197) Personal communication with Ross Edwards ; PerSeptive Biosystems, December 1997.

## APPENDIX 1

The data used in composing the Figures within this thesis are herein contained.

**Table A1.1** Data for sorption isotherm of naphthalene on PRP- $\infty$  column 1 from 70/30 methanol/water (Figure 3.3).

Concentration (M)	mol /g PRP- $\infty$ sorbed
$1.069 \times 10^{-6}$	$(9.4_{\pm 0.9}) \times 10^{-9}$
$1.069 \times 10^{-5}$	$(1.01 \pm 0.03) \times 10^{-6}$
$8.738 \times 10^{-5}$	$(9.4_{\pm 0.3}) \times 10^{-6}$
$2.149 \times 10^{-4}$	$(2.2_{\pm 0.1}) \times 10^{-5}$
$1.073 \times 10^{-3}$	$(7.0_{\pm 0.1}) \times 10^{-5}$
$1.980 \times 10^{-3}$	$(1.05 \pm 0.03) \times 10^{-4}$
$9.780 \times 10^{-3}$	$(3.6_{\pm 0.1}) \times 10^{-4}$
$1.962 \times 10^{-2}$	$(5.0_{\pm 0.1}) \times 10^{-4}$
$3.636 \times 10^{-2}$	$(6.3_{\pm 0.1}) \times 10^{-4}$
$4.661 \times 10^{-2}$	$(6.6_{\pm 0.1}) \times 10^{-4}$

**Table A1.2** Data for sorption isotherm of octyl p-hydroxybenzoate on PRP- $\infty$  columns 11-13 from 70/30 methanol/water (Figure 3.4).

Concentration (M)	mol /g PRP- $\infty$ sorbed
$4.604 \times 10^{-7}$	$(1.37 \pm 0.05) \times 10^{-7}$
$3.295 \times 10^{-6}$	$(6.0_1 \pm 0.1_5) \times 10^{-7}$
$2.083 \times 10^{-5}$	$(2.9_7 \pm 0.1_7) \times 10^{-6}$
$7.438 \times 10^{-5}$	$(9.9_3 \pm 0.2_4) \times 10^{-6}$
$1.190 \times 10^{-4}$	$(1.61 \pm 0.07) \times 10^{-5}$
$1.381 \times 10^{-4}$	$(1.82 \pm 0.04) \times 10^{-5}$
$2.072 \times 10^{-4}$	$(2.76 \pm 0.07) \times 10^{-5}$
$3.837 \times 10^{-4}$	$(3.9_6 \pm 0.1_9) \times 10^{-5}$
$7.078 \times 10^{-4}$	$(6.0_8 \pm 0.1_2) \times 10^{-5}$
$1.046 \times 10^{-3}$	$(8.5_2 \pm 0.4_4) \times 10^{-5}$
$1.555 \times 10^{-3}$	$(1.09 \pm 0.05) \times 10^{-4}$
$2.390 \times 10^{-3}$	$(1.34 \pm 0.06) \times 10^{-4}$
$3.510 \times 10^{-3}$	$(1.68 \pm 0.05) \times 10^{-4}$
$1.017 \times 10^{-2}$	$(2.42 \pm 0.08) \times 10^{-4}$
$1.981 \times 10^{-2}$	$(2.95 \pm 0.05) \times 10^{-4}$
$3.920 \times 10^{-2}$	$(3.2_2 \pm 0.1_0) \times 10^{-4}$
$5.165 \times 10^{-2}$	$(3.3_3 \pm 0.1_5) \times 10^{-4}$

**Table A1.3** Data for sorption isotherm of naphthalene on PRP- $\infty$  from 70/30 methanol/water, in volume units (Figure 3.5).

Concentration ( $\text{mL}_{\text{naph}}/\text{mL}_{\text{solution}}$ )	Volume sorbed/g PRP- $\infty$ ( $\text{mL/g}$ )
$8.426 \times 10^{-8}$	$(7.4_5 \pm 0.7_4) \times 10^{-6}$
$8.426 \times 10^{-7}$	$(7.9_4 \pm 0.2_7) \times 10^{-5}$
$6.888 \times 10^{-6}$	$(7.4_7 \pm 0.2_5) \times 10^{-4}$
$1.694 \times 10^{-5}$	$(1.78 \pm 0.08) \times 10^{-3}$
$8.458 \times 10^{-5}$	$(5.5_9 \pm 0.1_0) \times 10^{-3}$
$1.561 \times 10^{-4}$	$(8.2_7 \pm 0.2_4) \times 10^{-3}$
$7.709 \times 10^{-4}$	$(2.84 \pm 0.08) \times 10^{-2}$
$1.547 \times 10^{-3}$	$(3.97 \pm 0.08) \times 10^{-2}$
$2.866 \times 10^{-3}$	$(4.9_8 \pm 0.1_5) \times 10^{-2}$
$3.674 \times 10^{-3}$	$(5.4_2 \pm 0.1_4) \times 10^{-2}$

**Table A1.4** Data for sorption isotherm of octyl p-hydroxybenzoate on PRP- $\infty$  from 70/30 methanol/water, in volume units (Figure 3.5).

Concentration ( $\text{mL}_{\text{benz}}/\text{mL}_{\text{solution}}$ )	Volume sorbed /g PRP- $\infty$ ( $\text{mL/g}$ )
$6.928 \times 10^{-8}$	$(2.06 \pm 0.08) \times 10^{-5}$
$4.970 \times 10^{-7}$	$(9.0_{\pm} \pm 0.2_{\pm}) \times 10^{-5}$
$3.133 \times 10^{-6}$	$(4.4_{\pm} \pm 0.2_{\pm}) \times 10^{-4}$
$1.121 \times 10^{-5}$	$(1.50 \pm 0.04) \times 10^{-3}$
$1.792 \times 10^{-5}$	$(2.4_{\pm} \pm 0.1_{\pm}) \times 10^{-3}$
$2.078 \times 10^{-5}$	$(2.74 \pm 0.07) \times 10^{-3}$
$3.118 \times 10^{-5}$	$(4.1_{\pm} \pm 0.1_{\pm}) \times 10^{-3}$
$5.783 \times 10^{-5}$	$(5.9_{\pm} \pm 0.2_{\pm}) \times 10^{-3}$
$1.066 \times 10^{-4}$	$(9.1_{\pm} \pm 0.1_{\pm}) \times 10^{-3}$
$1.575 \times 10^{-4}$	$(1.28 \pm 0.07) \times 10^{-2}$
$2.342 \times 10^{-4}$	$(1.64 \pm 0.08) \times 10^{-2}$
$3.560 \times 10^{-4}$	$(2.0_{\pm} \pm 0.1_{\pm}) \times 10^{-2}$
$5.286 \times 10^{-4}$	$(2.53 \pm 0.07) \times 10^{-2}$
$1.532 \times 10^{-3}$	$(3.6_{\pm} \pm 0.1_{\pm}) \times 10^{-2}$
$2.984 \times 10^{-3}$	$(4.45 \pm 0.08) \times 10^{-2}$
$5.904 \times 10^{-3}$	$(4.8_{\pm} \pm 0.1_{\pm}) \times 10^{-2}$
$7.779 \times 10^{-3}$	$(5.0_{\pm} \pm 0.2_{\pm}) \times 10^{-2}$

**Table A1.5** Data from determination of shallow bed conditions on PRP- $\infty$  column 9 using a  $1.25 \times 10^{-6}$  M solution of octyl p-hydroxybenzoate in 70/30 methanol/water (Figure 3.6).

Linear velocity (cm/s)	Load time(s)	mol/g PRP- $\infty$ sorbed $\times 10^8$
11.6	5.0163	2.552
	9.9544	4.683
	15.1088	6.996
	20.0486	7.803
	25.1267	8.635
14.0	5.0768	2.496
	10.0704	4.684
	14.9800	5.766
	19.9997	7.174
	25.0034	8.931
15.8	4.7565	2.057
	10.0064	4.739
	15.0522	5.649
	19.9014	7.390
	25.0607	8.182
20.1	5.0145	2.521
	10.2016	4.659
	15.1274	5.978
	19.9892	7.572
	25.1154	7.621

**Table A1.6** Data for Trial 1 of naphthalene sorption kinetics on PRP- $\infty$  column 2 from  $9.685 \times 10^{-5}$  M solution of naphthalene in 70/30 methanol/water (Figure 3.7).

Load time (min)	mol /g PRP- $\infty$ sorbed x $10^6$	Fraction of equilibrium amount sorbed	Bt
0.25	$0.62 \pm 0.02$	0.065	0.0037
0.50	$1.12 \pm 0.03$	0.117	0.012
2	$2.15 \pm 0.05$	0.224	0.049
7.5	$5.5_6 \pm 0.1_3$	0.583	0.44
20	$7.2_6 \pm 0.1_7$	0.758	0.94
40	$8.6_4 \pm 0.2_0$	0.902	1.83
60	$9.2_7 \pm 0.2_1$	0.968	2.96
90	$9.3_2 \pm 0.2_1$	0.974	3.14

**Table A1.7** Data for Trial 2 of naphthalene sorption kinetics on PRP- $\infty$  column 3 from  $9.685 \times 10^{-5}$  M solution of naphthalene in 70/30 methanol/water (Figure 3.7).

Load time(min)	mol /g PRP- $\infty$ sorbed	Fraction of equilibrium amount sorbed	Bt
0.50	$(8.3_{\pm 0.2}) \times 10^{-7}$	0.094	0.0079
1	$(1.57 \pm 0.04) \times 10^{-6}$	0.177	0.030
5	$(4.14 \pm 0.08) \times 10^{-6}$	0.466	0.25
15	$(6.2_{\pm 0.1}) \times 10^{-6}$	0.707	0.76
30	$(7.3_{\pm 0.1}) \times 10^{-6}$	0.831	1.28
45	$(8.5_{\pm 0.1}) \times 10^{-6}$	0.947	2.44
60	$(8.4_{\pm 0.1}) \times 10^{-6}$	0.959	2.69
85	$(8.6_{\pm 0.1}) \times 10^{-6}$	0.978	3.33

**Table A1.8** Data for Trial 3 of naphthalene sorption kinetics on PRP- $\infty$  column 4 from  $9.685 \times 10^{-5}$  M solution of naphthalene in 70/30 methanol/water (Figure 3.7).

Load time(min)	mol /g PRP- $\infty$ sorbed x $10^6$	Fraction of equilibrium amount sorbed	Bt
0.50	$0.51 \pm 0.02$	0.055	0.0029
1	$1.12 \pm 0.03$	0.124	0.014
5	$3.71 \pm 0.09$	0.411	0.19
15	$5.6_8 \pm 0.1_3$	0.628	0.54
20	$6.5_9 \pm 0.1_5$	0.729	0.83
30	$7.2_1 \pm 0.1_6$	0.797	1.11
45	$8.1_7 \pm 0.1_8$	0.904	1.84
60	$8.4_7 \pm 0.1_9$	0.936	2.25
85	$8.5_6 \pm 0.1_9$	0.946	2.42

**Table A1.9** Data for determination of pre-equilibration time required for octyl p-hydroxybenzoate kinetics on PRP- $\infty$  (Figure 3.9). Solution was  $9.516 \times 10^{-5}$  M octyl p-hydroxybenzoate in 70/30 methanol/water.

Preconditioning time (min)	mol/g PRP- $\infty$ sorbed x $10^6$
0	$6.7_3 \pm 0.1_6$
10	$4.7_5 \pm 0.1_1$
20	$3.64 \pm 0.09$
30	$3.55 \pm 0.09$
40	$3.55 \pm 0.09$

**Table A1.10** Data for Trial 1 of octyl p-hydroxybenzoate sorption kinetics on PRP- $\infty$  column 14 from  $9.516 \times 10^{-5}$  M solution of octyl p-hydroxybenzoate in 70/30 methanol/water (Figure 3.10).

Load time (min)	Moles sorbed/g packing x $10^6$	Fraction of equilibrium amount sorbed	Bt
0.17	$0.54 \pm 0.03$	0.047	0.0019
0.50	$1.14 \pm 0.04$	0.099	0.0088
1	$2.37 \pm 0.06$	0.205	0.040
2	$2.88 \pm 0.07$	0.249	0.062
5	$4.2_0 \pm 0.1_0$	0.363	0.14
7.5	$5.0_0 \pm 0.1_2$	0.433	0.21
10	$5.5_7 \pm 0.1_3$	0.482	0.28
15	$6.3_2 \pm 0.1_4$	0.547	0.38
20	$6.9_8 \pm 0.1_6$	0.604	0.49
30	$8.1_5 \pm 0.1_9$	0.706	0.75
45	$9.9_0 \pm 0.2_2$	0.857	1.45
60	$10.0_1 \pm 0.2_3$	0.866	1.51

**Table A1.11** Data for Trial 2 of octyl p-hydroxybenzoate sorption kinetics on PRP- $\infty$  column 15 from  $9.516 \times 10^{-5}$  M solution of octyl p-hydroxybenzoate in 70/30 methanol/water (Figure 3.10).

Load time (min)	mol /g PRP- $\infty$ sorbed x $10^6$	Fraction of equilibrium amount sorbed	Bt
0.17	$0.61 \pm 0.02$	0.049	0.0021
0.50	$1.15 \pm 0.03$	0.092	0.0076
1	$1.97 \pm 0.05$	0.158	0.023
2	$2.46 \pm 0.06$	0.197	0.037
5	$4.04 \pm 0.09$	0.323	0.11
7.5	$5.3_0 \pm 0.1_2$	0.425	0.20
10	$5.7_6 \pm 0.1_3$	0.461	0.25
15	$7.0_7 \pm 0.1_6$	0.566	0.41
20	$7.4_4 \pm 0.1_7$	0.596	0.47
30	$8.3_6 \pm 0.1_9$	0.670	0.65
45	$9.7_5 \pm 0.2_2$	0.781	1.03
60	$10.7_7 \pm 0.2_4$	0.862	1.48

**Table A1.12** Data for sorption isotherm of naphthalene on PRP- $\infty$  column 5 from 68/2/30 methanol/THF/water (Figure 4.1).

Concentration (M)	mol /g PRP- $\infty$ sorbed
$1.321 \times 10^{-6}$	$(3.5 \pm 1.4) \times 10^{-7}$
$1.321 \times 10^{-5}$	$(8.4 \pm 0.5) \times 10^{-7}$
$6.604 \times 10^{-5}$	$(3.45 \pm 0.06) \times 10^{-6}$
$1.321 \times 10^{-4}$	$(6.9 \pm 0.2) \times 10^{-6}$
$2.093 \times 10^{-3}$	$(6.7 \pm 0.1) \times 10^{-5}$
$1.020 \times 10^{-2}$	$(2.39 \pm 0.02) \times 10^{-4}$
$2.488 \times 10^{-2}$	$(4.28 \pm 0.03) \times 10^{-4}$
$4.271 \times 10^{-2}$	$(5.70 \pm 0.05) \times 10^{-4}$
$5.025 \times 10^{-2}$	$(6.01 \pm 0.08) \times 10^{-4}$
$5.570 \times 10^{-2}$	$(6.14 \pm 0.08) \times 10^{-4}$

**Table A1.13** Data for sorption isotherm of naphthalene on PRP- $\infty$  column 7 from 60/10/30 methanol/THF/water (Figure 4.2).

Concentration (M)	mol/g PRP- $\infty$ sorbed
$1.000 \times 10^{-5}$	$(1.27 \pm 0.08) \times 10^{-6}$
$1.000 \times 10^{-4}$	$(2.85 \pm 0.08) \times 10^{-6}$
$1.006 \times 10^{-3}$	$(2.57 \pm 0.06) \times 10^{-5}$
$5.030 \times 10^{-3}$	$(9.5_6 \pm 0.3_2) \times 10^{-5}$
$9.949 \times 10^{-3}$	$(1.61 \pm 0.02) \times 10^{-4}$
$2.314 \times 10^{-2}$	$(2.91 \pm 0.05) \times 10^{-4}$
$4.051 \times 10^{-2}$	$(4.13 \pm 0.06) \times 10^{-4}$
$6.318 \times 10^{-2}$	$(5.15 \pm 0.05) \times 10^{-4}$
$8.298 \times 10^{-2}$	$(5.76 \pm 0.05) \times 10^{-4}$
$9.941 \times 10^{-2}$	$(5.7_4 \pm 0.1_2) \times 10^{-4}$

**Table A1.14** Data for sorption isotherm of naphthalene on PRP- $\infty$  from 68/2/30 methanol/THF/water, in volume units (Figure 4.3).

Concentration ( $\text{mL}_{\text{naph}}/\text{mL}_{\text{solution}}$ )	Volume sorbed/g PRP- $\infty$
$1.041 \times 10^{-7}$	$(2.7 \pm 1.2) \times 10^{-5}$
$1.041 \times 10^{-6}$	$(6.6 \pm 0.4) \times 10^{-5}$
$5.206 \times 10^{-6}$	$(2.72 \pm 0.05) \times 10^{-4}$
$1.041 \times 10^{-5}$	$(5.4 \pm 0.1) \times 10^{-4}$
$1.650 \times 10^{-4}$	$(5.2 \pm 0.1) \times 10^{-3}$
$8.040 \times 10^{-4}$	$(1.88 \pm 0.01) \times 10^{-2}$
$1.961 \times 10^{-3}$	$(3.37 \pm 0.03) \times 10^{-2}$
$3.367 \times 10^{-3}$	$(4.50 \pm 0.04) \times 10^{-2}$
$3.961 \times 10^{-3}$	$(4.74 \pm 0.06) \times 10^{-2}$
$4.391 \times 10^{-3}$	$(4.84 \pm 0.06) \times 10^{-2}$

**Table A1.15** Data for sorption isotherm of naphthalene on PRP- $\infty$  from 60/10/30 methanol/THF/water, in volume units (Figure 4.3).

Concentration ( $\text{mL}_{\text{naph}}/\text{mL}_{\text{solution}}$ )	Volume sorbed/g PRP- $\infty$
$7.882 \times 10^{-7}$	$(1.00 \pm 0.06) \times 10^{-4}$
$7.882 \times 10^{-6}$	$(2.25 \pm 0.06) \times 10^{-4}$
$7.930 \times 10^{-5}$	$(2.03 \pm 0.05) \times 10^{-3}$
$3.965 \times 10^{-4}$	$(7.4_{\text{g}} \pm 0.2_{\text{g}}) \times 10^{-3}$
$7.480 \times 10^{-4}$	$(1.27 \pm 0.01) \times 10^{-2}$
$1.821 \times 10^{-3}$	$(2.29 \pm 0.04) \times 10^{-2}$
$3.192 \times 10^{-3}$	$(3.26 \pm 0.05) \times 10^{-2}$
$4.982 \times 10^{-3}$	$(4.06 \pm 0.034) \times 10^{-2}$
$6.542 \times 10^{-3}$	$(4.54 \pm 0.04) \times 10^{-2}$
$7.836 \times 10^{-3}$	$(4.52 \pm 0.09) \times 10^{-2}$

**Table A1.16** Data for naphthalene sorption kinetics on PRP- $\infty$  column 6 from  $9.747 \times 10^{-5}$  M solution of naphthalene in 68/2/30 methanol/THF/water (Figure 4.4).

Load time (min)	mol /g PRP- $\infty$ sorbed x $10^6$	Fraction of equilibrium amount sorbed	Bt
0.5	$0.98 \pm 0.03$	0.152	0.022
1	$1.42 \pm 0.03$	0.218	0.046
3	$2.53 \pm 0.06$	0.390	0.17
7	$4.4_{\pm 0.1_0}$	0.693	0.71
15	$5.0_{\pm 0.1_0}$	0.783	1.04
20	$5.6_{\pm 0.1_2}$	0.866	1.51
30	$6.0_{\pm 0.1_3}$	0.931	2.18
40	$6.2_{\pm 0.1_3}$	0.959	2.69
60	$6.3_{\pm 0.1_4}$	0.974	3.16
90	$6.5_{\pm 0.1_4}$	1.014	$\infty$

**Table A1.17** Data for naphthalene sorption kinetics on PRP- $\infty$  column 8 from  $9.747 \times 10^{-5}$  M solution of naphthalene in from 60/10/30 methanol/THF/water (Figure 4.4).

Load time(min)	mol / g PRP- $\infty$ x $10^6$	Fraction of equilibrium amount sorbed	Bt
0.50	$0.62 \pm 0.02$	0.213	0.044
1	$0.86 \pm 0.03$	0.293	0.088
5	$1.85 \pm 0.05$	0.632	0.55
10	$2.09 \pm 0.06$	0.713	0.78
20	$2.54 \pm 0.07$	0.870	1.54
30	$2.74 \pm 0.07$	0.938	2.29
40	$2.81 \pm 0.07$	0.961	2.76
60	$2.92 \pm 0.07$	0.999	6.26
90	$3.03 \pm 0.08$	1.035	$\infty$

**Table A1.18** Data for methanol sorption isotherm on PRP- $\infty$  (Figure 4.7) (165)

Activity of methanol	Sorbed volume (mL/g)
0	0
0.00170	0.00188
0.00605	0.00392
0.0149	0.00508
0.0351	0.00871
0.0526	0.0107
0.0708	0.0152
0.0733	0.0146
0.214	0.0344
0.247	0.0401
0.37793	0.0668
0.408	0.0705
0.520	0.0915
0.839	0.122
0.997	0.131

**Table A1.19** Data for THF sorption isotherm on PRP- $\infty$  (Figure 4.7) (165).

Activity THF	Sorbed volume (mL/g)
0	0
0.00923	0.00937
0.0140	0.0109
0.0193	0.0154
0.0528	0.0269
0.0750	0.0356
0.163	0.0522
0.314	0.0717
0.485	0.0998
0.637	0.115
0.788	0.142
0.831	0.170
0.855	0.207
0.848	0.203
1.00	0.233

**Table A1.20** Data for swelling of PRP- $\infty$  in methanol (Figure 4.8)(165).

Activity methanol	Volume change (mL/g)
0.00621	0
0.0141	0.00664
0.0241	0.00932
0.0474	0.0178
0.0863	0.0213
0.214	0.0378
0.320	0.0464
0.411	0.0548
0.522	0.0593
0.625	0.0596
0.827	0.0653
0.946	0.0648

**Table A1.21** Data for swelling of PRP- $\infty$  in THF (Figure 4.8)(165).

Activity THF	Volume change (mL/g)
0	0
0.0132	0.00420
0.0266	0.0108
0.0679	0.0356
0.127	0.0461
0.261	0.0767
0.353	0.0922
0.516	0.103
0.776	0.112
0.812	0.116
0.832	0.120
0.878	0.125
1.00	0.127

**Table A1.22** Data for methanol swelling-sorption curve (Figure 4.9)(165).

Sorbed volume (mL/g)	Volume change (mL/g)
G	0
0.00389	0.00664
0.00609	0.00932
0.0100	0.0178
0.0162	0.0213
0.0366	0.0378
0.0545	0.0464
0.0700	0.0548
0.0875	0.0593
0.102	0.0596
0.123	0.0653
0.132	0.0645

**Table A1. 23** Data for THF swelling-sorption curve (Figure 4.10)(165).

Sorbed volume (mL/g)	Volume change (mL/g)
0	0
0.0107	0.00420
0.0182	0.0108
0.0330	0.0356
0.0453	0.0461
0.0627	0.0767
0.0727	0.0922
0.0911	0.103
0.121	0.107
0.138	0.112
0.155	0.116
0.177	0.120
0.203	0.124
0.217	0.125
0.229	0.127

**Table A1.24** Data for sorption isotherm of naphthalene on POROS 20 R2 column 1 from 70/30 methanol/water (Figure 5.4).

Concentration (M)	mol /g POROS sorbed
$1.094 \times 10^{-6}$	$(4.2_{\pm 0.4}) \times 10^{-7}$
$9.115 \times 10^{-6}$	$(1.9_{\pm 0.1}) \times 10^{-6}$
$4.558 \times 10^{-5}$	$(6.8_{\pm 0.2}) \times 10^{-6}$
$9.115 \times 10^{-5}$	$(1.31 \pm 0.05) \times 10^{-5}$
$5.001 \times 10^{-4}$	$(4.0_{\pm 0.1}) \times 10^{-5}$
$1.0370 \times 10^{-3}$	$(6.4_{\pm 0.2}) \times 10^{-5}$
$2.845 \times 10^{-3}$	$(1.21 \pm 0.05) \times 10^{-4}$
$7.065 \times 10^{-3}$	$(2.06 \pm 0.07) \times 10^{-4}$
$9.869 \times 10^{-3}$	$(2.62 \pm 0.08) \times 10^{-4}$
$2.490 \times 10^{-2}$	$(4.6_{\pm 0.1}) \times 10^{-4}$
$4.689 \times 10^{-2}$	$(7.8_{\pm 0.2}) \times 10^{-4}$

**Table A1.25** Data for sorption isotherm of naphthalene on POROS 20 R2 column 6 from 60/10/30 methanol/THF/water (Figure 5.6).

Concentration (M)	mol/g POROS sorbed x 10 <sup>6</sup>
$9.805 \times 10^{-6}$	$3.3_{\pm} \pm 0.1_0$
$7.844 \times 10^{-5}$	$3.7_{\pm} \pm 0.1_6$
$1.129 \times 10^{-3}$	$3.6_{\pm} \pm 0.1_5$
$4.667 \times 10^{-3}$	$9.7_{\pm} \pm 0.4_2$
$1.348 \times 10^{-2}$	$2.38 \pm 0.07$
$1.997 \times 10^{-2}$	$2.38 \pm 0.07$
$3.917 \times 10^{-2}$	$3.6_{\pm} \pm 0.1_1$
$5.892 \times 10^{-2}$	$4.7_{\pm} \pm 0.1_5$
$7.988 \times 10^{-2}$	$5.8_{\pm} \pm 0.1_9$
$9.321 \times 10^{-2}$	$6.1_{\pm} \pm 0.2_1$

**Table A1.26** Data from determination of shallow bed conditions on POROS 20 R2 column 1 from 2.052 M solution of naphthalene in 70/30 methanol/water (Figure 5.9).

Linear velocity (cm/s)	Time (s)	Area
4.0	0.0307	242650
	0.3985	942470
	0.4767	964450
	1.2005	1221000
	4.8779	1533100
	29.6640	2424200
7.0	0.0310	301860
	0.5807	1012200
	1.1908	1258200
	4.9622	1507800
	29.9230	2415900
8.9	0.0349	317430
	0.2848	834660
	0.6813	1053100
	4.8595	1481500
	29.8310	2398900

**Table A1.27** Data for Trial 1 of naphthalene sorption kinetics on POROS 20 R2 column 2 from  $7.844 \times 10^{-5}$  M solution of naphthalene in 70/30 methanol/water (Figure 5.10).

Load time (min)	mol/g POROS sorbed x $10^6$	Fraction of equilibrium amount sorbed	Bt
0.083	$1.33 \pm 0.07$	0.127	0.015
0.25	$1.76 \pm 0.08$	0.169	0.027
0.5	$2.36 \pm 0.09$	0.226	0.050
1	$3.0_2 \pm 0.1_2$	0.289	0.085
2.5	$4.1_5 \pm 0.1_6$	0.397	0.18
5	$6.0_9 \pm 0.2_2$	0.583	0.44
7.5	$7.7_6 \pm 0.2_8$	0.743	0.88
10	$8.7_6 \pm 0.3_2$	0.838	1.33
15	$9.3_4 \pm 0.3_4$	0.893	1.74
20	$9.7_7 \pm 0.3_5$	0.934	2.23
30	$9.9_4 \pm 0.3_6$	0.951	2.52
40	$10.2_0 \pm 0.3_7$	0.976	3.21
60	$10.4_9 \pm 0.3_8$	1.003	$\infty$
75	$10.4_4 \pm 0.3_8$	0.999	6.56
90	$10.4_1 \pm 0.3_7$	0.996	5.09

**Table A1.28** Data for Trial 2 of naphthalene sorption kinetics on POROS 20 R2 column 2 from  $7.844 \times 10^{-5}$  M solution of naphthalene in 70/30 methanol/water (Figure 5.10).

Load time (min)	mol/g POROS sorbed $\times 10^6$	Fraction of equilibrium amount sorbed	Bt
0.167	$1.43 \pm 0.07$	0.147	0.020
0.5	$1.98 \pm 0.09$	0.203	0.040
1	$2.6_3 \pm 0.1_1$	0.271	0.074
2	$3.4_7 \pm 0.1_4$	0.357	0.14
5	$5.2_8 \pm 0.2_0$	0.543	0.37
7.5	$6.7_5 \pm 0.2_5$	0.695	0.72
10	$8.0_1 \pm 0.2_9$	0.824	1.25
15	$8.4_7 \pm 0.3_1$	0.871	1.55
20	$8.8_6 \pm 0.3_2$	0.912	1.93
30	$9.2_6 \pm 0.3_3$	0.953	2.56
40	$9.6_3 \pm 0.3_5$	0.991	4.22
60	$9.5_8 \pm 0.3_5$	0.986	3.74
90	$9.6_0 \pm 0.3_5$	0.988	3.94

**Table A1.29** Data for naphthalene sorption kinetics on POROS 20 R2 column 3 from  $7.844 \times 10^{-5}$  M solution of naphthalene in 68/2/30 methanol/THF/water (Figure 5.13).

Load time (min)	mol/g POROS sorbed $\times 10^6$	Fraction of equilibrium amount sorbed	Bt
0.083	$1.89 \pm 0.09$	0.215	0.045
0.25	$2.7_5 \pm 0.1_0$	0.312	0.10
0.5	$3.8_7 \pm 0.1_5$	0.440	0.22
1	$5.2_9 \pm 0.2_0$	0.601	0.48
2	$6.5_3 \pm 0.2_4$	0.743	0.88
5	$8.1_0 \pm 0.2_9$	0.921	2.04
10	$8.6_1 \pm 0.3_1$	0.980	3.39
20	$8.6_2 \pm 0.3_1$	0.980	3.40
30	$8.7_8 \pm 0.3_2$	0.999	6.35
40	$8.7_8 \pm 0.3_2$	0.998	5.70
60	$8.8_4 \pm 0.3_2$	1.006	$\infty$
90	$8.8_0 \pm 0.3_2$	1.001	$\infty$

**Table A1.30** Data for naphthalene sorption kinetics on POROS 20 R2 column 4 from  $7.844 \times 10^{-5}$  M solution of naphthalene in 65/5/30 methanol/THF/water (Figure 5.13).

Load time (min)	mol/g POROS sorbed $\times 10^6$	Fraction of equilibrium amount sorbed	Bt
0.083	$1.91 \pm 0.08$	0.300	0.092
0.25	$2.7_6 \pm 0.1_1$	0.431	0.21
0.55	$3.6_4 \pm 0.1_4$	0.569	0.42
1	$4.6_5 \pm 0.1_7$	0.727	0.82
2	$5.4_6 \pm 0.2_0$	0.855	1.43
5	$6.1_7 \pm 0.2_2$	0.969	2.98
10	$6.3_0 \pm 0.2_3$	0.986	3.78
20	$6.3_8 \pm 0.2_3$	0.998	5.89
30	$6.4_2 \pm 0.2_3$	1.005	$\infty$
40	$6.4_5 \pm 0.2_3$	1.010	$\infty$
60	$6.4_7 \pm 0.2_3$	1.012	$\infty$
90	$6.4_9 \pm 0.2_4$	1.016	$\infty$

**Table A1.31** Data for naphthalene sorption kinetics on POROS 20 R2 column 5 from  $7.844 \times 10^{-5}$  M solution of naphthalene in 60/10/30 methanol/THF/water (Figure 5.13).

Load time (min)	Mol/g POROS sorbed $\times 10^6$	Fraction of equilibrium amount sorbed	Bt
0.083	$1.44 \pm 0.08$	0.391	0.17
0.25	$2.0_6 \pm 0.1_0$	0.559	0.40
0.5	$2.5_9 \pm 0.1_2$	0.703	0.74
1	$3.1_0 \pm 0.1_4$	0.843	0.35
2	$3.4_7 \pm 0.1_5$	0.942	2.35
5	$3.5_7 \pm 0.1_6$	0.971	3.03
10	$3.6_6 \pm 0.1_6$	0.993	4.45
20	$3.7_5 \pm 0.1_6$	1.012	$\infty$
30	$3.7_2 \pm 0.1_6$	1.011	$\infty$
45	$3.7_2 \pm 0.1_6$	1.011	$\infty$
60	$3.7_4 \pm 0.1_6$	1.015	$\infty$
90	$3.7_6 \pm 0.1_6$	1.020	$\infty$

## APPENDIX 2

This program was written in Matlab by David Gowanlock and is used in the prediction of elution profiles. Predictions are based on a bi-exponential fit to the sorption rate curves.

```

clc
clear
%   Elution Chromatogram from Kinetic Curve
%   David Gowanlock  May 31, 1991
%
%   The following was written to predict elution chromatogram profiles from
%   shallow bed kinetic plots. In this case, the shallow bed kinetic plots have been
%   fit to a bi-exponential of the following form:
%    $n_{obs} = n_0 - (n_1 * \exp(-k_1 * t)) - (n_2 * \exp(-k_2 * t))$ 
%       1 = fast sites
%       2 = slow sites
%
%   The equation used to produce the elution profiles corresponding to each of the
%   above type of site is given in the following reference (see function probdist):
%
%   J. C. Giddings, Anal. Chem., Vol. 35, Page 1999, Dec. 1963
%
%   Variable list
%   k_prime = k'
%   k = rate constant from kinetic curve
%   n = fraction of a particular type of site
%   ord = order of  bessell function
%   ts = t-tm

```

```

%      tm = time for mobile phase
%      t = time from injection
%      ka = adsorption rate constant
%      kd = desorption rate constant
%      Pts = probability distribution with respect to time
%      nanarl = used to detect NaN warnings that can arise in the calculation of
                bessell values in the function probdist
%      stepsz = stepsize along the time axis
%      fr_no_sl = fraction not interacting with the slow sites (fraction not slow)
%      fr_sl = fraction interacting with the slow sites (fraction slow)
%      theor_ratio = theoretical ratio of solute interacting with slow sites to solute
                not interacting with slow sites
%      act_ratio = actual ratio of solute interacting with slow sites to solute not
                interacting with slow sites
%      maxsz = maximum value of range of ts1 and ts2 values
%
%      -----
%      This section is where the initial parameters used throughout the rest of the
%      program are entered.
%
stepsz = 1000;
maxsz = 200001
k_prime = 246.1
k1 = 0.7822
k2 = 0.04532
n1 = 2.722e-6
n2 = 8.195e-6
tm = 182.5

n0 = n1 + n2

```

```

% -----
%   The following calculates the elution profile for the fast sites.
%
ord1 = 1
ts1 = 1:stepsz:maxsz;
k_prime1 = k_prime.*n1 ./ n0
ka1 = k1 ./ (1 + (k_prime1.^(-1)))
kd1 = k1 ./ (k_prime1 + 1)
tm1 = tm

[Pts1,nanalrt1] = probdistrib(ts1,ka1,kd1,tm1,ord1);
% -----
%   The following calculates the elution profile for the slow sites.
%
ord2 = 1;
ts2 = 1:stepsz:maxsz;
k_prime2 = k_prime .* n2 ./ n0
ka2 = k2 ./ (1 + (k_prime2.^(-1)))
kd2 = k2 ./ (k_prime2 + 1)
tm2 = tm

[Pts2,nanalrt2] = probdistrib(ts2,ka2,kd2,tm2,ord2);
% -----
%   The following convolves the elution profiles and plots the results along with
%   the elution profiles for each type of site acting alone.
%
Pts1_2 = conv(Pts1,Pts2);
ts1_2 = 1:stepsz:2.*(maxsz-.5);
ymax = max([max(Pts1),max(Pts2)])
P1s = 1.0 .* Pts1 .* ymax ./ max(Pts1);
P2s = .7 .* Pts2 .* ymax ./ max(Pts2);

```

```

P1_2s = .5 .*Pts1_2 .* ymax / max(Pts1_2);
axis([0,2.*maxsz,0,1.05.*ymax])
plot(ts1,P1s,ts2,P2s,ts1_2,P1_2s)
xlabel('ts'), ylabel('P(ts)')
pause
% -----
%      Integration of the peaks.
%
area1_2 = integrate_2pt(ts1_2,Pts1_2)
area1 = integrate_2pt(ts1,Pts1)
area2 = integrate_2pt(ts2,Pts2)
% -----
%      This section scales 1 with the convolution of 1 & 2
%
fr_no_sl = exp(-1 .* ka2 .* tm2);
fr_sl = 1.0 - fr_no_sl;
theor_ratio = fr_sl ./fr_no_sl;
act_ratio = area1_2 ./ area1;
correction = theor_ratio ./act_ratio;
Pts1_2 = Pts1_2 .*correction;
area1_2 = integrate_2pt(ts1_2,Pts1_2)
axis;
plot(ts1,Pts1,ts1_2,Pts1_2)
xlabel('ts'),ylabel('P(ts)')
pause
% -----
%      This section adds 1 to the convolution of 1 & 2
%
for l = 1:length(Pts1);
Ptsnet(1) = Pts1(1) + Pts1_2(1);
End

```

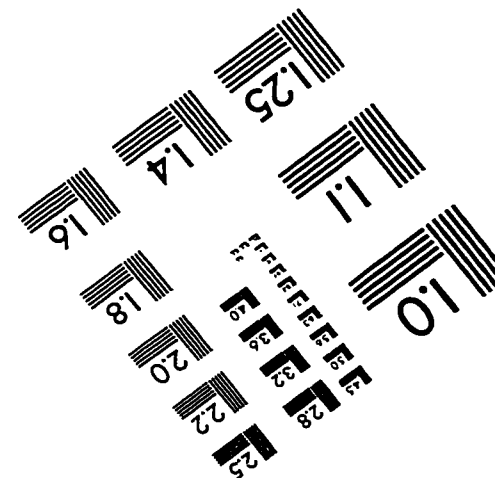
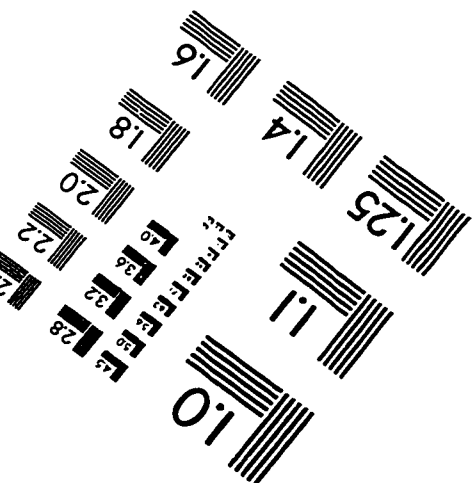
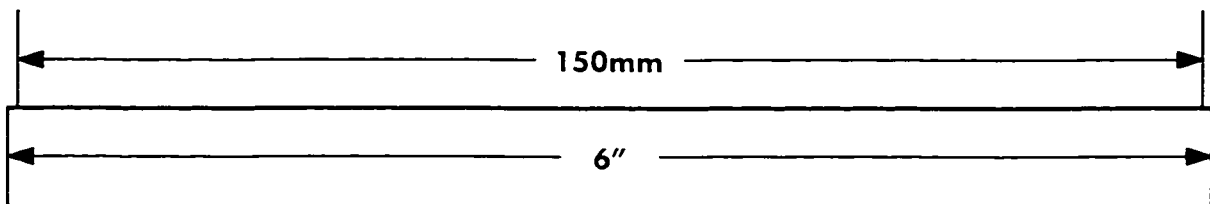
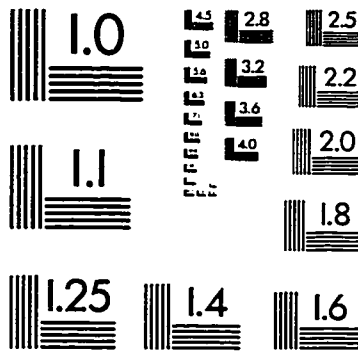
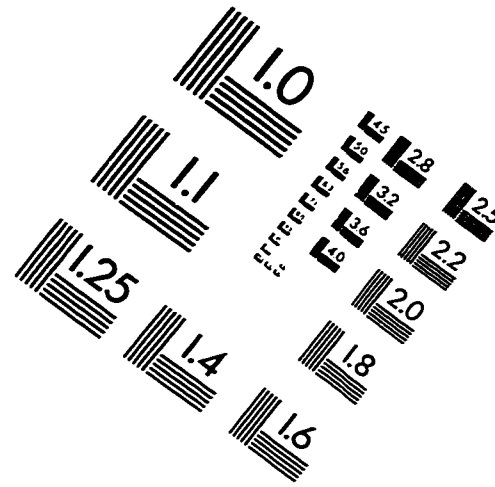
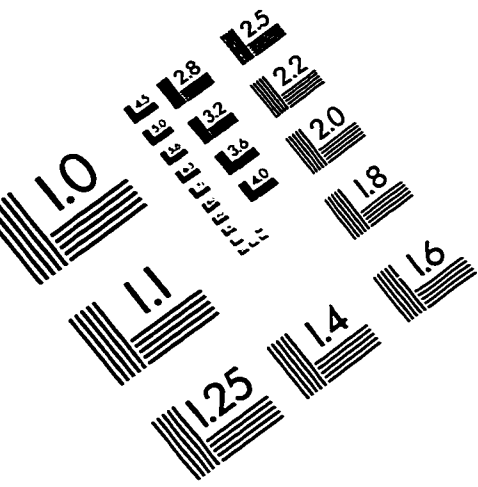
```

Axis([0,max(ts1),0,1.05.*max(ptsnet)])
Plot(ts1,Pts1,ts1_2,Pts1_2,ts1,Ptsnet)
Xlabel('ts'), ylabel('P(ts)')
Pause

% -----
%      This section plots the elution profile from time of injection, not ts
%      (ts = t=tm)
%
t1 = ts1 + tm;
axis;
plot(t1,Ptsnet)
xlabel('t'), ylabel ('P(t)')
x = t1';
y = Ptsnet';
z = [x,y];
save plot.dat z/ascii;

```

# IMAGE EVALUATION TEST TARGET (QA-3)



APPLIED IMAGE, Inc  
1653 East Main Street  
Rochester, NY 14609 USA  
Phone: 716/482-0300  
Fax: 716/288-5989

© 1993, Applied Image, Inc., All Rights Reserved